



TUM School of Engineering and Design

Non-Uniform Physical Properties and Operating Conditions in Lithium-Ion Batteries

Dipl.-Ing. Univ. Franz Benjamin Spingler

Vollständiger Abdruck der von der TUM School of Engineering and Design der
Technischen Universität München zur Erlangung des akademischen Grades eines

Doktors der Ingenieurwissenschaften (Dr.-Ing.)

genehmigten Dissertation.

Vorsitz: Prof. Dr.-Ing. Markus Lienkamp
Prüfer der Dissertation: 1. Prof. Dr.-Ing. Andreas Jossen
2. Prof. Dr.-Ing. Michael A. Danzer

Die Dissertation wurde am 18.01.2022 bei der Technischen Universität München eingereicht
und durch die School of Engineering and Design am 31.05.2022 angenommen.

Abstract

The increasing electrification of industry, households, and transport requires high-performance, safe lithium-ion batteries that can be manufactured with low resource input and at low cost. The constant endeavour to increase energy density and the need for economic, resource, and process efficiency imply, on the one hand, an increase in the inherent safety risk and, on the other hand, compromises in terms of battery design and manufacturing control. To find reasonable compromises between competing priorities whilst ensuring safe operation, it is necessary to know how deviations from ideal battery design and ideal manufacturing quality affect the operational behavior of lithium-ion batteries and how safety- and performance-critical conditions can be detected during operation.

To this end, novel experimental and theoretical characterization methods were developed and used to perform investigations on commercial and laboratory-produced lithium-ion cells. One focus was the non-destructive detection of inhomogeneous states during operation using the example of a locally contaminated cell. The investigations showed that locally resolved measurement of cell thickness has great potential for the early detection of aging phenomena. A second focus was the analysis of the relationship between intercalation-induced electrode expansion, non-uniform external mechanical loads, and local current density variations. It was demonstrated that local mechanical load peaks can generate current density variations of sufficient magnitude to cause damaging lithium plating. A third focus was the investigation of non-uniform lithiation states within cells and their significant effects on the usable capacity when cells are operated under certain load profiles. The question of the extent to which the current density distribution and the local lithiation states within a cell are influenced by the interaction of geometric effects and temperature gradients was also addressed.

Based on the results of these focus investigations, recommendations for further research projects are given and the industrial applicability of the findings is discussed. The work demonstrates the need to consider non-ideal properties in the design and operational management of battery systems.

Kurzfassung

Die zunehmende Elektrifizierung von Industrie, Haushalten und Verkehr erfordert leistungsfähige, sichere Lithium-Ionen-Batterien, die mit geringem Ressourceneinsatz und zu niedrigen Kosten hergestellt werden können. Die stets angestrebte Erhöhung der Energiedichte und der Zwang zur Rationalisierung bedingen einerseits eine Erhöhung des inhärenten Sicherheitsrisikos und andererseits Kompromisse hinsichtlich des Batteriedesigns sowie der Fertigungskontrolle. Zur Findung sinnvoller Kompromisse und Gewährleistung eines sicheren Betriebs ist es notwendig zu wissen, wie sich Abweichungen von idealem Batteriedesign und idealer Herstellungsqualität auf das Betriebsverhalten von Lithium-Ionen-Batterien auswirken und wie kritische Zustände im Betrieb erkannt werden können.

Im Rahmen dieser Arbeit wurden zu diesem Zweck neuartige experimentelle und theoretische Charakterisierungsmethoden entwickelt und damit Untersuchungen an kommerziellen und im Labor hergestellten Lithium-Ionen-Zellen vorgenommen. Ein Schwerpunkt war die zerstörungsfreie Detektion von inhomogenen Zuständen während des Betriebs am Beispiel einer lokal kontaminierten Zelle. Bei den Untersuchungen zeigte sich, dass die lokal aufgelöste Messung der Zelldicke großes Potential zur Früherkennung von Alterungsphänomenen aufweist. Ein zweiter Schwerpunkt war die Analyse des Zusammenhangs von interkalationsbedingter Elektrodenausdehnung, ungleichmäßiger mechanischer Zellverspannung und lokalen Stromdichteveränderungen. Es wurde dabei nachgewiesen, dass lokale mechanische Belastungsspitzen derartige Stromdichteveränderungen erzeugen können, dass es zum schädlichen Lithium Plating kommt. Einen dritten Schwerpunkt bildete die Untersuchung von ungleichmäßigen Lithiierungszuständen innerhalb einer Zelle und ihren signifikanten Auswirkungen auf die nutzbare Kapazität als Folge bestimmter Lastprofile. Es wurde dabei auch die Frage behandelt, inwieweit die Stromdichteverteilung und die lokalen Lithiierungszustände innerhalb einer Zelle durch das Zusammenspiel von geometrischen Effekten und Temperaturgradienten beeinflusst werden.

Basierend auf den Ergebnissen dieser Untersuchungsschwerpunkte werden Empfehlungen für weitere Forschungsprojekte gegeben und die industrielle Nutzbarkeit der Erkenntnisse diskutiert. Die Arbeit zeigt die Notwendigkeit, nichtideale Eigenschaften bei der Auslegung und Betriebsführung eines Batteriesystems zu berücksichtigen.

Contents

Abbreviations	V
Symbols	VII
1 Introduction	1
1.1 Considering Imperfection: From Cell Design to Operational Strategy	2
1.2 Non-Uniform Physical Properties and Operating Conditions	3
1.3 Research Aims, Scope and Delimitations	7
1.4 Thesis Outline	8
2 Method Development	11
2.1 Operando Detection of Lithium Plating via Thickness Measurements	11
2.1.1 Locally-Resolved Operando Thickness Measurements of Pouch Cells . .	13
2.1.2 Technical Limitations	15
2.2 Electrochemical Dilatometry	16
2.2.1 Improvements of the Electrochemical Performance	18
2.2.2 Technical Limitations	19
2.3 Detection and Quantification of Electrode State of Charge Inhomogeneity . . .	21
2.3.1 Post-Mortem Quantification of Electrode State of Charge Distribution via Coin Cells	23
2.3.2 Comparison to X-Ray Diffraction and Possible Improvements	23
3 Cell Diagnosis using Locally-Resolved Thickness Measurements	25
3.1 Application of a Locally-Resolved Thickness Measurement to Detect Cell In- homogeneity	26
3.2 Optimizing Operational Strategies by On-Line Detection of Lithium Plating . .	37
4 Linking Uneven Cell Compression to the Occurrence of Lithium Plating	51
4.1 Measuring Thickness Changes of Electrodes in Operation	52
4.2 Modeling the Effect of Local Compression on the Current Distribution and Propensity for Lithium Plating	65
5 The Effect of Lateral State-of-Charge Gradients on the Apparent Capacity	83
6 Summary, Discussion and Outlook	97
References	103

List of Publications	117
Acknowledgment	119

Abbreviations

BEV	battery electric vehicle
CC	constant current
CC-CV	constant current - constant voltage
CV	constant voltage
DEC	diethylene carbonate
DMC	dimethylene carbonate
DVA	differential voltage analysis
EC	ethylene carbonate
ICA	incremental capacity analysis
ICP-MS	inductively coupled plasma mass spectroscopy
ICP-OES	inductively coupled plasma optical emission spectroscopy
LCO	lithium cobalt oxide
LFP	lithium iron phosphate
LTO	lithium titanate oxide
NCA	lithium cobalt aluminum
NDP	neutron depth profiling
NMC	lithium nickel manganese cobalt oxide
OCV	open-circuit voltage
SEM	scanning electron microscopy
SOC	state of charge
SOH	state of health
XRD	X-ray diffraction

Symbols

Δt_{int}	thickens change caused by intercalation in μm
$\Delta t_{plating}$	thickens change caused by lithium plating in μm
e	elementary charge, $1.602\,176\,62 \times 10^{-19}$ A s
F	Faraday's constant, $96\,485$ C mol $^{-1}$
n	number of electrode layers
N_A	Avogadro constant, $6.022\,140\,86 \times 10^{23}$ mol $^{-1}$
R	universal gas constant, 8.314 J mol $^{-1}$ K $^{-1}$
σ	ionic conductivity in S m $^{-1}$
σ_{eff}	effective ionic conductivity in S m $^{-1}$
V_m	molar volume in mol $^{-1}$
ξ	porosity

1 Introduction

Ever since their commercialization in 1991 by Sony Corp., the use of lithium-ion batteries has grown exponentially. Between 2008 and 2018 the growth rate of lithium-ion battery capacity averaged 24 % per year [1] and is forecast to increase to 30 % per year for the decade 2020 - 2030 [2]. Until ca. 2012, the market growth was mainly propelled by consumer demand for portable electronic devices. In recent years, fueled by direct and indirect subsidies in G7 economies and China, electric vehicles have become the main driver for growth in the battery market. Already by 2025, electric vehicles are forecast to be the destination for 75 % of the battery capacity produced worldwide, followed by consumer electronics (ca. 15 %) and stationary energy storage (ca. 10 %). [2]

On the one hand, lithium-ion batteries are hailed as an enabler of CO₂ saving technologies: Combined with electric motors they are poised to replace fossil-fuel burning thermal engines in the transport sector. Such developments have the potential to significantly reduce greenhouse gas emissions if the energy is generated using renewable resources [3]. The latter is a goal in itself, and lithium-ion batteries, whether installed in designated stationary storage systems or connected to the grid temporarily when a battery electric vehicle (BEV) is parked, can help achieve this goal by smoothing the fluctuations in electricity generation from wind and solar energy [4].

On the other hand, lithium-ion batteries have come under scrutiny for their own significant carbon footprint and the environmental and societal implications of the sourcing of some of the primary materials required for their production [5–7]. In comparison to cars powered by internal combustion engines, where the vast majority of CO₂ equivalent associated with the life cycle of an individual car is produced during driving, BEVs carry a comparatively larger CO₂ burden when they leave the assembly line [3, 8]. With regards to consumer electronics, it is a frequent criticism that failing batteries put a premature end to the lifetime of otherwise functional devices, causing large amounts of electronics waste and resource consumption for replacements [9]. Last but not least, lithium-ion batteries are associated with serious safety risks. Although a rare occurrence, these batteries can self-ignite, producing toxic smoke and violent fires which are hard to extinguish [10].

Consequently, researchers and engineers need to find ways to expand the advantages of lithium-ion batteries and/or reduce the drawbacks of resource consumption and safety risks. Possible avenues include improving the efficiency of both primary materials sourcing and recycling processes [11], developing electrode materials free of problematic constituents like nickel or cobalt [12, 13], with higher energy or power densities as well as good chemical/thermal sta-

bility. The development of such materials is a regrettably slow process. At a time when lithium-ion batteries are on the verge of reaching a new level of mass production thanks to the proliferation of BEVs, this thesis aims to contribute to a more near-term solution: improving the safety and the utilization of both the energy and the power capabilities of existing lithium-ion battery technology by optimizing¹ cell design and operation strategies.

1.1 Considering Imperfection: From Cell Design to Operational Strategy

What is meant by optimizing cell design and operation strategies? The overarching goal is to achieve the desired operating performance at minimum resource input and minimum cost. The performance targets of battery cells typically relate to their ability to deliver and accept energy and power, to safety, and to lifetime [18, 19]. In this work, cell design refers to the definition of the internal components and the cell's outer shape and casing. The internal components are: the positive and negative porous electrodes, made of lithium insertion materials, binder, and additives applied on an aluminum or a copper current collector foil, the porous separator and the electrolyte solution which occupies the pores of the electrodes and the separator. For a description of the functionality of lithium-ion batteries, the reader is referred to textbooks [19–21]. Cell design choices include the layer thicknesses of the separator and electrodes, their composition and morphology, i. e. particle sizes and shapes, porosities, and the current collector thickness and tab arrangement [22]. Three state-of-the-art cell casings are in use: rigid metal cases in cylindrical or prismatic forms as well as pouch cells wrapped in aluminum-polymer composite foil [23]. There is a large variety of standardized cell formats with widely differing outer dimensions: In current BEVs alone, cell capacities range from ca. 3 Ah to ca. 130 Ah [24].

In the context of this work, operational strategy refers to the control of cells during use, taking into account the design-specific capabilities of the cell and situational and environmental variables. In real-life battery application, the operational strategy is always bound by the limits of safety. As such, essential safety and lifetime requirements are translated into concrete physical parameters at the cell level. These quantities represent operating conditions and internal states such as: maximum allowable temperatures and mechanical loads, a tolerable voltage window and situation-dependent current limits for charging and discharging. An optimized operational strategy can be understood as making available the maximum power and energy while not violating these global criteria anywhere in the cell and thereby ensuring safety and sufficient lifetime.

¹ A large part of the specific energy improvements of lithium-ion batteries since their commercialization can be attributed to engineering efforts: Panasonic's 18650 format cells used in the 2012 Tesla Model S yielded 673 Wh l^{-1} and 236 Wh kg^{-1} [14], representing 285 % and 216 % increases compared to Sony's first generation 18650 format cells which yielded 253 Wh l^{-1} and 108 Wh kg^{-1} [15]. The specific energy increases of the utilized electrode materials are only partly responsible: 100 % for graphite vs. petroleum coke [16] and ca. 35 % for lithium cobalt aluminum (NCA) vs. lithium cobalt oxide (LCO) [17].

The challenge is that the globally valid operating limits cannot be locally monitored everywhere inside a cell. Usually, the voltage and the current are measured at the tabs, and the temperature is measured at the cell surface or in its vicinity. At the same time, cells cannot be assumed to be homogeneous regarding their operating conditions and inner states. During operation, any practical cell can be expected to exhibit gradients of temperature and mechanical loads, and non-uniform distributions of current density and state of charge. To make matters worse, the physical properties of cells may not be uniform to begin with, meaning that the specified global operating limits may exceed the actual capabilities of the cell in specific spots [25, 26]. It is likely that critical safety events or the onset of aging processes are initiated in such spots, which are characterized by substandard physical properties, exposure to adverse operating conditions, or above-average current loads [27–29]. To complicate matters, those “weak” spots are likely to differ from cell to cell [26, 30].

If the potential energy and power capability of a cell is to be utilized to the maximum, the inevitable weak spots of real cells define the limits and need to be taken into account. Simulation models, which are used to align cell design and operation strategies when a cell is devised for a specific application, can only solve this problem to a limited extent. Typical simulation models assume an idealized version of reality, and ignore the non-uniform physical properties which may not be a part of the intended design. Consequently, these models cannot predict or help to take into account many of the non-uniform operating conditions and -states [31]. Therefore, it is necessary to reveal and characterize the non-uniform physical properties and operating conditions in lithium-ion cells and establish cause-effect relationships regarding operating states and cell performance. Understanding the causes and effects of non-ideal cells and operating conditions is a prerequisite for:

- devising cell designs which are more robust against non-uniformities and their effects.
- making informed trade-off decisions between cost and process quality in manufacturing.
- managing risk by exploring the possible outcomes of events that are beyond the engineers’ control.
- devising on-line detection methods which make it possible react to the local onset of aging or safety relevant events inside cells.

1.2 Non-Uniform Physical Properties and Operating Conditions

Non-uniform physical properties and operating conditions in lithium-ion cells complicate the relationship between cell design and operation strategies. This work considers the four different categories depicted in Figure 1.1: Manufacturing inhomogeneity, geometric effects, temperature and mechanical loads. These categories are not sharply delineated, as they merge into and influence each other, but they allow a conceptual classification. Together, they deter-

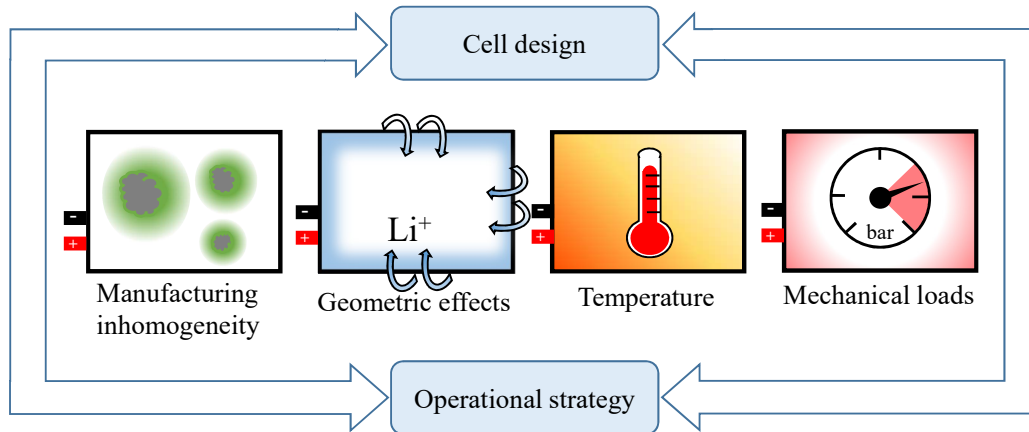


Figure 1.1: The four categories of non-uniform physical properties and operating conditions considered in this work. Together, they complicate the simultaneous optimization of cell design and operational strategy.

mine the current density distribution during charging and discharging, are responsible for the formation of non-uniform states of charge and local aging phenomena across the electrodes and ultimately decrease the usable capacity and power. The current state of research on their individual causes and effects will be reviewed in the following.

Manufacturing Inhomogeneity Along the complex process chain of battery manufacturing there are many possibilities for inconsistencies to occur: In the electrode slurry mixing process, active material particles, binder and additives may not be evenly distributed [32–34]. During coating, drying and calendaring, an even film thickness may not be achieved or the binder may migrate to the electrode surface [35–38]. These morphological imperfections can result in electrical or ionic isolation of areas of the active material, as well as pore blockages, and variations in porosity and tortuosity. In turn, these have been shown to cause a local increase in impedance, current density variations, local lithium plating and capacity loss [25, 27, 29, 39, 40]. In the stacking process of pouch cells the electrode edges and the separator may be imperfectly aligned which reduces the cell capacity and carries the risk of internal short-circuits [41, 42]. Furthermore, cells or module assemblies may be contaminated, altering the electrode morphology or causing indentations. Examples are particles emerging from the laser cutting process of electrodes [43] or during electrode processing and handling [28, 44] and auxiliary materials used to facilitate production processes [45].

If the inhomogeneities in a cell are known, models can be used to understand how they affect the cell performance [27, 39, 46]. In an individual cell, inhomogeneities can be detected by a wide variety of methods: Amongst others, X-ray diffraction (XRD), X-ray tomography, neutron diffraction and visual or microscopy-aided post-mortem inspection [26, 47]. However, all these methods are united by their laboriousness and unsuitability for end-of-line characterization of commercial cells or usage in their place of installation. It is usually not known

if inhomogeneities were introduced into a cell during its production and even less where they might be located.

Geometric Effects Some non-uniformities of operating states occur in spite of faultless manufacturing because they are inherent to the design of a practical battery. One cause of a non-uniform distribution of current and electrode utilization is the limited number of tabs in state-of-the-art cell designs [48]. To counter this effect, 'tabless' cylindrical cell designs with continuous tabs have been developed [49, 50]. However, especially in large format pouch cells, the polarization along the current collector remains unavoidable and leads to non-uniform electrode utilization [51, 52].

Furthermore, all sheet electrodes have edges. At the edges, not only is the face perpendicular to the electrode surface exposed to the liquid electrolyte, but also the edge face. This has been shown to result in locally elevated current densities [53]. Because this poses the risk of locally overcharging the anode near the anode-separator interface, i.e. lithium plating, the anode sheets are usually made slightly larger in area so that they project over the cathode sheets by one or two millimeters [53, 54]. The so-called *anode overlap* has been shown to act as a buffer for cyclable lithium, provoking anomalous variations in the coulombic efficiency in aging experiments [55]. In wound cells, sometimes much larger *overhang areas*, where the anode has no cathode counterpart, can be found at the beginning and end of the electrode tapes. These overhang areas can act as an even greater buffer for cyclable lithium, significantly altering the adjacent local state of charge (SOC), and have been shown to cause noticeable capacity losses that can be recovered when lithium is redistributed during storage at high SOC's [56–58].

Mechanical Loads Pressure gradients are routinely created by the cell casing. In pouch cells, depending on the deep-drawing process of the pouch foils and the sealing process, the edges may be either too loose or too taut. In [59] the cell layers were found to be more tightly compressed at the edges. In flat-wound prismatic cells, the casing is stiffer near the short edges and there is a considerable variation of contact pressure between layers within the radii [60]. Cylindrical cell cases are likely to exert more pressure at the bottom and top faces by virtue of the added structural rigidity in these areas. Pressure gradients can also originate from manufacturing inhomogeneities. Evidently, if an unevenly thick cell stack [61] is compressed by an even, rigid cell casing, the resulting pressure distribution will be non-uniform. Deliberate design compromises could also play a role. It may be that a cost-efficient clamping device for a stack of pouch cells exerts a slightly uneven pressure on the outer cells' surfaces. Finally, during operation, the dilation of the electrodes upon intercalation and deintercalation of lithium ions [62, 63] and thermal expansion can intensify an uneven pressure buildup in cell stacks. Regarding the effects of pressure, it has been shown that the lithium chemical potential in a thin-film lithium cobalt oxide (LCO) electrode varies under mechanical stress. Upon strain application in the direction perpendicular to the CoO_2 layer, a change of the voltage with respect to pressure of $6.1 \cdot 10^{-12} \text{ V} \cdot \text{Pa}^{-1}$ was found [64]. However, this is an extremely

small variation and other studies have found the electrochemical performance to be insensitive to external pressure [65–67]. Consequently, evidence of significant electrochemical effects due to mechanical pressure on lithium-ion cells is mostly related to morphology changes of the electrodes [68] and the separator [69–71] and varying contact pressure or interfacial resistance between layers [72].

In experimental coin cells, where the ion transport through parts of the separator was completely blocked by deliberately applying an excessive mechanical load to selected areas before assembly, the occurrence of local lithium plating around the blocked areas has been reported and explained by the induced current density variation [27, 40]. In unaltered, commercial cylindrical cells, researchers have found patterns of depositions in post-mortem inspection which they assumed were linked to the pressure distribution exerted by the cell casings, but the cause-effect relationships have not been clarified [73, 74]. This led to the question of whether local pressure variations that do not cause permanent material damage were capable of causing significant electrochemical effects.

Temperature The temperature distribution in cells is closely related to the cell geometry. The three-dimensional shape of battery cells, together with the fact that the cell reactions during operation are not thermoneutral, implies the presence of temperature gradients during charge or discharge. The characteristics of the temperature gradients depend mainly on the anisotropic thermal conductivity of the cell stack [75, 76] and the thermal connection of the cell with the environment, i.e. whether cooling is done via the tabs or the cell surface, and the cooling rate [77]. Safety devices in cylindrical cells have also been shown to cause temperature gradients due to their high contact resistances [78].

Higher temperature accelerates species transport and intercalation kinetics [79]. This makes temperature an important amplifier for operational state inhomogeneities: In areas with an intrinsically higher current density and utilization, more heat is produced, leading to even higher local currents. Depending on the entropic heat coefficient, which links temperature and the open-circuit voltage (OCV), the entropic effect has either a reinforcing or a mitigating effect. The temperature distribution in a cell seems also to be coupled to the mechanical boundary conditions as thermal conductivity has been found to increase significantly with compression of a cell stack [80]. In [81], the relationship between local utilization and temperature has been experimentally demonstrated, while in [82] it has been shown that the utilization non-uniformity caused by non-uniform temperatures is mitigated by higher average temperatures overall. In [83], an increased capacity loss in cells with a non-uniform temperature has been attributed to changes in the local electrode stoichiometry, whereas in [84, 85], in a combined modeling and experimental study, it was concluded that temperature gradients negatively affect the cell capacity mainly due to an increased charge transfer resistance.

Table 1.1: Summary of literature about non-uniform physical properties and operating conditions, and associated effects on cell behavior. The columns on the right indicate which of the effects are assumed to be further influenced by variations of mechanical pressure or temperature.

Manufacturing inhomogeneity	Suggested effects	Influenced by	
		press.	temp.
electrode / separator morphology [32–38]	current density variation [25]	✓	✓
	lithium plating [25, 29, 39]	✓	✓
contamination: particles [28, 43, 44]	short circuits [28]	✓	
contamination: pore-blocking [45]	lithium plating [27, 40]		✓
stack alignment [41, 42]	short circuits [42]		
<hr/>			
Geometric circumstances			
electrode edges	current density variation [53]		
cell dimensions, tab location	non-uniform utilization [51, 52]		✓
anode edge overlap [53, 54]	capacity fluctuations [55]		✓
electrode area w/o counterpart [56–58]	capacity fluctuations [56–58]		✓
<hr/>			
Non-uniform operating conditions			
temperature [75–78]	non-uniform utilization [81, 82]		
	capacity fade [84, 85]		
mechanical loads / pressure [59–61]	lithium plating [69, 70, 73, 74]		✓
	internal resistance [71, 72]		

This review of the literature shows that non-uniform physical properties, operating conditions and states introduced by manufacturing, non-uniform mechanical loads, temperature distribution, and geometric effects are standard features of lithium-ion cells. The findings are summarized in Table 1.1. Detrimental effects on the cell performance and lifetime have been reported, but in general, the cause-effect relationships remained unclear. There is also a shortage of methods for the detection of manufacturing inhomogeneities at the end of the production line or during use.

1.3 Research Aims, Scope and Delimitations

This thesis aims to improve the understanding of the cause-effect relationships between non-uniform physical properties, operating conditions, and operating states in lithium-ion cells. The results are expected to yield insights into optimal battery designs and operation strategies, and potentially open avenues for new in-situ methods to detect critical local phenomena. From the preceding literature review, the following research requirements emerge: The con-

sequences of inhomogeneity in manufacturing demand an investigation into new on-line detection methods and adapted operational strategies. Regarding mechanical loads, theoretical investigations and aging study results from the literature motivated an original investigation into the effects of local pressure variations within realistic bounds, i. e. below the threshold of a lasting material damage. Finally, the desire to better understand the unexpected capacity evolutions of cylindrical lithium iron phosphate (LFP)/graphite cells during prolonged shallow cycling observed in an earlier paper [86] led to the investigation of multiple factors. These included the reported geometry and temperature driven variations of electrode utilization and SOC distribution, along with capacity recovery strategies. The findings led to the question of whether the interplay between gradients of pressure and temperature alongside edge effects can provoke even larger redistributions of cyclable lithium than those reported thus far in connection with anode overhang areas.

The following three specific research questions were derived:

1. Is it possible to detect manufacturing inhomogeneity during cell operation and adjust the operational strategy accordingly?
2. Does an uneven compression of cell stacks provoke localized lithium plating?
3. Can non-uniform operating states cause significant variations in the usable capacity?

In order to find answers to these questions, an exploratory approach was followed based mainly on experimental investigation and complemented by modeling. New experimental methods and special test rigs were developed and implemented for this purpose. All full-cell experiments were done on commercial pouch and cylindrical cells from high-quality manufacturers to ensure that relevant conclusions could be drawn from them and that the findings can be applied to comparable high-quality cells. Only effects of non-uniformities within individual cells were investigated, with variations between cells in a module or pack assembly not considered. Most of the findings, however, should be transferable and equally relevant for cell assemblies.

1.4 Thesis Outline

A graphical overview of this thesis can be found on the following page. In chapter 2, the experimental methods developed in the course of this project, which go beyond the state of the art, will be discussed in detail. Chapters 3-5 are each devoted to one of the main research questions. In chapter 3, the locally-resolved measurement of swelling of lithium-ion pouch cells is explored as a technique to detect manufacturing inhomogeneities and to study their aging behavior under specific sets of operating conditions. In chapter 4, via experiments and modeling, the interactions between electrode swelling and non-uniform external mechanical constraints of cells are investigated, along with their impact on: the electrode morphology, effective transport properties, and risk of lithium plating. In chapter 5, the relationship between

alterations in usable capacity and lateral SOC gradients in cylindrical LFP/graphite cells is investigated. In addition, the interplay between pressure and temperature gradients and edge effects and their bearing on SOC gradients is analyzed. In chapter 6, the findings of the previous chapters are summarized, synthesized, and critically discussed. Finally, conclusions are drawn and suggestions for further research are made.

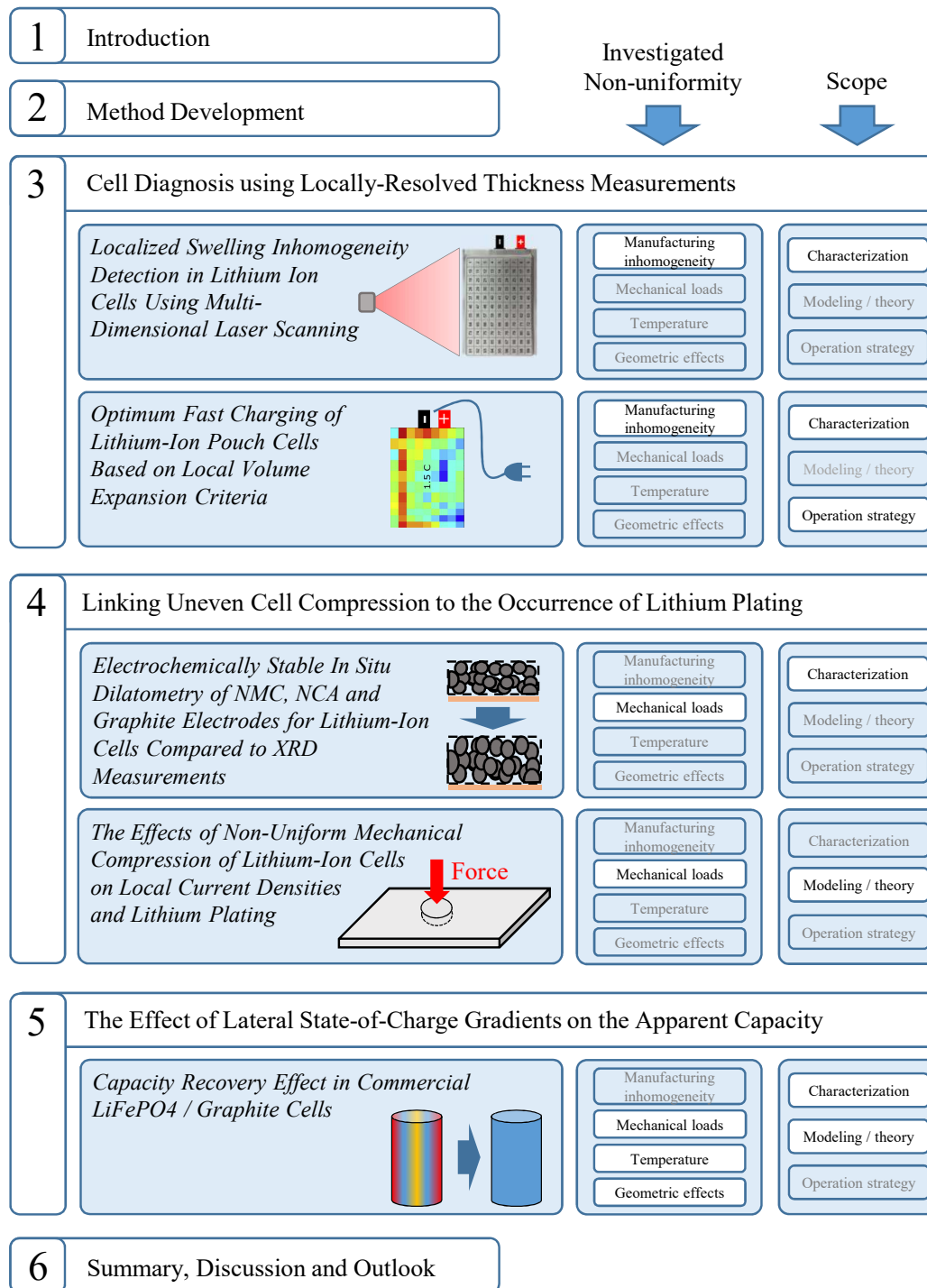


Figure 1.2: The contents of this thesis. In italics: The titles of the publications that constitute the main part of the chapters 3-5.

2 Method Development

The complex interrelationships of physical and operating-state inhomogeneities in lithium-ion cells make it difficult to derive cause-effect relationships directly from either theory or modeling. Therefore, an empirical approach was chosen to answer the research questions. Some of the research sub-questions required adapted, refined or novel experimental methods that go beyond the state of the art. Three key experimental methods that have been developed in the course of this work will be reviewed in detail: The detection of local lithium plating in an operating cell via locally resolved thickness measurements, electrochemical dilatometry on single electrodes and the determination of local electrode SOCs using coin cells.

2.1 Operando Detection of Lithium Plating via Thickness Measurements

The deposition of metallic lithium onto an electrode surface, commonly referred to as lithium plating, is an undesired process in lithium-ion batteries. It becomes thermodynamically favored over intercalation when the electrode potential versus a virtual, adjacent lithium reference immersed in the electrolyte, falls below zero. Between 50 % and 100 % of their total charge capacity, graphite-based negative electrodes operate at a reversible potential of only ca. 85 mV vs. Li/Li⁺ [87]. While this enables high energy densities, this small potential difference increases the risk of lithium plating when the mass transport limitations [88] and/or sluggish kinetics of the intercalation reaction lead to electrode polarization during charging [89].

In laboratory settings, lithium plating can be directly detected operando via neutron diffraction [90] or by special purpose-built cells [91]. Another widely-employed, indirect method for operando detection is the measurement of the negative electrode potential via a reference electrode [92]. Although it is possible to retrofit a commercial cell with a reference electrode, it is a difficult, manual procedure and implies some degree of physical alteration of the original cell. Furthermore, it is not possible to resolve the electrode potential locally across the cell. A relatively simple method is to analyze the gradient of the voltage drop immediately after the end of a charging phase for a characteristic plateau signaling lithium stripping [93, 94], which provides a proof of previous lithium plating. However, similar to the reference electrode method, the cell voltage measured at the tabs holds only aggregate information about the internal conditions of the cell. This means that the early, localized stages of lithium plating are likely to remain unnoticed and that the location of lithium plating, when it is detected, remains unknown.

Using the cell thickness changes produced by the deposition of metallic lithium as an indicator for lithium plating is a relatively new approach. It is based on the fact that metallic lithium deposited on the surface of a graphite electrode takes up more volume than the same quantity of lithium intercalated in graphite. The effect of a partial deposition of lithium during charge on thickness change is demonstrated using the example of a graphite anode from a Kokam SLPB526495 pouch cell: In the operating range of the full cell, the Kokam graphite anode, which is $98\ \mu\text{m}$ thick, stores $3\ \text{mAh cm}^{-2}$ of charge and in doing so it expands by 3.5% [95]. Thus, the expansion of the electrode at 100% SOC would be:

$$\Delta t_{int} = 98\ \mu\text{m} \cdot 0.035 = 3.43\ \mu\text{m} \quad (2.1)$$

If, instead, all of the $3\ \text{mAh cm}^{-2}$ would deposit as a dense film of metallic lithium, the film thickness would be:

$$\Delta t_{plating} = V_{m,Li} \cdot \frac{1}{e N_A} \cdot 3\ \text{mAh cm}^{-2} = 4.86\ \mu\text{m} \quad (2.2)$$

where $V_{m,Li} = 13.02 \times 10^{-6}\ \text{m}^3\ \text{mol}^{-1}$ is the molar volume of metallic lithium, $e = 1.602\ 176\ 62 \times 10^{-19}\ \text{As}$ the elementary charge and $N_A = 6.022\ 140\ 86 \times 10^{23}\ \text{mol}^{-1}$ the Avogadro constant. With equations (2.1) and (2.2), the number of electrode layers $n = 24$ and under the assumption that the electrode expansion due to intercalation is linear between 0% SOC and 100% SOC, the additional thickness increase of a partial deposition of the lithium can be calculated. When, for example, 10% of the lithium is deposited as a dense film on the anode at the separator/anode interface instead of intercalating into the graphite host structure during a full charge, the additional thickness increase of the cell can be calculated as:

$$\Delta t_{10\%plating} = n \cdot 0.1 \cdot (\Delta t_{plating} - \Delta t_{int}) = 3.43\ \mu\text{m} \quad (2.3)$$

This is an easily detectable quantity with commercially available tactile or optical sensors. It is equivalent to an additional thickness increase of ca. 3.3% relative to the Kokam cell expansion of ca. $103\ \mu\text{m}$ upon a full charge in the absence of lithium plating [96]. However, it has been shown that deposited lithium tends to form mossy or dendritic layers containing not only lithium but also lithium-electrolyte reaction products [97–100] which can be expected to take up more volume than a smooth surface film. Indeed, in Burow et al. [101], a lithium-rich deposit layer of $31\ \mu\text{m}$ was found on $60\ \mu\text{m}$ graphite electrodes at a state of health (SOH) of 60% . For comparison, if 40% of the Kokam cell capacity was consumed by lithium plating, the above calculations would predict a deposit layer thickness on each electrode of only $0.4 \cdot$

$\Delta t_{\text{plating}} = 0.4 \cdot 4.86 \mu\text{m} = 1.94 \mu\text{m}$. In conclusion, even if surface films of perfect density and smoothness were formed during lithium plating on graphite electrodes, they would produce a measurable thickness difference. Realistically, however, the deposited lithium is likely to form mossy/porous structures, which are thicker and easier to detect than smooth lithium films, but without exact knowledge of their composition, they can only serve as a qualitative, not quantitative indicator for lithium plating.

Bitzer et al.[102] have proven the feasibility of operando detection of lithium plating during low temperature charging using a tactile displacement sensor mounted on one side of a lithium nickel manganese cobalt oxide (NMC)/graphite pouch cell. At a temperature of -5°C and a current of 7/20 C, a clearly larger thickness increase in comparison to 3/20 C charging was detected and the existence of a deposit layer was confirmed via post-mortem analysis. In this case, the authors had conducted preliminary experiments to determine an appropriate position for the displacement sensor, citing the experimentally established fact that the location with the highest propensity for lithium plating varies across cell types and may also vary between individual cells of the same type. This suggests that a locally resolved measurement of the cell thickness could bring substantial benefits.

2.1.1 Locally-Resolved Operando Thickness Measurements of Pouch Cells

Such a locally resolved measurement of the cell thickness has been introduced in [103]. A schematic of the setup is shown in Figure 2.1: Single Gocator 2330 laser heads by LMI Technologies, Canada, are directed at each side of the cell and perform a continuous triangulation measurement. They are mounted on a linear axis aligned in parallel to the cell surface and move at a speed of 2 cm s^{-1} , requiring 5 s to capture the Kokam pouch cell. The differential of the height profiles recorded by each laser head is the cell thickness. In a post-processing step, the point cloud is reduced to a finite number of surface elements, across which the thickness is averaged. In most experiments, around 100 surface elements were defined with an area of approx. 0.5 cm^2 each. In these surface elements, the thickness is determined with a resolution of $0.01 \mu\text{m}$ and a repeatability of $0.8 \mu\text{m}$ [104]. The influence of dismounting and re-mounting of a test cell is negligible. The entire setup is encased in a temperature-controlled chamber and the cell surface temperature is tracked via an infrared sensor pointed at the center of the cell. Both thickness data and cell temperature are recorded via LabView. During the measurement the cell is cycled by a BaSyTec CTS battery tester.

Using this setup, the cell thickness was monitored while the cell was charged and discharged at different C-rates. As previously observed by Bitzer et al. [102] and Rieger et al. [103], distinct thickness overshoots appeared at high C-rates around the constant current - constant voltage (CC-CV) transition. The overshoot is calculated as the difference between the thickness maximum and the thickness 10 min after the end of the CV charge phase. As can be seen in the left graph of Figure 2.2, the overshoot at 1.5 C amounts to ca. $30 \mu\text{m}$. At, 1.0 C, no

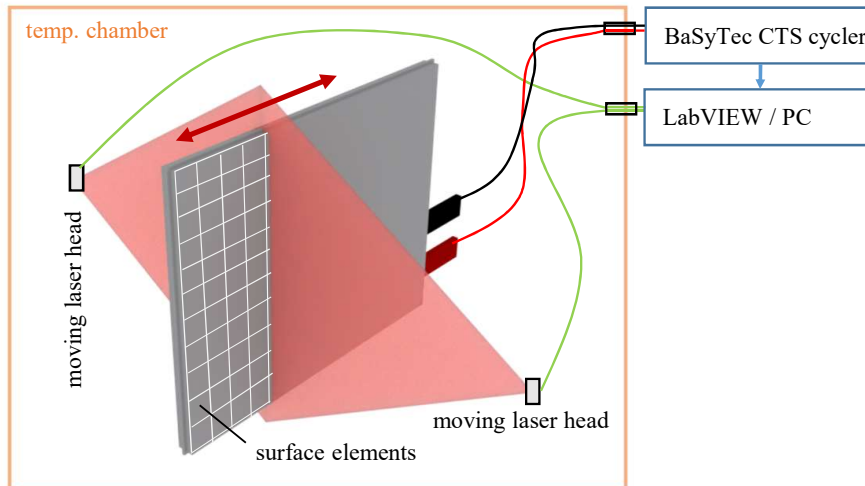


Figure 2.1: Schematic of the multi-dimensional laser scan setup. The laser heads are mounted on a linear axis and move along the length of the cell. The white grid illustrates the surface elements for which the point clouds generated by the laser heads are post-processed into an averaged thickness value.

significant overshoot can be discerned from the surface-averaged signal. However, the locally resolved data displayed in the right graph reveal that at 1.0 C, several areas experienced overshoots of around $5 \mu\text{m}$. Based on the simple calculations in section 2.1, these overshoots could represent a lithium deposition of ca. 15 % of the area-specific cycleable lithium in these spots. The question remains as to how much of this deposition can be reversed or *stripped* during the following pause or discharge. This is discussed further in chapter 3.

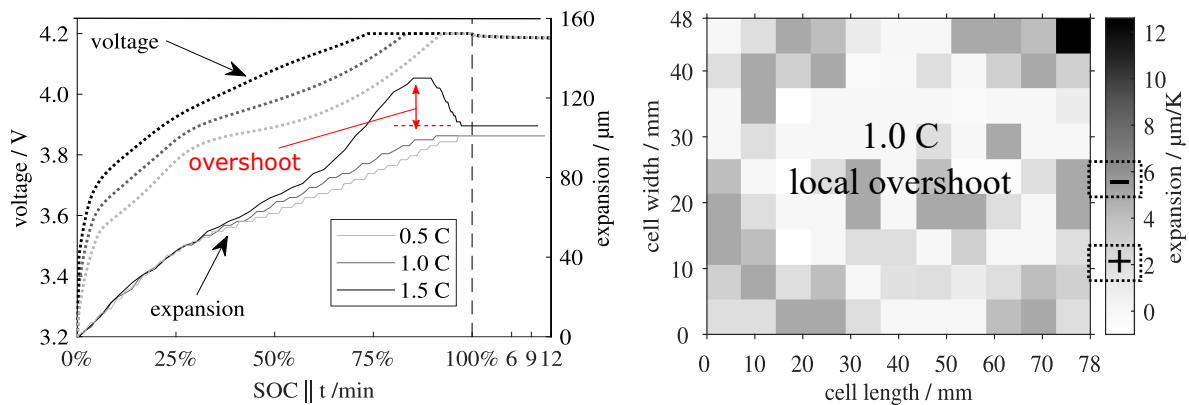


Figure 2.2: Surface-averaged and locally resolved cell thickness changes during charging of a pouch cell. At 1.0C, no thickness overshoot is discernible in the averaged signal, however, local thickness overshoots can be detected.

Controlling for thermal expansion In the expansion data shown above, the thermal expansion of the Kokam cell has already been taken into account using an average thermal expansion coefficient of $1.2 \mu\text{m K}^{-1}$. Two alternative methods were used to estimate the ther-

mal expansion coefficient. It was not a viable option to introduce a temperature gradient in the chamber and slowly heat up the cell while taking thickness measurements because the sensors' calibration is only valid if the chamber temperature is constant. Therefore, the first method consists of heating up the chamber to 45 °C, the highest possible stable temperature, calibrating the sensors and inserting a cell that has been cooled to 0 °C in a freezer. Then the thickness is measured continuously until the cell temperature is equal to the chamber temperature and equilibrated, which takes ca. 35 min. This is illustrated by the left graph in Figure 2.3. The second method consists of self-heating the cell via 1 s charge-discharge pulses in the temperature-controlled chamber which is held at 25 °C. As can be seen in the right graph in Figure 2.3, the cell heated with 3.0 C pulses reaches a surface temperature of 31 °C after ca. 7 min. The cell expansion lags behind somewhat and keeps growing at a low rate even after the cell temperature has equilibrated. With the pulsing method, the surface-averaged thermal expansion coefficient was determined to be $1.7 \mu\text{m K}^{-1}$, while the heating of the cool cell in the hot chamber resulted in $1.2 \mu\text{m K}^{-1}$. The *cool cell, hot chamber* experiment was considered more reliable because the high C-rate operation during pulsing may have triggered side reactions adding to the thickness increase. A more in-depth discussion including the locally resolved thermal expansion results of the Kokam cell can be found in section 3.2.

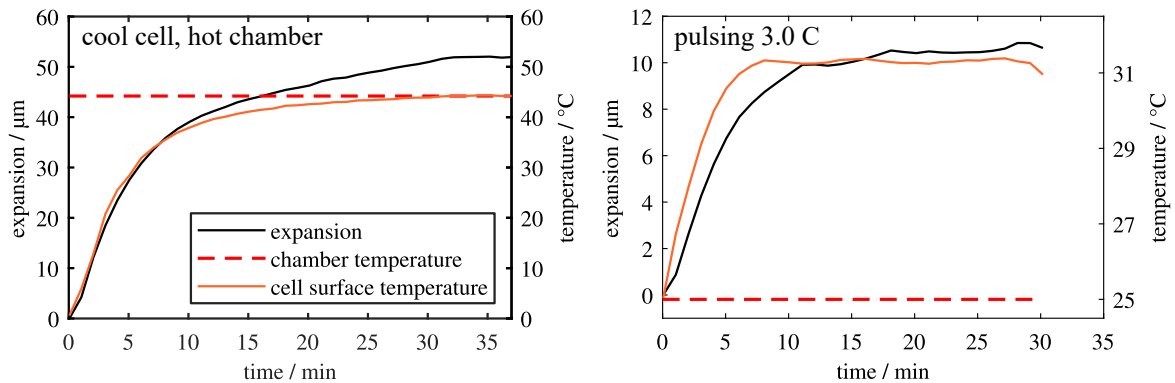


Figure 2.3: Temperatures of chamber and cell as well as cell thickness change as a function of time. Left: pre-cooled cell is placed in hot chamber. Right: cell is heated with current pulses.

2.1.2 Technical Limitations

The local resolution of the thickness measurement across the cell surface is, without doubt, highly beneficial in comparison to a single-point or surface-averaged measurement. However, it is still an aggregate signal of the internal layers of the cell. Phenomena that occur in single, individual layers may go unnoticed if they trigger thickness changes of less than ca. $1 \mu\text{m}$. For the same reason, this test rig is of limited use for experiments based on single-layer laboratory pouch cells. Finally, the measuring principle is incompatible with the mechanical compression

or clamping of the cell between rigid plates during the experiment, as the plates would shield the laser light from the cell surface.

2.2 Electrochemical Dilatometry

Electrochemical dilatometers are used to measure the macroscopic dilation and contraction of insertion electrodes in operation, while controlling electrochemical parameters like electrode current or potential versus a counter or a reference electrode. To this end, electrochemical dilatometers combine an electrochemical cell in a two or three electrode setup with a displacement sensor. In principle, this can be achieved using a single- or multilayer pouch cell [105], but this approach has important drawbacks: The preparation of laboratory pouch cells requires time and experience, especially in three-electrode configuration. Furthermore, the measured displacement includes the thickness changes of the counter electrode, the separator and the pouch foil. Herein, the term electrochemical dilatometer shall refer to devices with integrated designs, where the instrument body houses the electrochemical cell.

The earliest report of a dilatometric study of electrodes for lithium-ion cells using such an integrated dilatometer setup is Winter et al. from 2000 [106], where synthetic graphite was cycled in ethylene carbonate (EC) and dimethylene carbonate (DMC)-based electrolyte solutions. The dilatometer used in this report was based on a custom-built setup from 1982 [107]. In this dilatometer design, the working electrode is placed between a fixed current collector and a movable piston, which alters the resonance frequency of an oscillatory circuit consisting of two ferrite shells, one of them attached to the piston. The displacement is calculated from the frequency shift with a resolution estimated by the authors to be 25 nm. Lithium was reported to have served both as counter and as a reference electrode. In a 2011 study using the same setup, the typical graphite staging mechanism could be observed in a meso-carbon microbead electrode cycled in a 1M LiPF₆ EC/diethyl carbonate-based electrolyte solution. However, in none of the studies using the setup originating from [107] were consecutive expansion-contraction cycles reported. It is thus unclear whether the working electrode could be cycled efficiently and stably and if initial thickness changes of electrodes during the first cycles could be distinguished from reversible thickness changes.

Another custom-built electrochemical dilatometer was presented in [108]. In this design, the cell stack consists of an lithium titanate oxide (LTO) counter electrode, a polypropylene separator, and the working electrode. There is no reference electrode. A movable piston loaded with an adjustable spring rests on the cell stack while its translation is detected by a commercial displacement sensor (MT1281, Heidenhain, Germany, resolution 1 nm). The LTO electrode was assumed to not contribute to the measured dilation of the stack. Using this setup, the authors investigated the reversible and irreversible dilation of graphite and NMC111 electrodes as a function of the vinylene carbonate content of the electrolyte during the first three cycles [109]. It is unclear why the authors only discussed the first three cycles. The

electrochemical stability is difficult to assess because the authors did not provide information about the capacity retention. Reportedly, the dilatometer was operated under dry room conditions, which may have been a countermeasure against stability issues stemming from imperfect tightness of the cell.

A third dilatometer design was presented in [62, 110]. It has since been commercialized and was used for the experiments presented in this thesis (ECD-3-nano, El-Cell, Germany). The electrochemical cell is a three-electrode setup with a lithium reference electrode. A schematic of the cell is shown in Figure 2.4. A distinct feature is the rigid borosilicate T-frit which serves as the separator and shields any thickness changes which might occur in the counter electrode from the displacement sensor (PISeCa D-510, Physik Instrumente, Germany, resolution 5 nm). This instrument has been used in several studies to investigate the dilation of graphite [62, 111–113], LCO [111] and silicon-graphite composites [112]. However, none of these studies analyzed more than the three first cycles, nor did they discuss the capacity retention, except for [113], where a 50% capacity loss was reported after 20 cycles.

Such poor electrochemical performance raises doubts about the validity and consistency of the dilation results. For most applications, precise knowledge of both the irreversible thickness changes during the first cycles and the thickness changes during reversible, long term cycling is desired. This requires an appropriate mechanical design of the dilatometer, a reliable displacement sensor and, most importantly, an electrochemical cell which can be cycled with minimal capacity loss rates and high charge efficiency.

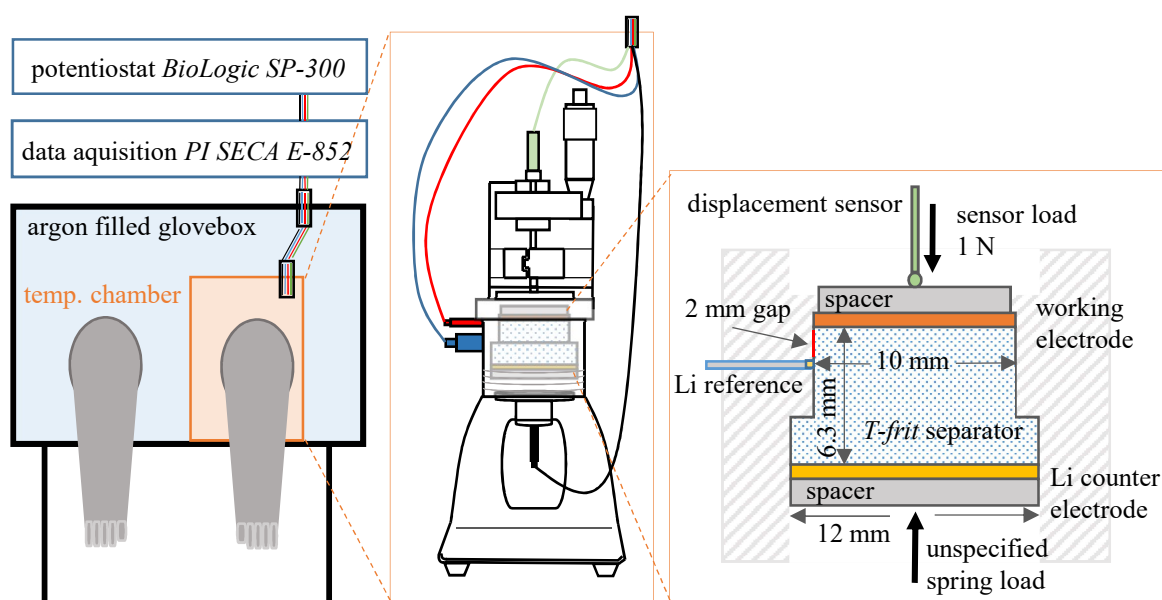


Figure 2.4: Schematic of the dilatometry setup housed in a temperature chamber inside an argon-filled glovebox. A detail of the electrochemical cell with the 6.3 mm thick T-frit separator is displayed on the right.

2.2.1 Improvements of the Electrochemical Performance

The preliminary dilatometry experiments with the ECD-3-nano were plagued by a similarly poor electrochemical performance to that reported in the literature. In the following, three adjustments that led to a greatly improved performance of the ECD-3-nano dilatometry cell are discussed in detail: Operating the dilatometer in argon atmosphere, meticulous washing of the porous T-frit and vacuum-drying of the T-frit at high temperatures. The final cell performance was on par with coin cells: As will be shown in chapter 3, the delithiation capacity of a graphite electrode was stable during 50 cycles while the coulombic efficiency was 99.7% or higher.

Operation in argon atmosphere The electrochemical cell of the ECD-3-nano has eight sealing points. Two between the split main body, two at an overpressure valve, one at the reference electrode and one each at the top and bottom taps. The eighth sealing point is between the T-frit and its housing, which is pre-assembled every time before it is placed in the main body. This sealing point at the inner wall of the frit housing is especially vulnerable because the hard borosilicate T-frit is likely to leave scratches in the surface of the plastic material during assembly and disassembly. In view of the dismal capacity retention of ca. 65% after six cycles of a state-of-the-art graphite electrode, see red data points in Figure 2.5, it was determined to be highly likely that ambient oxygen and humidity enters the electrochemical cell and triggers unwanted side reactions. To avoid any possible intrusion of oxygen and humidity, the experiment was set up as shown in Figure 2.4: The dilatometer was placed in a custom-built temperature chamber located inside of an argon-filled glovebox. This resulted in a significantly better capacity retention, as the orange data points in Figure 2.5 demonstrate. If a pure graphite electrode had been used instead of a silicon-graphite composite, the difference to the capacity retention in ambient air would likely have been even larger.

Component washing and drying procedures While operating the dilatometer in argon atmosphere resulted in a substantial improvement, the electrochemical performance was still quite inconsistent and in most experiments, the capacity loss rates were unacceptably high. The instrument manual recommends washing all of the the cell body parts in water and drying them for 12 h at 80 °C under vacuum. However, a significant improvement of the cell performance was realized by separately drying the porous borosilicate T-frit at the higher temperature of 180 °C for 12 hours. The rough inner surface of the T-frit and the high water adsorption of (silicate) glass [114] may make it difficult to remove the water from the T-frit completely. Any residual water, especially in combination with additive-free electrolyte solutions, has been shown to degrade cell performance significantly [115, 116]. With the drying of the T-frit at 180 °C, the capacity loss rate of the graphite-silicon electrode was halved (Figure 2.5, yellow vs. orange data points) and the pure graphite electrode, instead of losing reversible capacity, gained reversible capacity during the first cycles. This is commonly observed in ad-

equately prepared graphite/lithium coin cells and can be explained by the subsiding of the solid electrolyte interphase formation and the existence of a large reservoir of cyclable lithium provided by the lithium metal counter electrode. A final, minor improvement was realized by actively purging the T-frit by seeping water through it instead of performing ultrasonic cleaning. It may be that without this extra cleaning, residual electrolyte solution and/or its reaction products with water remain in the pores of the T-frit.

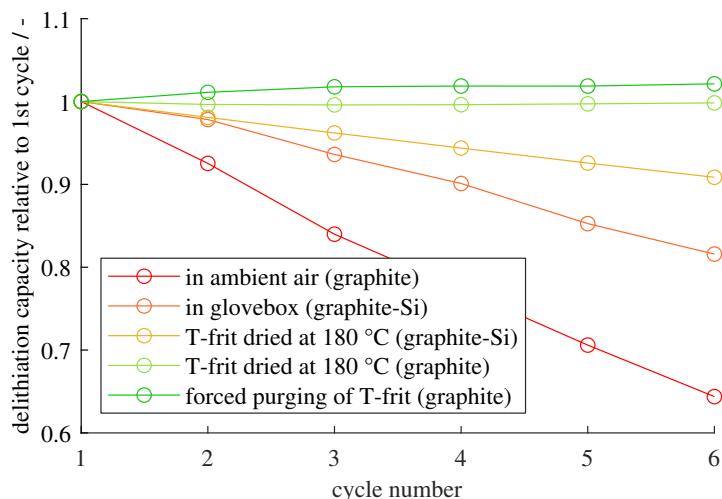


Figure 2.5: Delithiation capacity over cycles of graphite and graphite-silicon (93%/7% wt.) electrodes in the dilatometer under different experimental conditions and cell preparation regimes. The displayed data is from selected, representative experiments.

2.2.2 Technical Limitations

The improved capacity retention of the ECD-3-nano dilatometer cell has enabled the measurement of consistent and trustworthy SOC vs. dilation relationships. However, there are limits to the operative range dictated by the mechanical design of the dilatometer. Most importantly, the thick T-frit impedes ion transport between the electrodes, which complicates the use of high currents or C-rates. Furthermore, the mechanical load of 1 N is non-adjustable. Thus, an investigation of the reversible and irreversible thickness changes of electrodes as a function of mechanical pressure cannot be performed with this instrument.

Polarization due to the T-frit separator The T-frit is 6.3 mm thick, which is 394 times the thickness of a typical, 16 μm thick polyethylene separator [117]. Naturally, this results in a large cell resistance. In itself, this does not pose a problem: In scientific applications, the energy efficiency of a cell is of secondary importance. However, the larger the cell resistance, the greater the difference between the OCV and the voltage during current flow. This leads to the following problems: First, in the dilatometry experiments, the electrode dilation as

Table 2.1: T-frit properties and estimated voltage drop between working electrode and reference. Effective conductivities were calculated using the Bruggeman relationship [118], using conductivities of 1M LiPF₆ in EC/DMC of 11 mS/cm (25 °C) and 13 mS/cm (35 °C) [119, 120].

Phys. properties	Volume	Weight	Density borosilicate	Calc. porosity
	0.605 cm ³	0.773 g	2.23 g/cm ³	0.43
Temp. / Current	25 °C, 0.6 mA	35 °C, 0.6 mA	25 °C, 2.4 mA	35 °C, 2.4 mA
Voltage drop 2 mm	12.1 mV	10.3 mV	48.6 mV	41.2 mV

a function of the OCV is a quantity of interest. Second, and more importantly, the degree to which a cell is being charged or discharged is usually expressed by the cut-off voltages at which the current is interrupted. If the OCV after a sufficient resting period differs substantially from the cut-off voltage, the cut-off voltage loses significance as a criterion ². A third problem arises in the case of graphite electrodes, which are usually lithiated until they reach 10 mV: Since electrode potentials lower than 0 V vs. Li/Li⁺ favor lithium plating, it is risky to compensate a large cell polarization by lowering the cut-off voltage.

The dilatometer cell has a reference electrode against which the working electrode potential can be controlled. The problems described above would not apply if the reference electrode was positioned in the immediate vicinity of the working electrode. However, they are ca. 2 mm apart, see Figure 2.4, a sufficient distance to cause errors. Table 2.1 includes the physical properties of the T-frit and estimated voltage drops for two different currents and temperatures. These were calculated via a Bruggeman expression for the effective conductivity as a function of the porosity ξ : $\sigma_{eff} = \sigma * (\xi)^{1.5}$. Experimentally obtained voltage characteristics of a graphite electrode during lithiation and delithiation close to the point of full lithiation at a temperature of 35 °C and using the same currents as in the calculations are shown in Figure 2.6. The magnitude of the immediate voltage drops when the current is switched on and off correlates with the applied current, 8 mV at 0.6 mA and ca. 37 mV at 2.4 mA. The values are close to the calculated values, which are only 2 mV to 4 mV higher. This minor difference may originate from the uncertainty involved in the determination of the physical properties of the T-frit or from the Bruggeman approach being imperfectly suited for its porous borosilicate structure. After the immediate voltage drops, the voltage continues to recover during the 30 min rest, which could be related to the equalization of concentration gradients in the electrolyte. Given the above results, the use of low charging/discharging currents is a pragmatic solution to minimize cell polarization by the T-frit separator.

² Exception: Cut-off voltages at which the voltage characteristic of one or both electrodes has a large gradient, for example when a NMC/Li cell is discharged to 3.0 V. As a fully lithiated NMC electrode has an OCV vs. Li/Li⁺ of around 3.5 V, it will accept virtually no charge between 3.5 V and 3.0 V and quickly bounce back to ca. 3.5 V when the current is stopped.

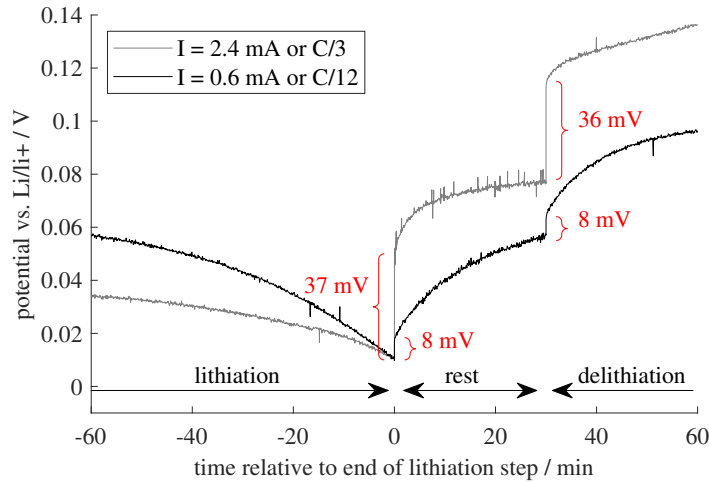


Figure 2.6: Potential of a graphite electrode during lithiation, rest and delithiation at two different currents and 35 °C. The red brackets highlight the ohmic voltage drop which occurs when the current is switched off or on.

2.3 Detection and Quantification of Electrode State of Charge Inhomogeneity

In this work, methods were needed with which SOC inhomogeneity could be detected and quantified. In the following, a range of relevant methods is reviewed. These consist of non-invasive and/or operando methods as well as invasive or post-mortem methods, which require the disassembly of the cell under investigation. Furthermore, the methods differ in their ability to provide qualitative or quantitative information about SOC inhomogeneities and in whether they provide locally resolved information.

Differential Voltage Analysis The non-invasive methods differential voltage analysis (DVA) and incremental capacity analysis (ICA) make use of the change of the OCV of a lithium-ion cell when the local SOCs in the cell diverge. In DVA, which was first proposed in [121] as a diagnostic technique for lithium-ion batteries, the voltage signal is differentiated by the charge throughput (vice-versa in ICA), so that changes in the voltage signal produce characteristic peaks. When the differentiated voltage signal is plotted over the charge throughput, changes of the absolute and relative positions and the intensity of those peaks can be used to draw conclusions about the relative capacities of the electrodes, the lithium inventory of the cell, and the degree of uniformity of the cell and individual electrode SOCs [57, 122–125]. However, it is not possible to draw spatially resolved information from this method as it relies on the aggregated voltage and current signals measured at the cell tabs.

Chemical Analysis Elemental analysis via inductively coupled plasma mass spectroscopy (ICP-MS) or inductively coupled plasma optical emission spectroscopy (ICP-OES), where the samples under investigation are vaporized, is an invasive method [126]. Using ICP, a

shift of the lithium content from the cathode to anode was demonstrated [127]. ICP can also be used to investigate the distribution of elements, including lithium, across electrodes [128]. Glow discharge optical emission spectroscopy enables depth profiling of element concentration in electrodes [129, 130]. Unfortunately, none of these methods are able to indicate which compounds of the elements in question were present in the sample before the measurement. Therefore, the cycleable lithium content cannot be distinguished from the potential decomposition products containing lithium or inaccessible lithium trapped in the electrodes.

Optical Inspection Graphite changes color in several steps when lithiated [87, 131, 132]. This can be used to quantitatively evaluate the distribution of the SOC, even if only roughly. An operando observation of the color change is possible using especially designed optical cells [133]. Commercially available, state-of-the-art cells would first have to be disassembled before such a measurement would be possible. An important disadvantage is that only the surface color is observed. Depending on the cycling conditions and the resting time between cycling and disassembly, the lithiation state in the depth of the electrode may differ from that of the surface [134].

Neutron and X-Ray Diffraction Neutron-based methods have been widely used in lithium-ion battery research to study the atomic structure and electrochemical processes of electrodes [135]. Due to the ability of thermal neutrons to penetrate metallic cell encasings and substrate foils [136], neutron powder diffraction can be applied to lithium-ion cells during operation. This ability has been employed to investigate the changing lithium distribution in commercial pouch cells [137, 138] and cylindrical cells as they operate [139, 140]. However, particularly in cylindrical cells, the spatially resolved analysis of the lithium concentrations is complicated by the fact that the *gauge volume*, the portion of the sample that is investigated at a time, usually incorporates several electrode layers [141].

Neutron depth profiling (NDP), an established method [142] which has been recently applied to lithium-ion batteries, enables the measurement of concentration profiles across the thickness of electrodes. It can be used operando in conjunction with specially designed optical cells [143, 144]. With less experimental effort than is necessary for neutron-based methods, the lateral charge distribution across electrodes after disassembly from a cell can be examined via XRD from layer spacing of the active materials [56]. However, the analysis of the XRD data is based on assumptions about the orientation of the crystals. Especially for flake-type graphite, where there is a pronounced preferential orientation, the evaluation error can be significant. A one- or two-axis rotation of the sample reduces the error but makes the probe preparation and experimental procedures more laborious [145].

In this work, DVA was used to track increasing and decreasing SOC inhomogeneity at the cell level and the optical inspection of harvested graphite anodes provided additional proof of those inhomogeneities. In order to complement the optical inspection and to quantify the electrode SOC deviations not only for the anode but also for the cathode, where no discernible

color changes occur with lithiation, XRD would have been a viable option. Instead, a very simple method using standard coin cells that requires only a glovebox and a battery cycler was developed and is presented in the following section.

2.3.1 Post-Mortem Quantification of Electrode State of Charge Distribution via Coin Cells

Coin cells have been used to assess the local degradation of electrodes in lithium-ion cells by measuring the maximum reversible capacity of harvested electrode material against a fresh lithium counter electrode [146–148]. It will be shown in this section that they can also be used to effectively determine the initial lithiation state of a harvested electrode. Figure 2.7 illustrates the procedure using the example of a cylindrical cell with an LFP cathode: After the jelly roll was unfurled, two 10 mm diameter coins were punched out at each location of interest (in this example at the outer, middle and inner section of the jelly roll). The coins were then left to dry in the glovebox for at least 24 h. CR2032-type coin cells were assembled with two layers of 16.0 mm diameter VWR 691 glass fiber (with a thickness of 260 μm each) as the separator, a 15.6 mm diameter lithium chip (thickness 250 μm) as the counter electrode, and two spacers of differing thicknesses (0.5 mm, 1.0 mm). 80 μl of LP57 (1 Mol LiPF_6 in 3:7 wt. EC:ethyl methyl carbonate) served as the electrolyte.

The cells were rested for 6 h before being cycled between 2.5 V and 4.0 V at 0.1 C using a CC/CC protocol. This choice of voltage limits ensures complete lithiation or delithiation of the LFP electrode. For materials that do not tolerate complete delithiation, like NMCs, the upper voltage limit can be set to the approximate electrode potential (vs. Li/Li^+) that the electrode has in a full cell at 100 % SOC. As shown in the graph in Figure 2.7, the cells were charged first which means that the harvested cathode was delithiated. The enlargement on the right shows clear differences in the initial delithiation capacity between the three different locations and little deviation between the two samples from each location. The cycles following this first delithiation show that the cells cycle stably and that the electrodes' reversible capacities are almost identical and constant. Some of the cells were cycled up to 50 times and exhibited no significant capacity losses (not shown).

2.3.2 Comparison to X-Ray Diffraction and Possible Improvements

It could be argued that XRD is better suited for obtaining concentration profiles across electrodes, especially in the presence of large gradients, due to its finely adjustable spot size. However, if the electrode coating is not to be scraped off to make powdered samples, which involves considerable effort, the resulting diffraction spectrum includes peaks caused by the metallic substrate foil, complicating the analysis. Additionally, it is difficult to perform a two-axis sample rotation of intact electrode samples to mitigate analysis errors caused by a preferential orientation of crystals. Furthermore, the coin cell method presents another significant advantage: It simultaneously provides information about the local SOC as well

as the local capacity, allowing more profound conclusions to be drawn. Of these, the most important, as in the example above, is that the difference in SOC cannot be attributed to inhomogeneous electrode capacity or loss of active material but must have other causes.

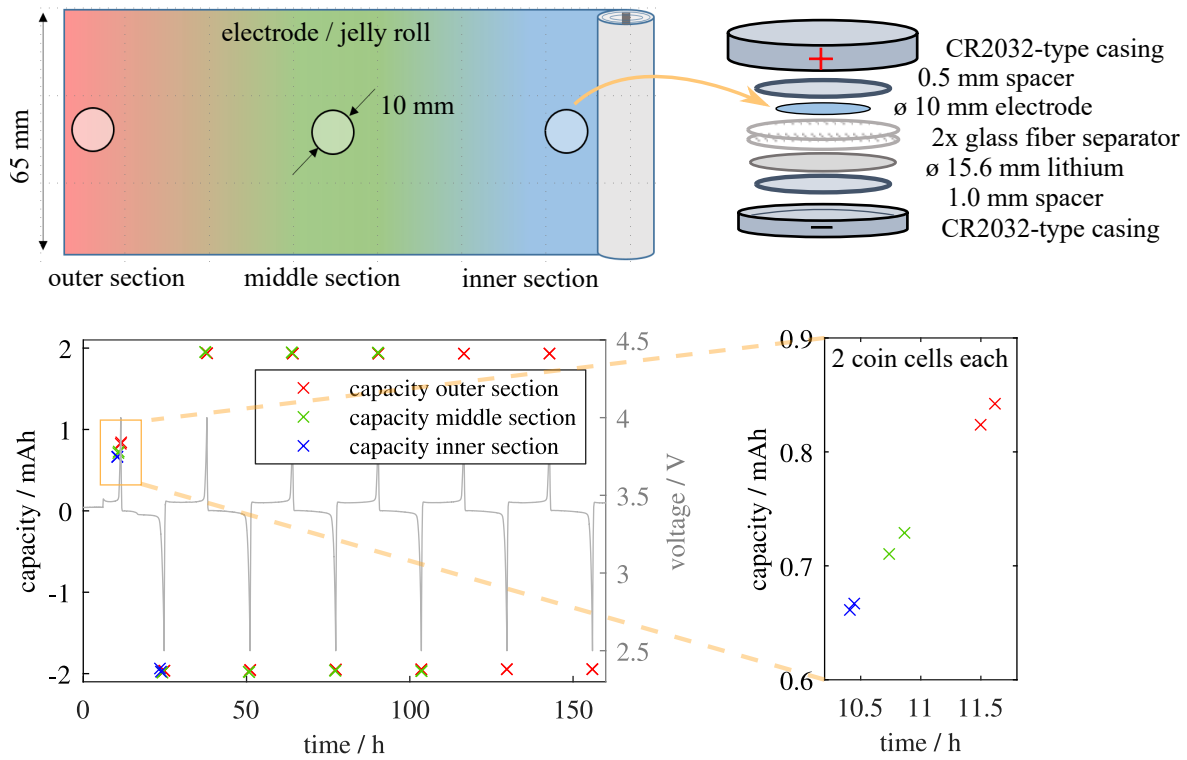


Figure 2.7: Procedure of using coin cells to measure the local electrode SOC in disassembled cells. The cells were opened in an argon filled glovebox, 10 mm diameter coins were punched out, dried, and assembled in coin cells using a lithium metal counter electrode. Cycling was performed at 0.1 C. The initial delithiation of the harvested electrode during the first charge can be used to determine the local SOC. The example plot shows data from an LFP electrode.

3 Cell Diagnosis using Locally-Resolved Thickness Measurements

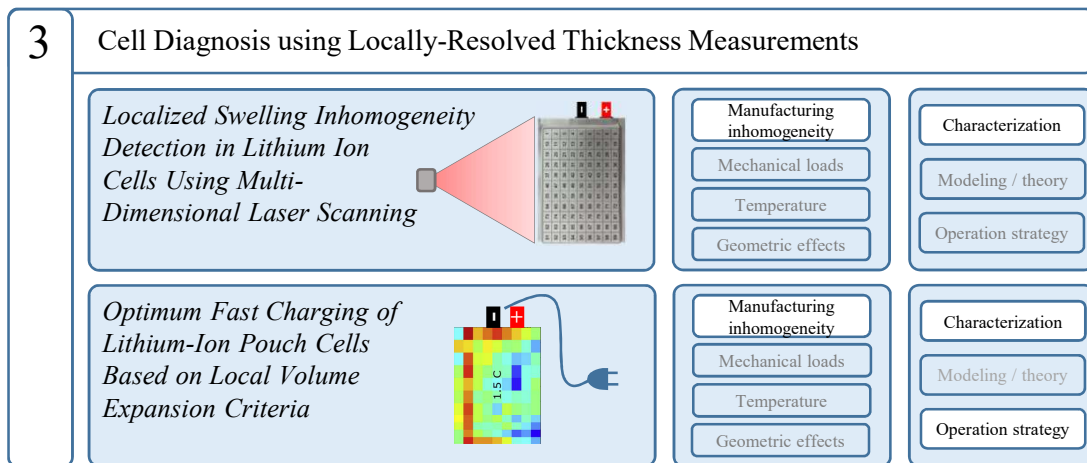


Figure 3.1: Outline of chapter 3.

This chapter is concerned with the on-line detection of manufacturing inhomogeneity, its effects on cell aging processes and implications for operational strategy. For this purpose, the locally-resolved thickness measurement introduced in section 2.1 is applied to characterize the inhomogeneous swelling of pouch cells. Through a range of experiments, the intercalation-based expansion, thermal expansion, and the occurrence of localized, anomalous expansions are disentangled. It is shown that the principal manufacturing inhomogeneity found in the cells under investigation, a pore-clogging contaminant found on the separator and the electrodes, provokes local lithium plating which, in turn, causes an increased expansion of the cell in the affected areas. Furthermore, the severity of the local expansion during a charging event is shown to correlate with the amount of plated lithium and with the loss of capacity upon repeated cycling. Based on this correlation, a method to derive fast charging current profiles from a limited number of local expansion measurements is developed and validated. It is demonstrated that the resulting charging protocols improve charging time and cell capacity retention compared to CC-CV charging. The findings pave the way to the on-line detection of inhomogeneous aging with simultaneous adjustment of the operational strategy.

Two articles, entitled *Localized Swelling Inhomogeneity Detection in Lithium Ion Cells Using Multi-Dimensional Laser Scanning* and *Optimum Fast Charging of Lithium-Ion Pouch Cells Based on Local Volume Expansion Criteria*, constitute the core of this chapter.

3.1 Application of a Locally-Resolved Thickness Measurement to Detect Cell Inhomogeneity

In the following section, an investigation of the thickness-change characteristics of a commercial 5 Ah pouch cell at various charge and discharge rates and SOC windows is presented. 2-D laser scanning revealed local swelling anomalies on pristine cells, which otherwise performed normally according to capacity measurements. Operating conditions that exacerbated the anomalies were successfully identified: There was localized excessive swelling during both charging and discharging and the intensity of the swelling increased with the C-rate in both cases. The swelling anomalies were most striking during discharge: While the average cell thickness decreased by 150 μm in the course of a 1C discharge, in some spots the thickness increased by 200 μm . Via post-mortem visual examination and scanning electron microscopy (SEM), the source of the anomalies could be tracked back to ‘adhesive like’ contaminants on the electrode surfaces and separator that are assumed to originate from the cell manufacturing process. Based on theoretical calculations and literature findings, it was argued that the swelling anomalies are likely to result from both blocking of ionic transport pathways which may have provoked lithium plating, and the thermal expansion characteristics of the adhesive-like material. From a more general perspective, this work shows that the local thickness measurement is a powerful non-destructive cell quality evaluation tool and could be useful for validating cell designs, evaluating manufacturing processes, and manufacturing quality control.

In the context of this thesis, this work provides a proof of concept for the detection of manufacturing inhomogeneities via a local thickness measurement using a 2-D laser scan test bench. It also provides an SEM characterization of the manufacturing inhomogeneity with which this and the work discussed in section 3.2 are concerned, i.e. the adhesive-like contaminant on four spots across the cell surface. The visibly clogged separator pores observed via SEM support the cause-effect analysis of the lithium plating investigation in section 3.2.

Author contribution Franz Spingler and Yan Zhao contributed equally as lead authors to this article. They initiated the research project together and conducted preliminary experiments in close collaboration. In the later stages of the article creation, Franz Spingler placed more focus on the cycling experiments and post-mortem analysis while Yan Zhao was more involved with the processing of the data and creating the graphs. The analysis and interpretation of the results, as well as the writing of the original draft, were performed equally by both lead authors. Yatish Patel, Gregory Offer, and Andreas Jossen provided supervision, and reviewed and edited the manuscript.

Localized Swelling Inhomogeneity Detection in Lithium Ion Cells Using Multi-Dimensional Laser Scanning

Yan Zhao, Franz B. Spingler, Yatish Patel, Gregory J. Offer, Andreas Jossen

Journal of The Electrochemical Society 166 (2), pp. A27–A34, 2019

Permanent weblink:

<http://dx.doi.org/10.1149/2.0011902jes>

Reproduced under the terms of the Creative Commons Attribution 4.0 License (CC BY, <http://creativecommons.org/licenses/by/4.0/>), which permits unrestricted reuse of the work in any medium, provided the original work is properly cited.



Localized Swelling Inhomogeneity Detection in Lithium Ion Cells Using Multi-Dimensional Laser Scanning

Yan Zhao,^{1,=} Franz B. Spingler,^{2,=,*} Yatish Patel,¹ Gregory J. Offer,^{1,**} and Andreas Jossen²

¹Department of Mechanical Engineering, Imperial College London, London SW7 2AZ, United Kingdom

²Institute of Electrical Energy Storage Technology, Technical University of Munich (TUM), 80333 Munich, Germany

The safety, performance and lifetime of lithium-ion cells are critical for the acceptance of electric vehicles (EVs) but the detection of cell quality issues non-destructively is difficult. In this work, we demonstrate the use of a multi-dimensional laser scanning method to detect local inhomogeneities. Commercially available cells with Nickel Cobalt Manganese (NMC) cathode are cycled at various charge and discharge rates, while 2D battery displacement measurements are taken using the laser scanning system. Significant local swelling points are found on the cell during the discharge phase, the magnitude of swelling can be up to 2% of the cell thickness. The results show that the swelling can be aggravated by a combination of slow charge rate and fast discharge rate. Disassembly of the cells shows that the swelling points are matched with the location of 'adhesive-like' material found on the electrode surfaces. Scanning Electron Microscope (SEM) images show that the material is potentially blocking the electrodes and separators at these locations. We therefore present laser-scanning displacement as a valuable tool for defect/inhomogeneity detection.

© The Author(s) 2019. Published by ECS. This is an open access article distributed under the terms of the Creative Commons Attribution 4.0 License (CC BY, <http://creativecommons.org/licenses/by/4.0/>), which permits unrestricted reuse of the work in any medium, provided the original work is properly cited. [DOI: 10.1149/2.0011902jes]



Manuscript submitted August 20, 2018; revised manuscript received November 30, 2018. Published January 4, 2019.

It is widely assumed that economies of scale will help solve the cost problem of lithium ion batteries in automotive and home or grid storage applications.^{1–3} Apart from reducing sourcing costs of primary materials, a large portion of the savings from scaling up production is realized through improving manufacturing processes.⁴ The most important characteristics of lithium-ion cells, namely safety, performance, and lifetime, are determined by their manufacturing quality as much as the material composition of the active and passive components and the cell design. As of today, a limited amount of research on the effects of imperfect manufacturing processes on cell performance has been published. In Mohanty et al.,⁵ the cell performance implications and the effect of electrode manufacturing defects were studied. In Cannarella et al.⁶ it was shown that deliberately manufactured pore closure in separators led to lithium plating on the graphite anode around the compressed areas. Both studies found that the negative impact of a defect depends disproportionately on its size, such that very small local defects may not lead to secondary defects like lithium plating during operation at all. Defect size dependence on lithium plating has been further investigated in Liu et al.⁷

In this paper, we show how local, macroscopic inhomogeneities in a commercial lithium-ion pouch cell that possibly originate from the manufacturing process, lead to unexpected local volume changes. Volume changes of lithium ion cells during operation can be attributed to several mechanisms. Firstly, intercalation materials used in lithium ion cells undergo volume changes as a function of their degree of lithiation.^{8–11} Secondly, every component of a cell swells and contracts as a function of its temperature and individual thermal expansion coefficient.^{12–14} Other reasons for volume changes are morphology changes in the porous electrodes and separators, side reactions that produce gas and/or passivating layers,^{15,16} and unwanted surface film forming mechanisms like lithium plating.^{16,17} From a practical point of view, understanding volume changes in lithium ion batteries is essential to ensure safe operation in applications where batteries are fitted into confined spaces, which is the case for virtually all mobile applications. Furthermore, dilation or resulting pressure is a relatively easily accessible quantity that holds information about the inner state of a lithium-ion cell, possibly making it a valuable input parameter for battery management systems.^{18–20}

Various approaches have been presented to measure the dilation of lithium-ion cells in operation. In Lee et al.²¹ a thickness gauge

was used to measure the average thickness change of a commercial pouch cell compressed between two plates. More accurate displacement sensors touching on a single location on the cell surface were used in Refs. 21–23 and on various locations simultaneously on both sides of the cell in Ref. 24. Local resolution of cell dilation has been achieved by 3-D image correlation²⁵ and laser triangulation.^{26–28} Other non-touching measurements include X-ray tomography²⁹ and neutron diffraction.¹⁵

Dilation measurements have been used to detect lithium plating²² and, by making use of local resolution across the cell surface, to investigate inhomogeneous aging.^{27,30} Here, we investigate and discuss the relationship of macroscopic inhomogeneities observable in fresh cells to anomalous local volume expansion and local deposits on the electrodes found post-mortem.

Experimental

Cells characterization and cycling.—The cells used in this study are commercial 5 Ah pouch cells with a nickel-manganese-cobalt-lithium oxide (NMC) cathode and graphite anode of the type SLPB 11543140H5 by Kokam Ltd. Cell characteristics are summarized in Table I. For each of the tests described in Table II, a fresh cell in condition as received from the supplier was used after the initial characterization. In a preliminary study, a wide range of charge and discharge rates were used across different cells to ensure the results observed were repeatable.

Before each test, the initial characterization test was performed on each fresh cell to ensure that the cells were in condition as specified by the manufacturer. The fresh cells were cycled 10 times with 100% depth of discharge at 0.5C using constant current, constant voltage (CC-CV) charge and constant current (CC) discharge protocol, followed by a CC-CV discharge capacity determination at 0.1C. All CV phases were interrupted when the current fell below 0.05C or 0.25A.

Cycling was done at current rates ranging from 0.2C to 4C using a CC-CV charge and CC discharge protocol. Full cycles at various combinations of charge and discharge rates were conducted to assess the rate dependency of local swelling. Chamber temperature was 15°C in all experiments.

2-D thickness scan.—Two laser heads directed at both sides of the cell are mounted on a linear axis aligned in parallel to the cell surface as shown in Figure 1. Each laser head performs a continuous triangulation measurement while the slide is moved along the cell surface. The slide moves at a speed of 2 cm/s, so the entire surface of the Kokam cell is captured in 6 s. The differential of the height

⁼These authors contributed equally to this work.

*Electrochemical Society Student Member.

**Electrochemical Society Member.

[†]E-mail: franz.spingler@tum.de

Table I. Characteristics of Kokam SLPB11543140H5 pouch cells used in this study.

Outer dimensions (LxWxH)	142.5 mm × 51 mm × 11.7 mm (data sheet)
Anode sheet size (LxWxH)	111 mm × 39 mm × 97 μm (measured)
Cathode sheet size (LxWxH)	110 mm × 38 mm × 79 μm (measured)
Current collector thickness	Anode: ~21 μm/Cathode: ~21 μm (measured)
Coating thickness	Anode: ~76 μm/Cathode: ~58 μm (measured)
Stack design	50 double side coated anodes, 49 double side coated cathodes + 2 single side coated cathodes. Separator Z-folded.
Max. charge/discharge rate	5C/20C
Upper and lower cutoff volt.	4.2 V/2.7 V
Rated capacity	5 Ah (0.5C, 25°C)
Gravimetric energy density	140 Wh/kg

profiles recorded by each laser head is the cell thickness. The setup is encased in a temperature-controlled chamber. The cell is connected to a BaSyTec CTS battery cycler. An infrared temperature sensor tracks the surface temperature at the center of the cell. More details about the test bench can be found in previous studies.^{26,27,30} The scan area was partitioned into 96 rectangles and the thickness was averaged across the surface of every rectangle in a pre-processing step. In these rectangles, thickness is resolved within $\pm 1 \mu\text{m}$ at a reproducibility of $\pm 2 \mu\text{m}$ including dismounting and re-mounting of a test cell. As the cell edges of the Kokam pouch cells are bent down and their shape varies slightly from cell to cell, the scan area excluded a few millimeters of the cell edge to each side to get consistent results.

Post-mortem and SEM.—Before disassembly, cells were discharged with CC-CV to 2.7 V and rested for one to two hours. Disassembly of cells took place inside an argon filled glove box ($<0.1 \text{ ppm O}_2 / \text{H}_2\text{O}$). Photographs of the cell stack and of single electrodes were taken immediately after disassembly. Separator and electrode probes were left to dry inside the glove box and then transferred out, where they were exposed to normal laboratory atmosphere. Separator probes were gold-sputtered in vacuum atmosphere for 90 s at 10 mA using a Cressington 108 series bench top SEM sputter coater before they were introduced into the SEM. A JCM-6000Plus Tabletop SEM by JEOL was used for electrode probes, separators were investigated using a ZEISS NV40 Crossbeam Workstation.

Results

Initial measurements.—Cells were charged with a CC-CV procedure to 4.2 V, rested for 30mins, and then discharged with 1C CC to 2.7 V, while the laser measurement was taken. Figure 2 shows snapshots of the normalized thickness distribution change during the 1C CC discharge step. To show the thickness change clearly, the thickness at the start of the discharge was subtracted from the raw measurement. Previous work³¹ shows that the cell thickness change roughly follows the state of charge change, where the cell thickness increases during charge and decreases during the discharge process. At time 776 s in Figure 2, four spots on the cell started to swell, while the rest of the cell contracted as expected. The approximate x-y coordinates of the swelling points are point 1 (−33,5); point 2 (35,7); point 3 (−33,−13) and point 4 (35,−14). These points and the surrounding area continued to swell as the discharge continued. At point (−33,5) the thickness increased from 0.034 mm to 0.062 mm between 776 s and 2716 s. The thickness of the rest of the cell continued to decrease with decreasing SoC. At time 2716 s, the cell thickness at the center (0,0) was reduced

by 0.049 mm. As a result, the difference in thickness between center (0,0) and the swelling point (−33,5) was around 0.1 mm. The thickness change behavior at these swelling points is unexpected; therefore more investigation was done to understand this behavior.

Cycling at different charge and discharge rates.—In this section, the effects of charge and discharge rate on the swelling points are investigated. A fresh cell was cycled at different charge rates followed by a CC discharge, and vice versa.

Effect of the charge rate.—Cells were charged using a CC-CV protocol at increasing current rates, 0.2C, 0.5C, 1C and 2C. Each charging event was followed by a 1C discharge. Figure 3 shows the thickness change as a function of time. The average thickness (black line) increased upon charging and decreased upon discharge. The average thickness is defined as the average of all recorded local

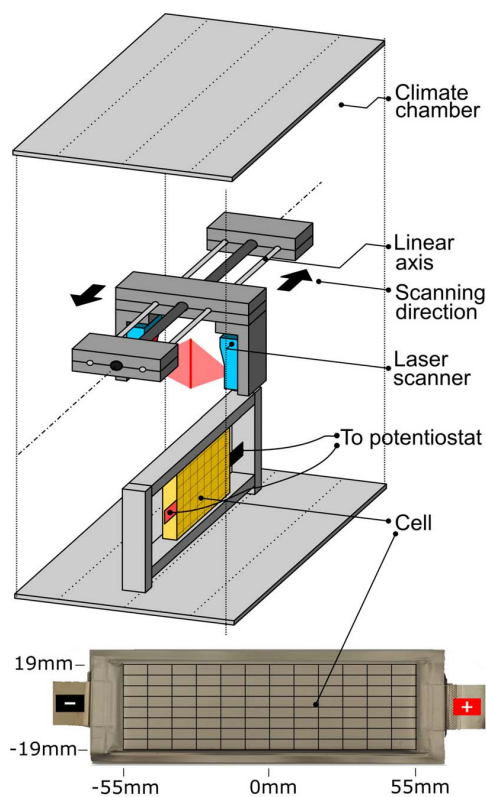


Figure 1. 2-D thickness scan setup used in this study. One laser head on each side of the cell scans the cell surface while moving in parallel to the cell surface. The cell surface is partitioned into 96 rectangles whose area-average thickness is computed after every scan.

Table II. Cycling conditions of Kokam SLPB11543140H5 cell. All experiments were conducted at 15°C chamber temperature.

	Charge rate	Discharge rate	Comments
Fig. 2	1C	1C	Full cycle
Fig. 3/Fig. 4	0.2C/0.5C/1C/2C	1C	Full cycle
Fig. 5	0.2C/0.5C/1C/2C	0.2C/0.5C/1C/2C	Full cycle
Fig. 6	0.2C/2C	2C/0.2C	Full cycle

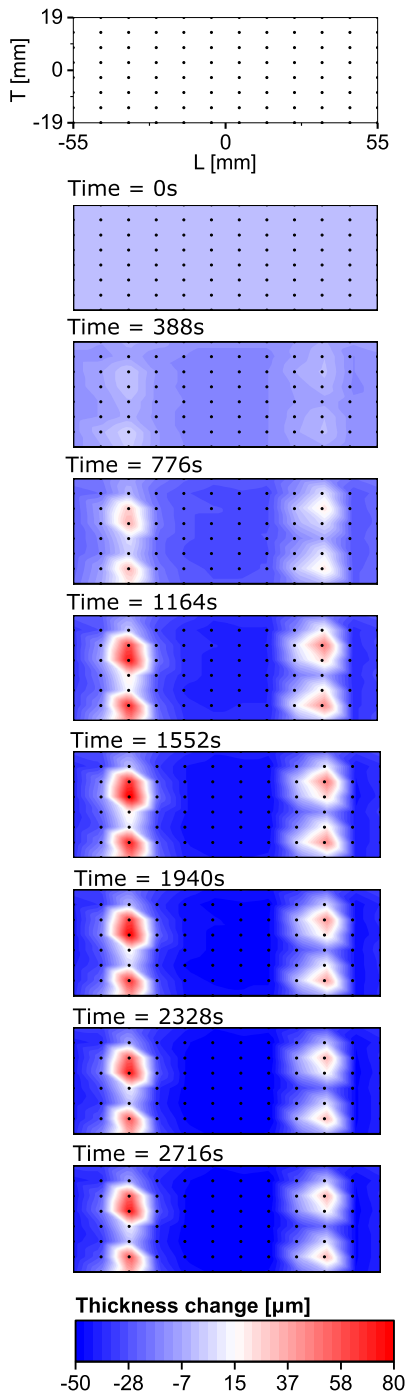


Figure 2. Normalized cell thickness distribution change during the 1C discharge following 1CCC-CV charging, where y-axis is the length and x-axis is the width of the cell in mm.

thickness measurements at a given point in time. The shape of the average thickness resembled that of the voltage curves. The thickness varied by approximately 0.23 mm (2% of the total thickness). The slight difference between different charge rates could be caused by variation in temperature and utilized SoC window.

At the four swelling points, local thickness revealed thickness overshoots close to the end of charge that increased in magnitude with

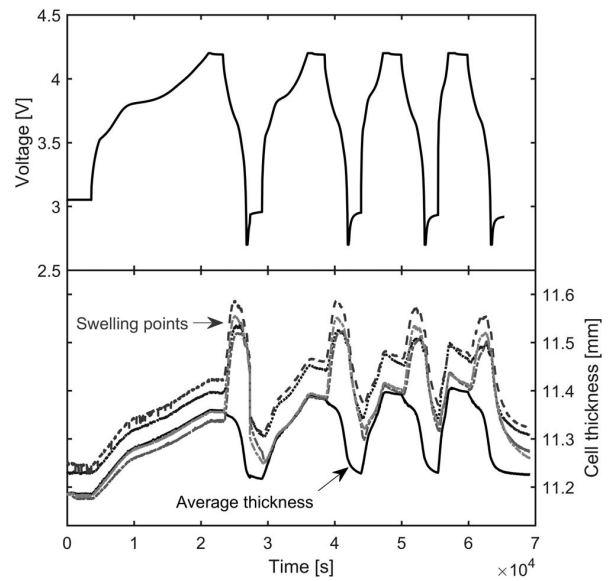


Figure 3. The thickness change as function of time with different charge rates (0.2C, 0.5C, 1C and 2C)- cell voltage (top) and thickness (bottom) at selected points, where the black line is the cell average thickness and the gray lines are thickness at swelling point 1–4.

the charging current. These thickness overshoots have been shown in a previous study and could be linked to partly reversible lithium plating.³⁰ Interestingly, at the beginning of the discharge phase, the points again swelled sharply. Thickness only started to decrease once the SoC dropped below approximately 30%–40%.

Thickness change as a function of preceding charge rates is shown in Figure 4 where the average thickness is plotted in gray and the swelling point 1 is plotted in black. On average, the cell contracted by

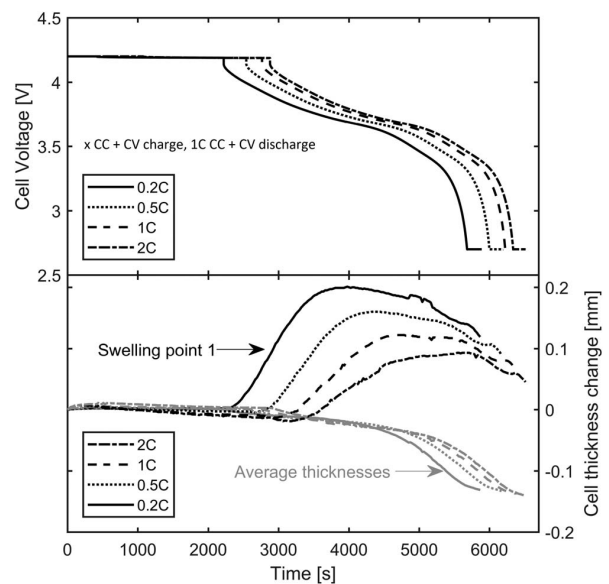


Figure 4. Comparison of the thickness change between swelling point (SP) 1 and the average cell thickness change during the 1C discharge phase after charging at 0.2C, 0.5C, 1C and 2C. The gray line is the cell average thickness and the black lines are thickness at swelling point 1, cell voltage (top) and thickness (bottom).

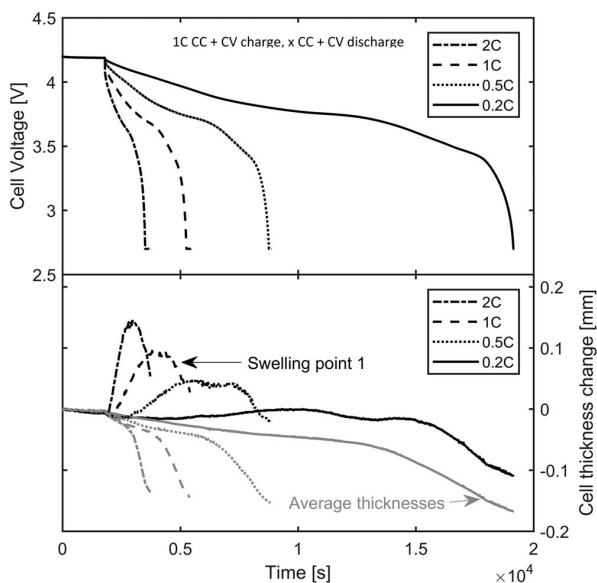


Figure 5. Comparison of thickness change between swell point 1 (SP1) and the average cell thickness change during the discharge (0.2C, 0.5C, 1C and 2C) phase following the 1C charge, where the black line is the cell average thickness and the gray lines are thickness at swelling point 1, cell voltage (top) and thickness (bottom).

approximately 0.14 mm during the 1C discharge. When it followed a 0.2C charge, the 1C discharge resulted in 0.012 mm more contraction than when it followed a 2C charge. This may be attributed to greater thermal expansion and contraction in the 2C charge case.

At swelling point 1, thickness started to increase at the beginning of discharge. The point started to contract after approximately 1500 s. Expansion upon discharge was most significant following the 0.2 C charge and the least significant following the 2C charge. The maximum local thickness increase was 0.198 mm, 0.158 mm, 0.122 mm and 0.095 mm following charge rates of 0.2C, 0.5C, 1C and 2C, respectively. At the end of discharge, the local thickness values were still +0.117 mm, +0.087 mm, +0.062 mm and +0.047 mm.

As swelling points expanded further while the rest of the cell contracted, the maximum difference in thickness change during the process was over 0.2 mm by the end of the discharge. The difference of 0.2 mm amounts to around 2% of total cell thickness. This could lead to significant mechanical stress within the electrode layers, and potentially result in mechanically driven damages.

Effect of the discharge rate.—In this section, the effect of the discharge rate on the behavior of the swelling points is presented. In each experiment, cells were charged at a rate of 1C, followed by discharge at rates of 0.2C, 0.5C, 1C and 2C. The thickness change during the discharge phase is shown in Figure 5, where the average thickness is plotted in gray and the swelling point 1 is plotted in black.

At all discharge rates, the average thickness decreased. The shape of the thickness curve resembled the shape of the voltage curve. The thickness changes at the end of discharge are similar, the thickness decreased by approximately 0.15 mm. At a discharge rate of 0.2C, the cell contracted by 0.167 mm in comparison to 0.136 mm at the end of the 2C discharge. The larger discharge current caused the cell's terminal voltage to reach the cutoff voltage sooner, limiting the usable capacity. The reduced capacity utilization could have caused the cell to contract less at the end of discharge at higher rates.

At the swelling point, thickness change during the discharge phase was positively correlated with the current rate. The maximum expansion at 0.2C, 1C, 0.5C and 2C were 0.144 mm, 0.095 mm, 0.046 mm and 0.003 mm. The swelling point started to contract when SoC dropped below approximately 60% SoC. At the end of the discharge, swelling point expansion were 0.058 mm, 0.027 mm, -0.022 mm and -0.108 mm. Interestingly, the discharge rate had the opposite effect as the charge rate. The higher the discharge rate, the higher the local swelling following the same charge event.

So far, the results indicate that the swelling points expand more significantly when charged slowly and the opposite is true for the discharge rate. To validate this observation, two tests were performed: 1. Charge 0.2C + Discharge 2C; 2. Charge 2C + Discharge 0.2C. The hypothesis was that the experiment 1 should indicate the most significant swelling under discharge and the experiments 2 would show the least amount of swelling.

Figure 6 shows the results of experiment 1 and 2. In experiment 1, the thickness increased significantly during the 2C discharge phase at the swelling points. The thickness increase peaked at approximately 0.18 mm during discharge. By the end of the discharge phase, thickness at the swelling points were approximately 0.11 mm higher

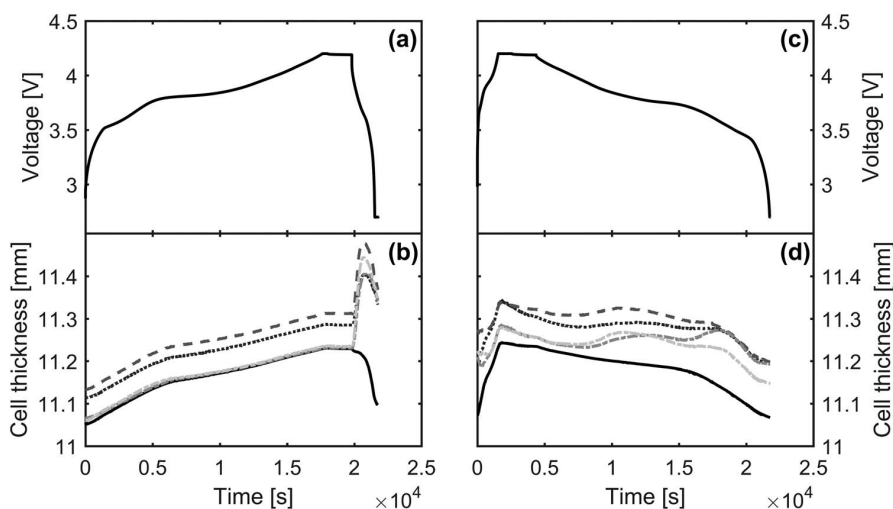


Figure 6. Voltage and thickness: experiment 1 (charge @ 0.2C + discharge @ 2C), (a) experiment 1 voltage measurement, (b) thickness of swelling points (gray lines) and average thickness (black); experiment 2 (charge @ 2C + discharge @ 0.2C), (c) experiment 2 voltage measurement, (d) thickness of swelling point (gray lines) and average thickness (black).

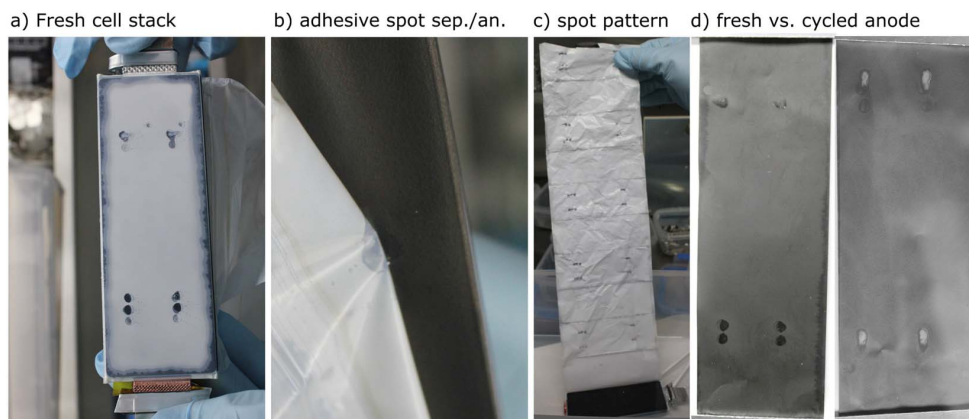


Figure 7. Post-mortem of the cell, (a) fresh cell stack; (b) adhesive like spots; (c) spots pattern on cycled separator roll; (d) spots on anode surface for fresh and cycled cell.

compared to the start of discharge. In comparison, the average thickness of the cell decreased by 0.13 mm during the discharge phase.

In experiment 2, where the minimum swelling was expected, the thickness at the swelling points decreased by 0.15 mm during discharge. The average thickness decreased by 0.17 mm at the same time. However, the thickness at the swelling points decreased initially, followed by small increases at 3.9 V and 3.5 V. In contrast, the cell average thickness decreased uniformly without increase during the discharge phase.

In accordance with our hypothesis, experiment 1 showed significantly more swelling during the discharge phase. Thickness at swelling points were 0.15 mm higher in comparison to experiment 2.

Post-mortem inspection.—Experimental results showed that low rate charging, high rate discharging causes four areas on the cell surface to swell abnormally during discharge. A fresh and a cycled cell were disassembled inside an argon filled glove box to examine the physical appearance of the cell material. The cycled cell underwent ca. 40 cycles and various current rates and had 98% remaining capacity before it was disassembled.

Upon unwrapping the electrode stack, four discolored spots were discovered on the separator surface. The spots were located at co-

ordinates $(-33,5)$, $(35,7)$, $(-33,-13)$ and $(35,-14)$. The locations of these spots are consistent with the location of the swelling points measured by the laser scan. The spots appeared to be contaminated by adhesive-like gel as shown in Figure 7b. The spot appeared on alternate layers of the separator as shown in Figure 7c. This pattern was repeated in the entire stack. Figure 7d shows the swelling spots of a fresh and a cycled cell. On the fresh anodes, dark spots are visible, these match the locations of the spots on the separator. When unwrapping the cell stack, separator and electrodes adhered to one another at these spots. On and around the spots, gray deposit appears to have accumulated on the anodes of the cycled cell. The zoom inset in Figure 7d shows a light-gray colored spot with a distinct seam of a different gray on its right side. This is consistent with the numerous disassembly observations made with the same and similar cell types from the same manufacturer by both battery research groups at TUM and Imperial College over the past 3 years.^{30,32,33} The adhesive-like contaminants were constantly found. These include cells in fresh and cycled condition. Cells were purchased from different suppliers and at different times. It could be that the contaminant is indeed an adhesive that is used on purpose in the manufacturing process to hold the layers (electrodes, separator) in place during stacking and subsequent handling.

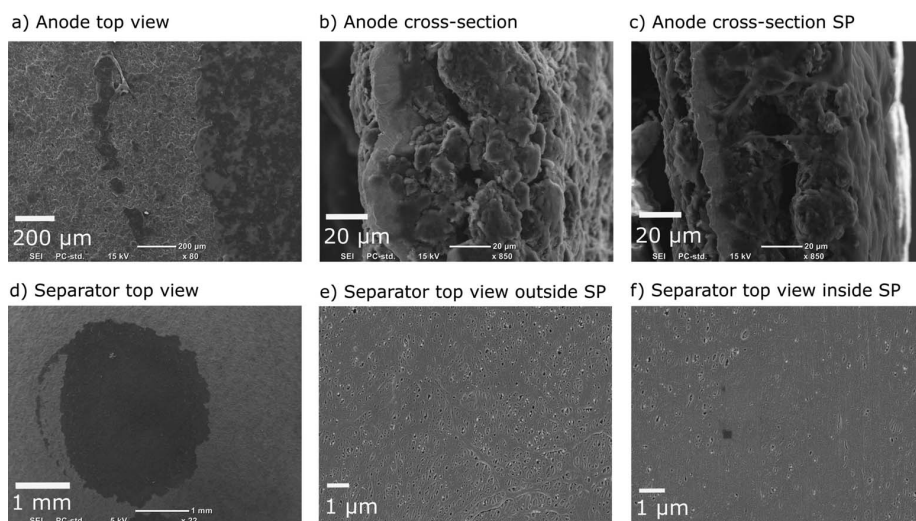


Figure 8. SEM imaging of the disassembled cells. An ‘adhesive’ like contaminant is visible on the anode surface at the location of the swelling points in a) and c) and on the separator in d). Details of the separator outside (e) and inside (f) the swelling point suggest that the contaminant filled the separator pores.

Table III. Thermal expansion coefficient calculation for 'normal' part of cell.

	Total thickness [mm]	Percentage of total	Expansion coefficient	Proportional coefficient	Reference
CC Cu	1.05	9.0%	1.60×10^{-5}	1.44×10^{-6}	38
CC Al	1.07	9.2%	2.30×10^{-5}	2.11×10^{-6}	38
Anode	3.95	33.8%	5.50×10^{-5}	1.86×10^{-5}	39
Cathode	2.90	24.8%	5.50×10^{-5}	1.36×10^{-5}	Assumed same as Anode ³⁹
Separator/SP	2.40	20.5%	2.50×10^{-3}	5.13×10^{-4}	40
Casing	0.32	2.7%			
Total	11.69			5.49×10^{-4}	

To investigate the contaminant on the electrode/separator structure, SEM imaging was used. Figure 8a shows the top view of the boundary between swelling spots and the rest of the electrode surface. The contaminant appears to have filled the gaps between individual graphite particles and made the originally rough surface smooth. The cross-sectional image of the 'normal' anode and the swelling point further confirms this observation. It appears that the contaminant blocked this part of the electrode surface. The blockage could limit the ion transport and reaction rate. At worst, the entire region could have become inactive. It is difficult to determine the effect of the contaminant from the SEM images alone.

On the separator, the contaminant appears to have closed the pores on the separator, when comparing Figure 8e and Figure 8f. The pore closure could lead to slower ionic transport through the separator. As shown by Cannarella et. al, pore closure can cause high local currents and overpotentials in the surrounding electrode area, rendering it susceptible to lithium plating.⁶

Discussion

In this section, we present hypotheses that could explain the experimental findings: Local swelling overshoots at the end of charge, local swelling at the beginning of discharge, localized gray deposits on the anode surface and adhesive-like contaminants found on the separator and both positive and negative electrodes.

Close to the end of charge, we observed that the cell thickness temporarily was higher than the final thickness after charging and relaxation, which has been referred to as swelling overshoot. The magnitude of these swelling overshoots was positively correlated with charging current and they were more pronounced at those locations where the adhesive-like contaminants were found. Local swelling overshoots comparable to those found here have been linked to lithium plating in a previous study.³⁰ Lithium plating on the graphite anode is thermodynamically favorable when the local potential, measured vs. a virtual Li/Li⁺ reference, falls below 0 V. This situation can result from limited transport in the liquid and solid phases^{34,35} and sluggish charge transfer kinetics³⁶ at the liquid-solid-interface. It has been shown experimentally that deliberately induced ion transport restrictions in separators lead to lithium plating on graphite anodes at the edges of the manipulated areas.^{6,7} Numerical analysis has shown that this is due to increased current densities in the vicinity of the manipulated areas that compensate for their restricted transport contribution.⁶ In our case, we may assume that the adhesive-like contaminants at the swelling points caused local transport non-uniformity. The swelling

points would have had a significantly higher transport limitation due to the blockage. As in the above reports, these effects could have induced local current density fluctuation and led to lithium plating. The localized gray deposits, which were found on the anode surface, especially the distinct seam around the spot that can be seen in Figure 7d, support this hypothesis.

As for the local swelling during discharge, the experimental results, as shown in Figure 5, indicate that the swelling positively correlated with the discharge rate after the cell was charged at same rate, i. e. a larger discharge current led to higher swelling. The cell thickness is influenced by both SoC reduction and temperature increase. SoC reduction will lead to a reduction in cell thickness and temperature increase will lead to an increase due to thermal expansion. Overall, the cell thickness decreases as it is being discharged. As for the swelling points, it was observed that the thickness increases significantly at the start of the discharge. To explain this observation, we hypothesize the following:

1. the adhesive like contaminants are preventing the swelling points from discharging locally at the same rate as the rest of the cell. This would lead to less reduction in SoC as the discharge starts locally at swelling points and, as a result, less thickness reduction.
2. a greater discharge rate causes more heat generation, leading to higher thermal expansion. The difference in material composition at the swelling points could also contribute to a greater thermal expansion.

Overall, the swelling points' thickness would increase on discharge if the thermal expansion could not be compensated for by the SoC-dependent thickness reduction when discharge is hampered in these areas. Combined with the thermal expansion a different thickness change pattern can be expected. Figure 9 illustrates the correlation of cell temperature increase with the normalized thickness evolution at the swelling spots for different discharge rates. The thickness at SP1 were normalized by the average thickness of the cell. At different C-rates, the normalized expansion at the SP1 and average cell expansion correlates well with the temperature increase. This correlation supports the hypothesis that the containment has a higher thermal expansion coefficient.

A simple calculation of thermal expansion during a 2C discharge is performed for both the 'normal' and the swelling parts of the cell. Equation 1 is used to calculate the overall thermal expansion coefficient of the cell from the individual components. A 4°C temperature increase was measured during 2C discharge. Table III shows the

Table IV. Thermal expansion coefficient calculation for swelling point (SP).

	Total thickness [mm]	Percentage of total	Expansion coefficient	Proportional coefficient	Reference
CC Cu	1.05	9.0%	1.60×10^{-5}	1.44×10^{-6}	38
CC Al	1.07	9.2%	2.30×10^{-5}	2.11×10^{-6}	38
Anode	3.95	33.8%	5.50×10^{-5}	1.86×10^{-5}	39
Cathode	2.90	24.8%	5.50×10^{-5}	1.36×10^{-5}	Assumed same as Anode ³⁹
Separator/SP	2.40	20.5%	9.00×10^{-3}	1.85×10^{-3}	Fitted
Casing	0.32	2.7%			
Total	11.69			1.88×10^{-3}	

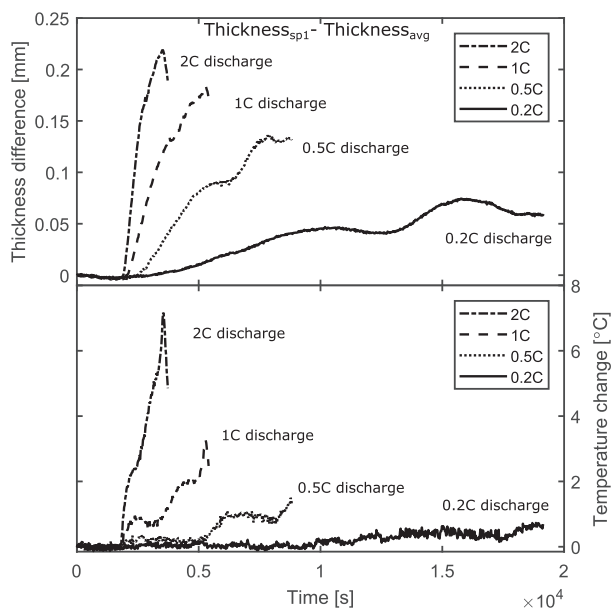


Figure 9. Comparison of the normalized thickness change at swelling point 1 (SP1). The cell surface temperature increases during discharge (0.2C, 0.5C, 1C and 2C) following the 1C charge: difference in thickness between SP1 and the average thickness (top) and temperature increase (bottom).

calculation of the thermal expansion coefficient for the ‘normal’ part of the cell. Based on the thermal expansion coefficient for individual components, the overall equivalent expansion coefficient is 5.49×10^{-4} 1/K. This corresponds to a 0.025 mm expansion for the 4°C temperature increase during a 2C discharge. The calculated equivalent expansion coefficient is consistent with measurements made in our previous study and with literature.^{14,30}

Assuming there is no thickness reduction due to SoC change at the swelling point, it would need to be 6°C hotter than the rest of the cell using the calculated expansion coefficient. As the cell is made of thermally conductive materials (aluminum and copper), we consider a hot spot of this magnitude to be unlikely. In our previous work, Zhao et al. showed that the maximum temperature gradient within a cell of the same type is approximately 2.5°C at the end of a 2C discharge under quiet aggressive thermal boundary conditions realized via metallic heat sinks.³⁷ In this work, all cell surfaces (electrode stack and electrical terminals) were exposed to ambient air, which should result in a much smaller thermal gradient than 2.5°C . Hence an alternative hypothesis must be considered. Based on the above, it is hypothesized that the swelling point may have a higher thermal expansion coefficient than the ‘normal’ parts of the cell.

$$\alpha_{total} L_{total} = \sum \alpha_i L_i \quad [1]$$

In Equation 1, α_{total} is the overall thermal expansion coefficient, L_{total} is the total cell thickness, α_i is the thermal expansion coefficient of individual components, and L_i is the thickness of individual components.

Table IV shows the value of the thermal expansion coefficient for the swelling point fitted to match the experiment if no local hotspot is assumed. It was found that a total thermal expansion coefficient of 1.88×10^{-3} 1/K would result in a 0.09 mm expansion during the discharge. This simple calculation demonstrates that if the contaminant has a higher thermal expansion coefficient than the separator, it could be the cause of the behavior observed during discharge. However, it was not possible to characterize the thermal expansion coefficient of the contaminants and/or modified region of the cell during this study. We consider the local swelling on discharge likely to result

from a combination of both effects, a thermal expansion coefficient that differs from the rest of the cell and a local hotspot.

Conclusions

Through a combination of cycling experiments, thickness measurements and post-mortem findings, this work shows that local inhomogeneities in a commercial pouch cell lead to irregular local volume changes and promote local lithium plating. It is hypothesized that the inhomogeneities in the form of an adhesive-like contaminant result from the manufacturing process of the cells. Analysis is provided that shows that the local expansion on discharge, which had not been observed in previous studies using a different cell,³⁰ could result from a relatively high thermal expansion coefficient of that contaminant and/or localized heating. Local lithium plating found post-mortem in the vicinity of the adhesive-like contaminants and SEM images of the separator and electrodes suggests that the contaminants restricted the ion pathways of the separator and/or blocks access to the electrodes’ surfaces. This would confirm existing theories about separator pore closure and localized lithium plating,^{6,7} which were based on experimental cells, by means of a commercially available cell. Further work is required to characterize the exact composition and property of the contaminant.

This work also demonstrates that the proposed local thickness measurement is a powerful non-destructive cell quality evaluation tool. We suggest that the laser scanning tool could be used to validate cell designs, to evaluate manufacturing processes and in manufacturing quality control.

Acknowledgments

We acknowledge the funding support received from the BIAM-Imperial Center for Materials Characterisation, Processing and Modelling at Imperial College London, from the Imperial-TUM Global Fellows Program and from the Federal Ministry of Education and Research of Germany (BMBF) under grant number 03XP0138B. We thank Jonathan Becker of WSI in Garching for his great help with SEM imaging and Prof. Dr. Karl-Heinz Pettinger of HAW Landshut for insightful discussions.

ORCID

Yan Zhao <https://orcid.org/0000-0002-3211-6740>
 Franz B. Spingler <https://orcid.org/0000-0002-6523-3986>
 Yatish Patel <https://orcid.org/0000-0001-7828-5315>
 Gregory J. Offer <https://orcid.org/0000-0003-1324-8366>
 Andreas Jossen <https://orcid.org/0000-0003-0964-1405>

References

1. B. Nykvist and M. Nilsson, *Nature Climate Change*, **5**, 329 EP - (2015).
2. M. Weiss, M. K. Patel, M. Junginger, A. Perujo, P. Bonnel, and G. van Grootveld, *Energy Policy*, **48**, 374 (2012).
3. L. Gaines and R. Cuenca, *Costs of lithium-ion batteries for vehicles*, (2000).
4. D. L. Wood, J. Li, and C. Daniel, *Journal of Power Sources*, **275**, 234 (2015).
5. D. Mohanty, E. Hockaday, J. Li, D. K. Hensley, C. Daniel, and D. L. Wood, *J. Power Sources*, **312**, 70 (2016).
6. J. Cannarella and C. B. Arnold, *J. Electrochem. Soc.*, **162**(7), A1365 (2015).
7. X. M. Liu, A. Fang, M. P. Haataja, and C. B. Arnold, *J. Electrochem. Soc.*, **165**(5), A1147 (2018).
8. M. Hahn, H. Buqa, P. W. Ruch, D. Goers, M. E. Spahr, J. Ufheil, P. Novák, and R. Kötz, *Electrochem. Solid-State Lett.*, **11**(9), A151 (2008).
9. M. Winter, G. H. Wroldnigg, J. O. Besenhard, W. Biberacher, and P. Novák, *J. Electrochem. Soc.*, **147**(7), 2427 (2000).
10. O. Dolotko, A. Senyshyn, M. J. Mühlbauer, K. Nikolowski, and H. Ehrenberg, *J. Power Sources*, **255**, 197 (2014).
11. Kejie Zhao, *Mechanics of Electrodes in Lithium-ion Batteries*, Cambridge (14.6.2012).
12. D. K. L. Tsang, B. J. Marsden, S. L. Fok, and G. Hall, *Carbon*, **43**(14), 2902 (2005).

13. E. A. Kellett and B. P. Richards, *Journal of Nuclear Materials*, **12**(2), 184 (1964).
14. K.-Y. Oh and B. I. Epureanu, *Journal of Power Sources*, **303**, 86 (2016).
15. J. B. Siegel, A. G. Stefanopoulou, P. Hagans, Y. Ding, and D. Gorsich, *J. Electrochem. Soc.*, **160**(8), A1031 (2013).
16. M. Petzl, M. Kasper, and M. A. Danzer, *J. Power Sources*, **275**, 799 (2015).
17. M. Lewerenz, A. Warnecke, and D. U. Sauer, *Journal of Power Sources*, **369**, 122 (2017).
18. N. A. Samad, Y. Kim, J. B. Siegel, and A. G. Stefanopoulou, *J. Electrochem. Soc.*, **163**(8), A1584 (2016).
19. S. Mohan, Y. Kim, J. B. Siegel, N. A. Samad, and A. G. Stefanopoulou, *J. Electrochem. Soc.*, **161**(14), A2222 (2014).
20. J. Cannarella and C. B. Arnold, *J. Power Sources*, **269**, 7 (2014).
21. J. H. Lee, H. M. Lee, and S. Ahn, *J. Power Sources*, **119–121**, 833 (2003).
22. B. Bitzer and A. Gruhle, *J. Power Sources*, **262**, 297 (2014).
23. I. Soga and Y. Kinoshita, *Japanese Journal of Applied Physics*, **41**(Part 1, No. 11A), 6616 (2002).
24. K.-Y. Oh, J. B. Siegel, L. Secondo, S. U. Kim, N. A. Samad, J. Qin, D. Anderson, K. Garikipati, A. Knobloch, B. I. Epureanu, C. W. Monroe, and A. Stefanopoulou, *J. Power Sources*, **267**, 197 (2014).
25. P. K. Leung, C. Moreno, I. Masters, S. Hazra, B. Conde, M. R. Mohamed, R. J. Dashwood, and R. Bhagat, *J. Power Sources*, **271**, 82 (2014).
26. B. Rieger, S. F. Schuster, S. V. Erhard, P. J. Osswald, A. Rheinfeld, C. Willmann, and A. Jossen, *Journal of Energy Storage*, **8**, 1 (2016).
27. J. Sturm, F. B. Spingler, B. Rieger, A. Rheinfeld, and A. Jossen, *J. Electrochem. Soc.*, **164**(7), A1342 (2017).
28. C. Birkenmaier, B. Bitzer, M. Harzheim, A. Hintennach, and T. Schleid, *J. Electrochem. Soc.*, **162**(14), A2646 (2015).
29. X. Wang, Y. Sone, and S. Kuwajima, *J. Electrochem. Soc.*, **151**(2), A273 (2004).
30. F. B. Spingler, W. Wittmann, J. Sturm, B. Rieger, and A. Jossen, *Journal of Power Sources*, **393**, 152 (2018).
31. B. Rieger, S. V. Erhard, K. Rumpf, and A. Jossen, *J. Electrochem. Soc.*, **163**(8), A1566 (2016).
32. I. A. Hunt, Y. Zhao, Y. Patel, and J. Offer, *J. Electrochem. Soc.*, **163**(9), A1846 (2016).
33. Y. Zhao, Y. Patel, I. A. Hunt, K. M. Kareh, A. A. Holland, C. Korte, J. P. Dear, Y. Yue, and G. J. Offer, *Journal of Energy Storage*, **13**, 296 (2017).
34. K. Zaghbi, F. Brochu, A. Guerfi, and K. Kinoshita, *J. Power Sources*, **103**(1), 140 (2001).
35. S. S. Zhang, K. Xu, and T. R. Jow, *Electrochimica Acta*, **48**(3), 241 (2002).
36. J. Li, C. F. Yuan, Z. H. Guo, Z. A. Zhang, Y. Q. Lai, and J. Liu, *Electrochimica Acta*, **59**, 69 (2012).
37. Y. Zhao, Y. Patel, T. Zhang, and G. J. Offer, *J. Electrochem. Soc.*, **165**(13), A3169 (2018).
38. Schaeffler, *Technisches Taschenbuch*, (2014).
39. Chetna Bindra, Vera A. Nalimova, Dmitry E. Sklovsky, William A. Kamitakahara, and John E. Fischer, *Phys. Rev.*, **B 57**, 5182 (1998).
40. James E. Mark, *The Polymer Data Handbook*.

3.2 Optimizing Operational Strategies by On-Line Detection of Lithium Plating

In section 2.1, the theoretically higher space requirement of plated lithium in comparison to lithium intercalated into graphite was discussed. Based on this, the following study attempted to establish relationships between thickness change characteristics and lithium plating/stripping processes. Using the 2-D laser scanning setup, the reversible and irreversible thickness changes of a commercial 3.3 Ah pouch cell were investigated as a function of the charging rate and the selected SOC window. A correlation between local thickness overshoots at the end of charging and reversible lithium plating was confirmed by exploiting the relationship between the voltage drop at the end of a charging event and the lithium plating/stripping process [93]. Local thickness overshoots of up to 50 μm coincided with clear plateaus in the voltage response to a shutting off of the charging current. To detangle thickness overshoots caused by plating from those caused by possible thermal expansion, the local thermal expansion coefficient was determined and included in the analysis. Finally, a post-mortem inspection confirmed the link between permanent local thickness changes and irreversible depositions on the graphite anodes. Motivated by the clear relationship between local thickness overshoots and lithium plating, a series of experiments was devised to create a map linking SOC, charging rate, and thickness overshoots. Based on this map, a step-wise fast charging protocol that limits thickness overshoots was created. A cycle study showed that the fast charging protocol compared very favorably to standard 1C CC-CV charging in terms of charging time and capacity retention. For a full charge from 0 % SOC to 100 % SOC, a charging time reduction of 11 % was realized while increasing capacity retention from 90 % to 91.6 % after 1000 cycles.

Building on the methods and results from the previous section, this study establishes the link between local thickness change and lithium plating. It is shown that limiting local thickness change alone can guide the design of appropriate fast charge protocols. Furthermore, this study explores the idea of using local thickness change as a control feedback during cell operation. At the application level, the findings suggest that, if the cell thickness could be monitored in a locally resolved manner, the operational strategy could be altered in real-time by the battery management system to adjust to the onset of localized lithium plating. The thickness measurement could potentially be replaced by a locally-resolved force measurement, which is more compatible with the frequent presence of mechanical constraints in module assemblies.

Author contribution Franz Spingler was responsible for the conceptualization, methodology, investigation, and writing of the original draft. Wilhelm Wittmann helped with the experiments. Johannes Sturm and Bernhard Rieger reviewed and commented on the manuscript. Andreas Jossen provided supervision, and reviewed and commented on the manuscript.

Optimum fast charging of lithium-ion pouch cells based on local volume expansion criteria

Franz B. Spingler, Wilhelm Wittmann, Johannes Sturm, Bernhard Rieger, Andreas Jossen

Journal of Power Sources 393 (2018), pp. 152–160

Permanent weblink:

<http://dx.doi.org/10.1016/j.jpowsour.2018.04.095>

Reproduced under the terms of the Creative Commons Attribution 4.0 License (CC BY, <http://creativecommons.org/licenses/by/4.0/>), which permits unrestricted reuse of the work in any medium, provided the original work is properly cited.



Contents lists available at ScienceDirect

Journal of Power Sources

journal homepage: www.elsevier.com/locate/jpowsour

Optimum fast charging of lithium-ion pouch cells based on local volume expansion criteria



Franz B. Spingler*, Wilhelm Wittmann, Johannes Sturm, Bernhard Rieger, Andreas Jossen

Institute for Electrical Energy Storage Technology, Technical University of Munich (TUM), Arcisstr. 21, 80333 Munich, Germany

HIGHLIGHTS

- Correlations of local expansion, lithium plating and capacity loss are presented.
- Lithium plating is assessed by voltage relaxation experiments and post-mortem.
- A method to design a fast charging protocol based on local expansion is introduced.
- The proposed fast charging protocol provides quick charging and long cycle life.

ABSTRACT

Fast charging of high-energy lithium-ion cells is desired in many applications but there is a lack of simple methods to determine the maximum charging current a cell will accept without sustaining damage. Here we explore the link between local volume expansion and lithium plating on the graphite anode of lithium-ion cells and propose a method that makes use of this link to design fast and gentle charging protocols. The expansion across the entire surface of a commercial nickel-manganese-cobalt-lithium oxide/graphite pouch cell is measured in short intervals using laser triangulation while operating the cell under various conditions. Irreversible expansion and expansion overshoots are correlated to voltage relaxation curves, post-mortem findings and capacity loss. Using the proposed method, a fast charging protocol is derived and validated in a cycle study covering 1000 cycles. The fast charging protocol enables both a 11% charging time reduction and a 16% reduction of capacity loss per cycle as compared to 1C constant current – constant voltage charging.

1. Introduction

Lithium-ion batteries are used for various mobile applications thanks to their high energy and power densities. During charging, however, mobile devices become stationary devices for a considerable period of time. In the case of electric vehicles (EVs), along with limited driving ranges on a fully charged battery, this hinders widespread customer acceptance. While today's fastest charging electric vehicles can accept 175 miles worth of charge in 32 min [1], many combustion engine driven cars can travel over 600 miles on a 2-minute refuel. To reduce this disadvantage, the charging power needs to be increased. Disregarding grid-side challenges, the main limitation to fast charging is accelerated cell aging [2]. Several aging mechanisms are linked to fast charging: It implies rapid intercalation of lithium ions into the electrode host structure which can induce great mechanical stress and may lead to particle delamination and fracturing, resulting in loss of capacity [3]. In Ref. [4] constant current — constant voltage (CC-CV)

and multi stage constant current — constant voltage (MCC-CV) charging methods are evaluated on the basis of mechanical stress calculated using a physics-based model. High charging currents and/or low temperatures can further lead to depositing of metallic lithium [5], also referred to as lithium plating, on the graphite negative electrodes, which is the material of choice in most state-of-the-art lithium-ion batteries. Lithium plating causes loss of capacity and is detrimental to cell safety, as it may grow in the form of dendrites that may penetrate the separator and cause a short circuit [6,7]. The onset of lithium plating, however, is difficult to detect. Lithium plating is assumed to be likely to occur where the local electrode potential with respect to a virtual lithium reference electrode is lower than 0 V. Inserting a real reference electrode into a cell is a viable method to obtain experimental access to half-cell potentials [8]. In Ref. [9] this technique was used to define MCC-CV charging protocols avoiding lithium plating. Another way to determine half-cell potentials is by simulating the internal states of lithium-ion cells using mechanistic electrochemical models. Based on

* Corresponding author.

E-mail address: franz.spingler@tum.de (F.B. Spingler).

<https://doi.org/10.1016/j.jpowsour.2018.04.095>

Received 28 February 2018; Received in revised form 17 April 2018; Accepted 27 April 2018
0378-7753/ © 2018 Elsevier B.V. All rights reserved.

a simplified Newman-type electrochemical model [10], Ref. [11] proposes to control the charging current by limiting the anode potential simulated on-line to values above 0V vs. Li+. Based on mechanistic electrochemical cell models as well, pulsed charging protocols have been derived by considering mass transport at the electrolyte-electrode interface [12–14]. Using a thermal-electric coupled cell model, Ref. [15] proposes a MCC-CV charging protocol based on temperature rise and polarization. In other studies, charging protocols featuring negative pulses [16,17] and CV hold at near-terminal voltage at a low state of charge (SOC) [18] are proposed and evaluated versus CC-CV charging in aging studies.

The authors of this work consider lithium plating the most crucial aging mechanism linked to fast charging, in particular with high-energy cells,¹ which are used in EVs. Hence, the aim of this work is to develop a fast charging method based on minimizing lithium plating. The approaches found in the literature either rely on a global criterion for plating in the case of reference electrodes, or do not consider local imperfections in the cell in the case of modeling.² Lithium plating, however, is a local effect [20] and closely linked to inhomogeneities induced by manufacturing [5,19] or usage [21]. Therefore, an optical thickness measurement across the cell's surface [22] was used in this work to spatially analyze the cell expansion caused by lithium plating during cell operation and link its severity to operational parameters. The advantage of this method is that it can detect “bad spots” where plating occurs at much lower loads than in the rest of the cell. This work builds on previous work [22] in which we established the usefulness of our local expansion measurement for detecting cell degradation.

In this paper, the relationship between local thickness changes of the cell and reversible and irreversible lithium plating is analyzed with the help of voltage relaxation and post-mortem analysis. The superposition of expansion due to intercalation and lithium plating with thermal expansion is discussed and accounted for in the experiment. A method to derive fast charging protocols that avoid lithium plating from thickness change measurements is proposed and applied to a commercial high-energy pouch cell. Finally, this method is validated in an aging study covering 1000 full cycles.

2. Experimental methods

2.1. Cells and preconditioning

The cells used in this study are commercial 3.3 Ah pouch cells with a nickel-manganese-cobalt-lithium oxide (NMC) cathode and graphite anode of the type SLPB 526495 by Kokam Ltd. A total of 24 cells was used in this study, 8 for the cycling study and 16 for the fundamental experiments. Cell characteristics are summarized in Table 1. Fresh cells were cycled 10 times with 100% depth of discharge at 0.5C using a CC-CV charge and CC discharge protocol, followed by a CC-discharge capacity determination at 0.1C. If not indicated otherwise, CV phases were at 4.2V and stopped when the current fell below C/20.

2.2. 2-D thickness scan

Inside a temperature-controlled chamber, two laser heads performing a continuous triangulation measurement are moved periodically along the length of a cell and in parallel to its surface, while the cell is connected to a BaSyTec CTS battery cycler. A schematic of the test bench is shown in Fig. 1. The differential of the recorded height profiles of each laser head is the cell thickness. The temperature inside the test chamber can be controlled between 15 °C and 45 °C. An infrared

Table 1
Characteristics of Kokam SLPB 526495 pouch cells used in this study.

Outer dimensions (LxWxH)	95 mm × 64 mm x 5.2 mm
Anode sheet size (LxWxH)	84 mm × 60 mm x 207 μm
Cathode sheet size (LxWxH)	82 mm × 58 mm x 149 μm
Current collector thickness	Anode: ~11 μm/Cathode: ~16 μm
Coating thickness	Anode: ~98 μm/Cathode: ~66.5 μm
Stack design	Two units wrapped in separator, each consisting of: 6 double side coated anodes, 5 double side coated cathodes + 2 single side coated cathodes. Separator Z-folded.
Max. charge/discharge rate	1C/2C
Upper and lower cut-off volt.	4.2 V/3.0 V
Gravimetric energy density	190 Wh/kg

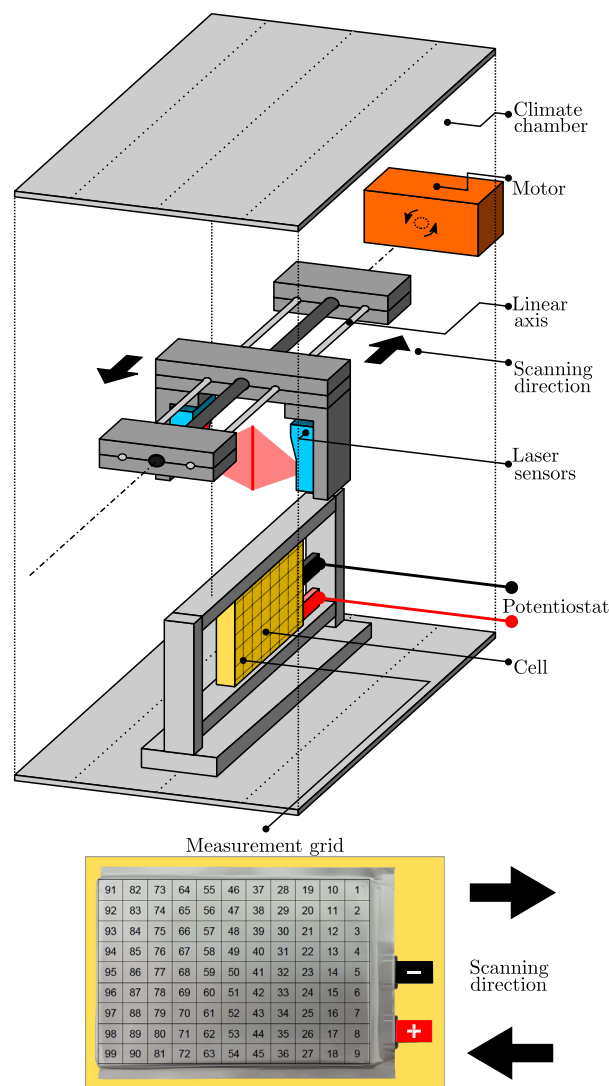


Fig. 1. Schematic of 2-D thickness scan test bench. Two laser heads perform a continuous vertical line scan while being moved in parallel to the cell surface, covering the entire cell. In a pre-processing step, the thickness data is discretized spatially into 99 rectangles.

¹ In order to maximize energy content rather than power capability, high-energy cells use relatively thick active material coatings and capacity ratios of anode to cathode close to one, which both favor the occurrence of lithium plating.

² Naturally, models can be used to assess the effects of local imperfections [19]. However, it is not usually known which specific imperfections an operating cell possesses.

temperature sensor tracks the surface temperature at the center of the cell. For more details on the test bench, the reader is referred to Rieger et al. [23] and Sturm et al. [22]. Each scan of the Kokam cell takes ca. 5 s. The measurement frequency in this study was 1–2 scans per minute. In order to reduce the amount of data, the scan area was partitioned into 100 rectangles and the thickness was averaged across the surface of every rectangle in a pre-processing step. In these rectangles, thickness is resolved within $\pm 1 \mu\text{m}$ at a reproducibility of $\pm 2 \mu\text{m}$ including dismounting and re-mounting of a test cell. As the cell edges are bent down and their shape varies slightly from cell to cell, the scan area excluded a few millimeters of the cell edge to each side to get a reliable measurement.

2.3. Thermal expansion experiments

Using the 2-D thickness scan, the thermal expansion of the Kokam cell was quantified in two different experiments: 1) At a constant chamber temperature of 25 °C, a current profile with alternating charge and discharge at 2C–3C with 2 s periodic time was applied to the cell. The cell's SOC could be assumed constant while the temperature of the cell increased due to the charge throughput. 2) A cell stored at 0 °C overnight was transferred into the chamber pre-heated to 45 °C. Periodic thickness scans were performed until the cell thickness became constant, indicating that the temperature throughout the cell had reached the chamber temperature. In both experiments, the surface temperature at the center of the cell was measured with an infrared thermometer.

2.4. Experiments on cell expansion vs. lithium plating

The objective of these experiments comprising 16 cells was to study the relationships between cell expansion overshoots and irreversible cell expansion, reversible and irreversible lithium plating, and capacity loss. Throughout this paper, cell expansion overshoot refers to the difference between maximum thickness during charge and the thickness at the end of charge (to any SOC) after a sufficient relaxation period, i.e. when no more thickness changes can be observed. Irreversible expansion refers to the thickness difference of the fully discharged cell before and after a charging event. Evidence of lithium plating was provided by a) voltage relaxation experiments, where voltage was recorded in 25 ms time increments for 30 min after the end of charge and b) post-mortem investigation of cells discharged to 3.0V that were opened inside a glovebox in $< 0.1 \text{ ppm H}_2\text{O/O}_2$ atmosphere. Capacity loss was calculated from 0.5C CC-CV discharges with a CV hold at 3.0V until current fell below C/100. All of the experiments were conducted inside the 2-D thickness scan chamber at 25 °C chamber temperature.

2.5. Cycle aging experiment

The cycling experiment comprised 8 cells in total, of which six cells were cycled up to 1000 times and two cells were opened after 200 cycles for post-mortem analysis. The cycling procedure was as follows: The cells were discharged to 0% SOC and a full cycle at 0.1C with CC-CV charge and discharge was performed in the laser scan chamber at 25 °C while recording the cell thickness. Subsequently, the cells were transferred to another temperature-controlled chamber at 25 °C and cycled periodically using their designated charging profile and a CC-CV discharge at 1C with 15 min pause between charge and discharge, respectively. After every 100 cycles, the procedure was repeated. In an effort to keep the specific load constant in each charging profile, C-rates were based on the actual capacities obtained from the periodical 0.1C discharges.

3. Results and discussion

3.1. Thermal expansion

The cell temperature was varied by short charge-discharge pulses and by inserting a cold cell into the pre-heated thickness scan chamber, respectively, as described in the experimental section. The cell's SOC were kept at 50%. The SOC change during the pulsing experiment was smaller than 1/1000. Since both experimental approaches yielded very similar results, the pulsing experiment data are presented in the supporting information. Fig. 2a shows the evolution of temperature and expansion of a cell pre-cooled to 0 °C after it was transferred into the thickness scan chamber preheated to 45 °C. The average expansion rate was $1.2 \mu\text{m}/^\circ\text{C}$, which corresponds well to an earlier measurement using tactile displacement sensors [24]. Fig. 2b reveals that the rate of expansion was uneven across the cell surface. The highest rates of expansion occurred at the edges of the cell. This may be caused by lower compression at the edges due to the use of deep drawn pouch foils. The local expansion rate ranged from $0.6 \mu\text{m}/^\circ\text{C}$ to $3.4 \mu\text{m}/^\circ\text{C}$. This translates into thermal expansion coefficients of $1.2\text{e-}4/^\circ\text{C}$ (min.), $7.0\text{e-}4/^\circ\text{C}$ (max.) and $2.5\text{e-}4/^\circ\text{C}$ (average), respectively. These expansion coefficients are smaller than those found in Ref. [25], where, depending on location, expansion coefficients between $7\text{e-}4/^\circ\text{C}$ and $12\text{e-}4/^\circ\text{C}$ were obtained for a NMC/Graphite prismatic cell at 50% SOC (expansion was lowest at 50% SOC, at other SOC, thermal coefficients were roughly $1\text{e-}4/^\circ\text{C}$ higher). An explanation for this discrepancy could be a higher volume ratio of separator and current collector to active materials³ in the high-power cell used in Ref. [25] compared to the cell used in the present study.

In the charging experiments, the measured expansion is partly due to self-heating and resulting thermal expansion of the cell. In the analysis, the thermal expansion was subtracted from the measured expansion. The thermal expansion was calculated from the local thermal expansion coefficients in Fig. 2b multiplied by the surface temperature at the center of the cell. The surface temperature reached a maximum of 32 °C at 25 °C ambient temperature upon charging at 2.0C. The error induced by the use of the surface temperature at the center of the cell was assumed to be acceptable in the context of the experiment. The temperature distribution across the surface during 2.0C charging was measured using a FLIR i7 thermo camera. The hottest spot was the center, and the temperature decreased uniformly toward the edges, where it deviated by a maximum of 0.9 °C from the center temperature (see supporting info). Comparably small temperature gradients were observed on the surface of a 5.0 Ah prismatic cell in [25]. Because of the low thickness of the cell, ca. 5 mm, the temperature gradient toward the core was assumed to be negligible.

3.2. Cell expansion linked to lithium plating

3.2.1. Expansion overshoots

Previous work on fast charging and cell expansion showed that high charging rates, which ultimately cause quick cell degradation, come with distinct thickness overshoots. With a CC-CV charging protocol, the overshoots occurred roughly at the transition between CC and CV phases [23]. These overshoots, which were obtained with a 2.28 Ah lithium-cobalt-oxide/graphite (LCO/G) pouch cell, could be replicated with the 3.3 Ah NMC/G cell used in this study. Fig. 3a shows the average cell expansion as a function of SOC and four C-rates during CC-CV charging and relaxation: 0.5C, 1.0C, 1.5C and 2.0C. The dashed line

³ Ref. [26] states thermal expansion coefficients of bulk polyethylene of between $1.4\text{e-}4/^\circ\text{C}$ and $2.5\text{e-}4/^\circ\text{C}$ and of bulk polypropylene of $1.2\text{e-}4/^\circ\text{C}$ to $1.5\text{e-}4/^\circ\text{C}$. For graphite $5.5\text{e-}5/^\circ\text{C}$ was found in Ref. [27]. NMC is assumed to have a similar thermal expansion coefficient as graphite in [25]. The cell used in Ref. [25] had cathode and anode sheets of 80 μm each and a 25 μm separator, while the cell used in the present study has double-side coated anode and cathode sheets of 207 μm and 149 μm , respectively.

3 Cell Diagnosis using Locally-Resolved Thickness Measurements

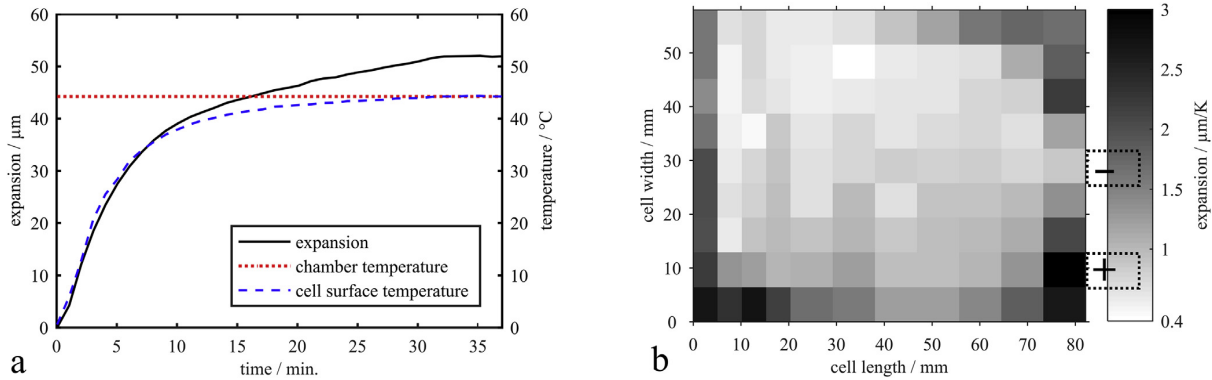


Fig. 2. Thermal expansion from 0 °C to 45 °C. a) shows the average expansion and surface temperature of a cell that was cooled to 0 °C before it was put into the thickness scan chamber preheated to 45 °C. b) shows the local therm. expansion coefficient linearized from 0 °C to 45 °C.

shows the measured expansion, and the solid line shows the measured expansion less the calculated thermal expansion based on the thermal expansion measurements presented above.

At 2.0C, the overshoot was nearly 40 μm. This amounts to 25% of the expansion from 0% SOC to 100% SOC and 0.8% of the cell thickness. The height of the overshoot depended on the charging rate. At 1.5C, the overshoot was still 25 μm. The overshoots began shortly before entering the CV phase and ended before the end of charge was reached. The average expansion showed no overshoot at 0.5C and 1.0C. The locally resolved data, shown in Fig. 3b-d, however, reveals that even at these lower charging rates, some areas of the cell exhibited

expansion overshoots. At 1.0C, while most of the cell surface did not overshoot, single spots overshoot by up to 15 μm. At 1.5C and 2.0C, local overshoots reached 50 μm. The areas that exhibited the largest overshoots are the edges at the tab side, opposite to the tabs and along a lateral strip on one of the sides (top part of the images). This vague pattern held at different charging rates and was reproducible with different cells. The expansion overshoots observed upon charging, did not occur upon discharging. Please see the supporting information for details. All of the data shown in Fig. 3 are from the same cell, which was charged successively at nine different rates ranging from 0.5C to 2.5C. Shifts in the “activity” of cell areas with severe cycle loads were

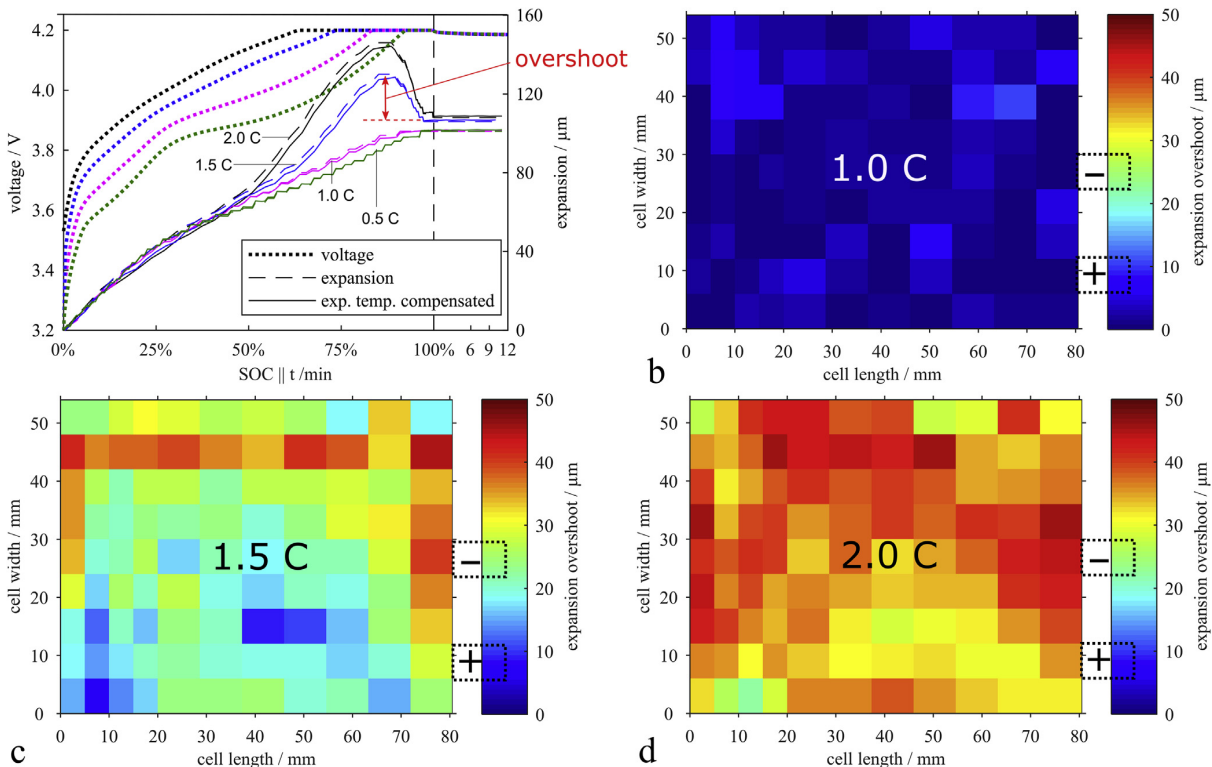


Fig. 3. Cell expansion upon charging from 0% SOC to 100% SOC at various C-rates. a) shows average expansion across the cell surface with severe expansion overshoots at 1.5C and 2.0C. At the end of the CC-CV charging, cells charged with higher C-rates exhibit greater average cell thickness, i.e. not all of the expansion overshoot is reversible. Possibly, the overshoot is caused by lithium plating and subsequent stripping of most but not all of the previously plated lithium b-d) show local overshoots of up to 50 μm at different C-rates.

reported in previous work [22] and may have occurred in this experiment as well.

What could cause these distinct overshoots with high rate charging? Thermal expansion is already taken into consideration. Even if the difference of volume-average temperature to ambient temperature is assumed to be twice as high as the difference of the cell surface temperature to ambient temperature, the overall picture remains unchanged. Gassing may be an issue at very high rates, but it should be considered a cause of balloon-like, irreversible expansion, not of local overshoots. In [28], gassing is shown to occur predominantly during formation of new cells and it is suggested that the amount of gas is reduced upon further cycling. In [29,30] reversible lithium plating on the graphite anode was assumed to cause expansion overshoots, while gassing and other side effects were rejected as insignificant. Possibly, in the experiment shown in Fig. 3a, when a certain SOC or the beginning of the CV phase was reached, high charging rates provoked the onset of lithium plating, which is reflected in the cell expanding disproportionately. Towards the end of the CV phase, as charging current and cell polarization decreased, lithium stripping set on and caused the cell to contract. If cell expansion may be used as an indicator of the occurrence of lithium plating and stripping, the bulk of the reversibly plated lithium should have been stripped and intercalated into the graphite by the end of the CV phase.

3.3. Voltage relaxation

In order to test the assumption of a relationship between expansion overshoots and lithium plating, voltage relaxation experiments were conducted. Stripping of previously plated lithium leads to a voltage plateau [31–34]. CC-CV charging at different rates was interrupted at 90% SOC, where the expansion overshoot reaches its climax, cf. Fig. 3. The results are displayed in Fig. 4: At 0.5C and 1.0C, the voltage drops exponentially. At 1.5C, the voltage drop is distorted, at 2.0C and 2.5C there is a clear plateau in the voltage and a corresponding hump in its time derivative, indicating that lithium plating occurred during charge. The duration of the voltage plateau, or the point in time where the voltage differential has its minimum, may be used as an indicator of the amount of plated lithium [35]. The results reflect that the severity of lithium plating increases with charging current. When comparing the voltage relaxation curves with the expansion overshoots in Fig. 3, it is important to keep in mind that the voltage relaxation curves are not locally resolved but originate from a lumped signal measured at the cell tabs. As the local expansion overshoots at 1.0C (Fig. 3b) are too small to be clearly reflected in the average expansion (Fig. 3a), so may their corresponding voltage plateaus not significantly alter the voltage measured at the tabs. As for 1.5C and 2.0C, the more severe the

expansion overshoots, the higher the duration of the voltage plateau when the charging process was stopped at the climax of the expansion overshoot. No voltage plateau could be observed after the end of the CC-CV charge at 100% SOC, independent of the C-rate applied during the CC-phase. We may conclude that the voltage relaxation results support the assumed correlation between expansion overshoots and lithium plating and stripping.

3.4. Irreversible expansion

In Fig. 3a, for both 1.5C and 2.0C charging rates, the final thickness at 100% SOC is significantly higher than at 0.5C and 1.0C, indicating that a portion of the expansion overshoot is irreversible, a lasting change in cell thickness. This irreversible expansion was determined by discharging the cell back to 0% SOC and comparing its thickness with the thickness at 0% SOC before the charge-discharge cycle. If it is irreversible lithium plating that causes the irreversible expansion, a loss of useable capacity is expected to come with it. Thus a survey of charging rates and their corresponding irreversible thickness changes and capacity losses was conducted. The discharge was rate 0.5C CC-CV throughout the experiment.

Fig. 5 shows capacity loss and both average and maximum local irreversible expansion per cycle as a function of charging rates between 1.0C and 2.0C. In general, irreversible expansion and capacity loss are correlated: The larger the irreversible expansion, the higher the capacity loss. Maximum local irreversible expansion is relatively high at low rates, but captures the growth of capacity loss with increasing C-rates quite well over the spectrum of examined C-rates. Bivariate correlation between maximum local irreversible expansion and capacity loss is 0.996 while between average irreversible expansion and capacity loss it is 0.945.

3.5. Post-mortem inspection

During multiple charging cycles at 0.5C–2.0C, that constitute the data set partly displayed in Figs. 3 and 4, the cell expanded irreversibly by 26 μm or 5.2% on average. Fig. 6a shows the local irreversible expansion across the cell. Post-mortem images of the front and back coating of one anode sheet are presented in Fig. 6b-c. While the amount of visible deposition varied across the 14 anode sheets in the cell, the distribution of the depositions across the electrode shown here is representative for the total of 14 anode sheets in the cell. It was assumed that the irreversible expansion correlates with the portion of the plated lithium during charge that is irreversibly plated. Overall, this assumption is supported by the post-mortem images of the anode in Fig. 6b-c: The deposit is most dense at the electrode edges, or at the

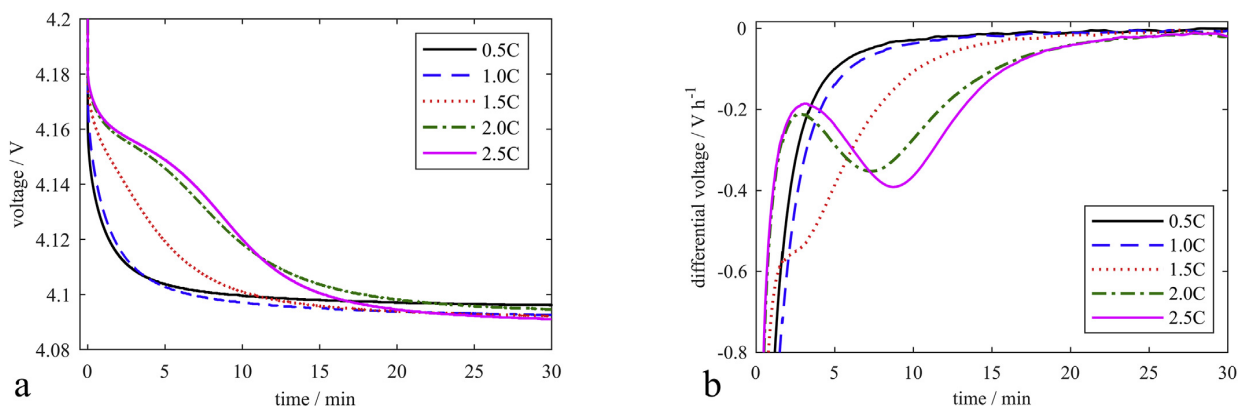


Fig. 4. a) Voltage curves after interrupting CC-CV charge with different C-rates at 90% SOC (where cell expansion overshoot peaks out). At 1.5C and higher, a voltage plateau, or a dip in the differential voltage (b), can be observed, which indicates the stripping of plated lithium.

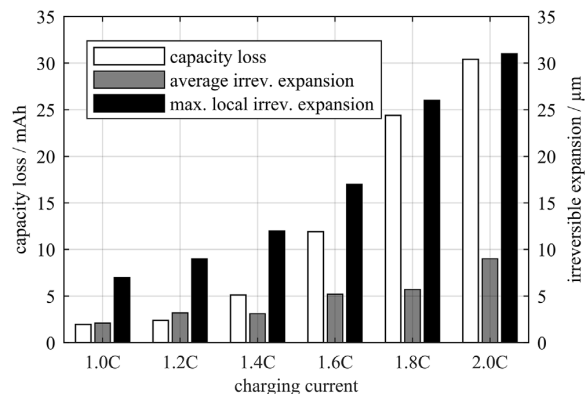


Fig. 5. Capacity loss and irreversible expansion per cycle as a function of C-rate in CC-CV charging. Higher irreversible expansion correlates with larger capacity losses per cycle.

edge of the measuring zone, in agreement with the irreversible expansion in Fig. 6a.

The pattern of the irreversible expansion bears a resemblance to the reversible expansion shown in Fig. 3b-d, however, reversible expansion was slightly lower at the very edges in relative terms, in contrast to the irreversible expansion. It is the second row from the top (Fig. 3b-d) that showed the largest expansion overshoots, but the largest irreversible expansions were detected in the first row from the top and at the tab and tab-opposite side edges. If it is assumed that expansion overshoots are a measure for lithium plating during charge, this would mean that the portion of plated lithium that is reversible varies with location. Or, if it is assumed that the portion of reversibly plated lithium does not depend on the location on the cell, then the expansion overshoots may not linearly correlate to the amount of lithium that is plated. This could be due to the morphology of the plated lithium or due to the uneven mechanical pressure by the pouch foil, especially at the edge areas. Of course, both may have an impact as well on the irreversible expansion.

In summary, it was shown that expansion overshoots and irreversible expansion, reversible and irreversible lithium plating and capacity

loss all correlate with each other. The strongest correlation is between (local) irreversible expansion, irreversible plating and capacity loss and it may be concluded with certainty that irreversible plating causes capacity loss and irreversible expansion of the cell. The correlation between expansion overshoots and reversible plating (as observed through voltage relaxation) is also quite consistent. The correlation of expansion overshoots and irreversible expansion, or, we may say reversible and irreversible plating, is weaker and varies with location.

The next section deals with how these qualitative relationships can be exploited for the design of a fast charging protocol.

3.6. Design and application of fast charging protocol

Based on the previously presented results, the authors argue that in the design of an expansion-based charging protocol it is crucial to focus on the local cell expansion, especially if the goal is to avoid lithium plating even at the “weak” spots of a cell.

The assumption was that designing a fast charging protocol exclusively by an appropriately chosen maximum allowable irreversible expansion may result in quick charging times, while offering a low and adjustable rate of cell deterioration, i.e. long and predictable cycle life.

First, an experimental screening of charging rates and their corresponding maximum local irreversible expansions as a function of SOC was conducted. Second, the highest charging rates that fulfilled the expansion criteria for a specific SOC range were combined into a charging protocol. Lastly, this charging protocol was tested and compared against CC-CV charging over 1000 full cycles.

3.7. Screening of charging rates and corresponding maximum irreversible expansion

Cells were charged to SOCs ranging from 10% to 100%, always starting at 0%. Charging rates were varied between 0.5C and 3.0C in a CC-CV protocol. Before and after every charge step, the cells were discharged to 0% SOC by a 0.5C CC-CV protocol and the cell thickness was measured. Fig. 7a provides an overview of the charging rates and end-of-charge SOC and resulting maximum local irreversible expansions. Here is an example to help the reader understand the figure: Continuous charging from 0% SOC to 60% SOC at a rate of 1.6C results

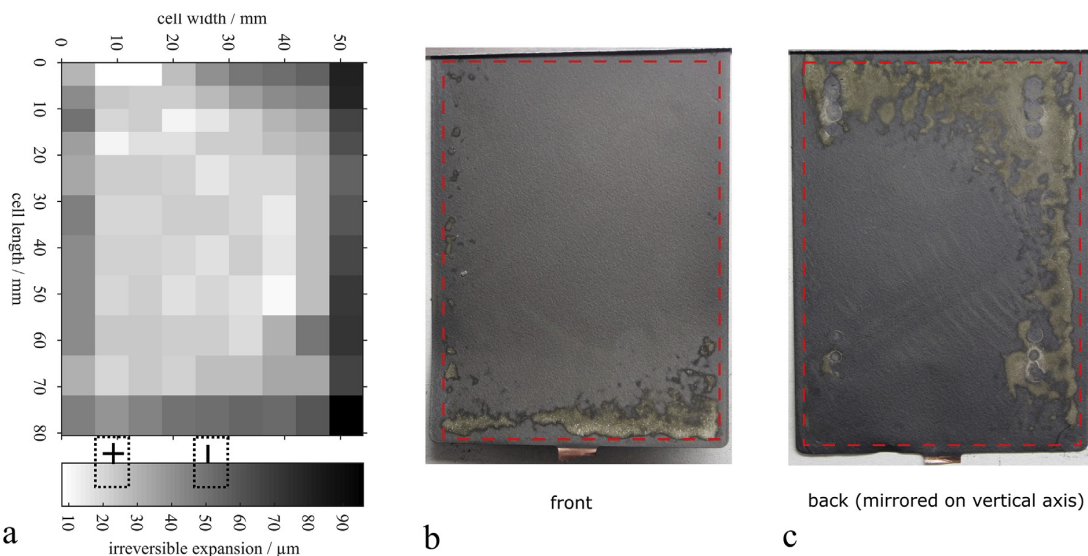


Fig. 6. Irreversible cell expansion (a) and post-mortem photographs of a sample anode (b–c) after repeated CC-CV cycling at various rates between 0.5C and 2.0C. Irreversible expansion is generally highest at the edges. Most severe expansion occurred on the top-right and bottom-left corners, which correlates with the visible surface deposition on both sides of the double-side coated anode sheet.

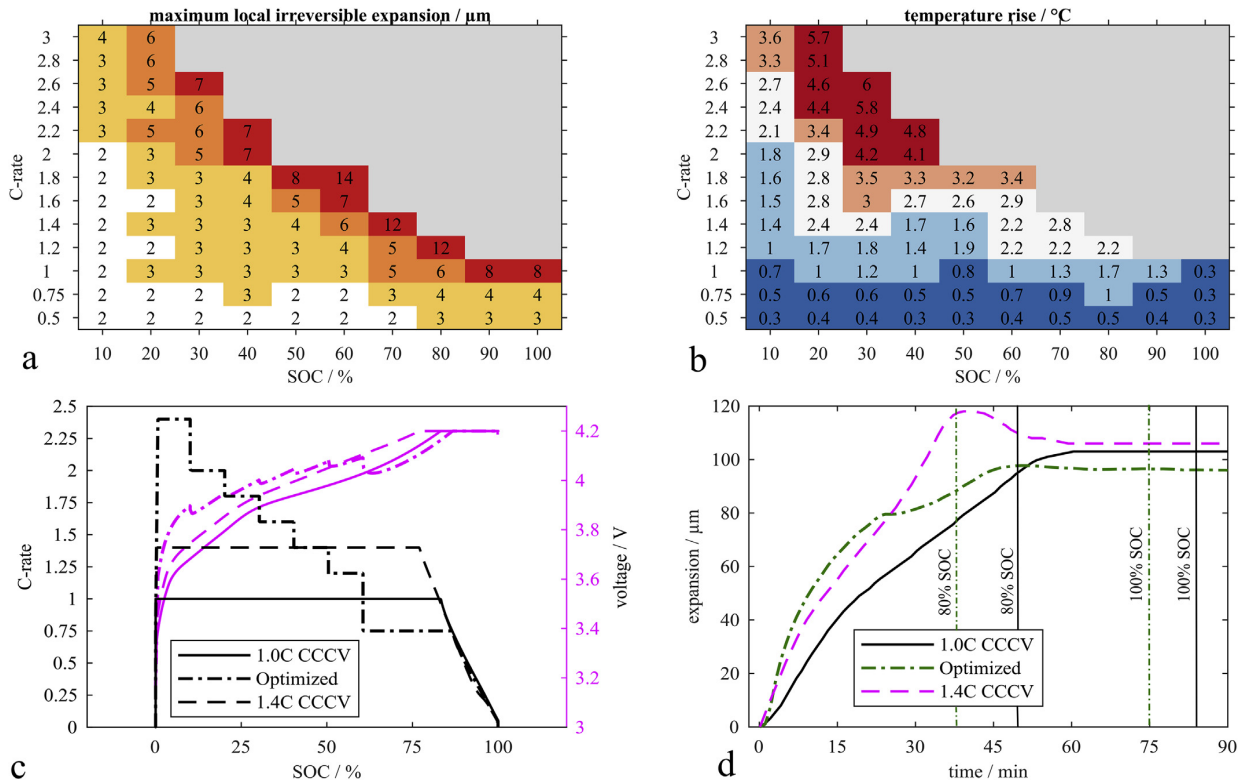


Fig. 7. Tuning a charge protocol to minimize charging time and irreversible expansion. a) shows irreversible expansion as a function of C-rate and end-of-charge SOC. 1C CC-CV charging results in 8 μm irreversible expansion. b) shows corresponding cell surface temperature at end-of-charge. c) shows C-rate and voltage vs. SOC of optimized charge protocol that limits irreversible expansion of constituting charge steps to 4 μm in comparison to 1.0C and 1.4C CC-CV charging. 1.4C CC-CV and optimized charging have equal full charge durations. d) shows expansion vs. time of optimized charging compared to 1.0C and 1.4C CC-CV charging. In correspondence to the current-dependent maximum local irreversible expansions in a), the cell thickness at the end of charge is lowest with the optimized protocol and highest with 1.4C CC-CV.

in an irreversible expansion of 5 μm in the “worst” area of the cell. The average irreversible expansion across the cell may be much lower. The location of the spot that showed the largest irreversible expansion usually did not change with C-rate or SOC. A clear trend can be observed: Both higher charging rates and ending the charge at higher SOC result in larger local irreversible expansion. The standard 1C CC-CV charge leads to a local expansion of 8 μm, which constituted the benchmark for the design of the “optimized” charging protocol. Where C-rate/SOC pairings resulted in similarly large expansions (red rectangles in Fig. 7a), the C-rate was not pushed further, as the focus was on finding an equally or less damaging charging parameter. Cell-to-cell variations regarding irreversible expansions were investigated beforehand and were found to be negligible.

3.8. Derivation of the charging protocol

Design of the “optimized” charging protocol had two objectives, reduced charging time and enhanced cycle life as compared to 1C CC-CV charging. In order to get clear feedback as to the effectiveness of the method, the design guiding principle was kept simple: The constituting charge steps should cause at most 50% of the largest irreversible expansion caused by 1C CC-CV charge, i.e. at most 4 μm. Consequently, all of the C-rate and end-SOC combinations marked white and yellow in the matrix in Fig. 7a were considered acceptable. Of these, the highest rates were chosen, with the exception of the 0% - 10% SOC range, where the 3.0C rate would have required a revision of the cell wiring and connectors, and hence 2.4C was chosen. The resulting charging

profile is shown in Fig. 7c along with 1C and 1.4C CC-CV charging profiles. 1.4C CC-CV was used as a second reference, because its full charging time corresponds to the “optimized” protocol. The voltage over SOC protocol of the optimized protocol was steeper at the beginning compared to 1.0C CC-CV but over 60% SOC the voltage was lower. This is a result of switching to a charge rate of 0.75C at 60% SOC. Consequently, the duration of the CV phase is reduced. The abrupt switching of the charging rates in the optimized protocol causes the unsteadiness of the voltage protocol. Smoothing out the C-rate steps using an analytical function would allow for tuning the charging rate more closely to the allowable maximum but was discarded for simplicity.

To provide a complete picture, Fig. 7b shows the end-of-charge cell surface temperatures corresponding to the C-rate/SOC matrix in Fig. 7a. At all rates, the temperature is slightly depressed at mid SOC, which is most likely an effect of the cells’ entropy profile. The higher heat generation and cell temperature caused by high rates surely helped to

Table 2

Comparison of charging durations of optimized and 1C CC-CV charging protocols for various start- and end-SOCs.

	Duration of Charge/min			
SOC range	0% - 80%	20%–80%	20% - 100%	0% - 100%
1C CC-CV	48.0	36.0	72.0	84.0
“Optimized”	37.8	32.3	69.5	75.0
Reduction	21%	10%	3%	11%

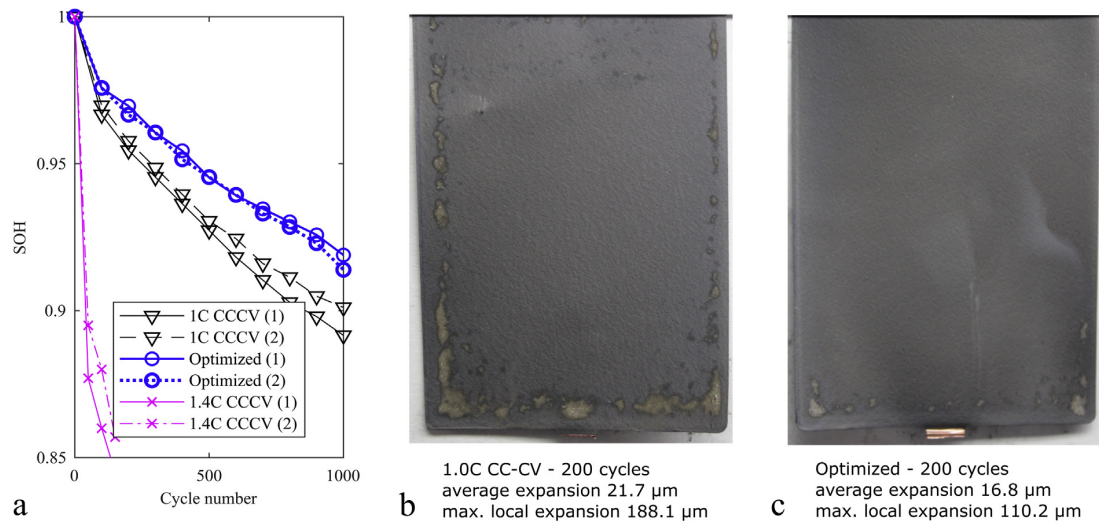


Fig. 8. a) state of Health as a function of cycle number of six cells charged with 1.0C, 1.4C CC-CV and “optimized” charging protocols. b,c): sample post mortem images of anodes taken from cell cycled for 200 cycles using 1.0C CC-CV and “optimized” charging protocol, respectively. “Optimized” charging protocol shows favorable SOH evolution compared to 1.0C, which is reflected in the amount of visible deposit on the electrodes. 1.4C CC-CV quickly deteriorates the cells.

Table 3

SOC, average and max. local irreversible expansion of cells charged with different protocols after 200 and 1000 cycles.

	200 cycles			1000 cycles		
	SOH/%	av. expansion/μm	max. expansion/μm	SOH/%	av. expansion/μm	max. expansion/μm
1C CC-CV (1)	95.5	18.1	291.3	89.2	93.9	440.4
1C CC-CV (2)	95.8	23.3	301.0	90.1	80.8	434.8
1C CC-CV (3)	96.2	21.7	188.1	–	–	–
“optimized” (1)	96.9	24.1	89.4	91.9	72.2	269.9
“optimized” (2)	96.8	30.8	110.6	91.4	77.9	344.9
“optimized” (3)	96.9	16.8	110.2	–	–	–

reduce overpotentials and thus lithium plating, which is reflected in the irreversible expansion.

The cell expansion over time during charging with the different charge profiles is shown in Fig. 7d: In correspondence to the C-rates, the cells charged with the optimized protocol expanded at a higher rate at low SOC compared to the CC-CV protocols. 1.4C CC-CV charging caused a large expansion overshoot, in agreement with the preliminary experiments presented in Fig. 3. Even though the irreversible expansion was defined herein as to be assessed at 0% SOC, the differences in expansion at 100% SOC caused by the different charging protocols are significant: The “optimized” protocol caused a few micrometers less irreversible expansion than 1C CC-CV, and 1.4C CC-CV a few micrometers more. The reduction of charging time with the “optimized” protocol over 1C CC-CV was significant: A full charge was completed within 75 min, compared to 84 min, a reduction of 11%. If charging is stopped at 80% SOC, the time reduction amounts to 21%. A comparison of charging times at different start- and end-SOCs is provided in Table 2. Generally, starting charge at lower SOC and ending charge at lower SOC magnifies the “optimized” charging protocol’s charging time benefits.

3.9. Comparative cycle study

Continuous cycling using the different charging protocols showed a clear advantage of the “optimized” protocol over standard 1C CC-CV charging. The reduction of useable capacity as a function of cycle number is shown in Fig. 8a: Generally, the cells cycled with the same

protocol showed consistent results. With all charging protocols there was a disproportionate capacity loss at the beginning, which is in accordance with other cycling studies using commercial cells with graphite anodes [36–39]. The rate of capacity loss of the cells cycled with the “optimized” charging protocol was consistently lower compared to 1.0C CC-CV. At 200 cycles, average SOH was 95.8% vs. 96.9%, and one cell of each charging protocol was opened for post-mortem inspection. Photographs of anodes of cells cycled with 1.0C CC-CV and with the “optimized” charging protocol are shown in Fig. 8b-c. On both anodes there were visible surface deposits, but to a much larger extent with 1.0C CC-CV charging, where the deposits were spread out at the tab-side edge and the lateral edges. On the cell cycled with the “optimized” charging protocol, minor deposits could only be found at the corners of the tab-side edge.⁴ These post-mortem observations are coherent with how much the cells had irreversibly expanded before they were opened: The average irreversible expansion was 21.7 μm vs. 16.9 μm and the maximum local irreversible expansion was 188.1 μm vs. 110.2 μm. The latter differ by a factor of 1.7, which corresponds roughly to the selection criterion (50% reduction of irreversible expansion of worst spot) for the individual charging steps that constitute the “optimized” charging protocol. Upon further cycling, capacity declined at rate of ~0.7%

⁴ In both cells there were differences in deposit quantity and local distribution among their respective 12 anode sheets. Notably the “back” side of each sheet always looked different from the “front” side, cf. Fig. 6, due to what is likely a manufacturing induced defect on the separator, whose further investigation was not within the scope of this study. The two anodes shown in Fig. 8 were picked because they represented well the overall differences between the two cells.

and ~0.6% per 100 cycles, with 1.0C CC-CV and “optimized” charging, respectively. After 1000 cycles, average SOH was 90.0% vs. 91.6%, indicating a clear life cycle advantage of the “optimized” protocol over 1.0C CC-CV charging. SOH, average and maximum local irreversible expansion of the examined cells are summarized in Table 3. If the rate of capacity loss between 200 cycles and 1000 cycles remained constant until the cells reach 80% SOH, which is a typical end-of-life criterion, the cells charged with 1C CC-CV would make ca. 2400 cycles while the cells charged with the “optimized” protocol would make ca. 2900 cycles, a plus of 20%. Meanwhile, time would be saved during charging: After 2000 cycles at 100% DOD, a hypothetical user would have saved 300 h if he used the “optimized” charging protocol instead of 1.0C CC-CV charging.

4. Conclusions

This work shows that a fast, gentle charging protocol for graphite-based high-energy lithium-ion cells can be developed exclusively on the basis of the volume expansion of the cells in operation. As the occurrence of lithium plating leaves a footprint in the form of a lasting local expansion that can be detected by an in-situ thickness measurement, there is no need for inserting a reference electrode into the cell or for making model-based assumptions about the inner states of the cell. This method should be generally applicable to any type of cell that is susceptible to lithium plating and does not require any specific knowledge about the cell. The correlations of reversible expansion overshoots and irreversible expansion shown in this work suggest that it could be a viable strategy to monitor the local rate of expansion on-line and control charging current accordingly. It remains to be investigated how the local expansion in freestanding cells translates into local pressure buildup in constrained cells.

Acknowledgements

This work has received funding from the European Union's Horizon 2020 research and innovation program under the grant “Electric Vehicle Enhanced Range, Lifetime and Safety Through INGenious battery management” (EVERLASTING-713771).

Appendix A. Supplementary data

Supplementary data related to this article can be found at <http://dx.doi.org/10.1016/j.jpowsour.2018.04.095>.

References

- A. Meintz, J. Zhang, R. Vijayagopal, C. Kreutzer, S. Ahmed, I. Bloom, et al., Enabling fast charging – Vehicle considerations, *J. Power Sources* 367 (2017) 216–227.
- P. Keil, A. Jossen, Charging protocols for lithium-ion batteries and their impact on cycle life—an experimental study with different 18650 high-power cells, *J. Energy Storage* 6 (2016) 125–141.
- A. Mukhopadhyay, B.W. Sheldon, Deformation and stress in electrode materials for Li-ion batteries, *Prog. Mater. Sci.* 63 (2014) 58–116.
- B. Lu, Y. Song, J. Zhang, Selection of charge methods for lithium ion batteries by considering diffusion induced stress and charge time, *J. Power Sources* 320 (2016) 104–110.
- Z. Li, J. Huang, B. Yann Liaw, V. Metzler, J. Zhang, A review of lithium deposition in lithium-ion and lithium metal secondary batteries, *J. Power Sources* 254 (2014) 168–182.
- W. Lu, C.M. López, N. Liu, J.T. Vaughey, A. Jansen, D.W. Dees, Overcharge effect on morphology and structure of carbon electrodes for lithium-ion batteries, *J. Electrochem. Soc.* 159 (5) (2012) A566.
- P. Bai, J. Li, F.R. Brushett, M.Z. Bazant, Transition of lithium growth mechanisms in liquid electrolytes, *Energy Environ. Sci.* 9 (10) (2016) 3221–3229.
- Q. Wu, W. Lu, J. Prakash, Characterization of a commercial size cylindrical Li-ion cell with a reference electrode, *J. Power Sources* 88 (2) (2000) 237–242.
- J.S. Newman, K.E. Thomas-Alyea, N.J. Hoboken (Ed.), *Electrochemical systems*, third ed., J. Wiley, 2004.
- M. Doyle, T.F. Fuller, J. Newman, Modeling of galvanostatic charge and discharge of the lithium/polymer/insertion cell, *J. Electrochem. Soc.* 140 (6) (1993) 1526–1533.
- Z. Chu, X. Feng, L. Lu, J. Li, X. Han, M. Ouyang, Non-destructive fast charging algorithm of lithium-ion batteries based on the control-oriented electrochemical model, *Appl. Energy* 204 (2017) 1240–1250.
- B.K. Purushothaman, P.W. Morrison, U. Landauz, Reducing mass-transport limitations by application of special pulsed current modes, *J. Electrochem. Soc.* 153 (2006) A533–A542.
- B.K. Purushothaman, U. Landauz, Rapid charging of lithium-ion batteries using pulsed currents, *J. Electrochem. Soc.* 152 (2005) J33–J39.
- M.F. Hasan, C.-F. Chen, C.E. Shaffer, P.P. Mukherjee, Analysis of the implications of rapid charging on lithium-ion battery performance, *J. Electrochem. Soc.* 162 (7) (2015) A1382–A1395.
- C. Zhang, J. Jiang, Y. Gao, W. Zhang, Q. Liu, X. Hu, Charging optimization in lithium-ion batteries based on temperature rise and charge time, *Appl. Energy* 194 (2017) 569–577.
- M. Abdel Monem, K. Trad, N. Omar, O. Hegazy, B. Mantels, G. Mulder, et al., Lithium-ion batteries: evaluation study of different charging methodologies based on aging process, *Appl. Energy* 152 (2015) 143–155.
- M. Abdel-Monem, K. Trad, N. Omar, O. Hegazy, P. van den Bossche, J. van Mierlo, Influence analysis of static and dynamic fast-charging current profiles on ageing performance of commercial lithium-ion batteries, *Energy* 120 (2017) 179–191.
- P.H.L. Notten, J.H.G. Veld, J.R.G. van Beek, Boostcharging Li-ion batteries: a challenging new charging concept, *J. Power Sources* 145 (1) (2005) 89–94.
- J. Cannarella, C.B. Arnold, The effects of defects on localized plating in lithium-ion batteries, *J. Electrochem. Soc.* 162 (7) (2015) A1365–A1373.
- M. Tang, P. Albertus, J. Newman, Two-dimensional modeling of lithium deposition during fast charging, *J. Electrochem. Soc.* 156 (5) (2009) A390–A399.
- J. Cannarella, C.B. Arnold, Stress evolution and capacity fade in constrained lithium-ion pouch cells, *J. Power Sources* 245 (2014) 745–751.
- J. Sturm, F.B. Spingler, B. Rieger, A. Rheinfeld, A. Jossen, Non-Destructive detection of local aging in lithium-ion pouch cells by multi-directional laser scanning, *J. Electrochem. Soc.* 164 (7) (2017) A1342–A1351.
- B. Rieger, S.F. Schuster, S.V. Erhard, P.J. Osswald, A. Rheinfeld, C. Willmann, et al., Multi-directional laser scanning as innovative method to detect local cell damage during fast charging of lithium-ion cells, *Journal of Energy Storage* 8 (2016) 1–5.
- B. Rieger, Methodik zur Simulation des mechanischen Verhaltens von Lithium-Ionen-Zellen, (2016).
- K.-Y. Oh, B.I. Epreanu, A novel thermal swelling model for a rechargeable lithium-ion battery cell, *J. Power Sources* 303 (2016) 86–96.
- H. Saechtling, *Kunststoff-taschenbuch*, 29th ed, Hanser, München, 2004.
- C. Bindra, V.A. Nalimova, D.E. Sklovsky, W.A. Kamitakahara, J.E. Fischer, Statics and dynamics of interlayer interactions in the dense high-pressure graphite compound LiC₂, *Phys. Rev. B* 57 (9) (1998) 5182–5190.
- C.P. Aiken, J. Xia, D.Y. Wang, D.A. Stevens, S. Trussler, J.R. Dahn, An apparatus for the study of in situ gas evolution in Li-ion pouch cells, *J. Electrochem. Soc.* 161 (10) (2014) A1548–A1554.
- B. Bitzer, A. Gruhle, A new method for detecting lithium plating by measuring the cell thickness, *J. Power Sources* 262 (2014) 297–302.
- C. Birkenmaier, B. Bitzer, M. Harzheim, A. Hintennach, T. Schleid, Lithium plating on graphite negative electrodes: innovative qualitative and quantitative investigation methods, *J. Electrochem. Soc.* 162 (14) (2015) A2646–A2650.
- M.C. Smart, B.V. Ratnakumar, L. Whitcanack, K. Chin, M. Rodriguez, S. Surampudi, Performance characteristics of lithium ion cells at low temperatures, Seventeenth Annual Battery Conference on Applications and Advances, 2002.
- M.C. Smart, B.V. Ratnakumar, Effects of electrolyte composition on lithium plating in lithium-ion cells, *J. Electrochem. Soc.* 158 (4) (2011) A379.
- M. Petzl, M. Kasper, M.A. Danzer, Lithium plating in a commercial lithium-ion battery – a low-temperature aging study, *J. Power Sources* 275 (2015) 799–807.
- S. Schindler, M. Bauer, M. Petzl, M.A. Danzer, Voltage relaxation and impedance spectroscopy as in-operando methods for the detection of lithium plating on graphite anodes in commercial lithium-ion cells, *J. Power Sources* 304 (2016) 170–180.
- C von Lüders, V. Zinth, S.V. Erhard, P.J. Osswald, M. Hofmann, R. Gilles, et al., Lithium plating in lithium-ion batteries investigated by voltage relaxation and in situ neutron diffraction, *J. Power Sources* 342 (2017) 17–23.
- G. Ning, B. Haran, B.N. Popov, Capacity fade study of lithium-ion batteries cycled at high discharge rates, *J. Power Sources* 117 (1–2) (2003) 160–169.
- J. Arai, R. Nakahigashi, T. Sugiyama, A study on the cycle life of lithium-ion batteries using in situ 7 Li solid-state nuclear magnetic Resonance, *J. Electrochem. Soc.* 163 (6) (2016) A1064–A1069.
- K. Maher, R. Yazami, A study of lithium ion batteries cycle aging by thermodynamic techniques, *J. Power Sources* 247 (2014) 527–533.
- Y. Wu, P. Keil, S.F. Schuster, A. Jossen, Impact of temperature and discharge rate on the aging of a LiCoO₂/LiNi_{0.8}Co_{0.15}Al_{0.05}O₂ lithium-ion pouch cell, *J. Electrochem. Soc.* 164 (7) (2017) A1438–A1445.

4 Linking Uneven Cell Compression to the Occurrence of Lithium Plating

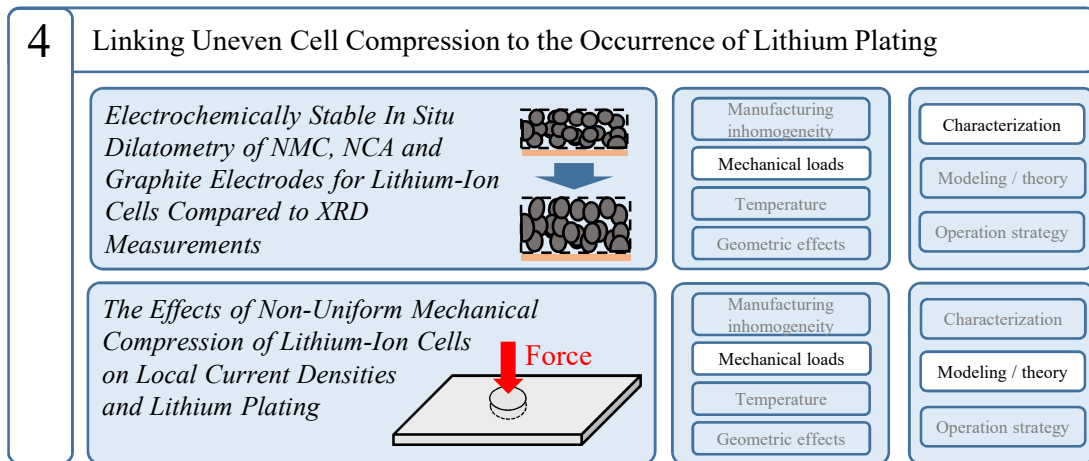


Figure 4.1: Outline of chapter 4.

This chapter addresses the effects of non-uniform mechanical loads on the electrochemical behavior of lithium-ion cells. The presumed cause-effect relationship of lithium plating from chapter 3 is generalized by investigating whether local separator pore closure, regardless of its cause, provokes lithium plating. In addition, the more realistic scenario of local porosity reduction due to non-uniform external mechanical loads is analyzed. The investigation of the interplay between the mechanical activity of the electrodes and mechanical constraints, e.g. by the housing, is separated into two parts: First, the intercalation-based expansion of anode and cathode materials is investigated in section 4.1 using a commercial dilatometer which is validated in a detailed manner. Subsequently, in section 4.2, modeling is combined with experiments to analyze the effect of external mechanical loads on the current density distribution and the risk of lithium plating. The results from section 4.1 as well as material tests of electrodes and separators are used to parameterize the model. This chapter clarifies the causal chain of mechanical loads, porosity changes, and resulting current density distributions. The methods developed in this chapter allow the determination of the maximum local mechanical load above which lithium plating occurs.

Two articles, entitled *Electrochemically Stable In-Situ Dilatometry of NMC, NCA and Graphite Electrodes for Lithium-Ion Cells compared to XRD measurements* and *The Effects of Non-Uniform Mechanical Compression of Lithium-Ion Cells on Local Current Densities and Lithium Plating*, constitute the core of this chapter.

4.1 Measuring Thickness Changes of Electrodes in Operation

In this section, an investigation of the intercalation-based expansion of anodes and cathodes composed of state-of-the-art active materials is presented. This was carried out using a commercial dilatometer which allows the measurement of the thickness change of single electrodes during cycling. As detailed in section 2.2, significant efforts were directed towards improving and validating the electrochemical performance of the dilatometric apparatus as well as examining the reliability of the displacement measurement. Through this process, cycling stability equivalent to that of coin cells was achieved.

Having improved the reliability of the measurement setup, both the irreversible and reversible dilation of two different graphite electrodes and various transition metal oxide electrodes were examined. Studies on the dilation of graphite are found frequently in the scientific literature, allowing the comparison of the measurements of graphite electrodes with the results of similar experiments. The level of agreement with literature values provided additional confirmation of the validity of the experiment. In contrast to those investigating graphite, publications regarding the dilation of transition metal oxide electrodes are scarce. Neither the electrode-level dilation of lithium cobalt aluminum (NCA) nor that of most of the NMC combinations investigated in the following have been reported elsewhere. For many of these materials, the crystal structure changes measured via XRD have been the only available data to estimate the electrode-level thickness-change behavior. To understand the relationship between changes to crystal structure and electrode level thickness change, the dilatometry results of NMC materials were compared to the XRD data from the literature. The comparison reveals significant quantitative deviations between the crystal-level volume changes and the electrode-level thickness change. Qualitatively, while expansions on the crystal level translate into expanding electrodes, contractions of the unit cells do not necessarily lead to the shrinking of the electrodes. These results show that the relationship between crystal structure change and the mechanical behavior of electrodes is not straightforward.

The importance of this study in the context of this thesis lies in providing the methods required to analyze the thickness changes of electrodes as a function of their degree of lithiation. The results are valuable input parameters for the analysis of the mechanical loads acting on the cell components when cells are mechanically constrained during operation. In this thesis, they were used to parameterize the mechanical model presented in section 4.2.

Author contribution Franz Spingler was responsible for the conceptualization, methodology, investigation and the writing of the original draft. Simon Kücher helped with the experiments. Robert Phillips helped with the analysis of the preliminary experiments and the instrument validation. Erfan Moyassari reviewed and commented on the manuscript. Andreas Jossen provided supervision, and reviewed and commented on the manuscript.

Electrochemically Stable In-Situ Dilatometry of NMC, NCA and Graphite Electrodes for Lithium-Ion Cells compared to XRD measurements

Franz B. Spingler, Simon Kücher, Robert Phillips, Erfan Moyassari, Andreas Jossen

Journal of The Electrochemical Society 168 040515, 2021

Permanent weblink:

<https://doi.org/10.1149/1945-7111/abf262>

Reproduced under the terms of the Creative Commons Attribution 4.0 License (CC BY, <http://creativecommons.org/licenses/by/4.0/>), which permits unrestricted reuse of the work in any medium, provided the original work is properly cited.



Electrochemically Stable In Situ Dilatometry of NMC, NCA and Graphite Electrodes for Lithium-Ion Cells Compared to XRD Measurements

Franz B. Spingler,^{1,*} Simon Kücher,¹ Robert Phillips,¹ Erfan Moyassari,¹ and Andreas Jossen^{1,2}

¹Institute of Electrical Energy Storage Technology, Technical University of Munich (TUM), 80333 Munich, Germany

²Munich School of Engineering (MSE), Technical University of Munich (TUM), 85748 Garching, Germany

Virtually all types of electrodes used in lithium-ion batteries expand and contract during cycling, which poses an engineering and design challenge. Information provided by X-ray diffraction (XRD) about alterations in the crystal structure of active materials may be insufficient to inform these engineering tasks. This is because it is unclear how these evolutions of the crystal structure translate into the measurable thickness changes at the electrode or cell level. In this study we investigate the thickness changes of electrodes during cycling using a dilatometry setup and compare them to XRD-measured crystal structure changes from scientific literature. Both the reliability of the dilation measurement and the electrochemical performance of the dilatometry setup are thoroughly validated and significantly exceed those of related studies that have been published in recent years. Various laboratory-made graphites as well as LiNi_{1/3}Co_{1/3}Mn_{1/3}O₂ (NMC111), LiNi_{0.6}Co_{0.2}Mn_{0.2}O₂ (NMC622), LiNi_{0.8}Co_{0.1}Mn_{0.1}O₂ (NMC811) and LiNi_{0.8}Co_{0.15}Al_{0.05}O₂ (NCA) electrodes and the positive electrode from a Kokam SLPB356495 pouch cell are investigated. The results show that electrode expansion does not necessarily correlate with the unit cell volume changes of its active materials in any meaningful way and thus only by measuring the expansion of the full electrode can we fully understand and predict its behavior during cycling.

© 2021 The Author(s). Published on behalf of The Electrochemical Society by IOP Publishing Limited. This is an open access article distributed under the terms of the Creative Commons Attribution Non-Commercial No Derivatives 4.0 License (CC BY-NC-ND, <http://creativecommons.org/licenses/by-nc-nd/4.0/>), which permits non-commercial reuse, distribution, and reproduction in any medium, provided the original work is not changed in any way and is properly cited. For permission for commercial reuse, please email: permissions@iopublishing.org. [DOI: 10.1149/1945-7111/abf262]



Manuscript submitted February 11, 2021; revised manuscript received March 12, 2021. Published April 7, 2021.

Supplementary material for this article is available [online](#)

When a lithium-ion battery is charged or discharged, lithium ions intercalate and deintercalate from their host lattices in the positive and negative electrodes. Depending on the host material, the intercalation process is accompanied by an expansion or contraction in the volume of the host lattice. The magnitude of the host lattice volume change between 0% and 100% SOC can be measured via X-ray diffraction (XRD) and for full lithiation, range from 0%–2% in the case of transition-metal-oxides (TMOs) over ca. 12% for graphite to 280% in the case of silicon.^{1,2} Although measuring the host lattice volume change is helpful in the understanding of interparticle stresses, which may lead to microscopic cracks and progressive film formation,^{3,4} the quantity of interest in this study is the bulk expansion of practical electrodes: Knowledge of how electrodes expand and contract upon lithiation can guide battery housing/module design,⁵ improve battery diagnostics based on cell expansion or pressure,^{6,7} help in the assessment of the mechanical stress batteries experience in operation and provide feedback for electrode design. The latter point is especially significant for graphite/silicon composites, where the large volumetric expansion of the silicon lattice must be contained by the other electrode components to minimize intraparticle stress and mechanical decomposition of the bulk electrode.^{8,9}

Practical electrodes are porous, have complex microstructures and contain non-active materials such as binder, all of which helps accommodate primary particle expansion. The combination of these factors dictates that the change in unit cell volume experienced by the active material's crystal structure does not unequivocally determine the electrode volume or its thickness change.

At the other end of the length scale, the expansion of multi-layer pouch cells can be measured with relative ease using optical^{10–12} or tactile^{13–16} methods, but the resulting measurement quantity is the superposition of the thickness changes of both the negative and positive electrodes and potentially the compression of the separator. Purpose-built electrochemical dilatometers that either employ a non-expanding counter electrode^{17,18} or exclusively measure the

thickness change of a single working electrode^{19–21} offer more precise data on the expansion of individual electrodes.

With the help of electrochemical dilatometers, expansions as a result of complete lithiation have been measured at between 4% and 6.5% for graphite,^{19,20} between 0% and 0.8% for LiNi_{1/3}Mn_{1/3}Co_{1/3}O₂ (NMC111)^{17,18} and 1.8% for LiCoO₂ (LCO).²⁰ However, possibly due to cycling stability issues, these studies only report the first few cycles. There is also some uncertainty regarding the amount of irreversible expansion taking place in the first few cycles and the quantity of reversible expansion during long-term cycling. In a recent publication²² using the same ECD-3-nano dilatometry cell (El-Cell GmbH) as in this work, the authors encountered severe capacity loss, which they attributed to electrode exfoliation and the separator design of the electrochemical cell. We believe that the principal reason behind the poor capacity retention in their experiments was the permeability of the cell to atmospheric gases and humidity. In this work, the ECD-3-nano cell was operated in an argon atmosphere and displayed excellent reproducibility as well as a cycling stability on par with coin cells. The dilatometry setup was used to investigate the reversible and irreversible thickness changes of a variety of electrodes. These were composed of either graphite or transition-metal-oxides containing varying proportions of nickel, manganese, aluminum and cobalt and were either prepared from powder or harvested from a commercial cell.

This paper is structured as follows: In the experimental section, electrode and coin cell preparation and the dilatometry setup as well as the cycling procedures are discussed. This is followed by a thorough validation of the dilatometry cell in regard to its electrochemical performance and the reliability of the dilation measurement. In the results section, the thickness changes measured in the electrodes of the various materials are discussed and compared to similar measurements and host lattice volume change data from XRD measurements reported in the literature.

Experimental

Electrode preparation from powder.—Electrode slurries were prepared from powders obtained from SGL, BASF and MTI Corp

*Electrochemical Society Student Member.

[†]E-mail: franz.spingler@tum.de

Table I. Coating thicknesses and porosities of the electrodes used in this study.

Type	Coating thickness/ μm	Porosity/%	Active material loading/ $\text{mg}^*\text{cm}^{-2}$
Graphite (SGL)	60	40	7.28
Graphite (CSCC)	31	65	2.21
NMC 111 (BASF)	64	35	13.51
NMC 622 (BASF)	33	35	8.13
NMC 811 (MTI)	40	35	10.27
NCA (BASF)	40	35	10.00
Kokam cathode	66.5	unknown	unknown

which were dispersed in N-Methyl-2-pyrrolidinone (NMP) from Sigma Aldrich. Solef 5130 PVDF by Solvay and Kynar HSV by Arkema were used as binders and Super C65 Carbon black by Timcal as the conductive agent. All transition-metal-oxide-based slurries were prepared in a Thinky ARV-310 planetary vacuum mixer, coated on $16\ \mu\text{m}$ thick aluminum foil using a table top K Control Coater by RK Print Coat Instruments, dried at $60\ ^\circ\text{C}$ for 6 h and then compacted to a porosity of 35% using a Saueressig GK 3001 calender. Graphite slurries were prepared in a Hauschild Speedmixer DAC 3000 planetary mixer, coated and dried on $11\ \mu\text{m}$ thick copper foil using a roll-to-roll Coatema BC50 coating machine with an inline infrared dryer and compacted to a porosity of 35% using a Coatema EA50 calender. The slurry recipes can be found in the Appendix in Table A.I. The slurry mixing procedures are provided in detail in the supplementary information (available online at stacks.iop.org/JES/168/040515/mmedia). The final coating thicknesses and porosities of the electrodes are summarized in Table I.

Harvested electrodes from a commercial cell.—A fresh 2.1 Ah Kokam SLPB 356495 cell was discharged at 0.1 C to 3.0 V and disassembled in an argon filled glovebox ($<0.1\ \text{ppm}\ \text{H}_2\text{O}/\text{O}_2$). Before cutting out 10 mm disks (for the dilatometry cell) and 14 mm disks (for coin cells) with a handheld precision punch (Nogamigiken Co.), the coating of the anode sheets was pulled off on one side using off-the-shelf isolating tape. Attempts were also made to remove the coating by scraping it off using a scalpel and by rubbing it off using an electrical oscillating toothbrush in combination with various

solvents (diethyl carbonate, acetone and NMP) but the pull-off method resulted in the best electrochemical performance and reproducibility in both the coin cells and the dilatometry cell. After testing both non-washed samples and samples washed in diethyl carbonate for 3 min, it was decided to use non-washed samples for the same reasons as above. In the case of the cathodes, no coating removal was necessary because the two outermost cathode sheets of these cells are single-side coated. The disks were left to dry inside the glovebox for at least 24 h before being used in coin cells or the dilatometry cell.

Coin cell preparation.—CR2032-type coin cells were prepared inside an argon-filled glovebox using two layers of 16.0 mm diameter VWR 691 glass fiber ($260\ \mu\text{m}$ each) as the separator, a 15.6 mm lithium chip as the counter electrode and two spacers of 1.0 mm and 0.5 mm thickness. The working electrode diameter was 14.0 mm. $80\ \mu\text{l}$ of LP57 (3:7 wt. EC:EMC 1 M LiPF₆) was used as electrolyte solution.

Dilatometry cell.—The dilation experiments were conducted using an ECD-3-nano dilatometry cell from El-Cell GmbH which uses a capacitive displacement sensor. The sensor resolution is specified by the manufacturer at 5 nm and drift at $20\ \text{nm}\ \text{h}^{-1}$. Figure 1 shows a schematic of the setup. The electrochemical cell holds working electrodes of 10 mm diameter. A 12 mm diameter lithium chip ($250\ \mu\text{m}$) serves as counter electrode. Working and counter electrode are separated by a porous borosilicate glass separator. A blind bore filled with lithium at the end of a metal tip

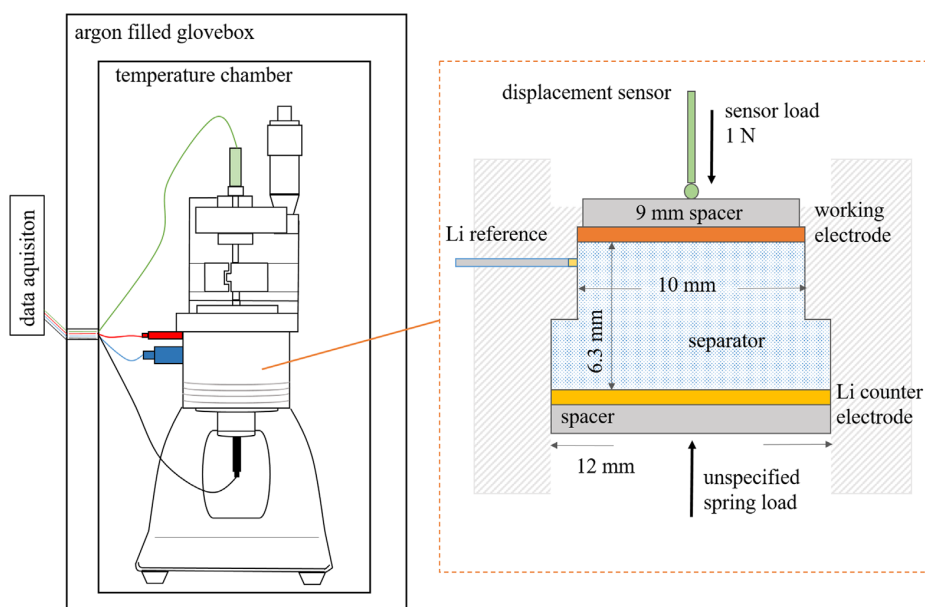


Figure 1. Schematic of dilatometry cell setup in temperature-controlled argon atmosphere and of the electrochemical cell with a t-shaped frit, which shields the displacement measurement of the working electrode from any dilation that may occur in the counter electrode.

serves as reference electrode and touches the separator from the side. The separator has a thickness of 6.3 mm which causes significant overpotentials during charging and discharging of the cell. A series of experiments in temperature-controlled ambient air, where the reversible capacity deteriorated quickly, suggested that the dilatometry cell is insufficiently airtight. It was subsequently operated in a custom-built temperature chamber inside an argon filled glovebox, resulting in low rates of capacity loss comparable with those seen in coin cells.

Cycling procedures.—After assembly, both coin cells and the dilatometry cell were rested for 6 h and then cycled using a constant current charge/constant current discharge protocol (CC/CC). If not otherwise specified, graphite electrodes were cycled at a current density of $75 \mu\text{A cm}^{-2}$ and transition-metal-oxide electrodes were cycled at a current density of $180 \mu\text{A cm}^{-2}$. The areal current densities were kept constant within the graphite and transition-metal-oxide groups in order to keep the dominant overpotential across the separator constant. This results in varying C-rates between C/8 and C/33, which are indicated in every figure along with the areal current density. The low current density for the graphite electrodes was chosen to get as close as possible to full lithiation despite the relatively large overpotentials of the dilatometry cell. The overpotentials are less of a limitation when cycling transition-metal-oxide electrodes because they can be compensated for by placing the cut-off potentials lower or higher than the desired equilibrium potentials at the end of charge/discharge. The graphite electrodes were cycled between 10 mV and 1.5 V. The transition-metal-oxide electrodes were cycled in four voltage windows between 3 V and four different upper cut-offs: 4.1 V, 4.3 V, 4.5 V and 4.7 V. Three cycles took place in each voltage window. After numerous validation experiments with all of the tested electrode materials, the final experiments shown in the results section were generally not repeated unless indicated otherwise.

Validation of the Dilatometry Setup

Chamber/cell temperature.—Preliminary experiments with the dilatometry cell had shown large overpotentials on charge and discharge, which were attributed to the cell design, more specifically the relatively thick borosilicate glass separator. As a countermeasure, it was decided to use a higher chamber temperature of 35°C instead of the standard 25°C , which was expected to have a positive effect on ion transport through the separator. To better understand the impact of the temperature change, the temperature was increased from 25°C to 35°C five cycles into a measurement on a graphite electrode. After 10 h of resting to let the temperature in the cell equalize, cycling was resumed. Figure 2a shows the electrode voltage vs Li/Li+ and the thickness change measured by the sensor. It can be seen that at 35°C the voltage during lithiation was slightly higher, indicating less polarization, and that a higher cell capacity was reached. Moreover, it was found that the displacement signal fluctuated less. Figure 2b illustrates the likely cause: The Peltier-element-powered temperature chamber was less able to maintain a steady temperature at 25°C than at 35°C , possibly due to elevated temperatures inside the glove box itself on summer days. The chamber temperature for all dilatometry experiments was thus set at 35°C . The temperature dependence of the displacement signal will be discussed in more detail at the end of this chapter.

Electrochemical performance of the dilatometry cell (vs coin cells).—In order to assess the electrochemical performance of the dilatometry cell, the voltage characteristics, specific capacity and charge/discharge efficiency of a graphite electrode were compared to those of 2032 coin cells, which serve as a reference. Figure 3 shows the voltage profile vs specific capacity of the 15th cycle. In the case of the coin cell, the full cell voltage of a graphite/lithium cell is shown, while in the case of the dilatometer, the graphite electrode potential vs the lithium reference is shown. The areal current

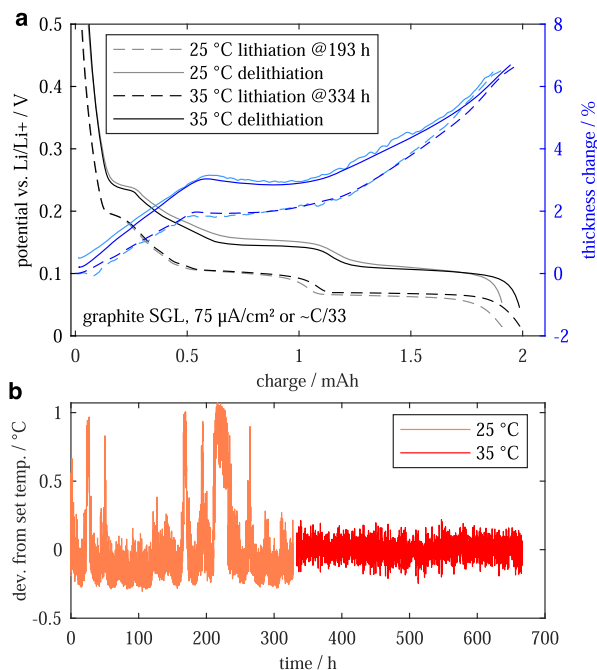


Figure 2. (a) Potential and height change vs the amount of charge in a graphite electrode when cycled at 25°C and 35°C . (b) temperature deviation vs time in the instrument chamber for the two set temperatures. The temperature deviations at 25°C correlate with deviations in the displacement sensor signal. At 35°C , in addition to a smoother signal, the obtained capacity of the graphite electrode was ca. 4% higher.

densities in both cells were set at $75 \mu\text{A cm}^{-2}$. The coin cell reached a specific capacity on delithiation of 366 mAh g^{-1} compared to 357 mAh g^{-1} in the dilatometry cell, a difference of 2.5%. This may be explained by larger overpotentials in the dilatometry cell: In the $\text{LiC}_{12}/\text{LiC}_6$ plateau between $\sim 200 \text{ mAh g}^{-1}$ and $\sim 350 \text{ mAh g}^{-1}$, there is a 4 mV difference between the potentials of the dilatometry cell and the coin cell. One reason may be the distance of 2–3 mm (in perpendicular direction to the electrode surface) between the reference electrode tip and the working electrode.

Figure 4 shows charge/discharge capacities and coulombic efficiencies of both cell types over a period of 1500 h or ca. 50 cycles. The dilatometry cell had a lower coulombic efficiency in the

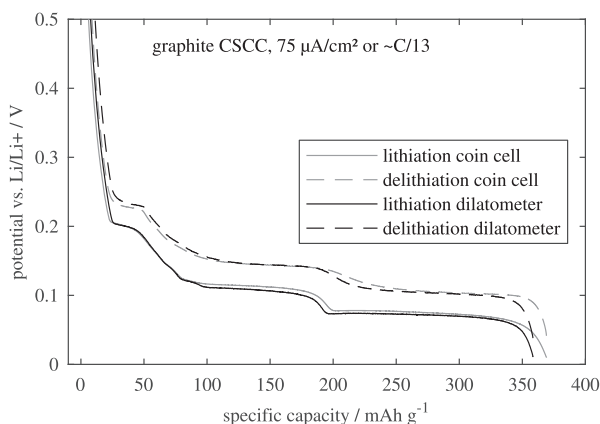


Figure 3. Comparison of potential vs specific capacity of a graphite electrode cycled in a coin cell and in the dilatometry cell using the same area specific current. The polarization in the dilatometry cell is slightly larger, resulting in ca. 3% lower capacity utilization.

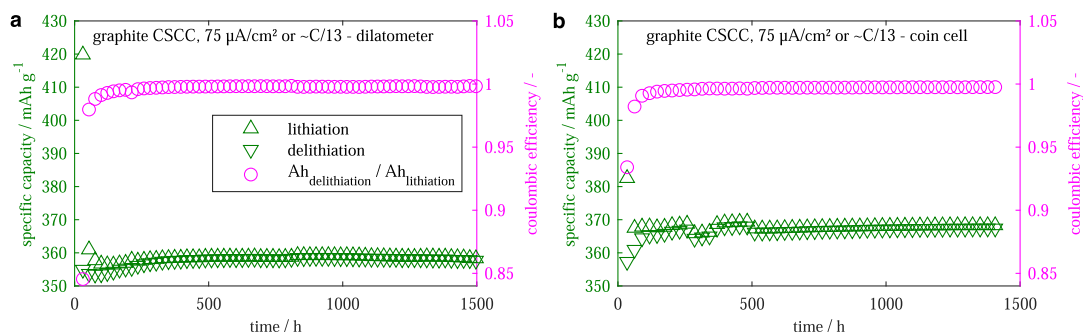


Figure 4. Specific charge/discharge capacities of a graphite electrode in the dilatometry cell (left) and in a coin cell (right) over 50 cycles (ca. 1500 h). Both cell types show good cycling stability and a coulombic efficiency of 99.7% – 99.8%. The two episodes of slightly elevated capacities of the coin cell coincide with and are likely caused by two episodes of ca. 5 K higher chamber temperature caused by a defective controller.

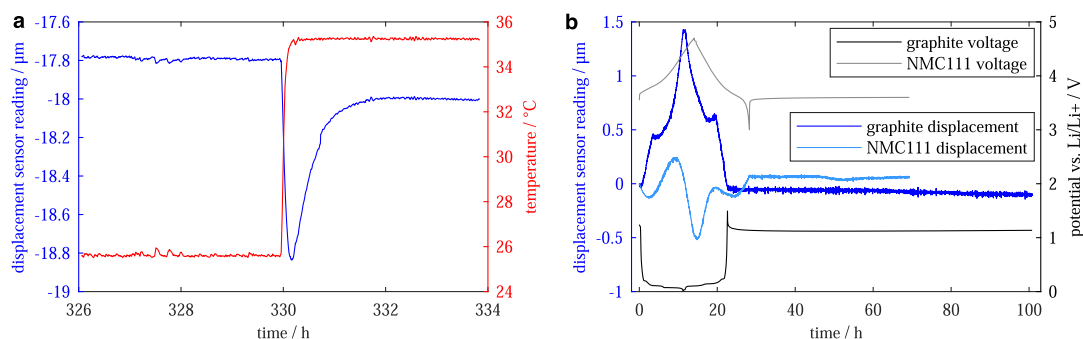


Figure 5. Displacement sensor reading vs time before and after a temperature shift (a) and during one full cycle followed by an OCV resting period of a graphite electrode and an NMC111 electrode spanning several days (b).

first three cycles, which may be due to its larger excess electrolyte volume, but after about 15 cycles, the coulombic efficiencies of both cells remained between 99.7% and 99.8%.

Reliability of the height change measurement.—The displacement sensor is mounted on a metal frame and there are intermediate metal parts between the sensor and the working electrode. Consequently, a measurement error related to thermal expansion of the instrument body can be expected. Additionally, capacitive sensors are inherently temperature sensitive due to changes to the dimensions of the sensor and guard electrode, the permittivity of the space between the electrodes and related alterations to edge effects and stray capacitances. Nojdelov et al.²³ describe these factors in detail and provide a typical compensation model for nm scales, which can be applied by the measurement electronics. Figure 5a shows the displacement sensor reading response for a cell containing a 60 μm thick graphite electrode to a chamber temperature shift from 25 °C to 35 °C. The reading dropped spontaneously by 1 μm and recovered 0.8 μm within 1.5 h, which is probably the time period necessary for full thermal equilibration of the dilatometer. Assuming 5.5e-5/K as thermal expansion coefficient for graphite, only 0.033 μm of the remaining deviation of 0.2 μm would be due to the expansion of the electrode itself. As the temperature fluctuations in the temperature chamber occur in shorter time frames, the more relevant measure should be the spontaneous drop of 1 μm or 0.1 μm K⁻¹, which is likely to be caused by a software correction factor. Another factor impacting the height change measurement is sensor drift. According to the manufacturer's specifications the drift is 20 nm h⁻¹. Figure 5b shows the relative displacement sensor reading during full cycles and subsequent resting periods of a 31 μm thick graphite electrode and a 64 μm thick NMC111 electrode. If the sensor drifted constantly at 20 nm h⁻¹ in one direction during 80 h, the sensor reading would change by 1.6 μm. This is clearly not the

case, as the reading change at the end of the 80 h resting period of the graphite electrode is less than 0.05 μm. The highest rate of change is measured at 50 h into the NMC111 experiment. Here a change of ca. 20 nm h⁻¹ during 1 h is seen, which agrees with the specifications. In comparison to the 0.7 μm thickness change that this electrode undergoes during a cycle, the sensor drift appears to be negligible.

Results and Discussion

As the expansion of graphite electrodes has been studied in several publications, the decision was made to include an analysis of graphite to enable us to benchmark our results against previous measurements. The graphite dilatometry results will be discussed first, followed by a discussion of different nickel/manganese/cobalt/aluminum-based positive electrode materials and a harvested positive electrode from a commercial cell.

Graphite expansion: first cycles.—Two different graphite electrodes are discussed in this section, a flake-type graphite from SGL calendered to 35% porosity, and a non-calendered, spherical MCMB-type graphite from CSCC with a porosity of ca. 65%. Figures 6a/6b shows the height change and charge balance of the first 10 cycles of the SGL and CSCC^a graphite electrodes. We will begin by focusing on the SGL graphite electrode. The height change upon first lithiation was 12.5%, accompanied by a 12% charge loss in the 1st cycle. The irreversible height change seen in the 1st cycle amounts to 7%. The initial expansion of this calendered graphite electrode was significantly larger than that reported so far for non-calendered graphite electrodes¹⁹ as well as calendered electrodes.²²

^aOwing to a problem with a power connector in the long-term cycling experiment on CSCC graphite shown in Figs. 4b and 7b, the displacement sensor reading of the first 8 of the total of 50 cycles was lost. The experiment was repeated with a fresh electrode until 10 cycles were completed. This data is shown in Fig. 6.

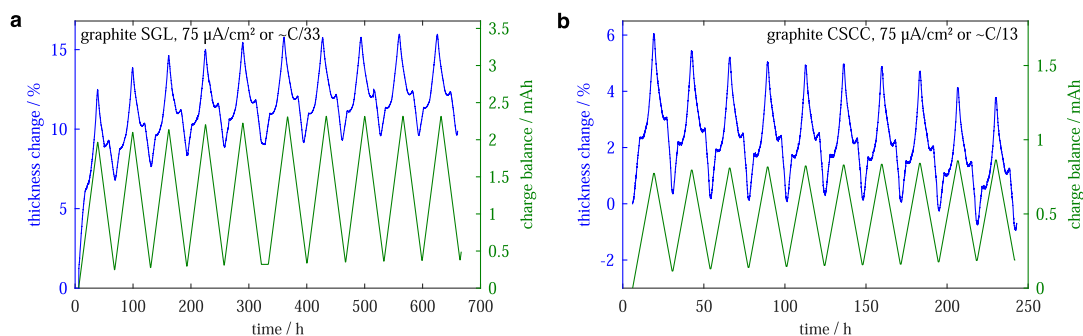


Figure 6. Thickness change and charge balance of SGL (calendered) and CSCC (non-calendered) graphite electrodes during the first 10 cycles. The initial irreversible thickness change in the calendered SGL electrode is significantly larger. The non-calendered CSCC electrode seems to contract rather than expand in the course of the first 10 cycles.

While the coulombic efficiency nears a plateau as early as the 2nd cycle, considerable irreversible height changes can be observed until the 5th cycle. Almost zero irreversible height change can be observed from the 8th to the 10th cycle, by which point the completely delithiated electrode has expanded by a total of 9% vs the fresh state. In contrast, the non-calendered CSCC electrode expanded by only 6% in the first cycle, and most of that expansion was reversed. Beginning with the 2nd cycle, and with the exception of cycle no. 5, the electrode contracted slightly more during each delithiation than it expanded on the preceding lithiation, leading to a net contraction of the electrode of -1% after 10 cycles or ca. $-0.3\ \mu\text{m}$ in 240 h. On the basis of the specified sensor drift, this result would fall within the margin of error. However, in light of the lower practical sensor drift shown in Fig. 5, it should not be prematurely rejected. In any case, the stark difference between the irreversible expansion of the calendered SGL electrode and the tendency to contract of the non-calendered CSCC electrode warrants explanation. It is conceivable that the calendered electrode reverses some of the compaction introduced by the calendering step: The first expansions and contractions of the particles may alter the morphology irreversibly in such a way that the expansions of the particle can be accommodated, leading to an overall expansion. This may be viewed as resulting from the structure's preference of minimizing elastic stress energy. In the non-calendered electrode, the expansions and contractions of the particles likely trigger a re-arrangement of the microstructure, too, but here the new local minimum of elastic stress energy may entail a more compact arrangement, leading to the slight overall contraction we observed. For a discussion of internal stress-strain relationships of electrodes the reader is referred to Rieger et al.²⁴

Reversible expansion of graphite.—Figures 7a/7b shows potential and height change as a function of specific capacity. Six

consecutive cycles of the SGL graphite and 20 consecutive cycles of the CSCC graphite illustrate the good reproducibility of both the voltage and the height change reading. Regarding the minor differences in the height change measurements with cycling, there is a weak trend towards decreasing change as the cycle number increases. In the dilatometry cell, the SGL graphite reaches a reversible capacity of $345\ \text{mAh g}^{-1}$ – $348\ \text{mAh g}^{-1}$ with a height change of 6.5%, while the CSCC graphite reaches $357\ \text{mAh g}^{-1}$ with 4.9% height change. The 6.5% height change of the calendered SGL graphite (35% porosity) agrees well with a previous measurement of a calendered graphite electrode in Rieger et al.²⁰ (33% porosity). The smaller height change of the non-calendered CSCC graphite seems to agree with results of non-calendered graphite electrodes in Hahn et al.,¹⁹ although only first cycle data is presented in the study.

The numbers in Fig. 7b designate the different graphite stages. Their assignment to the voltage readings is based on Dahn et al.²⁵ and Asenbauer et al.²⁶ According to the “staging” mechanism of intercalants into graphite, the graphene layers are not occupied evenly by ions during lithiation, but in such a fashion, that one intercalant layer is completely filled before the next layer starts incorporating lithium ions. The intercalant layers are separated by a decreasing number of graphene layers as the lithiation progresses: In “stage 4,” 4 graphene layers separate each intercalant layer, in “stage 1,” only alternating layers of graphene and intercalant remain. For a comprehensive review of the “staging” mechanism the reader is referred to Bresser et al.²⁶ Figure 7a shows that, during lithiation, the electrode thickness increased linearly at first, reaching 1.8% when stage 3 is reached. During the transition between stage 3 and stage 2, which includes the “liquid” intermediate stage “2L,” the thickness increased at a much lower rate, reaching 2.3% at stage 2. Most of the height change, an additional 4.3%, occurred in the transition between stage 2 and stage 1. This progression is in qualitative

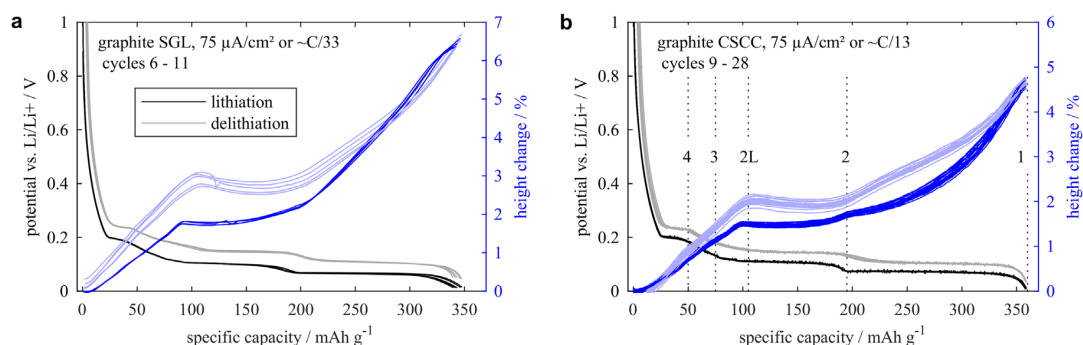


Figure 7. Thickness change vs specific capacity of SGL and CSCC graphite electrodes during multiple consecutive cycles. The thickness change on full lithiation is higher in the flake-type and calendered SGL graphite electrode than in the non-calendered MCMB-type CSCC graphite electrode.

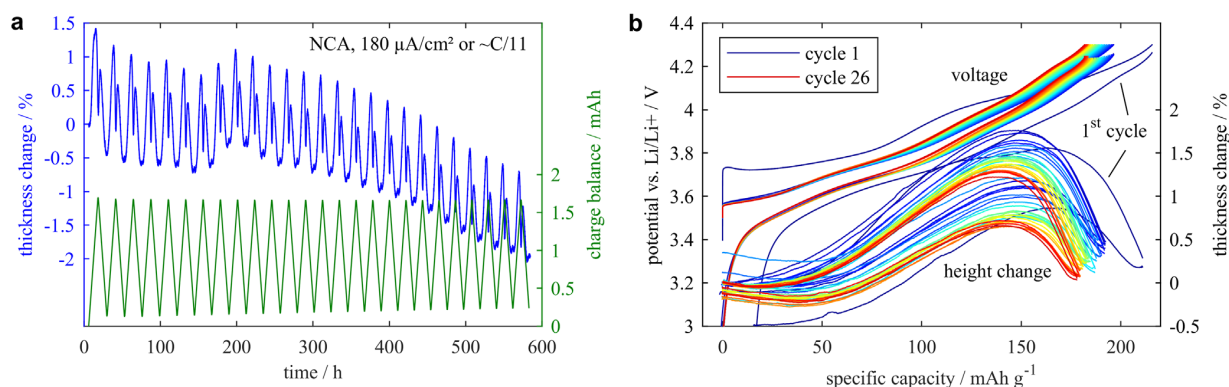


Figure 8. (a) Thickness change and charge balance, (b) voltage and thickness change per cycle during the first 26 cycles of an NCA electrode. The electrode contracted significantly during the first cycle, thereafter it generally seems to continue to contract slightly, but these reading changes are well within the specified sensor drift. Regarding the thickness changes within each cycle, there is a clear trend towards lower maximum expansions with higher cycle numbers.

agreement with measurements of interlayer spacing and unit cell volume evolution obtained via XRD.^{25,27} In absolute terms, the interlayer spacing and the unit cell volume increase by ca. 10% and 13%²⁷ respectively, which would translate into a 4.2% ($\sqrt[3]{1.13} \approx 0.042$) thickness increase if random crystal orientation and hence isodirectional expansion are assumed. This is less, however, than the 6.5% thickness increase that was measured for the flake-type SGL graphite. Indeed, XRD-based studies have shown that the crystals in flake-type graphite electrodes are oriented preferentially in such a way that the intercalant layers are parallel to the current collectors.^{28,29} In consequence, a thickness increase closer to the 10% interlayer spacing change would be expected, lessened only by the degree to which the particle volume change can be absorbed by the electrode structure, decreasing the porosity. For the flake-type graphite which expanded by 6.5%, this would mean that up to 3.5% of the solid particle volume may be absorbed by porosity reduction. Regarding the CSCC electrode made of spherical MCMB, which displayed reversible expansion of 4.9%, a more isodirectional expansion of the particles would be expected, making 4.2% the reference mark. As an explanation of this difference, it is conceivable that in such thin objects, strain is more likely to be released in the vertical direction than laterally.²⁴ However, this electrode was non-calendered and had a high porosity of 65%, providing plenty of room for accommodation of expanding particles. Unfortunately, the effect of initial electrode porosity on expansion cannot be clarified in this study because of the unfortunate sample combination of a calendered flake-type graphite electrode with a non-calendered spherical MCMB electrode.

NCA extended cycling.—In order to facilitate the interpretation of the following experiments in which various TMOs are compared, an NCA electrode was subjected to extended cycling over 580 h/26 cycles between 3.0 V and 4.3 V. The results are also shown here to give a sense of the displacement sensor drift when measuring TMOs, which expand significantly less than graphite. Figure 8a shows the thickness change and charge balance, Fig. 8b the voltage and thickness change per cycle. Figure 8a suggests that the NCA electrode contracted significantly during the first cycle, and then continued to contract at a lower variable rate, interrupted by a slight increase during cycles no. 8 and no. 9. All of these displacement sensor reading changes could be explained by the specified sensor drift: For example, the -0.15% change of the NCA electrode thickness from cycle no. 12 to no. 15 corresponds to only 83 nm in 66 h. However, observations of the sample after cycling, see Fig. 5b, demonstrate that the quantity of short-term drift significantly outweighs that of long-term drift. It also appears that the majority of the errors self-correct over a longer period. The thickness change measured by the dilatometer at the end of the experiment was -2%

or $0.8 \mu\text{m}$, however a post-experiment thickness measurement of the electrode using a micrometer screw yielded no change relative to before the experiment. The $1 \mu\text{m}$ resolution of the micrometer screw only allows the conclusion that the displacement sensor signal is probably accurate to within $\pm 1 \mu\text{m}$ even after 580 h of continuous use. It is however unable to confirm the slight contraction of the NCA electrode measured by the displacement sensor.

A decrease in the magnitude of the thickness changes as the cycles progress is demonstrated by Fig. 8b. The slowing rate of this decrease suggests that a “steady state” would be reached upon continued cycling. The maximum expansion per cycle decreases from 1.7% in the first cycle, to 1.5% in the 6th cycle, to 1.2% in the 26th cycle, while the overall shape remains constant.

Comparison of different lithium-transition-metal-oxides.—The TMO electrodes were cycled to four different upper voltage cut-offs, 4.1 V, 4.3 V, 4.5 V and 4.7 V, for 3 cycles within each voltage window^b. The cycling voltage profile is shown in Fig. 9a along with the coulombic efficiency of each cycle. At the end of the 30 min resting periods after each CC charging phase, the open-circuit voltages (OCV) were ca. 50 mV below the cut-off voltage. In two cases, Kokam 1st cycle and NMC622 4th cycle, the coulombic efficiency was higher than one. This was likely caused by temporary issues with the electrochemical cell, as in both cases there were alterations in the voltage signal during lithiation, perhaps due to incomplete wetting of smaller pores or gas bubbles at the electrode/T-frit/spacer interfaces. Otherwise, the highest coulombic efficiency was reached at the 3rd 3 V–4.3 V cycle. The lower efficiency at the 3rd 3 V–4.1 V cycle was probably due to initial side reactions taking place at a higher rate at that early stage. In each of the four sets of three cycles, coulombic efficiency dropped initially (compared to the 3rd cycle of the previous set of three) and then increased again. This indicates that every time a higher voltage regime was reached, new initial side reactions are triggered which then, at least partially, faded. At the 4.7 V cut-off, however, these side reactions seem to be more severe and persistent, as the reversible capacity was significantly diminished and all of the electrodes remained below 99% efficiency in the 3rd cycle. NMC111 and the Kokam cathode, which both have a relatively high cobalt content, have lower coulombic efficiencies at 4.7 V than the other materials. In light of the above, the different TMOs will be compared a) based on the 3rd cycle/4.3 V cut-off to study their thickness change in a highly stable regime and because the OCVs after the 30 min rest of about 4.25 V come close to the maximum voltages experienced by these electrodes in practical

^bThere are two exceptions: For NMC811, the first three cycles with 4.1 V cut-off were skipped due to a very large initial polarization. For the Kokam electrode, the first three cycles already had a 4.3 V cut-off, but were performed with a lower current.

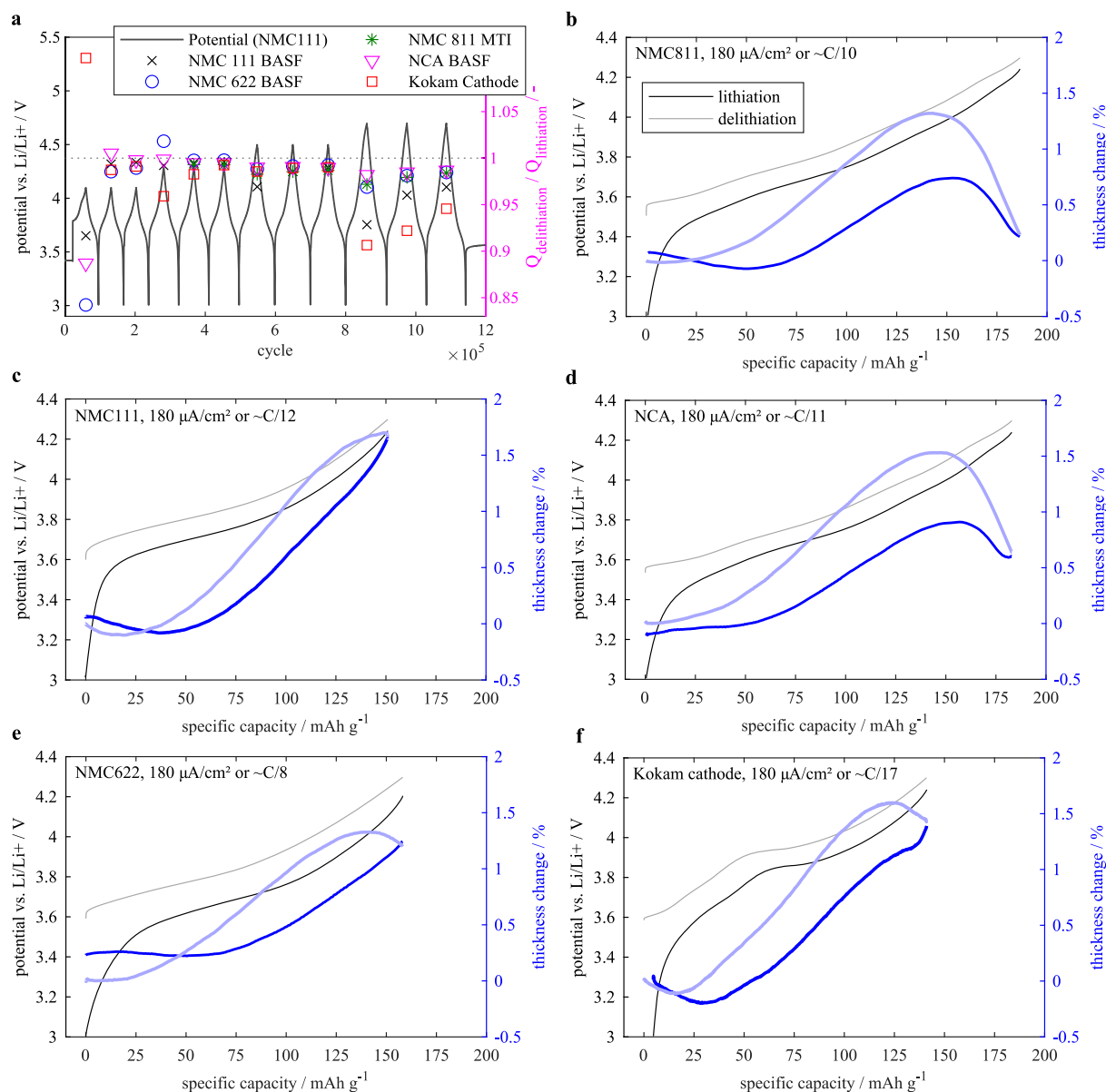


Figure 9. (a) Coulombic efficiency of TMO electrodes in the dilatometry cell for different upper-cut off voltages. (b)–(f) thickness change vs specific capacity of TMO electrodes during the 3rd cycle with a 4.3 V upper cut-off.

cells, b) based on the 1st cycle/4.7 V to discuss their thickness change at higher voltages. Regarding the latter, it should be pointed out that, for each individual material, the thickness change characteristics of cycles with different cut-off voltages agree well in their common voltage ranges. The NCA cycling results from the previous section suggest that the “steady state” thickness change characteristics upon continued cycling would be slightly reduced compared to those in the 6th and 9th cycles, which are analyzed in the following.

Figures 9b–9f show potential and height change vs specific capacity during the 3rd 3 V–4.3 V cycle for each of the TMO electrodes investigated here. Taking into account that the OCV after charging was ca. 50 mV below the cut-off voltage of 4.3 V, the reversible specific capacities of 150 mAh g⁻¹ (NMC111), 158 mAh g⁻¹ (NMC622), 187 mAh g⁻¹ (NMC811) and 183 mAh g⁻¹ (NCA) are in agreement with those in the literature.^{30–33} Assuming an active material content of 96 wt-%, the Kokam cathode reaches 142 mAh g⁻¹. As its composition

is proprietary, probably an NCA/LCO blend (see Fig. A-1, Appendix), there is no benchmark for the specific capacity.

The highest maximum expansion among the TMO electrodes tested here, was 1.7% and was measured for both the NMC111 and the Kokam cathodes. This was followed by NCA with 1.5% and NMC622 and NMC811 with 1.3%. The thickness changes of all the materials followed an S-shaped curve, with no expansion or a slight contraction at the beginning of delithiation, followed by a steep, almost linear increase, a subsequent leveling off of the expansion and a final contraction. There is significant hysteresis in the expansion/state-of-charge relationship: Differences in the thickness changes measured for a material during lithiation and delithiation reached a maximum of 0.5% of the initial sample thickness, or 30%–50% of the sample’s maximum thickness change.

In the case of NMC111, NMC622 and the Kokam cathode, the expansion maximum coincides approximately with the end of charge

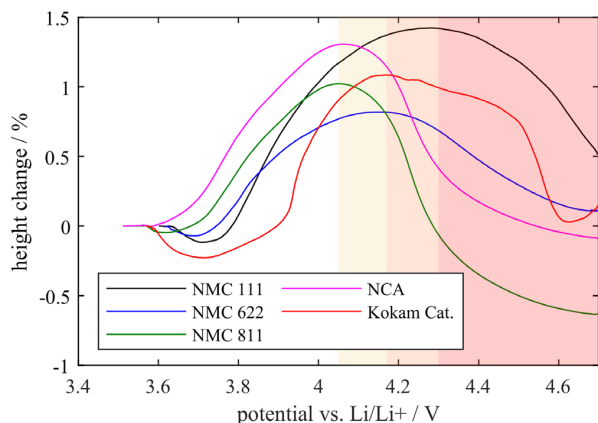


Figure 10. Thickness change of TMO electrodes vs voltage during delithiation. The higher the nickel content, the lower the voltage at which the electrodes reach their maximum expansion and start to contract.

to 4.3 V, but NMC811 and NCA contract abruptly during the last 20 mAh g⁻¹ of delithiation, recuperating most of the previous expansion. Plotting the thickness change during the first delithiation to 4.7 V vs voltage as in Fig. 10, reveals that a higher nickel content correlates with a shift of the expansion maximum or beginning of contraction to lower voltages: NMC811 and NCA reached their maximum expansion at ca. 4.05 V (beginning of yellow shading), NMC622 and the Kokam cathode at ca. 4.15 V (orange shading) and NMC111 at 4.3 V (red shading). While NMC811 and NCA contracted strongly between 4.15 V and 4.3 V, NMC111 only contracted significantly above 4.4 V.

These differences in contraction at high voltages may be explained by results from XRD studies: In Li(Ni_{1-x-y}Co_xMn_y)O₂ materials, a phase transition involving a greatly reduced *c*-axis of the hexagonal lattice is suppressed or occurs at higher voltages when the content of nickel, relative to cobalt and manganese, is lower.^{34,35} It has been reported that aluminum, may also help to suppress this phase transition.^{36,37} This effect could explain why the contraction of the NCA electrode is less steep than that of NMC811 in the orange-shaded voltage region in Fig. 10.

Electrode expansion vs crystal structure change.—The Li(Ni_{1-x-y}Co_xMn_y)O₂ cathode is a layered crystalline structure of the α-NaFeO₂-type (space group *R*3̄*m*, *Z* = 3). The absolute lengths as well as the change upon lithium insertion/extraction of the lattice parameters *a* and *c* of the hexagonal transition metal layers can be determined via operando XRD. The technique yields highly

reproducible results, with differences of less than 1% between measurements of the NMC111 lattice parameters reported in different studies.^{38–41} The following analysis uses XRD results from de Biasi et al.,⁴¹ who investigated Li(Ni_{1-x-y}Co_xMn_y)O₂ electrodes with different nickel contents.

Figure 11 shows the change of the lattice parameters and the unit cell volume along with the thickness change registered by dilatometry of different NMC electrodes as a function of voltage. Both *a* and *c* change upon lithium extraction. The magnitude of this change is more drastic for high nickel NMCs. Initially, *a* decreases in a linear fashion until 4.0 V, then remains constant until 4.4 V where it begins to increase again. The drastic initial decrease can be attributed to the decreasing ionic radii of the transition metals as they are oxidized in the delithiation process. With *c*, the opposite trend can be seen. It initially expands until a potential of 4.0 V is reached, followed by a plateau until 4.2 V. At higher voltages, *c* decreases drastically. The initial expansion in *c* is attributed to increasing coulomb repulsion upon lithium extraction from interslab sites. As the extraction of lithium proceeds, the interslab width contracts due to the emergence of empty sites and *c* decreases. While the evolution of *a* is quite similar in all three NMCs, the slope of *c* varies strongly with the relative nickel content: In NMC811 (Fig. 11c), the contraction of *c* is much more pronounced than in NMC622 (b) and NMC111 (a) and is shifted towards lower voltages. The unit cell volume of NMC in hexagonal closed pack (hcp) configuration, $V = \frac{\sqrt{3}a^2c}{2}$, has a quadratic dependence on *a* and a linear dependence on *c*. Consequently, as long as *a* and *c* evolve in opposite directions, the unit cell volume roughly follows *a* until, above 4.2 V, it follows the strong decrease of *c*.

The electrode thickness as measured by dilatometry agrees best with *c*, or, also displayed in Fig. 11, the sum of *a* and *c*. Given that the investigated materials are all polycrystalline and contain a collection of randomly orientated layered-oxide grains, this seems counter intuitive as one could expect the unit cell volume to determine the thickness evolution. This was found to be the case for a LiCoO₂ electrode, where a unit cell volume change of +2.32% triggered a thickness increase of ca. 1.8%.²⁴ However, it may be that microscopic expansions in all directions lead to elastic, reversible macroscopic expansions while contractions, rather than leading to macroscopic contractions, instead lead to an increase of void space in the electrode structure. This could be explained by the binder forming a type of skeleton which provides stability against compression but out of which the microstructure could expand. The existence of such a structure would explain why the thickness change follows the growth of *c* and shrinking back to its initial value but seems largely unaffected by both the shrinking of *a* and the further shrinking of *c* to negative relative values. At this juncture, the inflexible binder skeleton would prevent a further reduction in thickness being measured. A minor divergence from that overall

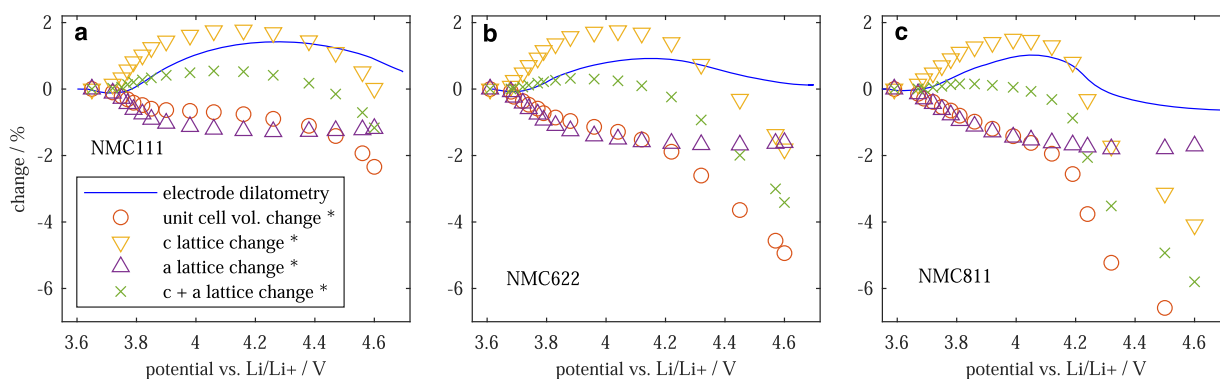


Figure 11. Thickness change of TMO electrodes compared to crystal structure changes measured via XRD. Electrode thickness change correlates weakly with the *c* lattice parameter, but does not follow the unit cell volume, especially at higher voltages, where the unit cell volume decreases significantly. All XRD data (marked with *) are reproduced from de Biasi et al.⁴¹

behavior occurs at the beginning of the lithium extraction, where all electrodes contract slightly and the sum of a and c agrees better with the electrode thickness evolution than c alone. Regarding the magnitude of the changes, it is plausible, as with the graphite electrodes discussed above, that the percentage electrode thickness change is smaller than the largest unidirectional lattice expansion occurring at the microscopic level. This may be due to some absorption of the particle expansion by the electrode structure, reducing the porosity, and the non-preferential orientation of the grains.

Conclusions

A dilatometry setup was validated and used to investigate the thickness changes of various negative and positive electrode materials used in lithium-ion batteries. By operating the dilatometry setup in a temperature-controlled argon atmosphere, cycling stability comparable to coin cells and high reproducibility of the dilation measurements was achieved. It was shown that the uncertainty related to drift of the capacitive displacement sensor is negligible compared to the dilation even of transition metal oxide electrodes with relatively low areal loadings. For two different types of graphite electrodes, maximum reversible thickness changes of 4.9% (spherical MCMC type) and 6.5% (flake type) were obtained. It could not be established to which extent this difference was caused by calendaring, resulting in different electrode porosities, or by the particle type. In the case of the flake type graphite, we argued that due to preferential orientation of crystals, the interlayer spacing change of ca. 10% is a more adequate reference measure than the ca. 4.2% isodirectional expansion that would result from the unit cell volume change under the assumption of random crystal orientation. This raised the question of how much of the particle volume change is absorbed by the porous structure of the electrode, and an upper limit of ca. 3.5% was calculated. TMO electrodes showed maximum expansions of 1.3% to 1.7% upon delithiation to an equilibrium potential of ~ 4.25 V, and, when further delithiated to an equilibrium potential of ~ 4.65 V vs Li/Li⁺, contractions of up to -0.5% vs the fully lithiated state. Higher nickel contents seemed to reduce the equilibrium potential at which the expansion reached its maximum and contraction began. Finally, electrode thickness changes were compared to crystal structure change data from scientific literature. No correlation could be established between the expansion of the porous composite electrodes and the unit cell volume change, although a relationship to the evolution of the c lattice parameter of the hexagonal layered structure suggested itself. The results also indicated that a contraction that takes place in the crystal structure or on the primary particle level does not necessarily lead to a contraction on the electrode level. This study demonstrated that electrode level thickness changes as a result of lithiation and delithiation can be measured with high accuracy in a dilatometry

cell and that extrapolating such changes from the structural change of active materials at the single-crystal level involves significant uncertainty.

Acknowledgments

We thank former student research assistant Igor Senna for his help with electrode preparation and preliminary dilatometry experiments. We thank Stefan Oswald (TUM, Germany) for his advice regarding electrode preparation and for fruitful discussions and Fabian Linsenmann (TUM) for more fruitful discussions. We also thank Prof. Chia-Chin Chang of the National University of Tainan, Taiwan, and Dr. Shang-Chieh Hou of the National Cheng Kung University, Taiwan, for providing the CSCC graphite electrodes. This work was financially supported by the German Federal Ministry of Education and Research (BMBF) in the projects HighSafe (03XP0138B), HighSafe II (03XP0306B), ExZellTUM II (03XP0081), ExZellTUM III (03XP0255) and by the Technical University of Munich. The responsibility for this publication rests with the authors.

Appendix

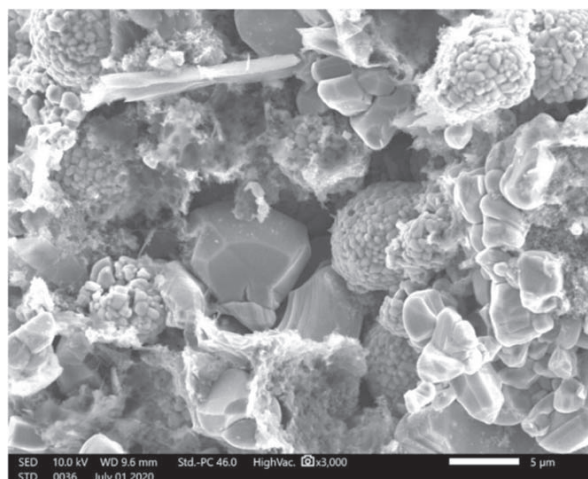


Figure A-1. SEM image of the Kokam cathode. A cobalt/nickel ratio of 8/5 was detected by EDX, with no manganese present. Comparison to SEM images of NCA and LCO electrodes^{42–44} suggests it is an NCA/LCO blend, which has been reported for other types of Kokam pouch cells.

Table A-I. Slurry recipes of the electrodes prepared for this study.

Type	Component	Fraction of solid content/wt.-%
Graphite (SGL)	Active material	95.0
	PVDF Kynar HSV900	5.0
	NMP	45.0 (of total mass)
Graphite (CSCC)	Active material	95.0
	MMM Carbon SuperP	2.0
	Sigma-Aldrich CMC/Zeon Co. SBR	2.5/0.5
	De-ionized water	65.0 (of total mass)
NMC 111 (BASF)	Active material	96.0
	PVDF Solvay Solef 5130	2.0
	Timcal Super C65	2.0
	NMP	37.50 (of total mass)
NMC 622 (BASF)	Active material	92.50
NMC 811 (MTI)	PVDF Solvay Solef 5130	3.50
NCA (BASF)	Timcal Super C65	4.0
	NMP	46.50 (of total mass)

ORCID

Franz B. Spingler <https://orcid.org/0000-0002-6523-3986>Simon Kücher <https://orcid.org/0000-0003-2230-7356>Robert Phillips <https://orcid.org/0000-0001-7332-6739>Erfan Moyassari <https://orcid.org/0000-0002-3037-202X>Andreas Jossen <https://orcid.org/0000-0003-0964-1405>

References

- J. Gonzalez, K. Sun, M. Huang, J. Lambros, S. Dillon, and I. Chasiotis, *J. Power Sources*, **269**, 334 (2014).
- L. Y. Beaulieu, T. D. Hatchard, A. Bonakdarpour, and M. D. Fleischauer, *J. Electrochem. Soc.*, **A1457** (2003).
- R. Xu and K. Zhao, *J. Electrochem. En. Conv. Stor.*, **13**, 30803 (2016).
- A. O. Kondrakov, A. Schmidt, J. Xu, H. Geßwein, R. Mönig, P. Hartmann, H. Sommer, T. Brezesinski, and J. Janek, *J. Phys. Chem. C*, **121**, 3286 (2017).
- Y. H. Choi, H. K. Lim, J. H. Seo, W. J. Shin, J. H. Choi, and J. H. Park, *SAE International Journal of Alternative Powertrains*, **7**, 195 (2018).
- S. Mohan, Y. Kim, J. B. Siegel, N. A. Samad, and A. G. Stefanopoulou, *J. Electrochem. Soc.*, **161**, A2222 (2014).
- N. A. Samad, Y. Kim, J. B. Siegel, and A. G. Stefanopoulou, *J. Electrochem. Soc.*, **163**, A1584 (2016).
- C. M. DeLuca, K. Maute, and M. L. Dunn, *J. Power Sources*, **196**, 9672 (2011).
- M. L. Terranova, S. Orlanducci, E. Tamburri, V. Guglielmotti, and M. Rossi, *J. Power Sources*, **246**, 167 (2014).
- P. K. Leung, C. Moreno, I. Masters, S. Hazra, B. Conde, M. R. Mohamed, R. J. Dashwood, and R. Bhagat, *J. Power Sources*, **271**, 82 (2014).
- B. Rieger, S. F. Schuster, S. V. Erhard, P. J. Osswald, A. Rheinfeld, C. Willmann, and A. Jossen, *Journal of Energy Storage*, **8**, 1 (2016).
- C. Birkenmaier, B. Bitzer, M. Harzheim, A. Hintennach, and T. Schleid, *J. Electrochem. Soc.*, **162**, A2646 (2015).
- I. Soga and Y. Kinoshita, *Japan. J. Appl. Phys.*, **41**, 6616 (2002).
- B. Bitzer and A. Grubbe, *J. Power Sources*, **262**, 297 (2014).
- Z. J. Schiffer, J. Cannarella, and C. B. Arnold, *J. Electrochem. Soc.*, **163**, A427 (2015).
- J. H. Lee, H. M. Lee, and S. Ahn, *J. Power Sources*, **119-121**, 833 (2003).
- M. Nagayama, K. Ariyoshi, Y. Yamamoto, and T. Ohzuku, *J. Electrochem. Soc.*, **161**, A1388 (2014).
- D. Sauerweig, S. Ivanov, H. Reinshagen, and A. Bund, *J. Power Sources*, **342**, 939 (2017).
- M. Hahn, H. Buqa, P. W. Ruch, D. Goers, M. E. Spahr, J. Ufheil, P. Novák, and R. Kötz, *Electrochem. Solid-State Lett.*, **11**, A151 (2008).
- B. Rieger, S. Schlueter, S. V. Erhard, J. Schmalz, G. Reinhart, and A. Jossen, *J. Energy Storage*, **6**, 213 (2016).
- W. Biberacher, A. Lerf, J. O. Besenhard, H. Möhwald, and T. Butz, *Mater. Res. Bull.*, **17**, 1385 (1982).
- H. Michael, F. Iacoviello, T. M. M. Heenan, A. Llewellyn, J. S. Weaving, R. Jervis, D. J. L. Brett, and P. R. Shearing, *J. Electrochem. Soc.*, **168**, 10507 (2021).
- M. R. Nojdelov, D. Dirk Voigt, M. Arthur, S. van de Nes, and M. S. Nihtianov, *2015 9th International Conference on Sensing Technology (ICST): 2015 9th International Conference on Sensing Technology (ICST) took place 8-11 December 2015 in Auckland (IEEE, New Zealand, Piscataway, NJ) (2015)*.
- B. Rieger, S. Schlueter, S. V. Erhard, and A. Jossen, *J. Electrochem. Soc.*, **163**, A1595 (2016).
- J. Dahn, *Phys. Rev. B*, **44**, 9170 (1991).
- J. Asenbauer, T. Eisenmann, M. Kuenzel, A. Kazzazi, Z. Chen, and D. Bresser, *Sustainable Energy Fuels*, **4**, 5387 (2020).
- S. Schweidler, L. de Biasi, A. Schiele, P. Hartmann, T. Brezesinski, and J. Janek, *J. Phys. Chem. C*, **122**, 8829 (2018).
- P. Baade, M. Ebner, and V. Wood, *J. Electrochem. Soc.*, **164**, E348 (2017).
- S. Malifarge, B. Delobel, and C. Delacourt, *J. Power Sources*, **343**, 338 (2017).
- T. Ohzuku and Y. Makimura, *Chem. Lett.*, 642 (2001).
- P. Y. Liao, J. G. Duh, and S. R. Sheen, *J. Power Sources*, **143**, 212 (2005).
- R. Robert and P. Novak, *J. Electrochem. Soc.*, **162**, A1823 (2015).
- M.-H. Kim, H.-S. Shin, D. Shin, and Y.-K. Sun, *J. Power Sources*, **159**, 1328 (2006).
- W.-S. Yoon, K. Y. Chung, J. McBreen, and X.-Q. Yang, *Electrochem. Commun.*, **8**, 1257 (2006).
- J. Xu, E. Hu, D. Nordlund, A. Mehta, S. N. Ehrlich, X.-Q. Yang, and W. Tong, *ACS Appl. Mater. Interfaces*, **8**, 31677 (2016).
- T. Ohzuku, T. Yanagawa, M. Kouguchi, and A. Ueda, *J. Power Sources*, **68**, 131 (1997).
- M. Guilmond, *J. Power Sources*, **115**, 305 (2003).
- J.-M. Kim and H.-T. Chung, *Electrochim. Acta*, **49**, 937 (2004).
- S.-C. Yin, Y.-H. Rho, I. Swainson, and L. F. Nazar, *Chem. Mater.*, **18**, 1901 (2006).
- X.-L. Wang et al., *Sci. Rep.*, **2**, 1 (2012).
- L. de Biasi, A. O. Kondrakov, H. Geßwein, T. Brezesinski, P. Hartmann, and J. Janek, *J. Phys. Chem. C*, **121**, 26163 (2017).
- E. J. Cheng, N. J. Taylor, J. Wolfenstine, and J. Sakamoto, *Journal of Asian Ceramic Societies*, **5**, 113 (2017).
- M. Ebner, D.-W. Chung, R. E. García, and V. Wood, *Adv. Energy Mater.*, **4** (2014).
- P. Xiao, T. Lv, X. Chen, and C. Chang, *Sci. Rep.*, **7**, 1408 (2017).

4.2 Modeling the Effect of Local Compression on the Current Distribution and Propensity for Lithium Plating

In the following, an investigation into the cause-effect relationships of local compression, electrode and separator transport properties, current density distribution, and the risk of local lithium plating is presented. The investigation uses a combination of modeling and experiments.

The results from section 3.2 indicated that a local pore closure in the separator of a commercial pouch cell provokes lithium plating. This notion is supported by the results of an earlier study using a controlled coin cell setup with which it was shown that the depositions occur predominantly at the edges of such closures [27]. In contrast, preliminary experiments on locally compressed cells yielded deposits all over the compressed area of the anode, rather than only at the edges. This ostensible contradiction was found to be worthy of further investigation particularly as the scenario of a locally elevated compressive force on the cell stack appears to be more relevant in application than a local pore closure restricted to the separator. First, a pseudo-3D Newman-type electrochemical model was parameterized based on coin cell quasi-OCV measurements of the electrodes harvested from a commercial 2.1 Ah pouch cell. As a reference point, the separator pore closure scenario was simulated and the results confirmed the high risk of lithium plating at the edges of the affected area. Afterwards, a simple mechanical model of the electrodes and the separator was added based on two experimental inputs: The pressure-compression relationships of each cell component and the electrode dilation as a function of the degree of lithiation from section 4.1. Using the resulting electrochemical-mechanical model, the effects of local compressive pressures on the current distribution and the local electrode potentials were analyzed. The local electrode potential distribution, with lower potentials in the compressed area, was in line with the preliminary experimental finding that depositions accumulated in the compressed areas. A systematic experimental study in which the same pressure levels were applied as in the simulation, confirmed the results of both the preliminary experiments and the simulation.

This work contributes to the overarching theme of the thesis in so far that it shows that non-uniform compression of cells carries the risk of lithium plating and that it reveals the underlying mechanisms of the phenomenon. It also provides a method for evaluating the allowable local mechanical pressure on a cell stack when plating is to be avoided.

Author contribution Franz Spingler was responsible for the conceptualization, methodology, investigation, and writing of the original draft. Sven Friedrich provided laboratory work and the data analysis of the materials testing and commented on the manuscript. Simon Kücher helped with the laboratory work. Simon Schmid and Daniel López-Cruz helped with the modeling part. Andreas Jossen provided supervision, and reviewed and commented on the manuscript.

The Effects of non-uniform Mechanical Compression of Lithium-Ion Cells on Local Current Densities and Lithium Plating

Franz B. Spingler, Sven Friedrich, Simon Kücher, Simon Schmid, Daniel López-Cruz,
Andreas Jossen

Journal of The Electrochemical Society 168 110515, 2021

Permanent weblink:

<https://doi.org/10.1149/1945-7111/ac33e1>

Reproduced under the terms of the Creative Commons Attribution 4.0 License (CC BY, <http://creativecommons.org/licenses/by/4.0/>), which permits unrestricted reuse of the work in any medium, provided the original work is properly cited.



The Effects of Non-Uniform Mechanical Compression of Lithium-Ion Cells on Local Current Densities and Lithium Plating

Franz B. Spingler,^{1,z} Sven Friedrich,¹ Simon Kücher,¹ Simon Schmid,¹ Daniel López-Cruz,¹ and Andreas Jossen^{1,2}

¹Institute of Electrical Energy Storage Technology, Technical University of Munich (TUM), Arcisstr. 21, 80333 Munich, Germany

²Munich School of Engineering (MSE), Technical University of Munich (TUM), Lichtenbergstr. 4a, 85748 Garching, Germany

Lithium-ion batteries can experience mechanical loads for a variety of reasons, including the rigidity of the cell casing itself, bracing of cell stacks in a module, which is generally due to limited space in the place of installation, or as a result of accidents or abuse. In all of these cases, and exacerbated by faulty manufacturing or assembly, the mechanical loads may be non-uniform across the cell surface. Here, we present an analysis of the effects of such non-uniform mechanical loads on the current density distribution during charging and show that they can provoke localized lithium plating. Pressure-compression relationships of individual cell components were determined experimentally and implemented into a pseudo-3D axisymmetric electrochemical-mechanical cell model of a 2.1 Ah pouch cell by Kokam, South Korea. The modeling results were successfully validated by comparison to a post-mortem evaluation of pouch cells that were cycled while being locally compressed.

© 2021 The Author(s). Published on behalf of The Electrochemical Society by IOP Publishing Limited. This is an open access article distributed under the terms of the Creative Commons Attribution Non-Commercial No Derivatives 4.0 License (CC BY-NC-ND, <http://creativecommons.org/licenses/by-nc-nd/4.0/>), which permits non-commercial reuse, distribution, and reproduction in any medium, provided the original work is not changed in any way and is properly cited. For permission for commercial reuse, please email: permissions@iopublishing.org. [DOI: [10.1149/1945-7111/ac33e1](https://doi.org/10.1149/1945-7111/ac33e1)]



Manuscript submitted July 28, 2021; revised manuscript received September 27, 2021. Published November 9, 2021.

List of symbols

Symbol Unit

Greek Symbols

α_a		Kinetic transfer coefficient of the anode
α_c		Kinetic transfer coefficient of the cathode
α		Bruggeman coefficient
ε		Relative compression
η	V	Overpotential
κ	S m ⁻¹	Ionic conductivity liquid phase
ν		Poisson's number
ξ_s		Volume fraction of the active material
ξ_t		Volume fraction of the electrolyte (=porosity)
$\xi_{s,na}$		Volume fraction of non-active components
ρ	g cm ⁻³	Mass density
σ_s	S m ⁻¹	Electrical conductivity solid phase
Φ_s	V	Electrical potential solid phase
Φ_l	V	Electrical potential liquid phase
Latin Symbols		
c_s	mol m ⁻³	Lithium ion concentration in the solid phase
c_l	mol m ⁻³	Lithium ion concentration in the liquid phase
$c_{s,0}$	mol m ⁻³	Initial lithium concentration
$c_{s,max}$	mol m ⁻³	Maximum achievable lithium concentration
D_l	m ² s ⁻¹	Lithium-ion diffusion of the liquid phase
D_s	m ² s ⁻¹	Diffusion coefficient of lithium in the solid phase
E_A	J mol ⁻¹	Activation energy
E_{eq}	V	Equilibrium voltage
F	C mol ⁻¹	Faraday constant 9.64853321233100184 · 10 ⁴
i_0	A m ⁻²	Exchange current density
i_s	A m ⁻²	Current density solid phase
i_l	A m ⁻²	Current density liquid phase
i_{app}	A m ⁻²	Applied current density

(Continued).

i_n	A m ⁻²	Molar ion flux density
K	MPa	Compression module
k_a	m s ⁻¹	Reaction coefficient of the anode
k_c	m s ⁻¹	Reaction coefficient of the cathode
l	m	Component or domain thickness
l_0	m	initial component or domain thickness
N_i	mol m ⁻² s	Ion flux density
N_M		MacMullin-Number
P_{stack}	Pa	Cell stack pressure
P_{dyn}	Pa	Stack pressure change
$P_{initial}$	Pa	Initial stack pressure
R	J mol ⁻¹ K ⁻¹	Gas constant 8.314 462 618 153 24
R_{cell}	mm	Radius of the cylindrical model
R_{comp}	mm	Radius of the compressed part of the cylindrical model
r_p	m	Particle radius
T	K	Temperature
T_0	K	Initial temperature
T_{ref}	K	Ambient temperature
t_+		Transference number
U_{OCV}	V	Open-circuit voltage
U_{cell}	V	cell voltage
x		Degree of lithiation of the anode
y		Degree of lithiation of the cathode
Indices		
a		Anodic reaction
c		Cathodic reaction
con		Heat conduction
$conv$		Heat convection
eff		effective parameter (Bruggeman correlation)
l		Liquid phase
neg		Negative electrode
pos		Positive electrode
s		Solid phase
sep		Separator
sur		Surface
$+$		Positive current collector
$-$		Negative current collector

^zE-mail: franz.spingler@tum.de

Table I. Characteristics of Kokam SLPB 356495 pouch cells used in this study.

Outer dimensions (LxWxH)	95 mm × 64 mm × 3.5 mm
Anode sheet size (LxWxH)	84 mm × 60 mm × 207 μm
Cathode sheet size (LxWxH)	82 mm × 58 mm × 149 μm
Current collector thickness	Anode: 11 μm/Cathode: 16 μm
Coating thickness	Anode: 98 μm/Cathode: 66.5 μm
Stack design	8 double-side coated anodes 7 double-side coated cathodes 2 single-side coated cathodes
Max. charge/discharge rate	1C/2C
Upper and lower cutoff volt.	4.2 V/3.0 V

In virtually all applications of lithium-ion batteries, the cell stack experiences variable amounts of mechanical pressure. A part of this pressure is provided by the encasing of cells: In the case of pouch cells, which are sealed at low absolute pressures of ca. 50 mbar, the atmospheric pressure acts on the cell surface through the pouch foil. This results in relatively uniform pressure on the faces with the exception of the stack edges, which can be more or less constrained depending on the deep-drawing process of the pouch bags and the sealing process during cell assembly. In the case of prismatic and cylindrical cells, the casing is more rigid at the edges than at the center of the faces or the circumferences. Additional mechanical load on the cells is caused by the module casing or results from the boundaries of the installation space itself, e.g., in cell phones. Due to the structural changes of the active materials in the electrodes during intercalation, which in state-of-the-art cells using graphite-based negative electrodes result in an expansion of the cell, the pressure acting on the cell stack varies with the state of charge (SOC). This raises two important questions: a) what is the optimum pressure on the cell stack and b) what are possible adverse effects of excessive amounts of pressure and of non-uniformly distributed pressure?

The question of the optimum stack pressure has been studied using pouch cells compressed between two rigid plates. Although the reported optimum varies between studies, some compression has consistently been found to be beneficial compared to no compression, and compression pressures of more than 1 MPa generally resulted in severe capacity fade rates.^{1–3} Other studies additionally investigated the effect of non-rigid bracing of pouch cells.^{4–6}

The effect of excessive and/or non-uniform pressure, which this paper is concerned with, has also been studied in the literature in various ways. Local lithium plating in cylindrical cells has been suspected to have resulted from irregularities in the jelly roll that led to pressure variations.^{7,8} Experiments of a pouch cell indented with a steel ball have also suggested a relationship between local compression and lithium plating.⁹ In several publications, the Arnold group of Princeton University has investigated the mechanical behavior of separators under compressive loads^{10,11} and the propensity of lithium plating due to localized separator pore closure resulting from extreme mechanical pressures up to 60 MPa.^{12,13}

In one of their papers,¹² coin cell experiments using separators with local pore closure and a two-dimensional model incorporating zero ion transport in a part of the separator provided experimental and theoretical proof of a high propensity of lithium plating at the edge areas where no ion transport through the separator takes place. In our own experiments, however, where the cell components' porosity was reduced but not eliminated by compression with a planar punch, lithium plating was found to be evenly distributed in the compressed area, not just at the edges. We consider this *local porosity reduction* scenario worthy of further investigation, as it may occur in cylindrical cells, as discussed above, or when a module of pouch cells is assembled incorrectly, containing foreign objects, etc.. It is difficult to assess the amount of pressure generated in these scenarios. As a first step, we aim to identify the magnitude of local pressure where lithium plating begins to occur.

In this work, a 2D-axisymmetric Newman-type model of a lithium-ion cell similar to that of Cannarella et al. is parameterized based on a Kokam SLPB 356495 pouch cell. We show that when ion transport is eliminated in a part of the separator, our model also predicts lithium plating at the edge of that area. Going from there, we have extended the model by a mechanical-electrochemical coupling mechanism to emulate our local compression experiment: In a part of the cell, the separator and electrode porosity are reduced according to an external force acting on the cell surface. The necessary mechanical parameters of the separator and electrodes are determined in additional experiments. Using this mechanical-electrochemical coupled model and a validation experiment, we show that the risk of lithium plating in compressed areas increases with the applied pressure. Obvious deposits on the anode can be found post-mortem after cycling at a local compression pressure of 3 MPa, while the first signs of deposits can be seen at 1 MPa.

This paper is structured as follows: In the experimental section, the local compression cycling experiment for pouch cells is presented, as well as the parameterization experiments for the modeling part, which consists of coin cell pseudo-OCV measurements with harvested electrode material and the measurement of pressure-compression relationships of electrodes and separator. The modeling part discusses the mechanical model, its coupling to the electrochemical model via the porosity-dependent ion transport, the model geometry and the parameterization and validity of the base model. The results and discussion part includes the discussion of the pressure-compression relationships of the cell components as well as the discussion of the model results which are compared to a post-mortem analysis of locally compressed and cycled pouch cells.

Experimental

Commercial pouch cells.—The cells used in this study were Kokam SLPB 356495 with a nominal capacity of 2.1 Ah, a pouch cell with stacked electrodes and Z-folded separator. Cell characteristics are displayed in Table I. Electrodes and separator taken from these cells were used for coin cells and mechanical characterization experiments. The cycling protocols are summarized in Table II.

Cell material harvesting, post-mortem inspection, coin cells.—Before cells were transferred to an argon-filled glove box for opening, fresh cells were discharged to 3.0 V and cycled cells were either discharged to 3.0 V or charged to 4.2 V. In all cases a constant current—constant voltage (CC-CV) protocol with a CC current corresponding to 0.1 C and a CV phase that ended when the current fell below 0.01 C was used. Disassembled electrode sheets and the separator from fresh cells were left to dry inside the glove box for a minimum of 24 h. To make samples for the compression tests, 15 mm discs were punched out from the unwashed electrode sheets using a handheld precision punch. For coin cells, 14 mm discs were made. The separator tapes were transferred out of the glove box and washed in isopropanol before 15 mm discs were punched out. The electrode sheets from cycled cells were photographed using an Inspec II digital microscope by Ash Technologies, Ireland. as soon

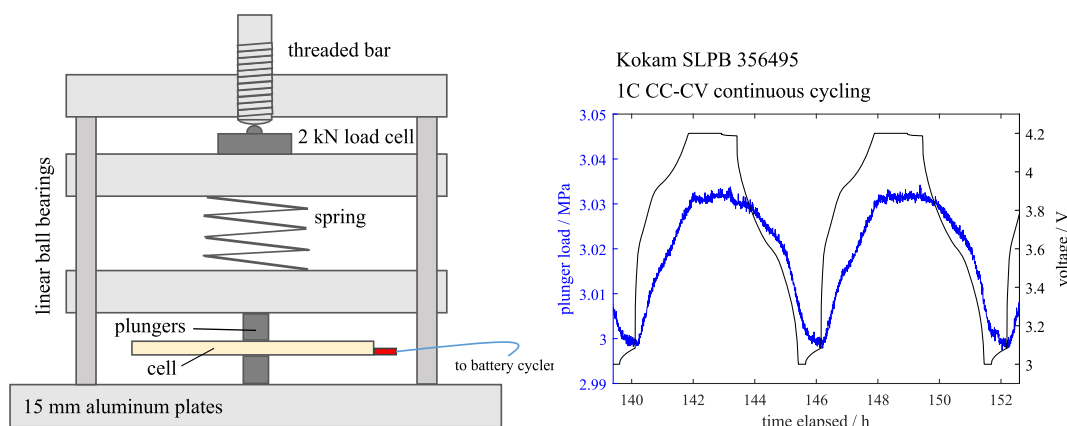


Figure 1. Schematic of the local compression setup. Two 14 mm diameter plungers act on the cell from both sides, loaded by a spring to achieve a compression with quasi-constant force. As illustrated by the right graph, the plunger load remains close to the set value during cycling of the cell.

Table II. Cycling conditions of coin cells and locally compressed pouch cells.

	Protocol	Termination	Local Pressure/MPa
Pouch cells			
Cycling	1C CC-CV	$I < C/20$	0, 10, 30, 60, 120
Capacity check-up	0.1 CC-CV	$I < C/100$	as above
Coin cells pseudo-OCV			
Anode	0.01C CC	10 mV/1.5 V	
Cathode	0.01C CC	3.0 V/4.3 V	

Table III. Specimen details for pressure-compression tests.

	No. of layers	Layer composition	Total thickness	Amount of DEC
Anode	60	coating/Cu foil/coating	19.9 mm	1.5 g
Cathode	60	coating/Al foil/coating	15.1 mm	1.0 g
Separator	100	—	1.5 mm	0.5 g

as the electrolyte solution had evaporated from the electrode surface, ca. 15 min after cell disassembly.

CR2032-type coin cells were built inside the glove box using two layers of 16 mm diameter VWR 691 glass fiber (thickness of 260 μm each) as the separator, the 14 mm harvested discs as the working electrode and a 15.6 mm lithium chip as the counter electrode. Two stainless steel spacers were used, 1×1.0 mm plus 1×0.5 mm. 80 μl of LP57 (3:7 wt. EC:EMC 1 mol LiPF_6) served as the electrolyte solution. Quasi-open circuit voltage (OCV) measurements were conducted at a C/100 rate using a CC charge, CC discharge protocol in a 25 °C temperature chamber.

Local compression cycle experiment.—A custom-built setup, shown in Fig. 1, was used to compress pouch cells locally while being cycled. Two 14 mm diameter plungers act on the cell from both sides, resulting in a compressed area of 1.54 cm^2 . The load is regulated via a threaded bar and a spring. The spring is relatively long, which helps minimize the load variation resulting from the SOC-dependent thickness changes of the cell. As can be seen in the graph on the right in Fig. 1, the plunger load varies by only 0.03 MPa or 1% during cycling. The plunger load is measured by a 2 kN load cell. A BaSyTec CTS served as the battery cycler.

Cells were compressed by 0.05 mpa, 1 mpa, 3 mpa, 6 mpa, and 12 mpa. After an initial charge-discharge cycle using a 0.1 C CC-CV protocol with a C/100 cutoff in both directions, the cells were cycled

100 times using a 1 C CC-CV protocol with a C/20 cutoff. At the end of the experiment, another cycle at 0.1 C was performed to assess the amount of capacity lost and to set the SOC for post-mortem inspection to 0% or, via an additional semicycle, to 100%.

Measurement of pressure-compression relationships.—Cylindrical specimens of 15 mm diameter were prepared from electrodes and separators harvested from discharged fresh cells opened in an argon-filled glove box. Each specimen contained only negative electrodes, positive electrodes, or separators, respectively. In order to improve the signal-to-noise ratio of the measurement, each specimen consisted of many layers stacked on top of each other, see details in Table III. The stacks were soaked in diethyl carbonate (DEC) and sealed in a pouch foil under a vacuum using a half-automated dosing/sealing apparatus in a vacuum chamber (Harro-Höfliger Verpackungsmaschinen GmbH). This was done to emulate the in situ configuration as closely as possible. DEC instead of an electrolyte solution was chosen for safety reasons.

The relationships between pressure and compression of these specimens were measured using an universal testing machine with a maximum load of 2 kN and a resolution of 0.0277 μm (ZwickRoell, Germany). A 0.5 mm thick stainless steel disc wrapped in pouch foil was used for reference measurements, which were of great importance due to the significant elastic deformation of the testing machine or the clamping jaws, as shown in Fig. 5 in the results section.

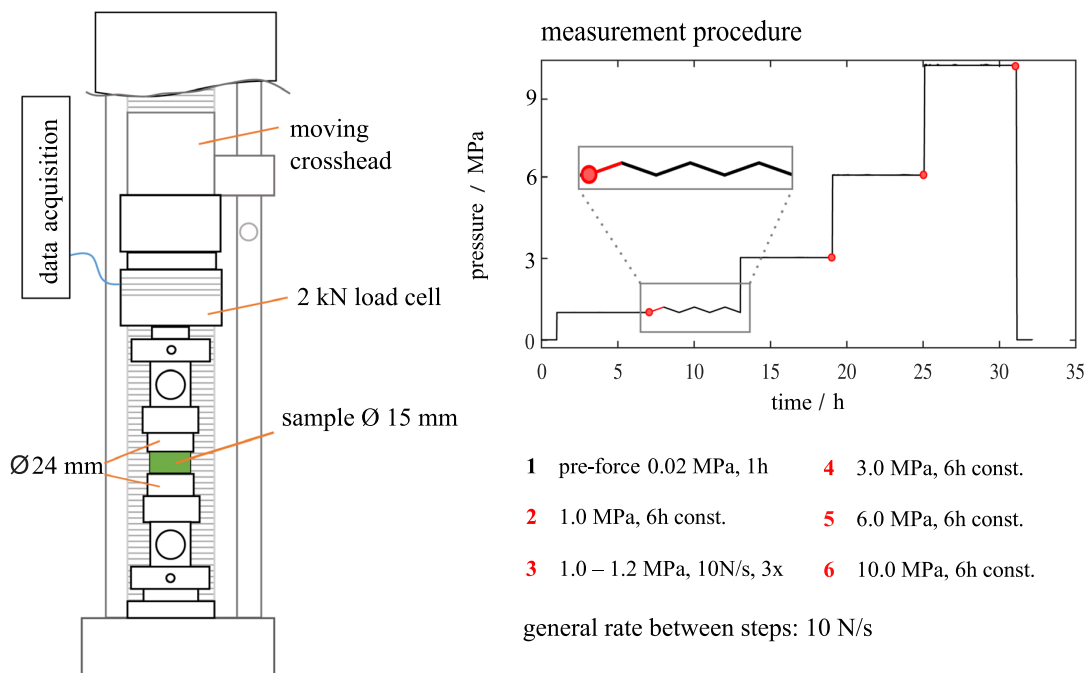


Figure 2. Schematic of the universal testing machine used to measure the load vs compression characteristics of electrodes and the separator of the Kokam cell. The graph illustrates the measurement procedure. The red dots indicate the data points which were used to parameterize the mechanical model.

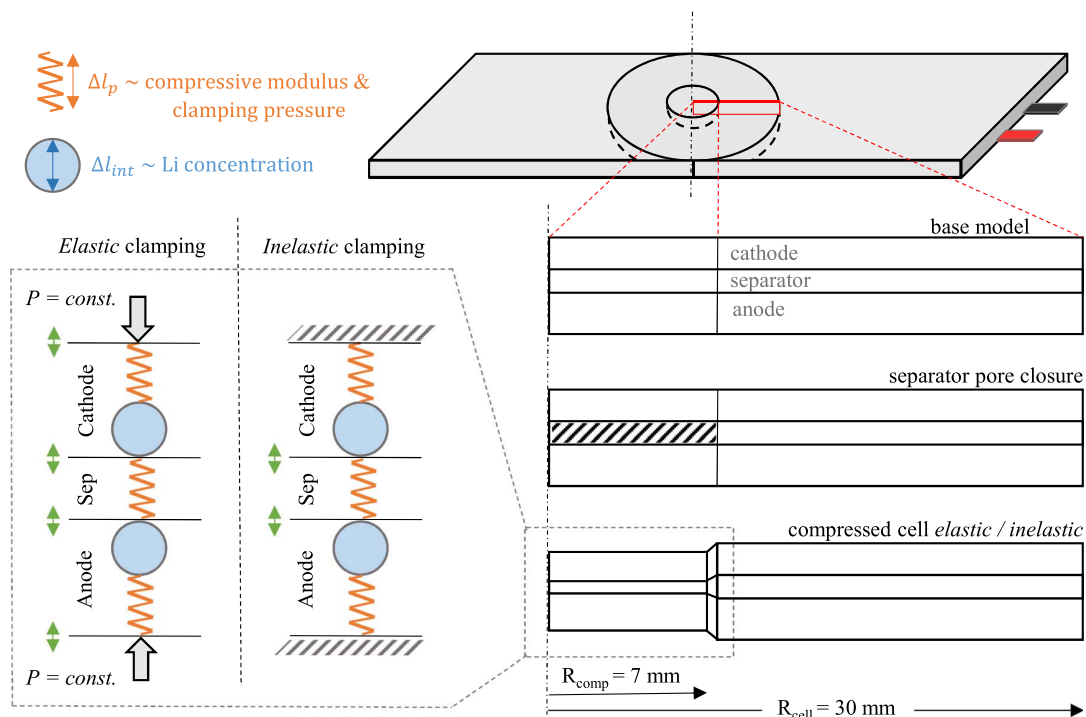


Figure 3. Schematic of the mechanical model of electrodes and the separator. The orange springs represent the elastic characteristics of electrodes and the separator. The blue spheres represent the lithium concentration-dependent volume change of the active material particles, which, for simplicity, is assumed to be independent of the mechanical pressure acting on them. Any change in Δl_p will change the porosity of the component. Two different boundary conditions are implemented: a constant external force/pressure (“elastic clamping”) and a fixed support (“inelastic clamping”). The green double arrows indicate the movable component boundaries.

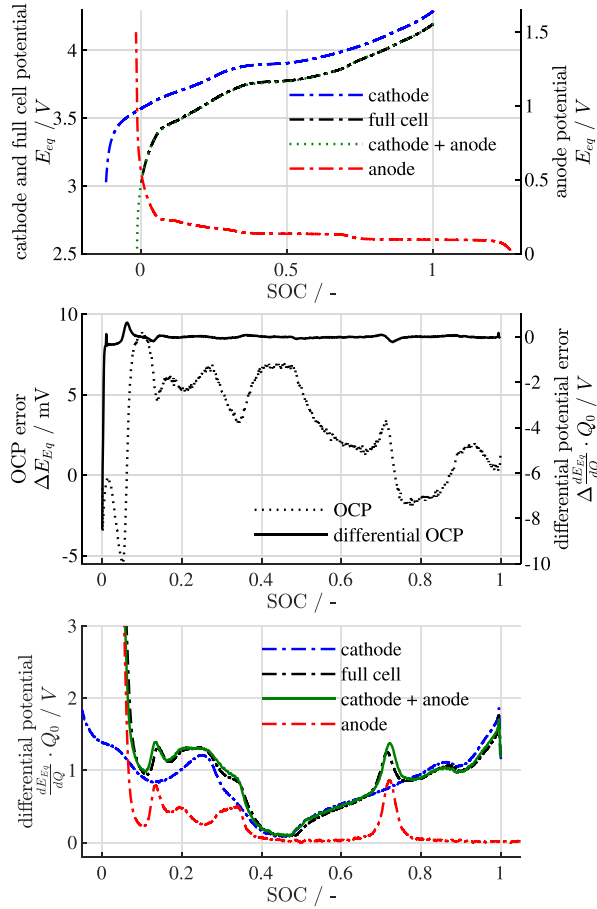


Figure 4. Top: Quasi-OCV characteristics of the Kokam anodes and cathodes from coin cell measurements of harvested electrodes, superpositioned and shifted relative to each other to match the full cell characteristic. Middle: Deviation between the reconstructed OCV and the full cell. Bottom: Differentials of the quasi-OCV characteristics with coinciding peaks of reconstructed OCV and full cell. All potentials are relative to Li/Li^+ .

Figure 2 shows a schematic of the testing machine and an overview of the measurement procedures. The main data points or Sections which were later analyzed are marked in red. Preliminary tests had shown that the compression characteristics of all cell components are highly non-linear, i.e., that the rate of compression is dependent on the rate of the force increase, and that creep plays an important role. In practical applications, lithium-ion batteries are likely to experience compression over longer time spans, so that the material behavior under static loads should be taken into consideration. Accordingly, the experiment was set up as follows: After applying a pre-force of 6 N or 0.02 MPa for 1 h, the force was increased stepwise to the equivalents of 1 MPa, 3 MPa, 6 MPa and 10 MPa, each increase followed by 6 h constant pressure periods. Additionally, at the end of the rest period at 1 MPa, three up-and-down cycles to a pressure of 1.2 MPa were conducted to study the dynamic compression characteristic during cycling after a long-term constant-pressure compression. The choice of a cyclic alternation by 0.2 MPa was informed by preliminary full-cell compression experiments, cf. Figure 13 in Appendix C. All force changes were conducted at a rate of 10 N s^{-1} . After the final 6 h rest period at 10 MPa, the force was decreased again to 0.02 MPa. These stepwise measurements were complemented by continuous measurements between 0.02 MPa and 10 MPa at a rate of 10 N s^{-1} .

Electrochemical-Mechanical Modeling

The electrochemical model used in this work is based on an axisymmetric p3D version of the well-known Newman-type p2D model¹⁴ implemented in COMSOL Multiphysics. In this p3D model, the principal equations are solved in two dimensions instead of one, plus a third pseudo-dimension in which transport inside of the active material particles is calculated. The base model equations are summarized in Appendix A, Table V. The modifications added to the model in this work and the parameterization based on the Kokam pouch cell are described in this section.

Mechanical model of electrodes and separator.—When a lithium-ion cell is subject to mechanical pressure, the electrodes and the separator will get compressed, resulting in a porosity decrease. This leads to the slower transport of ions across the cell. The simplified mechanical cell model illustrated in Fig. 3 was conceived to link the clamping pressure to the porosity change via the compressive moduli/compression-pressure relationships of the electrodes and the separator and the lithium concentration-dependent volume changes of the active material particles. This model is not a realistic representation of the underlying physics but rather a mechanical analogue to an electrical equivalent-circuit model. It is intended for estimating the porosity changes in the cell based on experimentally accessible quantities. To this end, the electrodes are represented by a “soft” element which contains all of the porosity and whose size is determined by the experimentally determined compression-pressure relationships and the clamping pressure, and a “hard” element, whose size follows the experimentally determined electrode dilation characteristic. If the cell is fixated between two rigid plates (“inelastic clamping”), an expansion of the “hard” element will further compress the “soft” element and the clamping pressure will increase. If the cell is subjected to a constant external pressure (“elastic clamping”), the expansion of the “hard” element will lead to an expansion of the respective electrode, but will not cause a porosity change because the “soft” element will not experience a change in mechanical pressure.

The mechanical model is implemented in COMSOL as follows. The thickness change portion of each component i (cathode/separator/anode) due to the stack pressure (the “soft” element) is:

$$\Delta l_{p,i} = l_{i,0} \cdot \varepsilon(P_{stack}) \quad [1]$$

where ε is the relative compression and $P_{stack} = P_{dyn} + P_{initial}$, $P_{initial}$ being the initial clamping pressure and P_{dyn} the clamping pressure change during cycling. The thickness change portion of cathode/anode due to intercalation (the “hard” element) is:

$$\Delta l_{int,i} = l_{i,0} \cdot \left(\int_0^l \Delta V_p \left(\frac{c_s}{c_{s,max}} \right) dy - \Delta V_p \left(\frac{c_{s,0}}{c_{s,max}} \right) \right) \quad [2]$$

where ΔV_p is the relative volume change over the lithiation degree of the cathode and anode, respectively, in sum define the total thickness change of each domain:

$$\Delta l_{cathode} = \Delta l_{p,cathode} + \Delta l_{int,cathode} \quad [3]$$

$$\Delta l_{anode} = \Delta l_{p,anode} + \Delta l_{int,anode} \quad [4]$$

$$\Delta l_{sep} = \Delta l_{p,sep} \quad [5]$$

with the exception of the separator, which has no intercalation driven thickness change. Finally, the elastic and inelastic scenarios are implemented via two different boundary conditions. In the elastic

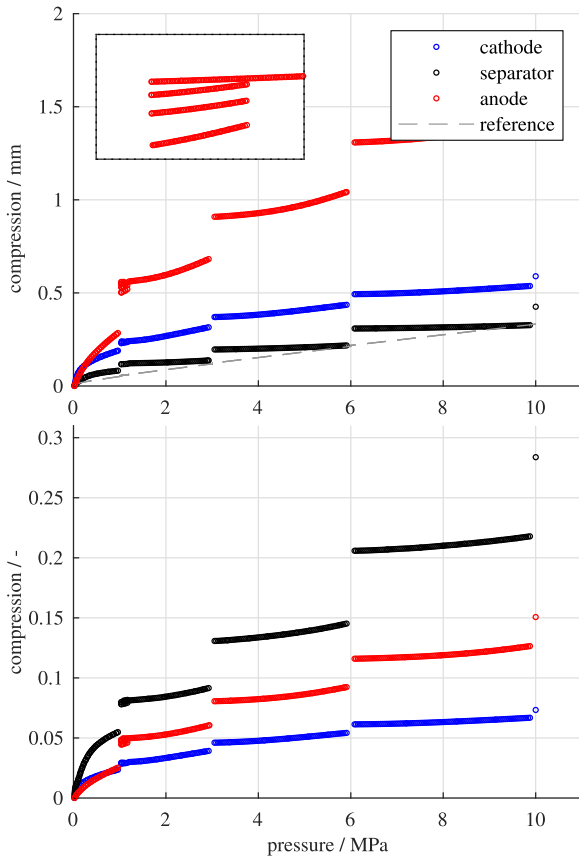


Figure 5. Absolute and relative compression of electrode and separator specimens (cf. Table III) during stepwise compression tests using the measurement procedure detailed in Fig. 2. The gray dashed line is the reference, obtained from a test with a 0.5 mm stainless steel disc wrapped in pouch foil. The gaps between the curves correspond to the creep during the 6 h constant pressure periods. The separator specimen experiences the largest relative compression, followed by the anode and cathode. The zoom plot shows the three load phases between 1 MPa and 1.2 MPa.

scenario the stack pressure is constant:

$$P_{dyn} = 0 \text{ MPa} \quad [6]$$

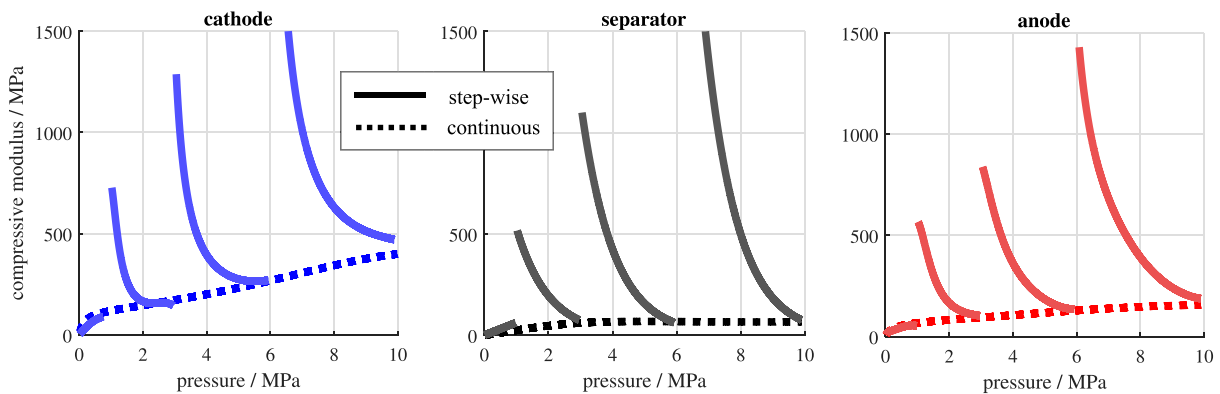


Figure 6. Compressive moduli of electrode and separator specimens from stepwise and continuous experiments. After the 6 h constant-pressure periods, the compressive moduli from the stepwise experiments are initially very high but subsequently approach those obtained from continuous experiments.

In the inelastic scenario the cell cannot expand, therefore the sum of all thickness changes must be zero:

$$0 = \Delta l_{sep}(P_{stack}) + \Delta l_{cathode}(P_{stack}) + \Delta l_{anode}(P_{stack}) \quad [7]$$

The coupling of the mechanical model to the electrochemical model is achieved via the porosity and tortuosity-dependent effective ion transport. All of the compression of the components is assumed to occur at the expense of the porosity, i.e., the bulk materials are assumed to be incompressible. As in Sauerteig et al.,¹⁵ it is further assumed that the porosity of the components decreases linearly with compression. This is equivalent to assuming that the shape of the pores remains unchanged while they shrink. The resulting porosity or liquid volume fraction is:

$$\xi_l = \frac{\xi_{l,0} \cdot l_i/l_{i,0}}{1 - l_i/l_{i,0}} \quad [8]$$

In imitation of the Bruggeman relationship,¹⁶ the effective ion diffusivity and conductivity are calculated based on ξ_l and the Bruggeman-exponent α :

$$D_{l,eff} = D_l \cdot (\xi_l)^{\alpha+1} \quad [9]$$

$$\kappa_{l,eff} = \kappa_l \cdot (\xi_l)^{\alpha+1} \quad [10]$$

Model geometry and model setups.—As displayed in Fig. 3, the model geometry is a cylinder slice whose radius is equal to half of the width of the Kokam pouch cell. The inner part of the cylinder represents the compressed cell area, the outer part represents the uncompressed cell area. This model design guarantees a close representation of the experiment, as only the outer edges of the cell, which are far away from the compressed/uncompressed transition, are excluded from the model. Since the one-sided alteration of the effective ion transport leads to lateral current flow in the cell, the ratio of through-plane and in-plane dimensions is a critical parameter. Therefore, the model geometry reflects the full dimensions of the Kokam cell, resulting in a total length of 30,000 μ m. The large one-time computational effort that this approach involves is uncritical here.

Three different setups of the model are implemented: 1) A base model, where the inner part is equal to the outer, uncompressed part. This base model is used for the electrochemical parameterization and validation against the voltage characteristic of the Kokam pouch cell. 2) Separator pore closure in the inner part, i.e., no ion transport in the separator domain, in analogy to and for comparison with Cannarella et al.¹² 3) The main model for the simulation of the local

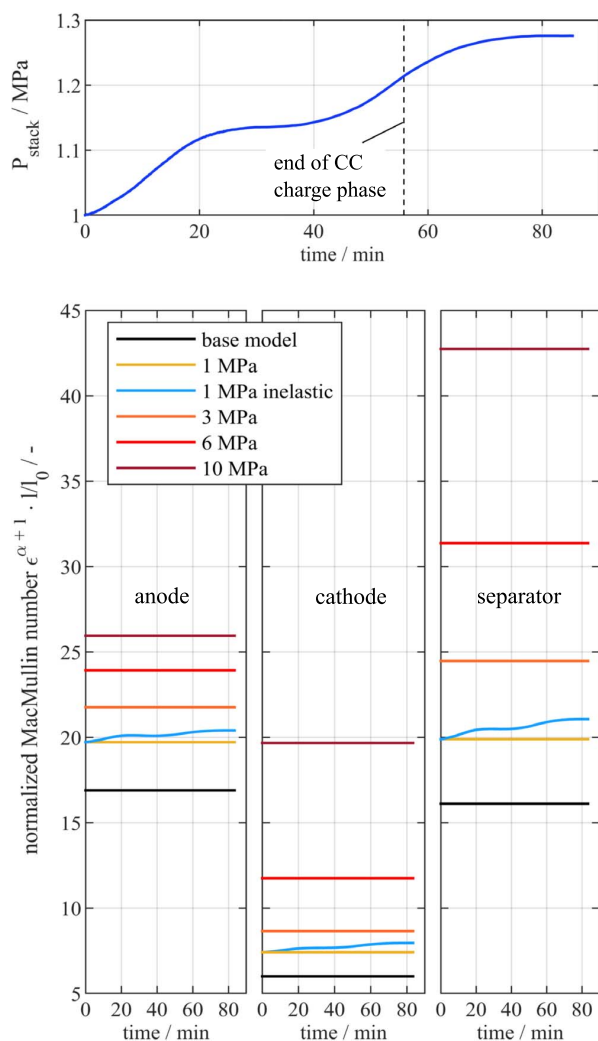


Figure 7. Top: Stack pressure increase during 1C CC-CV charging in the inelastic clamping scenario. Bottom: MacMullin numbers of electrodes and separator (normalized to the change of their individual thicknesses). As a result of its relative stiffness, the MacMullin number of the cathode is the least affected by pressure. The separator, which is the softest component, shows a 3-fold increase of the MacMullin number. In accordance with the stack pressure increase, the MacMullin numbers in the inelastic case increase slightly during charging.

compression experiment in the two variants a) elastic clamping and b) inelastic clamping.

Model parameterization.—The electrochemical model is parameterized using quasi-OCV voltage characteristics of the positive and negative electrodes extracted from the Kokam pouch cell, see Fig. 4a. Differential voltage analysis (DVA) is used to identify the active intervals of both voltage characteristics: The characteristic peaks visible in Fig. 4c help define the relative positions or overlap of the negative and positive voltage profiles in the model. The deviation of the resulting model OCV characteristic to a quasi-OCV of the Kokam cell (C/100 charge characteristic) is in the single-digit mV-range, as shown in Fig. 4b. Most electrode, kinetic, and transport parameters which govern the model behavior during charge and discharge were taken from the scientific literature, most notably from Ecker et al.,¹⁷ who determined a large number

of electrochemical parameters for a similar Kokam cell. The Bruggeman exponents were used as fitting parameters while it was taken care that the resulting MacMullin numbers were within reasonable bounds.¹⁸ All of the parameters are listed in Table VI in Appendix B.

The electrode expansion as a function of the degree of lithiation, ΔV_p , is determined via electrochemical dilatometry. For a detailed description of the instrument and the experimental procedures, the reader is referred to an earlier publication of ours¹⁹. The expansion characteristics of the Kokam cell are shown in Fig. 12 in Appendix B. They are implemented as a look-up table in COMSOL. The pressure-compression relationships and compressive moduli of the Kokam cell components shown in the results Section are implemented as look-up tables, too.

Results: Pressure-Compression Tests of Cell Components

This chapter covers the results from the pressure-compression tests of the separate cathode, separator and anode specimens described in Table III. As discussed in the experimental section, a stepwise procedure was used with 6 h constant pressure phases to account for the significant creep of the cell components under load. First, the immediate results from the mechanical testing is discussed, i.e., the absolute and relative compressions of specimens and the reference measurements. Thereafter, compressive moduli calculated from the measurement data will be presented and compared to literature values. For a better comparison to existing studies, the compressive moduli are derived not only from the stepwise measurement but also from a complementary, continuous measurement.

Compression-pressure relationships of cell components.—The top graph in Fig. 5 shows the referenced, absolute compressions of cathode, separator, and anode specimens and of the reference as a function of the applied pressure. The gaps between the curves correspond to the creep during the 6 h constant pressure periods. The final compressions at the end of the 6 h period at 10 MPa are marked by single circles. The reference specimen is a 0.5 mm stainless steel disc wrapped in pouch foil. Most of the ca. 0.35 mm relative movement of the clamping jaws recorded between 0 MPa and 10 MPa is therefore likely to result from a deformation of the clamping jaws themselves. It is important to note that the (referenced) compression of the 100-layer separator specimen, ca. 0.42 mm, is only slightly larger than the reference deformation. This means that the separator compression results need to be interpreted with prudence and it underlines the importance of taking the testing machine deformation into account when performing compression tests. Generally, it stands out that the first load segments exhibit a convex shape, i.e., strain-hardening behavior, while the other load segments have concave shapes, i.e., a strain-softening behavior. This may be caused by the fact that these load segments are preceded by 6 h constant pressure periods during which the materials creep considerably, exhausting a large portion of the potential viscoelastic compression of the respective load range. It is possible that when the compressive load is again considerably increased, additional viscoelastic and plastic responses are triggered.

The zoom plot showcases the three 1 h load phases between 1 MPa and 1.2 MPa of the anode—the characteristics are similar for the cathode and the separator: 1) The curves are concave, as discussed above for the other load segments, but flatten with every repetition. 2) The creep portion of the strain is considerable, causing the strain to increase even during the load reduction phases (not plotted). The third load phase was used to parameterize the inelastic clamping model.

Compressive moduli.—The compressive modulus K is the derivative of an infinitesimal increase of compressive pressure P with respect to the resulting infinitesimal strain ϵ resulting from it:²⁰

$$K = \frac{\partial P}{\partial \varepsilon(P)} \quad [11]$$

To calculate the compressive moduli, both specimen and reference measurement data were fitted to polynomial functions which were then subtracted from each other. The obtained functions were analytically differentiated. The curve fitting implicated deviations at the data set edges, which are partly responsible for extremely high moduli at the beginning of load increase phases.

Figure 6 shows the compressive moduli of the electrodes and the separator obtained from the stepwise experiment as well as from complementary, continuous experiments. As discussed in the above paragraph, the materials show a strain-softening behavior in the load increase segments after the 6 h constant pressure periods, which translates into very high initial compressive moduli which subsequently subside. With increasing load and compression, the magnitude of the initial compressive moduli increases. Towards the end of each load increase segment, the compressive moduli from the stepwise experiment approach those obtained from continuous measurements. The results from the continuous experiments qualitatively agree with Sauerteig et al.¹⁵ The compressive moduli of all components increase with pressure, but at a decreasing rate. The cathode is the stiffest component, followed by the anode and the separator. Quantitatively, our results and those of Sauerteig et al., who investigated pressures up to 5 MPa, compare as follows: At 5 MPa, Sauerteig et al. found values ca. 8% higher for their cathode, 25% higher for their anode, and 30% lower for their separator. These deviations may have originated from different electrode compositions, coating thicknesses, porosities and separator designs.

While the good agreement between the two studies speaks to the validity of the general experimental approach, the dependency of the compressive moduli at a given load level on the load history deserves attention. It may be that the long-time mechanical characteristics of cell components which are important in application cannot be adequately captured in these relatively short experiments.

Results: Simulation and Experiments of a Locally Compressed Cell

In the following, 1C charging simulations and experiments of the locally compressed Kokam cells are compared. The charging current of 1C was kept constant in all simulations and experiments and is based on the nominal capacity of 2.1 Ah, i.e., it was not adjusted for the reduced utilization in the compressed areas. In any case the differences would be negligible: The share of the compressed area is 3.2% in the experiments and 5.4% in the model. The latter is higher because the model dimensions correspond to the largest round slice which could be fitted within the rectangular pouch cell, leaving out the edges. After a discussion of the effects of the cell compression on the effective transport properties expressed by the MacMullin

number, the effect of the local compression is assessed in terms of the local electrode potential vs a virtual lithium reference adjacent to the electrode and immersed in the electrolyte, $\phi_s - \phi_l$, which indicates that lithium plating is thermodynamically favorable when it falls below zero. The magnitude of $\phi_s - \phi_l$ does not serve as a quantitative indicator of the amount of plated lithium, but the more negative it becomes and the longer it stays negative, the larger is the amount of lithium expected to be plated.

The effect of compression on the effective ion transport.—The degree to which each component of the cell is compressed upon the local application of pressure is calculated in the simulation by solving the implicit Eq. 7, which incorporates the experimentally determined pressure-compression relationships. The reduction of the components' porosities is assumed to be proportional to their degree of compression. The resulting MacMullin numbers $N_M = \kappa_i / \kappa_{i,eff}$, multiplied by the components relative thickness reduction to reflect the overall impact on the ion transport in through-layer direction, are shown in Fig. 7 (bottom) for the different investigated pressure levels. The base model MacMullin numbers are comparable to experimentally obtained values by other researchers for comparable materials.¹⁸ With pressure, the calculated MacMullin numbers increase substantially. For the separator, which is the softest component, a 3-fold increase takes place between zero compression and 10 MPa. The anode, for which a similar Bruggeman exponent is assumed as for the separator (cf. Table VI, Appendix B) but which is more rigid, shows a slightly smaller increase. The cathode is the most rigid component and thus displays the least increase of the MacMullin number with pressure. These results agree reasonably well with an experimental determination of ionic resistances of compressed cell components by Sauerteig et al.¹⁵ For a ceramic coated PE separator, they found an increase of ca. 60% between 0.36 MPa and 5.0 MPa, which compares well to the increase of ca. 60% between 1 MPa and 6 MPa shown in Fig. 7. With reference to the same pressure ranges, they reported an increase of 42% vs our 57% for the graphite anode and 14% vs our 20% for the cathode. The local stack pressure increase during charging in the inelastic clamping scenario is shown in Fig. 7 (top). The shape of the increase with its plateau at 30 min or mid-SOC resembles the anode's thickness change characteristic which is shown in Fig. 12 in Appendix B. The stack pressure, initially set to 1 MPa, increases to 1.28 MPa at the end of charge. This agrees well with a validation experiment in which the Kokam cell was cycled while being compressed on its entire surface using a rigid clamping setup. In the experiment, the pressure increased to 1.30 MPa. Details are provided in Fig. 13 in Appendix C.

Base model and local separator pore closure.—In the study by Cannarella et al.¹² mentioned in the introduction, the effect of closed pores in the separator was simulated by removing parts of the separator domain from the model so that ionic currents would be

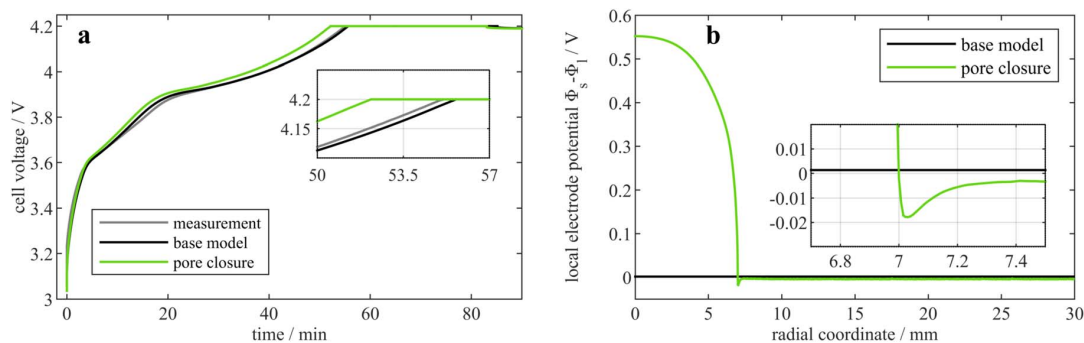


Figure 8. (a) Cell voltage from the experiment and simulated using the base model and the separator pore closure model. (b) Local electrode potentials at the negative electrode/separator interface at the end of the CC phase. At the edge of the pore closure area of the cell, the potential dips to -18 mV. In the pore closure area, the local potential is much higher than in the rest of the cell.

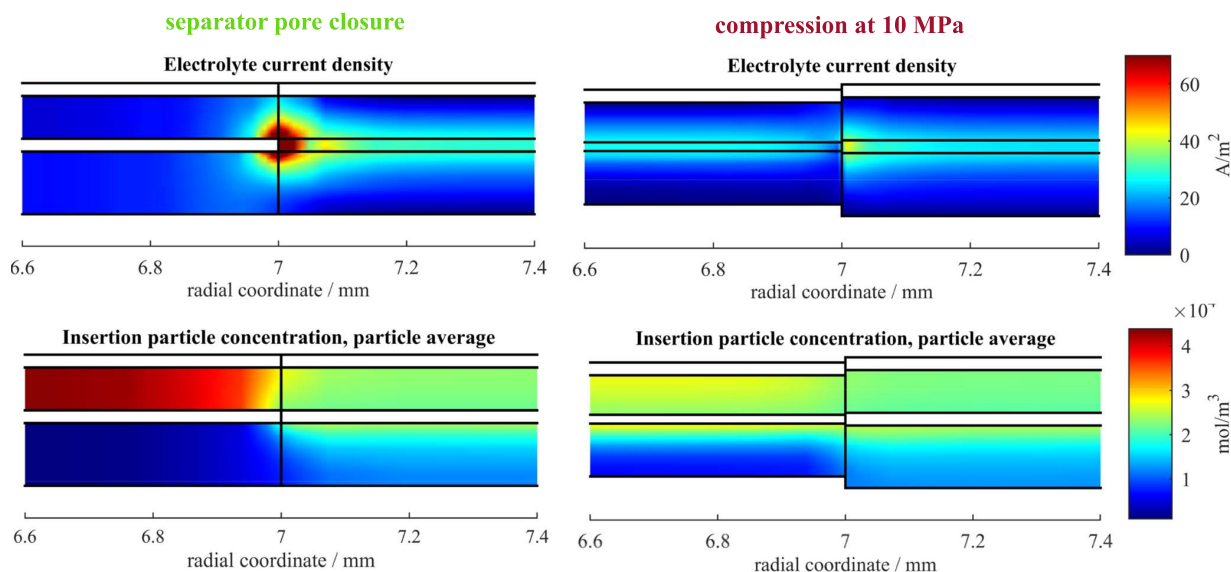


Figure 9. Top: Electrolyte current density distributions at the end of the 1C CC charging phase in the pore closure case and for a compression at 10 MPa. In the separator pore closure case, local current densities reach extreme values. Bottom: Distribution of the lithium concentration in the active material particles. The part of the negative electrode under the area of closed pores in the separator remains almost un lithiated. All graphs show the end of the CC phase. Note that only a small area around the boundary of the unmodified and modified cell part is displayed.

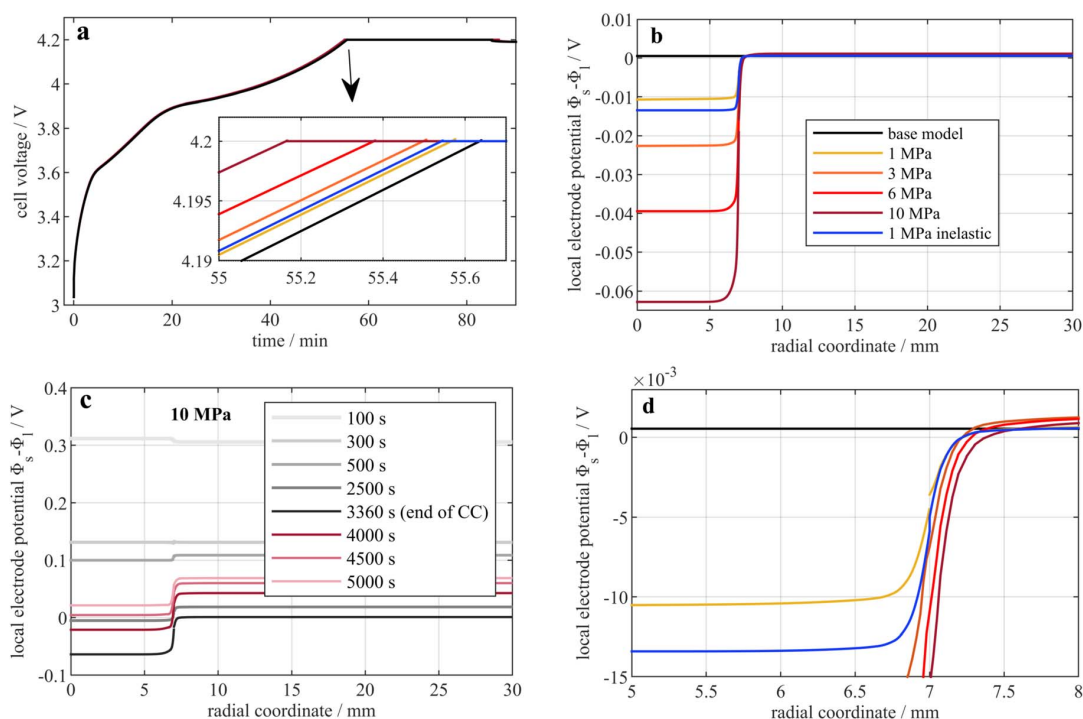


Figure 10. Local electrode potential at the end of the 1C CC charge phase for different compression scenarios. (a) Local pore closure: At the boundary with the unaltered area of the cell, the potential dips to -18 mV. In the pore closure area, the local potential is much higher than in the rest of the cell. (b), (d) Local elastic and inelastic compression: Depending on the pressure, the potential falls to between -11 mV and -65 mV and is quite constant across the compressed area. (c) Evolution of the local electrode potential at 10 MPa compression over time.

impeded in these areas. As a reference for comparison to the local compression scenario, this model configuration was replicated and is shown in the "separator pore closure" model schematic in Fig. 3. Figure 8a shows the simulated cell voltage during 1C CC-CV charging using the base model and the separator pore closure model

along with the measured cell voltage during 1C CC-CV charging of the Kokam cell. It can be seen that the base model characteristic agrees well with the measurement. As expected, the partial removal of the separator domain increases the cell polarization and as a result, the end of the CC phase is reached 3 min earlier. Figure 8b

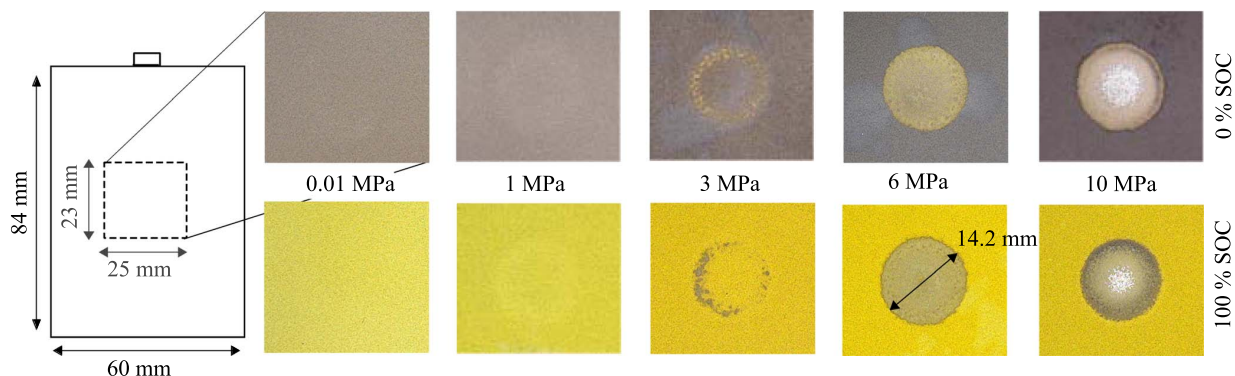


Figure 11. Post-mortem photographs of the anode surfaces of 10 different cells opened at 0% SOC or 100% SOC after 100 cycles/1C while exposed to local pressures ranging from 0.01 MPa to 10 MPa. Of each cell, the first anode layer from the stack is shown. At 0.01 MPa, the electrode surface is uniform. At 1 MPa, a slight discoloring in the compressed area is visible. At 3 MPa, there are depositions at the inner edges, but not in the center. At 6 MPa, the entire compressed area is covered with depositions. At 10 MPa there is an additional, glittering, silver-colored circle at the center of the compressed area.

Table IV. Simulated charging times to reach the upper cutoff voltage and the first occurrence of a negative anode potential as a function of the local pressure.

Scenario	0 MPa	1 MPa	1 MPa inelastic	3 MPa	6 MPa	10 MPa	pore closure
Time to 4.2 V	3339 s	3333 s	3331 s	3330 s	3322 s	3310 s	3132 s
Time to $\phi_s - \phi_l < 0$	—	3080 s	3000 s	2770 s	2530 s	2370 s	2740 s
Voltage when $\phi_s - \phi_l < 0$	—	4.14 V	4.12 V	4.07 V	4.03 V	4.01 V	4.10 V
Duration of $\phi_s - \phi_l < 0$	—	360 s	470 s	830 s	1340 s	1980 s	650 s
Minimum $\phi_s - \phi_l$	0.5 mV	-10 mV	-13 mV	-22 mV	-40 mV	-62 mV	-19 mV

shows the local electrode potentials at the anode/separator interface at the end of the CC phase as a function of the radial coordinate. The end of the CC phase generally corresponds to the minima of these potentials during CC-CV charging. At the center of the pore closure area the local electrode potential is high because the current density there is suppressed. However, there is a localized dip of ca. -18 mV at the boundary caused by a peak in current density: Additional lithium-ions from the pore closure area travel around the edge through the "intact" separator. The characteristic is fully consistent with Cannarella et al.

Local cell stack compression compared with local separator pore closure.—The effect of a local compression of the cell, including both electrodes and the separator, is quite different from a local pore closure in the separator. First of all, as shown in Fig. 10a, the overall cell polarization is lower. Even at a local compression of 10 MPa, the end of the CC-phase is reached only 0.5 min earlier than in the base case. This is because the flow of current is reduced due to the porosity decreases resulting from the compression but not impeded completely as in the separator pore closure scenario. The electrolyte current density distributions in the neighborhood of the boundary between the modified/non-modified part of the cell, shown in the top graphs of Fig. 9 illustrate the difference well: The current density in the area of the electrodes without the separator domain is low, except for an area of ca. 0.1 mm from both sides of the boundary, where it is extremely high (the color scale value range has been cut off at 70 A m^{-2} for better comparison between the two scenarios, the actual maximum in that area is 140 A m^{-2}) as the ions travel around the obstruction. In contrast, in the case of a local compression at 10 MPa, almost the same current density can be observed in the affected areas as in the rest of the cell. The phenomenon of a localized current density peak next to the boundary can be observed also, but it is much less extreme.

The reduced current density in the compressed area is reflected by the local electrode potential at the negative electrode/separator

interface, Fig. 10c, which is initially higher in the compressed area than in the rest of the cell (light gray line, 100 s into the charging phase). As the charging progresses, however, the local potential in the compressed area falls more rapidly than in the rest of the cell: The incoming charge accumulates at the top of the negative electrode disproportionately because mass transport into the depth of the negative electrode, too, is limited by the reduced porosity. After 2500 s, the local potential reaches negative values and at the end of the CC-phase, it reaches its minimum of -62 mV. Correspondingly, the insertion particle concentration at the end of the CC-phase, Fig. 9 bottom-right, has a larger through-plane gradient and higher values at the top of the electrode in the compressed area. Only after ca. 4500 s, well into the CV-phase, do those concentration differences subside enough for the local potential to become positive again.

The influence of the local compression pressure on the minimal electrode potential (at the end of the CC charge phase) is shown in Fig. 10b. In the base model, which serves as a reference, the potential at the top of the negative electrode stays above 0.5 mV. The minimum electrode potential correlates with the local compression pressure: Already at 1 MPa, the potential reaches a minimum of -10 mV. In the inelastic scenario with an initial compression of 1 MPa, the electrode potential is slightly lower at -13 mV. 3 MPa and 6 MPa of compression pressure result in -22 mV and -40 mV minimum potentials.

Table IV summarizes the minimum electrode potentials, the duration of negative potentials, and the corresponding cell voltages of each scenario. Interestingly, at 3 MPa and higher, the minimum electrode potential is lower and the negative potentials persist for a longer time than in the pore closure scenario, suggesting more severe lithium plating.

Experimental validation.—To validate the modeling results discussed above, the local elastic compression scenario was replicated in an experiment. Using the custom-built setup detailed in the experimental section, an area of 1.54 cm^{-2} in the center of the

Kokam cell was compressed by a flat piston during charge-discharge cycling at 1 C CC-CV. The same pressure levels were investigated as in the simulation. The cells were cycled for 100 times so that the effect of lithium plating would become clearly visible. A single charging event, even if severe lithium plating occurred, is unlikely to produce a clearly visible deposition pattern because large parts of the plated lithium get stripped near the end of charge or afterwards.^{21,22} Upon completion of the 100 cycles, the cells were either fully discharged or charged and then opened in an argon environment. Figure 11 shows the post-mortem photographs. Since there was some variation of the deposition pattern within each cell stack, all photographs show the first anode layer of a given stack for consistency. Although temperature measurements under the piston and on the cell surface next to the piston showed no significant differences, the reference experiment was conducted with the piston touching the cell surface (with a pressure of 0.01 MPa) to rule out the possibility that lithium plating could also be provoked by the piston conducting heat away from the cell surface and not mainly result from the compression. The anode surface after the 0.01 MPa experiment looked uniform. At 1 MPa, a slight discoloring in the compressed area can be discerned, but it may well be a result of the compression itself, and not of lithium depositions. At 3 MPa, there are clear depositions at the inner edges, but not in the center. At 6 MPa, the entire compressed area is covered with depositions that appear yellow/gold in the images from delithiated anodes and more grayish in the lithiated anodes. At 10 MPa there is a distinct circle at the center of the disposition area with an agglomeration of individual silver-colored particles, which may indicate a more severe form of lithium plating. In the sense that the severity of lithium plating increases with compression, the overall qualitative picture of the experimental results matches the modeling predictions well. The overall diameter of the dispositions is ca. 14.2 mm, slightly larger than the piston which has a diameter of 14.0 mm. In the simulation, too, the perturbation caused by the compression could still be observed 0.1 mm to 0.2 mm away from the compressed area. In contrast to the experimental results, however, the model does not suggest a shifting of the risk of lithium plating from near the edges of the compressed area toward the center of the compressed area with increasing pressure.

Conclusions

The effects of a localized compression of a lithium-ion battery were investigated with a combination of experimental and modeling approaches. First, an axisymmetric p3D cell model was parameterized on the basis of a 2.1 Ah Kokam SLPB 356495 pouch cell and validated using experimental data. This electrochemical model was then complemented by a simplistic mechanical model which incorporates experimentally determined compression-pressure relationships of both electrodes and the separator and SOC-dependent electrode dilation curves and allows the definition of constant pressure ("elastic clamping") or zero displacement ("inelastic clamping") boundary conditions. The mechanical model output, the porosity of each cell component, feeds back into the electrochemical model via an effective mass transport expression.

The mechanical model could not be validated in a straightforward way because the cell components porosities are difficult to access experimentally during operation. However, the calculated pressure buildup in the course of a full charge in the inelastic clamping scenario matched well with a separate full cell experiment, which speaks to the adequacy of the model.

Using the electrochemical-mechanical model, the effects of local compression pressures up to 10 MPa on the current density distribution, on concentration gradients, and on the occurrence of negative local electrode potentials were studied. The latter were

taken as an indicator of the propensity of lithium plating. In a validation experiment where the Kokam pouch cell was locally compressed according to the simulated scenarios and cycled at 1C, the existence of depositions on the negative electrode could be verified. The location and intensity of those depositions agreed qualitatively with the model predictions of the local electrode potential.

The actual deposition process of lithium, e.g., with a film thickness as an output, was not included in the model. Presumably, the deposition of lithium in a mechanically restrained cell would have a self-reinforcing effect due to an additional pressure buildup which may be caused by the extra space requirement when lithium is deposited on, rather than intercalated into, graphite electrodes.²³

From an academic point of view, this study expanded on the work by Cannarella et al. by analyzing the differences between the effects of a local, complete ion transport blockage in the separator and a local ion transport reduction in both the separator and electrodes resulting from a compression of the cell stack on the current density distribution around the local anomaly. The combined modeling and experimental approach was shown to be able to reveal the cause and effect relationships between non-uniform compression and localized lithium plating and to enable the assessment of the lithium plating risk in commercial lithium-ion cells.

In practical terms, it was demonstrated that non-uniform compression of a cell stack, which could be caused by foreign objects inside module assemblies that indent the surface of pouch cells or by uneven stiffness of the cell casing in the case of cylindrical and prismatic cells, carries the risk of localized lithium plating if the resulting compressive pressures exceed a certain limit, in the case of the commercial cell used in this study, ca. 1 MPa. With cells that are more optimized for specific energy via thicker or more dense electrodes, this threshold may be significantly lower.

Acknowledgments

This work was financially supported by the German Federal Ministry of Education and Research (BMBF) in the projects ExZellTUM II (03XP0081) and ExZellTUM III (03XP0255) and by the Technical University of Munich. The responsibility for this publication rests with the authors.

Appendix A. Model Equations

Table V. Principal equations of the axisymmetric Newman-type model.

Mass balance ^{a)}	$\xi_l \frac{\partial c_l}{\partial t} = \nabla \cdot (D_l^{eff} \cdot \nabla c_l + \frac{i_l \cdot (1-t_+^0)}{F})$
Charge balance ^{a)}	$\xi_s \frac{\partial c_s(r)}{\partial t} = \frac{1}{r^2} \frac{\partial}{\partial r} (D_s r^2 \cdot \frac{\partial c_s(r)}{\partial r})$ $\nabla \Phi_l = -\frac{i_l}{\kappa_l^{eff}} + \frac{2RT}{F} (1-t_+^0) \left(1 + \frac{\partial \ln f_{\pm}}{\partial \ln c_l}\right) \cdot \nabla \ln c_l$ $\nabla \Phi_s = -\frac{i_s}{\sigma_s} \text{ with } i_{app}(t) = i_s + i_t$
Charge conservation ^{a)}	$\nabla i_s + \nabla i_t = 0 \text{ with } \nabla i_s = -\frac{3\xi_s}{R_p} F \cdot j_n$
Electrode	$j_n = \frac{i_0}{F} \left[\exp\left(\frac{\alpha_a F \cdot \eta}{RT}\right) - \exp\left(-\frac{\alpha_c F \cdot \eta}{RT}\right) \right]$
Kinetics	$\eta = \Phi_s - \Phi_l - E_{eq}$
Transport	$N_{tot} = N_{mig,i} + N_{diff,i} = -z_i \frac{D_i}{RT} F c_i \nabla \Phi - D_i \nabla c_i$

a) with the Nabla operator for cylindrical coordinates: $\nabla = \vec{e}_r \cdot \frac{\partial}{\partial r} + \frac{1}{r} \vec{e}_\varphi \cdot \frac{\partial}{\partial \varphi} + \vec{e}_z \cdot \frac{\partial}{\partial z}$

Appendix B. Model Parameters

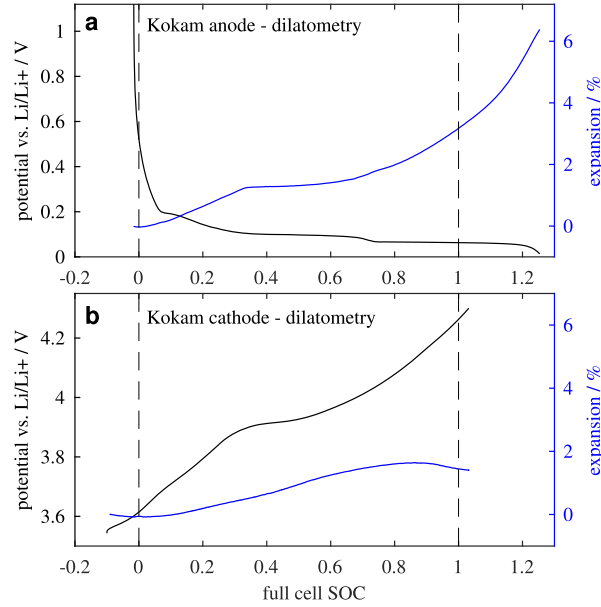


Figure 12. Thickness change characteristic obtained from dilatometry of the positive and negative electrodes harvested from the Kokam pouch cell.

Table VI. Model parameters for the axisymmetric Newman-type model.

Geometry	Anode	Separator	Cathode
Layer thickness l	98 μm^{m}	20 μm^{m}	66.5 μm^{m}
Particle radius r_p	8.7 $\mu\text{m}^{\text{a)}$		6.5 $\mu\text{m}^{\text{a)}$
Volume fraction of the active material ξ_s	62.1% ^e		66.4% ^e
Initial porosity ξ_l	32.9% ^{a)}	50.8% ^{a)}	29.6% ^{a)}
Volume fraction of non-active additives $\xi_{s,na}$	5% ^e		4% ^e
Bruggeman exponent α	1.5 ^e	1.59 ^e	1.32 ^e
Thermodynamics			
Equilibrium voltage E_{eq}	Fig. 4		Fig. 4
Maximum lithium concentration $c_{s,max}$	27 320 $\text{mol m}^{-3\text{e}}$		50 930 $\text{mol m}^{-3\text{e}}$
Concentrations 100%SOC $c_{s,100}$	21 668 $\text{mol m}^{-3\text{e}}$		20 785 $\text{mol m}^{-3\text{e}}$
Concentrations 0%SOC $c_{s,0}$	273 $\text{mol m}^{-3\text{e}}$		49 351 $\text{mol m}^{-3\text{e}}$
Kinetics			
Reaction rate coefficient k	$2 \times 10^{-11} \text{ m s}^{-1\text{b)}$		$0.8 \times 10^{-11} \text{ m s}^{-1\text{b)}$
Activation energy reaction rate $E_{A,k}$	35 000 $\text{J mol}^{-1\text{d)}$		51 000 $\text{J mol}^{-1\text{c)}$
Transfer coefficient α_a	0.5 ^{e)}		0.5 ^{e)}
Transfer coefficient α_c	0.5 ^{e)}		0.5 ^{e)}
Exchange current density i_0	0.75 $\text{A m}^{-2\text{a)}$		2.23 $\text{A m}^{-2\text{a)}$
Mass transport			
Diffusion constant solid phase $D_{s,0}$	$3.5 \times 10^{-14} \text{ m}^2 \text{ s}^{-1\text{b)}$		$5 \times 10^{-13} \text{ m}^2 \text{ s}^{-1\text{b)}$
Activation energy diffusion $E_{A,D}$	35 000 $\text{J mol}^{-1\text{d)}$		51 000 $\text{J mol}^{-1\text{d)}$
Electrical conductivity solid phase σ_s	100 $\text{S m}^{-1\text{b)}$		5 $\text{S m}^{-1\text{b)}$
Lithium-ion diffusion liquid phase D_l			
Ionic conductivity liquid phase κ			
Activity coefficient $\frac{\partial \ln f_{\pm}}{\partial \ln c_l}$			
Transport number t_+			

m = measured e = estimated. a) 17. b) 24. c) 25. d) 26. e) 27. f) 28.

$$D_l(c_l, T) = \frac{\kappa(c_l, T) \cdot k_B \cdot T^{\text{a)}}}{e^2 \cdot N_A \cdot c_l}$$

$$\kappa(c_l, T) = \frac{c_l \cdot (-5.384 + (0.03213 \cdot T) + (-0.00368 \cdot c_l \cdot T) + (1.320 \cdot e^{-2.235 \cdot c_l^2} \cdot e))}{10}$$

$$\frac{\partial \ln f_{\pm}}{\partial \ln c_l}(c_l, T) + 1 = \frac{0.601 - 0.24c_l^{0.5} + 0.982(1 - 0.0052(T - T_0))c_l^{1.5}}{1 - t_+}$$

 0.26^{a)}

Appendix C. Inelastic Clamping Validation

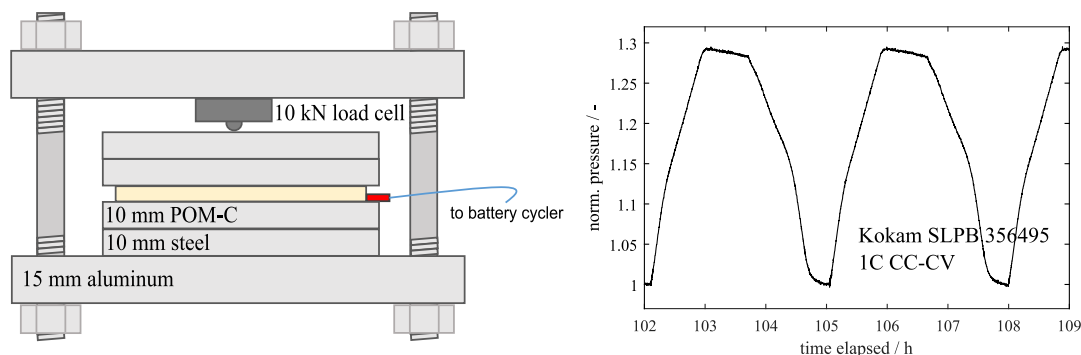


Figure 13. Left: Experimental setup for the inelastic clamping of a pouch cell. Right: Normalized pressure during continuous 1C CC-CV cycling of the Kokam pouch cell after initial compression at 1 MPa. The 2 cycles shown in the graph are 28, 29 of a total of 100.

ORCID

Franz B. Spingler <https://orcid.org/0000-0002-6523-3986>
 Sven Friedrich <https://orcid.org/0000-0003-1772-8076>
 Simon Kücher <https://orcid.org/0000-0003-2230-7356>
 Andreas Jossen <https://orcid.org/0000-0003-0964-1405>

References

- J. Cannarella and C. B. Arnold, "Stress evolution and capacity fade in constrained lithium-ion pouch cells." *Journal of Power Sources*, **245**, 745 (2014).
- A. S. Mussa, M. Klett, G. Lindbergh, and R. W. Lindström, "Effects of external pressure on the performance and ageing of single-layer lithium-ion pouch cells." *Journal of Power Sources*, **385**, 18 (2018).
- V. Müller, R.-G. Scurtu, M. Memm, M. A. Danzer, and M. Wohlfahrt-Mehrens, "Study of the influence of mechanical pressure on the performance and aging of Lithium-ion battery cells." *Journal of Power Sources*, **440**, 227148 (2019).
- F. Ebert, G. Sextl, and M. Lienkamp, "Effect of a flexible battery module bracing on cell aging." *2017 Twelfth International Conference on Ecological Vehicles and Renewable Energies (EVER)*, 1 (2017).
- M. Wunsch, J. Kaufman, and D. U. Sauer, "Investigation of the influence of different bracing of automotive pouch cells on cyclic lifetime and impedance spectra." *Journal of Energy Storage*, **21**, 149 (2019).
- T. Deich, M. Storch, K. Steiner, and A. Bund, "Effects of module stiffness and initial compression on lithium-ion cell aging." *Journal of Power Sources*, **506**, 230163 (2021).
- M. Klett, R. Eriksson, J. Groot, P. Svens, K. Ciosek, R. W. Lindström, H. Berg, T. Gustafson, G. Lindbergh, and K. Edström, "Non-uniform aging of cycled commercial LiFePO₄/graphite cylindrical cells revealed by post-mortem analysis." *Journal of Power Sources*, **257**, 126 (2014).
- T. C. Bach, S. F. Schuster, E. Fleder, J. Müller, M. J. Brand, H. Lormann, A. Jossen, and G. Sextl, "Nonlinear aging of cylindrical lithium-ion cells linked to heterogeneous compression." *Journal of Energy Storage*, **5**, 212 (2016).
- G. Fuchs, L. Willenberg, F. Ringbeck, and D. U. Sauer, "Post-Mortem Analysis of Inhomogeneous Induced Pressure on Commercial Lithium-Ion Pouch Cells and Their Effects." *Sustainability*, **11**, 6738 (2019).
- J. Cannarella and C. B. Arnold, "Ion transport restriction in mechanically strained separator membranes." *Journal of Power Sources*, **226**, 149 (2013).
- J. Cannarella, X. Liu, C. Z. Leng, P. D. Sinko, G. Y. Gor, and C. B. Arnold, "Mechanical Properties of a Battery Separator under Compression and Tension." *J. Electrochem. Soc.*, **161**, F3117 (2014).
- J. Cannarella and C. B. Arnold, "The Effects of Defects on Localized Plating in Lithium-Ion Batteries." *J. Electrochem. Soc.*, **162**, A1365 (2015).
- X. M. Liu, A. Fang, M. P. Haataja, and C. B. Arnold, "Size Dependence of Transport Non-Uniformities on Localized Plating in Lithium-Ion Batteries." *J. Electrochem. Soc.*, **165**, A1147 (2018).
- M. Doyle, T. F. Fuller, and J. Newman, "Modeling of Galvanostatic Charge and Discharge of the Lithium/Polymer/Insertion Cell." *J. Electrochem. Soc.*, **140**, 1526 (1993).
- D. Sauersteig, N. Hanselmann, A. Arzberger, H. Reinschagen, S. Ivanov, and A. Bund, "Electrochemical-mechanical coupled modeling and parameterization of swelling and ionic transport in lithium-ion batteries." *Journal of Power Sources*, **378**, 235 (2018).
- D. A. G. Bruggeman, "Berechnung verschiedener physikalischer Konstanten von heterogenen Substanzen. I. Dielektrizitätskonstanten und Leitfähigkeiten der Mischkörper aus isotropen Substanzen." *Ann. Phys. (Berlin)*, **416**, 636 (1935).
- M. Ecker, T. K. D. Tran, P. Dechent, S. Kabitz, A. Warnecke, and D. U. Sauer, "Parameterization of a Physico-Chemical Model of a Lithium-Ion Battery: I. Determination of Parameters." *J. Electrochem. Soc.*, **162**, A1836 (2015).
- J. Landesfeind, J. Hattendorff, A. Ehl, W. A. Wall, and H. A. Gasteiger, "Tortuosity Determination of Battery Electrodes and Separators by Impedance Spectroscopy." *J. Electrochem. Soc.*, **163**, A1373 (2016).
- F. B. Spingler, S. Kücher, R. Phillips, E. Moyassari, and A. Jossen, "Electrochemically Stable In Situ Dilatometry of NMC, NCA and Graphite Electrodes for Lithium-Ion Cells Compared to XRD Measurements." *J. Electrochem. Soc.*, **168**, 040515 (2021).
- D. Sauersteig, *Implementierung und Parametrierung eines physikalischen Simulationsmodells einer Lithium-Ionen Zelle zur Analyse elektrochemisch-mechanischer Wechselwirkungen. Dissertation*, Technische Universität Ilmenau (2018), https://www.db-thueringen.de/servlets/MCRFileNodeServlet/dbt_derivate_00043840/ilm1-2018000407.pdf.
- M. C. Smart, B. V. Ratnakumar, L. Wbitcanack, K. Chin, M. Rodriguez, and S. Surampudi, *Performance Characteristics of Lithium Ion Cells at Low Temperatures. Seventeenth Annual Battery Conference on Applications and Advances* (2002).
- C. von Lüders, J. Keil, M. Webersberger, and A. Jossen, "Modeling of lithium plating and lithium stripping in lithium-ion batteries." *Journal of Power Sources*, **414**, 41 (2019).
- F. B. Spingler, W. Wittmann, J. Sturm, B. Rieger, and A. Jossen, "Optimum fast charging of lithium-ion pouch cells based on local volume expansion criteria." *Journal of Power Sources*, **393**, 152 (2018).
- S. Erhard, *Mehrdimensionale elektrochemisch-thermische Modellierung von Lithium-Ionen-Batterien, Dissertation.*, Technische Universität München (2017), <https://mediatum.ub.tum.de/doc/1338266/1338266.pdf>.
- X.-G. Yang, Y. Leng, G. Zhang, S. Ge, and C.-Y. Wang, "Modeling of lithium plating induced aging of lithium-ion batteries: Transition from linear to nonlinear aging." *Journal of Power Sources*, **360**, 28 (2017).
- T. L. Kulova, A. M. Skundin, E. A. Nizhnikovskii, and A. V. Fesenko, "Temperature effect on the lithium diffusion rate in graphite." *Russian Journal of Electrochemistry*, **42**, 259 (2006).
- J. Schmalstieg, C. Rahe, M. Ecker, and D. U. Sauer, "Full Cell Parameterization of a High-Power Lithium-Ion Battery for a Physico-Chemical Model: Part I. Physical and Electrochemical Parameters." *J. Electrochem. Soc.*, **165**, A3799 (2018).
- L. O. Valøen and J. N. Reimers, "Transport Properties of LiPF₆-Based Li-Ion Battery Electrolytes." *J. Electrochem. Soc.*, **152**, A882 (2005).

5 The Effect of Lateral State-of-Charge Gradients on the Apparent Capacity

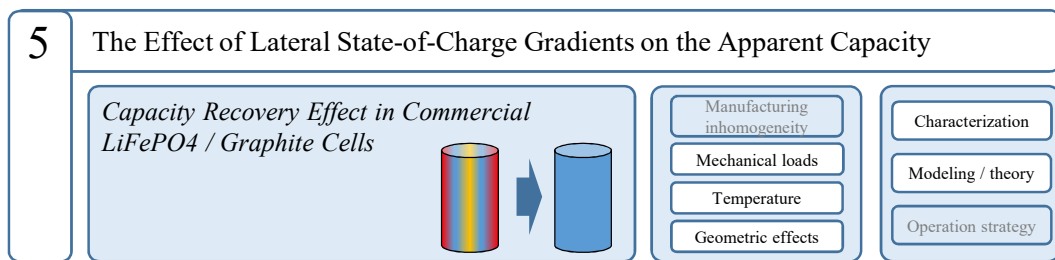


Figure 5.1: Outline of chapter 5.

In this chapter, the origins of non-uniform cell operating states and their effects on cell performance are investigated. It is demonstrated that capacity losses of up to 20 % coincide with laterally non-uniform distributions of lithium within the positive and negative electrodes. The non-uniformity of the lithium distribution is assessed via DVA and the coin cell-based method introduced in section 2.3. The article entitled *Capacity Recovery Effect in Commercial LiFePO₄ / Graphite Cells* constitutes the core of this chapter.

In the course of an earlier study not included in this thesis, commercial, cylindrical LFP/-graphite cells were found to lose capacity at a much higher rate when undergoing shallow cycles centered around 50 % SOC than when subjected to full cycles [86]. The finding that the capacity losses could be reversed, a result of follow-up experiments, was the starting point of the investigation presented here. Using the same type of cells, the capacity loss over 10,000 full equivalent cycles as a function of cycle depth and mean state of charge was examined. In shorter experiments spanning ca. 700 full equivalent cycles, the influence of temperature and C-rate was investigated, and it was also confirmed that shallow cycles had the same detrimental effect on capacity in two other types of cylindrical LFP/graphite cells. Capacity recuperation strategies were tested and compared while differential voltage analysis suggested that lithium distribution had changed in the cells that had undergone shallow cycles. This was confirmed by post-mortem investigations: Using the color change undergone by graphite at different levels of lithiation and through coin-cell measurements, it was shown that there was significantly more cyclable lithium concentrated at the electrode edges compared to the rest of the electrode surface. These results suggested that the lithium distribution was responsible for the reversible capacity losses. In view of the experimental evidence, mechanisms that could lead to such non-uniform lithium distributions during cycling were proposed and discussed.

These mechanisms include a temperature-dependent shift of the equilibrium voltage due to the entropic effect, an assumed preferential accumulation of lithium at the electrode edges due to a "piston pump" effect, and a heightened electrochemical activity in the vicinity of the top and bottom of the cell due to the higher compression exerted in these areas by the cell casing. Finally, some of the edge areas seemed to have experienced lithium plating. Here, lithium plating appears to have occurred not because of extreme local current densities, leading to an anode overcharge near the separator interface, but because of an overall overlithiated anode due to the lateral electrode SOC shift.

In the context of this thesis, this investigation explores the effects of non-uniform operating states on the usable capacity of cells and also establishes the link to aging mechanisms like lithium plating. Furthermore, it provides a framework for the establishment of causal relationships between electrode geometry, temperature inhomogeneities, mechanical loads, and the internal distributions of SOC and current density.

Author contribution Franz Spingler was responsible for the conceptualization, methodology, investigation, and writing of the original draft. Maik Naumann was responsible for the methodology and investigation of the cycling experiments and reviewed and commented on the manuscript. Andreas Jossen provided supervision, and reviewed and commented on the manuscript.

Capacity Recovery Effect in Commercial LiFePO₄ / Graphite Cells

Franz B. Spingler, Maik Naumann, Andreas Jossen

Journal of The Electrochemical Society 167 040526, 2020

Permanent weblink:

<https://doi.org/10.1149/1945-7111/ab7900>

Reproduced under the terms of the Creative Commons Attribution 4.0 License (CC BY, <http://creativecommons.org/licenses/by/4.0/>), which permits unrestricted reuse of the work in any medium, provided the original work is properly cited.



Capacity Recovery Effect in Commercial LiFePO₄ / Graphite Cells

Franz B. Spingler,^{1,z} Maik Naumann,^{1,z} and Andreas Jossen^{1,2,z}

¹Institute of Electrical Energy Storage Technology, Technical University of Munich (TUM), 80333 Munich, Germany

²Munich School of Engineering (MSE), Technical University of Munich (TUM), 85748 Garching, Germany

We report a significant capacity recovery effect of more than 10% after continuous shallow cycling of commercial LiFePO₄/Graphite cells. In a previous study on a LiFePO₄/Graphite cell, we observed that capacity losses were more severe with shallow cycles than with full cycles. Herein, the effects of shallow cycling on aging are investigated in detail using three different LiFePO₄/Graphite cell models, two 26650-type and one 18650-type. It is shown that a large portion of the capacity losses that occur with shallow cycling can be recovered by holding the cells at 0% or 100% state of charge. Differential voltage analysis and post-mortem experiments suggest that these capacity losses are caused by strongly non-uniform lithium distributions in the electrodes. Hypothetical mechanisms are presented and discussed that could lead to such non-uniform distributions of lithium.

© 2020 The Author(s). Published on behalf of The Electrochemical Society by IOP Publishing Limited. This is an open access article distributed under the terms of the Creative Commons Attribution 4.0 License (CC BY, <http://creativecommons.org/licenses/by/4.0/>), which permits unrestricted reuse of the work in any medium, provided the original work is properly cited. [DOI: 10.1149/1945-7111/ab7900]



Manuscript submitted November 20, 2019; revised manuscript received February 10, 2020. Published March 5, 2020.

The existence of a steady, irreversible loss of the usable capacity of lithium-ion batteries as a function of time, charge throughput and other operating parameters is an established fact among researchers and users of battery technology. Reversible losses, however, are rarely observed. In Refs. 1–3, large “anode overhang” areas, which refers to areas of active material that do not face a cathode counterpart, have been identified as a cause of reversible losses of the usable capacity. Depending on the usage profile of the cell, lithium-ions may diffuse into these overhang areas and, in consequence, be inaccessible in the short term. In this paper, we investigate a different, but related, phenomenon, where continued shallow cycling around medium states of charge (SOCs) leads to non-uniform lithium distribution in the electrodes of a commercial LiFePO₄/Graphite (LFP/C) cell, which results in a reversible loss of capacity. The observed capacity losses of up to 20% are too great to be caused by the cell’s overhang areas. Smaller reversible losses of capacity of up to 1.5% in NiMnCoO₂/Graphite cells have been associated with non-uniform lithium distribution.⁴

The phenomenon of reversible capacity losses with shallow cycles was first observed in the course of a 29-month aging study.^{5,6} Herein, we present a thorough experimental study of this phenomenon using three different cylindrical cells with a LFP/C chemistry. First, the capacity loss is quantified as a function of various cycle depths and mean states of charge (SOCs). Second, recovery strategies are tested and discussed with the help of differential voltage analysis (DVA). Third, the assumption of uneven lithium distribution in the electrodes is underpinned with post-mortem findings and lastly, hypotheses are presented that could explain the formation of such a non-uniform lithium distribution during cycling.

The main part of this paper is divided into an experimental section, a mostly descriptive results section and a discussion of the results.

Experimental

Commercial cylindrical cells.—Widely available Sony/Murata US26650FTC1 LFP/C cells were used in the main experiments. The rated capacity of these cells is 2.85 Ah at 0.1 C and 25 °C, however, here and in previous studies,^{6,7} we have consistently obtained around 3.0 Ah. Further technical data is presented in Table I. The jelly roll design is shown in Fig. 1. In the outermost winding of the jelly roll, the anode sheet is single-side coated, resulting in a relatively small *overhang area*, where the anode has no cathode counterpart. In experiments that were conducted to test whether the effects we

observed with the Sony cells also appear in other LFP/C cells, 2.3 Ah ANR26650M1B and 1.1 Ah APR18650M1A cells from A123 were used.

Cycle aging procedure.—All cycling except capacity check-ups was done at 1 C charge/1 C discharge. Cut-off voltages were 2.0 V and 3.6 V, respectively. In full cycles, a constant voltage (CV) phase until C/20 on discharge and until C/30 on charge was included, as indicated in the cell data sheet. In a previous study,⁸ we found accelerated aging in cells that experienced repeated shallow cycles around medium SOCs. In this study, in order to investigate this phenomenon thoroughly, cells were cycled around different mean SOCs ranging from 25% to 75% and with various symmetrical charge-throughputs per charge/discharge ranging from 5% to 100% of the cell capacity. Table II provides an overview of the cycling conditions.

Temperature during cycling.—The initial set of experiments, covering 11000 FEC (full equivalent cycles) of the Sony cell, was conducted at 40 °C, corresponding to the experimental design of our previous study.⁸ After it was determined that the reversible capacity loss was similar at a temperature of 25 °C, the second set of experiments was done at 25 °C.

Charge/discharge rates.—Charge and discharge rates during cycle aging were mostly 1 C. A limited number of experiments were conducted at 0.5 C and 2 C to investigate the effect of the charge/discharge rate on the capacity loss with shallow cycles.

Capacity check-ups.—Capacity was measured by a 0.1 C discharge with a C/20 CV phase following a 0.5 C charge with a C/30 CV phase in 100-FEC-intervals.

Recuperation of usable capacity.—Preliminary tests had shown that the application of several full cycles as well as storage at 100% SOC or 0% SOC could help restore a large part of the capacity lost due to shallow cycles. It is hypothesized that the main cause of the loss of useable capacity is a lateral reallocation of lithium-ions in the electrodes. A potential gradient across the electrodes would be a driving force to re-homogenize the electrodes. A significant potential gradient due to non-uniform lithium distribution is most likely to occur at SOCs where the cells’ equilibrium voltage characteristic has a large gradient, too. In an LFP/C cell, the voltage characteristic is very steep both at 0% SOC and at 100% SOC, as both materials exhibit a steep increase in potential when they are almost completely delithiated. In consequence, the effects of holding the cell both at 0% SOC and 100% SOC for an extended period of time were investigated in detail. Cells that had previously been cycled for

^zE-mail: franz.spingler@tum.de; maik.naumann@tum.de; andreas.jossen@tum.de

Table I. Characteristics of Sony US26650FTC1 cylindrical cells.

Cell type and chemistry	Cylindrical 26650, Lithium-Iron-Phosphate/Graphite
Anode sheet size (L × W × H)	1590 mm × 57 mm × 131 μm
Cathode sheet size (L × W × H)	1485 mm × 56 mm × 161 μm
Current collector thickness	Anode: ~11 μm/Cathode: ~13 μm
Coating thickness	Anode: 60 μm/Cathode: ~74 μm
Max. cont. charge/discharge rate	1 C/6 C
Upper and lower cut-off volt.	3.6 V/2.0 V

600 FEC with 20% cycle depth around 50% SOC and had reached approx. 83% relative capacity were used for the recuperation study. They were held at 0% or 100% SOC for 7 d by keeping their voltage constant (“voltage hold”) at 2.0 V and 3.6 V respectively, and were then subjected to a capacity check-up. This procedure was repeated five times, resulting in a total of 35 d of recovery. Generally, chamber temperature was 25 °C. Two cells, however, were tested at 45 °C and 0% SOC, to find out whether the recovery process was temperature dependent. Another two cells were alternated between 0% SOC and 100% SOC in four 42 h intervals with an initial charge/discharge time of approx. 1 h and subsequent maintenance of the charge level until the end of the interval. This meant that they underwent 7 d of recuperation in between each capacity check-up.

dV/dQ analysis.—Discharge data from the 0.1 C capacity check-ups were used for dV/dQ analysis. Cells were cycled to 600 FEC and thereafter underwent recuperation at 0% SOC (voltage hold 2.0 V) over 3 d intervals interrupted by capacity check-ups.

Cell opening and post-mortem inspection.—Cells were opened in an argon filled glovebox with oxygen and water levels below 0.1 ppm. 24 h prior to opening, the cells were charged to 50% SOC at a 0.1 C rate. The jelly rolls were disassembled while still wet and then left to dry in the glovebox for approx. one hour. Photographs were taken of the electrodes in front of a gray background paper.

Local SOC measurement via CR2032 half cells.—The aim of the coin cell measurements was to assess the local SOC in each

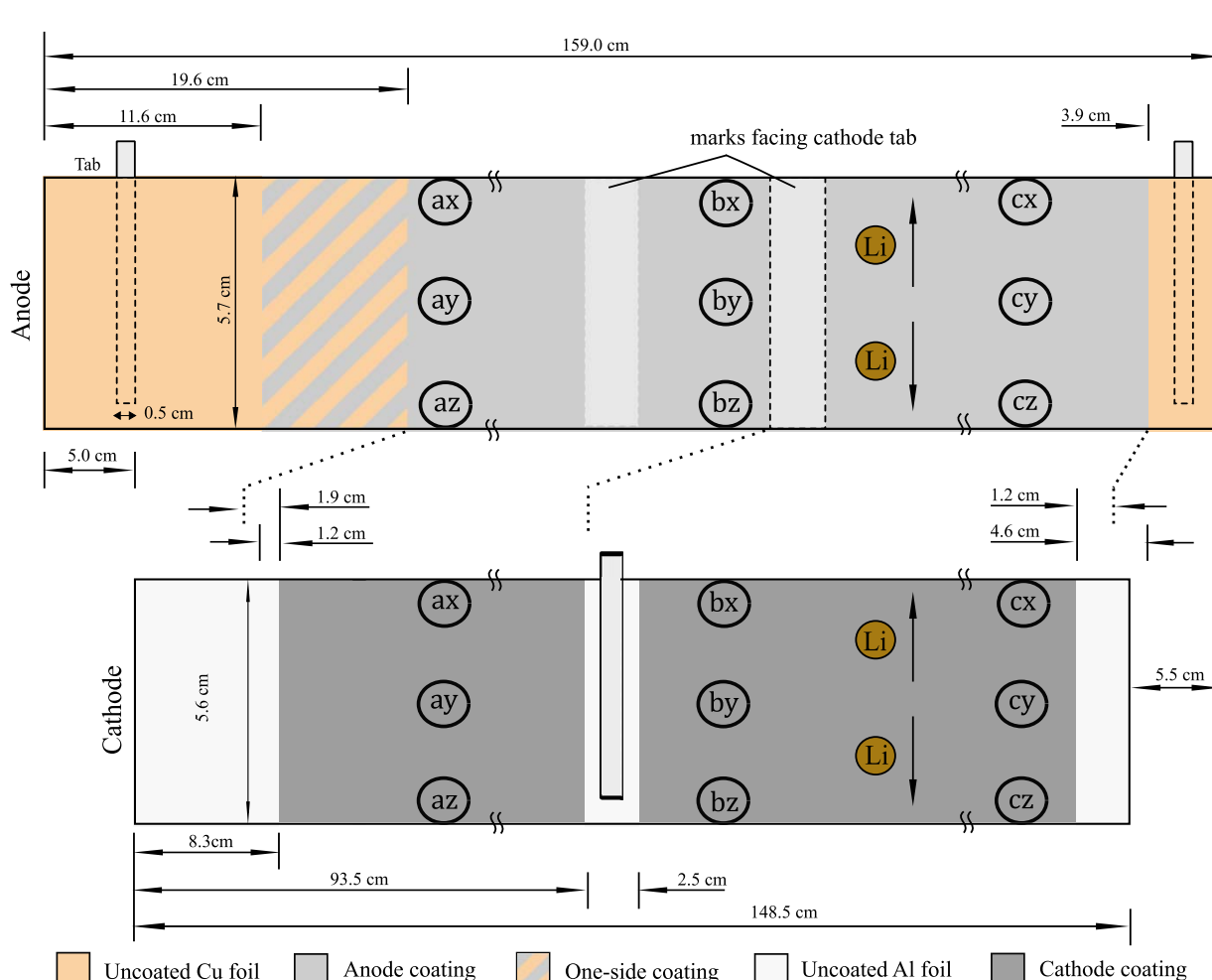


Figure 1. Schematic of the SONY US26650FTC1 jelly roll and electrodes. The graphite anode has one tab on each end, the cathode has a single tab in the center. The nine locations from where coin electrodes were punched out are shown. The “x” and “z” coins were punched out as closely as possible to the edges.

electrode (via the initial discharge) as well as their area-specific reversible capacities. Using a precision punch, 10 mm coins were obtained from nine locations across the electrodes, as shown in the schematic in Fig. 1. Three coins were punched out next to each other at each location. The coin electrodes were dried in the glovebox for at least 24 h. CR2032-type coin cells were assembled using two layers of 16.0 mm diameter VWR 691 glass fiber (260 μm each) as the separator, a 15.6 mm diameter lithium chip (250 μm) as the counter electrode and 1.0 mm plus 0.5 mm spacers. 80 μl of LP57 (3:7 wt EC:EMC 1 Mol LiPF₆) were used as the electrolyte. After assembly, the cells were rested for 6 h and then cycled at 0.1 C using a constant current/constant current protocol (CC/CC). The cells made from the graphite anodes were cycled between 10 mV and 1.5 V, beginning with a delithiation of the graphite until the cell reached 1.5 V. The cells made from the LFP cathodes were cycled between 2.0 V and 3.6 V, beginning with a delithiation of the LFP until the cell reached 3.6 V. As the total number of coin cells to be cycled was very large and the number of test channels was limited, cycling was generally stopped after three cycles. However, to test the quality of the cells, some cells were cycled 20 times or for approx. 500 h. No significant capacity fade in the working electrodes was detected.

Results

Loss of usable capacity associated with shallow cycles.—Cells were cycled around various mean SOC_s and with different cycle depths as detailed in Table II. Figure 2b illustrates the cycle aging scheme: every 100 FEC, cycling is interrupted by a capacity check-up. Capacity retention vs FEC for over 10,000 FEC is shown in Figs. 2a and 2c. Figure 2a shows the results of varying cycle depth while keeping the mean SOC constant at 50%. Figure 2c shows the results of varying the mean SOC while keeping the cycle depth constant at 20%. In both graphs, the capacity retention with full cycles (0% SOC–100% SOC) is shown for reference. In cells subject

Table II. Overview of mean SOC_s and cycle depths investigated in this study.

Mean SOC/%	Cycle depth/%
25	20
40	10, 20
45	10
50	5, 10, 20, 40, 60, 80, 100
55	10
60	10, 20
65	10
70	10
75	10, 20

to full cycles, capacity loss is almost linear after slightly higher losses in the first 300 cycles. 80% relative capacity is reached only after approx. 6500 full cycles. When the cycle depth is reduced to 80%, the initial rate of capacity loss is slightly higher until 2000 FEC and is slightly lower thereafter. For further reduced cycle depths, which maintain a charge/discharge symmetry around 50% SOC, initial capacity loss is more drastic. With cycle depths between 5% and 40%, the loss of usable capacity is between 13% and 21% after 1000 FEC, compared to only 6% with full cycles. The most severe capacity loss occurs with 20% (40% SOC–60% SOC) and 10% (45% SOC–55% SOC) cycle depth. These results are in agreement with Ref. 8, where, for a LFP/C cell, capacity loss with cycle depths from 10% to 60% was found to be higher than with full cycles during 2000 FEC. The capacity retention vs FEC curves of both reach a minimum at approx. 1500 FEC, after which the capacity recuperates slightly and levels off between 4000 and 7000 FEC and then decreases slightly again, at a slower rate than with full cycles. Cycling between 30% SOC and 70% SOC leads to a similarly fast

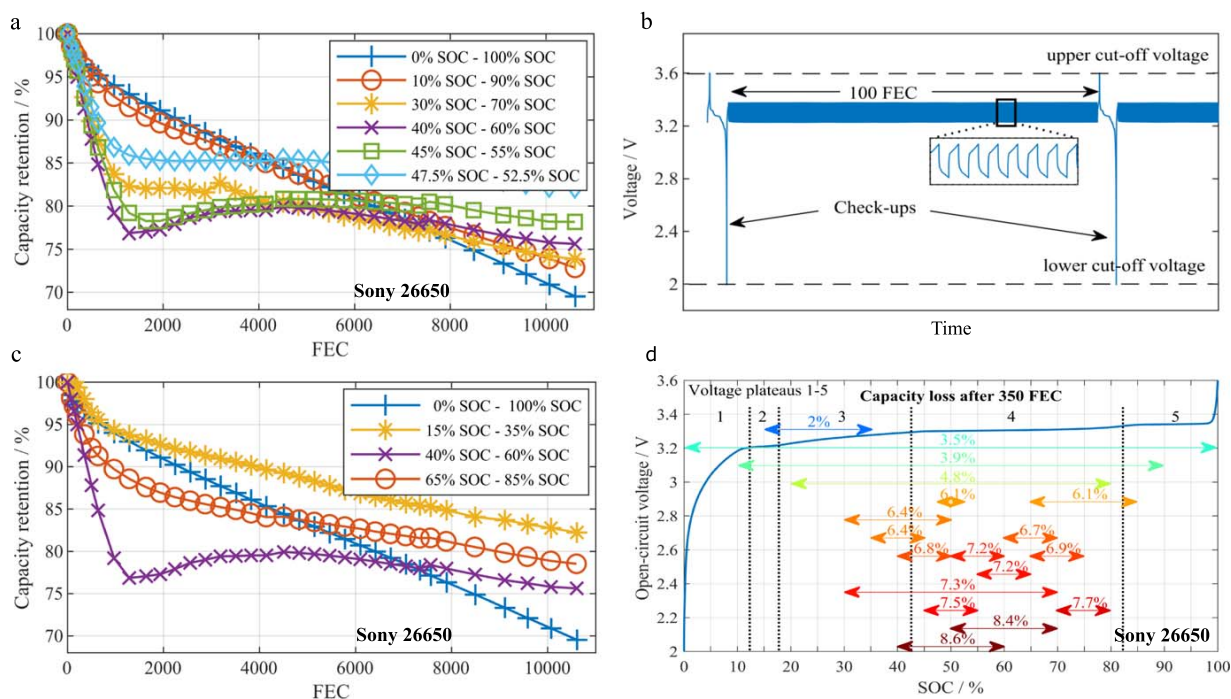


Figure 2. (a) Capacity retention vs FECs as a function of cycle depth and mean SOC (c). Capacity retention with full cycles is shown in blue in both graphs for reference. Cycling with low cycle depths around 50% SOC leads to much faster capacity losses than full cycles. (b) Cycling procedure exemplarily shown for 40% – 60% SOC. (d): Capacity losses in % after 350 FEC as a function of cycle depth and mean SOC. The equilibrium voltage curve of the cell with its characteristic plateaus is displayed for reference. In SOC windows without significant gradients in the equilibrium voltage curve, capacity losses are relatively small.

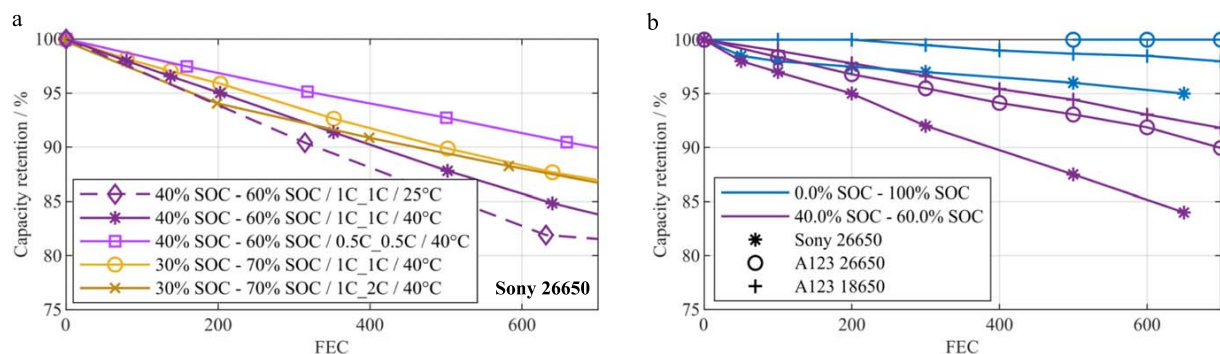


Figure 3. (a) Variation of temperature and C-rate. At a current of 0.5 C, the cells lose less capacity than at 1.0 C. Reducing the temperature to 25 °C increases the capacity losses as compared to 40 °C. (b) Comparison of the Sony cell with two LFP/C cells from manufacturer A123 (all at 25 °C). While the A123 cells generally have a higher capacity retention, all of these cells lose significantly more capacity with shallow cycles than with full cycles. A123 18650 full cycle data is adopted from Ref. 9.

capacity decrease, which levels off shortly after 1500 FEC and continues after 4000 FEC. Beyond 7000 FEC, capacity retention with shallow cycles is higher than with full cycles. Finally, at 10,000 FEC, the amount of capacity lost is a function of cycle depth with higher cycle depth corresponding to higher capacity loss. The best capacity retention at 10,000 FEC is obtained by cycling between 47.5% SOC and 52.5% SOC: After an initial decay to 86% relative capacity at 1500 FEC, capacity remains almost constant.

Figure 2c shows that the rate of capacity loss is just as dependent on mean SOC as it is on cycle depth: The capacity decay when cycling between 65% SOC and 85% SOC is much slower than with cycling between 40% SOC and 60% SOC. However, in the first 1000 FEC, capacity still decays quicker than with full cycles. Only cycling at lower mean SOC, i.e. between 15% SOC and 35% SOC, leads to a slower capacity decay than full cycles in this FEC interval. The combination of the results shown in Figs. 2a and 2c suggests that the SOC window is the relevant parameter, rather than cycle depth or mean SOC alone. This idea is reflected in the experiments presented in Fig. 2d, which shows the capacity losses after 350 FEC associated with all of the cycle depth and mean SOC combinations tested. The highest losses, over 8%, occur between 40% SOC and 60% SOC and between 50% SOC and 70% SOC. Several other SOC windows between 30% SOC and 80% SOC lead to considerable losses over 6%. When the SOC window exceeds the voltage plateaus designated “3” and “4”, the cycling losses are considerably lower.

Temperature, and C-rate variation, other cells.—Figure 3a shows capacity retention over 700 FEC for different C-rates and temperatures. In addition to testing 1 C charge/1 C discharge, 0.5 C charge/0.5 C discharge and 1 C charge/2 C discharge at a chamber temperature of 40 °C, the 1 C charge/1 C discharge experiment was repeated at 25 °C. The effect of changing the discharge rate from 1 C to 2 C was negligible. At 0.5 C/0.5 C, however, capacity retention was higher than at 1 C/1 C. Temperature seems to have a limited effect on capacity loss, as the cells at 25 °C lost capacity at a slightly higher rate compared to 40 °C.

Figure 3b compares the capacity retention over 700 FEC of the A123 18650 and A123 26650 to the 26650 Sony cell. Chamber temperature was 25 °C throughout and only full cycles and 40% SOC–60% SOC cycles were investigated. The A123 cells exhibit the same behavior as the Sony cell: shallow cycles lead to a much more rapid capacity decay than full cycles. In both cycling scenarios, the A123 has a better overall capacity retention. Considering the fact that their capacity loss during the first 300 full cycles is zero or negative, their better overall capacity retention may be due to some capacity recovery from the overhang areas, which, at least in the case of the A123 18650, is known to be of significant size.¹

Recuperation of usable capacity.—The recuperation tests were performed on cells that had been cycled between 40% SOC and 60% SOC for 700 FEC and had reached around 83% relative capacity. Two cells that had undergone 700 full cycles and had reached 95% relative capacity were included for reference. The recuperation strategies were i) voltage hold at 2 V/0% SOC ii) voltage hold at 3.6 V/100% SOC and iii) alternating between 2 V and 3.6 V. More details are provided in the experimental section. Figure 4 shows an exemplary recuperation process with voltage hold at 2 V. The upper graph shows voltage during check-ups and recuperation and the capacity retention, which increases after every interval. The lower graph shows current and accumulated charge throughput of every recuperation interval. Charge throughput decreases rapidly as the recuperation proceeds. The total charge throughput from all intervals is –690 mAh, while the total change in capacity retention amounts

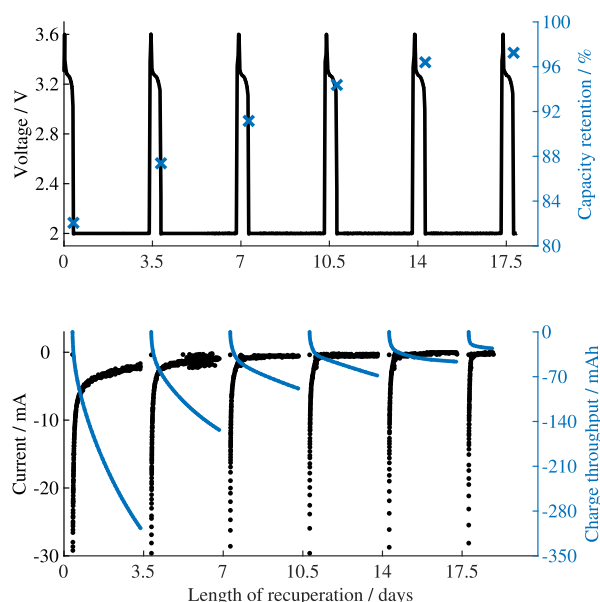


Figure 4. Recuperation procedure for 2 V hold strategy. Upper graph: Voltage during capacity check-ups and recuperation intervals; capacity retention as determined in check-ups. Lower graph: Current and charge throughput during recuperation intervals. The total charge throughput from all intervals is –690 mAh, while the total change in capacity retention amounts to 455 mAh.

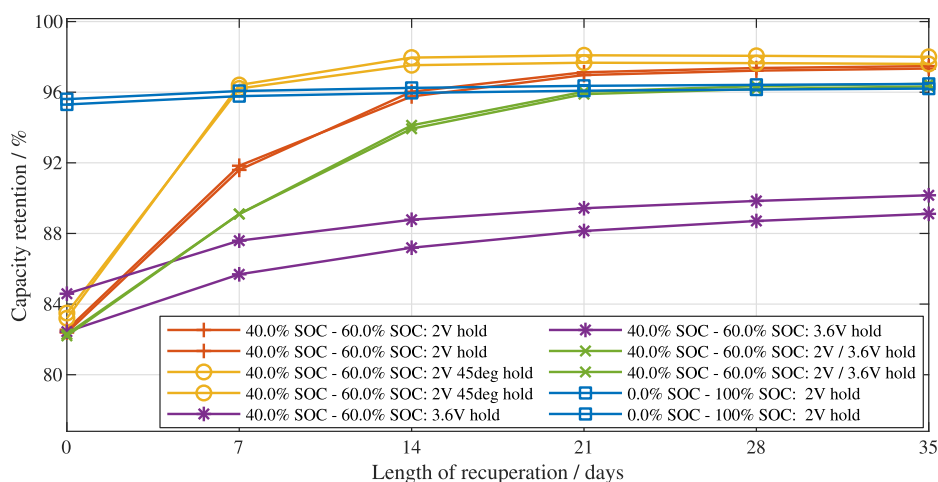


Figure 5. Recuperation of usable capacity as a function of days for various recuperation strategies. Cells held at 2 V or 0% SOC recuperate at the highest rate. Increased temperature further accelerates the recuperation process. After full cycle aging, almost no capacity can be recuperated. If not indicated otherwise, temperature was 25 °C. (Note: insert degree symbol.)

to 455 mAh. These numbers suggest that the “inactive” capacity that is being accessed during recuperation is partly re-activated.

The results of the recuperation tests shown in Fig. 5 show a clear trend: both the rate of capacity recuperation and the final amount of capacity recuperated are highest at 2 V hold, followed by alternating between 2 V/3.6 V hold and 3.6 V hold. Increasing the temperature to 45 °C seems to accelerate the recuperation process. Generally, the rate of recuperation declines rapidly with time. After 35 d of 2 V hold at 25 °C, the relative capacity was 98%, which means that approx. 89% of the lost capacity had been recovered. At this temperature, between 14 and 21 d were needed to reach 97% relative capacity. In contrast, 97% relative capacity was reached after only 7 d at 45 °C. The relative capacity of the cells that had undergone full cycles before the recuperation test, recovered only slightly from 95% to 96.5%.

dV/dQ analysis.—Another set of cells was cycle aged between 40% SOC and 60% SOC for 620 FEC and thereafter underwent the 2 V hold recuperation strategy over 72 h periods, interrupted by capacity check-ups. 72 h periods were implemented instead of 168 h (7 d) uninterrupted, so that capacity recuperation could be tracked more closely. Figure 6 shows the discharge voltage curves of capacity check-ups during aging. After 200 FEC, a voltage plateau is visible at the beginning of discharge and becomes more distinct as the number of FECs increases. Such plateaus typically occur during a lithium stripping process on discharge following lithium plating during charging.^{10–15} The amount of stripped lithium is thought to be

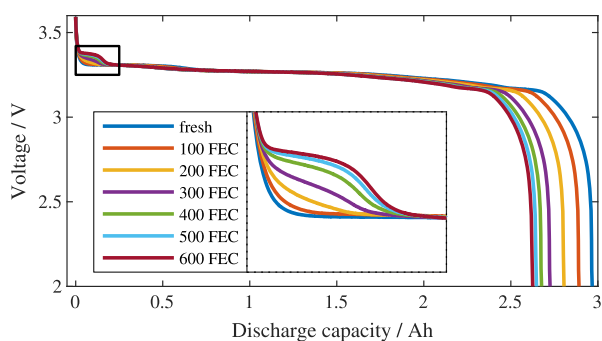


Figure 6. Discharge voltage curves from capacity check-ups during aging. A distinct voltage plateau appears as the number of FECs increases. The voltage plateau may indicate a lithium stripping process.

equivalent to the length of the plateau¹⁰ which is approx. 0.15 mAh in the discharge curve after 600 FEC. Figure 7 shows the dV/dQ curves obtained from discharge voltage curves of capacity check-ups during aging and recuperation. The first two graphs on the right, b) and d), are details of the graphs a) and c) on the left. The dV/dQ curves run from right (100% SOC) to left (0% SOC) in each graph. In Figs. 7a and 7b, a peak in the curve of the fresh cell is visible when about 2.3 Ah capacity remains, which is thought to demark the end of the LiC₆/LiC₁₂ voltage plateau (Upon delithiation, the graphite anode undergoes a structural change from LiC₆ to several discrete lower-lithiated phases. The co-existence of phases leads to characteristic voltage plateaus.^{16,17}) of the graphite anode. This peak serves as a well-defined anode-SOC marker. The charge throughput between 0% SOC and this marker is denoted Q₁, while Q₂ represents the number of ampere hours between the plateau and 100% SOC, as illustrated by the arrows in Fig. 7f. Both Q₁ and Q₂ decrease with cycling and increase again during recuperation, see Fig. 7e. The values of Q₁ and Q₂ are provided in Table III. A decrease of Q₁ is linked to a decrease of the (accessible) anode capacity. A change of Q₂, which represents the distance between the graphite peak and the fully delithiated state of the cathode, indicates a shift of the electrode balancing due to a loss of (accessible) cycleable lithium.^{18,19} Figure 7b shows that the height of the peak at 2.3 Ah decreases with cycling, while the peak width increases. The broadening of this graphite peak has been associated with non-uniform lithium distribution.²⁰ In Figs. 7a and 7b, another peak appears at around 2.5 Ah remaining capacity after 200 FEC. The peak’s height increases dramatically until 620 FEC. The peak results from the voltage plateaus in the discharge curves as shown in Fig. 6, which, as discussed above, may indicate a lithium stripping process.

Non-uniform lithium distributions in both anode and cathode could potentially explain all of these phenomena: The mixed potential of a more delithiated part of the cathode and the rest of the cathode, could be large enough to trigger the upper voltage cut-off that defines 100% SOC. The same mechanism could shift the location and width of the graphite peak. The areas with higher local SOC would contain the non-accessible cycleable lithium. Those areas with higher local SOC would then be at a higher risk of lithium plating during the capacity check-up cycles (0.5 C charge/0.1 C discharge).

Figures 7c and 7d show the dV/dQ curves of check-ups between recuperation intervals of 72 h. After the first 72 h of keeping the cell at 2 V, the prominent peak at 2.5 Ah disappears. The LiC₆/LiC₁₂ peak height increases after every recuperation interval, although it does not reach the original height of the fresh cell. Figure 7f shows

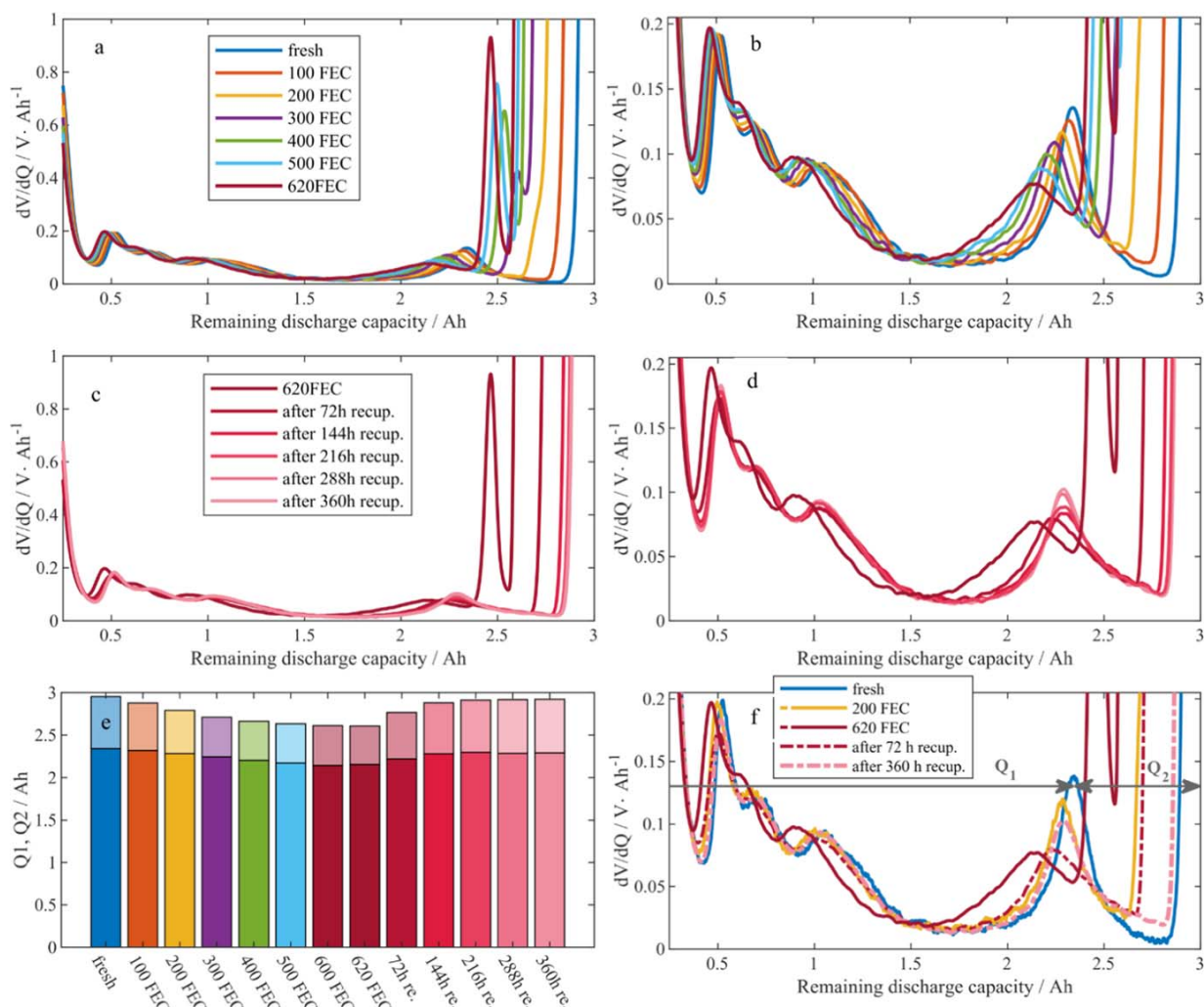


Figure 7. dV/dQ on discharge between 100 FEC-cycling-intervals until 600 FEC (first row) and between 72 h recuperation intervals at 0% SOC (second row). A selection of curves is shown in the third row. Plots on the right are details of the plots on the left. Evolution of usable capacity, Q1 and Q2 during cycle aging and recuperation via 2 V hold. Q1 represents the number of ampere hours between 0% SOC and the LiC6-LiC12 peak, Q2 between the peak and 100% SOC.

selected dV/dQ curves of both aging and recuperation for easier comparison.

Post-mortem analysis.—In order to find evidence for or against non-uniform lithium distribution as suggested by the dV/dQ analysis, a post-mortem analysis was conducted. A total of five cells were opened in the course of this study: Two new/fresh cells, two that had been cycled for 700 FEC between 40% SOC and 60% SOC, and one that had been cycled for 700 FEC with full cycles. In all cells, the overhang areas were clearly visible. Their locations and sizes are shown in the schematic in Fig. 1. The three tabs (two on the anode, one on the cathode) left visible pressure marks on the

electrodes at a distance of up to three windings along the coil. All cycle aged cells had a slightly different-colored stripe in the center of the anodes over their full length. Otherwise, the electrodes of the cell aged with full cycles looked the same as those of the fresh cells. Interestingly, the cells cycled between 40% SOC and 60% SOC displayed a distinctive feature: an approx. 5 mm wide distinctly-colored stripe at the upper and lower edges. As can be seen in the photographs in Fig. 8, the stripe is grey in the outer section (the outermost part of the coil) of the anode, and is gold with a violet edge in the middle and core sections. The stripe was also found to be consistently slightly wider towards the core. It is generally accepted that this gold color coincides with the highest lithiation state of

Table III. Evolution of usable capacity, Q1 and Q2 during cycle aging and recuperation via 2 V hold. Q1 represents the amount of ampere hours between 0% SOC and the LiC6-LiC12 peak, Q2 between the peak and 100% SOC.

	Fresh	100 cyc.	200 cyc.	300 cyc.	400 cyc	500 cyc	600 cyc	620 cyc	72 h	144 h	216 h	288 h	360 h
Q1/Ah	2.341	2.319	2.283	2.245	2.202	2.170	2.145	2.155	2.220	2.280	2.299	2.285	2.292
Q2/Ah	0.615	0.560	0.509	0.467	0.462	0.464	0.469	0.454	0.548	0.601	0.614	0.634	0.631
Q1 + Q2/Ah	2.96	2.88	2.79	2.71	2.66	2.63	2.61	2.61	2.77	2.88	2.91	2.92	2.92

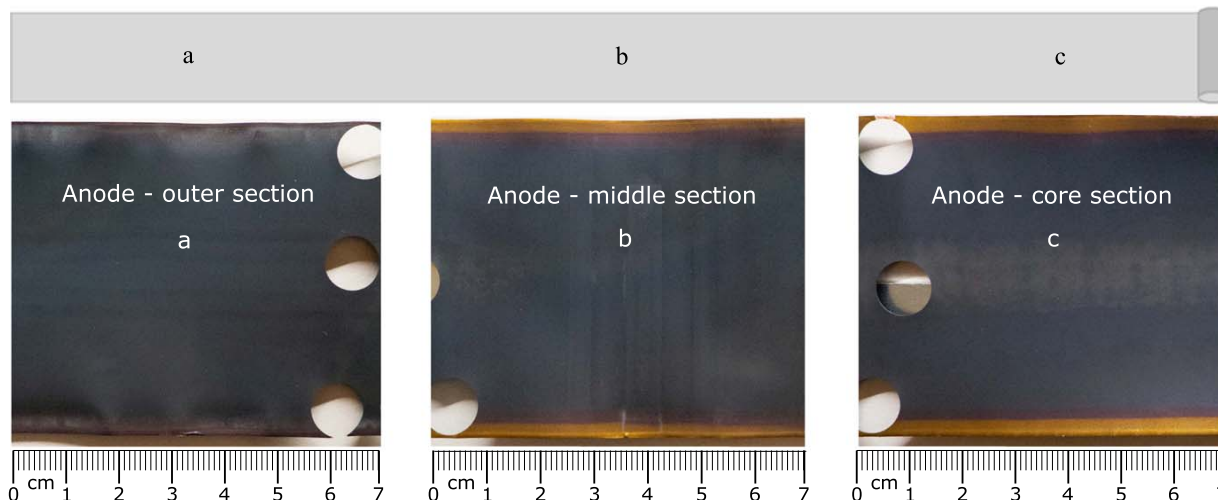


Figure 8. Post-mortem photographs of the anode after 700 FEC between 40% and 60% SOC. From (a) to (c): Outer, middle, and inner sections of the anode roll with circular holes from punching out the 10 mm electrodes. While the outer section exhibits a grey stripe of approx. 5 mm width along the edges, this band is gold in the middle and inner sections. The cells that were cycled with 700 full cycles had a similar grey stripe in the center but no grey or gold stripe at the edges.

graphite, followed by violet.^{17,21–23} This means that the lithiation state at the edges of the anode would have been much higher than in the average cell at 50% SOC. As for the grey stripe in section a of the anode, see Fig. 8, it could be hypothesized that this could be an example of lithium plating, which is associated with grey or silver colored deposits.^{24–27} The discharge voltage curve and dV/dQ have already hinted at this possibility. If we assume that on the 5 mm wide stripe across the full length of the electrode, all of the charge between 50% SOC and 100% SOC corresponding to that area were plated during charging in the capacity check-up, the amount of plated lithium would be: $5\text{ mm}/57\text{ mm} \times 1.5\text{ Ah} = 0.13\text{ mAh}$. This number is close to the approximate amount of charge of 0.15 mAh ascribed to lithium stripping above. The slightly lower temperature in the outer section “a” may have led to stronger lithium plating and a higher degree of irreversibility of the plated lithium relative to the other sections.

Charge distribution.—From anode and cathode, coin electrodes were punched out from the upper and lower edges and in the center (“x”, “y”, “z”) of the outer, middle and core sections (“a”, “b”, “c”). The reader is referred to Fig. 1 for reference. These electrodes were assembled in coin cells with a lithium counter electrode and

discharged. The resulting charge distributions in a cycled and in a new cell, both at 50% SOC, are shown in Fig. 9. Each rectangle represents the charge of the respective 10 mm circle. The exact values are provided in Table IV. A quantitative evaluation or the investigation of a charge gradient from edge to the center of the electrode is difficult because the gold-colored stripe at the edge covers only about a third of the 10 mm electrodes that were punched out. Notwithstanding these limitations, Fig. 9 shows that there is clearly more charge, i.e. lithium-ions, at the edges (“x”, “z”) than in the center (“y”) of the anode of the cycled cell. The cathode of the cycled cell has slightly more charge at the edges as well. In the case of the new cell, charge is generally more evenly distributed. While in the new anode no significant charge differences can be observed, the new cathode has slightly more charge in the center compared to the edges. This overall trend is best observed in the lower two graphs of Fig. 9 that show the sum of anode and cathode charge: The cycled cell has a considerably higher cycleable lithium content at the edges, while the new cell has a slightly higher cycleable lithium content in the center. Lithium content also seems to be unevenly distributed along the length of the electrodes. While the middle (“b”) and core (“c”) sections are quite similar, the outer (“a”) section stands out as

Table IV. Areal capacities of coin cells in first discharge. Coin cells were punched out from harvested electrodes at three positions along the electrodes’ length (“a”, “b”, “c”) and three positions along the electrodes’ height (“x”, “y”, “z”).

Areal capacity of coin cells in first discharge/mAh/cm ²						
	Cathode cycled			Cathode new		
x	1.16	1.29	1.23	1.08	1.00	0.82
y	1.06	0.92	0.83	1.18	1.34	1.42
z	0.81	1.02	1.29	1.16	1.02	0.94
	Anode cycled			Anode new		
x	1.21	1.58	1.52	1.11	1.13	1.08
y	1.01	1.08	1.11	1.11	1.12	1.15
z	1.22	1.54	1.62	1.10	1.13	1.10
	Cat.+An. cycled			Cat.+An. New		
x	2.37	2.87	2.74	2.19	2.13	1.90
y	2.06	2.00	1.94	2.29	2.46	2.57
z	2.03	2.56	2.92	2.26	2.15	2.04
Loc.	a	b	c	a	b	c

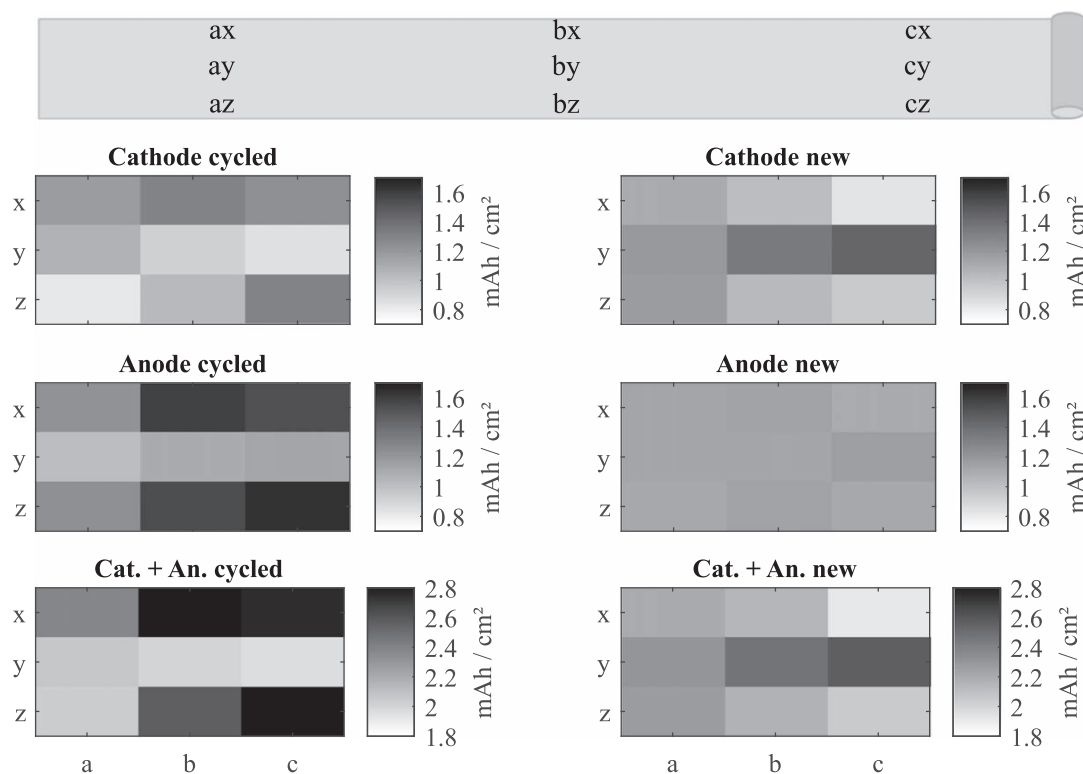


Figure 9. Distribution of charge in the electrodes of cells at 50% SOC. Left column: cell cycled between 40% SOC and 60% SOC for 700 FEC. Right column: fresh cell. Generally, the cycled cell exhibits an accumulation of charge at the edges of both electrodes, while the fresh cell tends to be more homogenous (anode) or has higher area-specific charge in the center than at the edges (cathode).

lithium is more evenly distributed between the edges and the center at this point.

Discussion

The experimental results can be summarized as follows:—Cycling cylindrical LFP/C cells anywhere between 30% SOC and 70% SOC, i.e. where the equilibrium voltage curve's gradient is low, produces significantly higher capacity losses than full cycles.—Keeping the cells at 0% SOC or 100% SOC, i.e. where the equilibrium voltage curve's gradients are high, recovers most of the lost capacity within a couple of days.—Peak broadening observed in the dV/dQ analysis suggests non-uniform lithium distributions in the electrodes—Post-mortem investigations confirm non-uniform lithium distributions in the cells. The areas near the edges had a significantly higher lithium content than the average of both electrodes. This seems likely to be the reason for the loss of usable capacity: The local cell SOC depends on the local SOC of the anode and cathode. The lower SOC areas would provoke an early “cut-off” on discharge, the higher SOC areas on charge.

Based on the results, it could be hypothesized that the low equilibrium voltage curve's gradient at medium SOC of LFP/C cells is an insufficient driving force to re-homogenize the SOC within the electrodes should it become non-uniform. Only when the non-uniformity reaches a certain critical point, would the homogenizing forces become more powerful. As a result, the capacity loss levels off after 2000 FEC, cf. Fig. 2b. The hypothesis leads to the question: what causes the SOC to become non-uniform in the first place? Several causes can be envisaged: temperature gradients,^{28,29} pressure gradients,^{29,30} tab location^{31,32} or effects related to non-uniform current density due to defects,³³ covering layers, anode/cathode overlap³⁴ or overhang areas.^{1,3} It could be argued that in the absence of a re-homogenizing driving force, it would be highly

unlikely that local lithium concentrations would remain homogeneous during cell operation. This would only be the case if an improbable combination of perfectly homogeneous electrodes, operating conditions and current density distribution were to occur. From the above mentioned, however, defects are unlikely to have played an important role in the investigated Sony cell. The same is true for overhang areas at the beginning or the end of the electrode spiral. This is the case because firstly, their area is negligible compared to the total electrode area in the case of the Sony cell (see Fig. 1) and secondly, because they could not explain the inhomogeneity in perpendicular direction to the length of the spiral.

Temperature gradients.—During operation, heat is generated quite uniformly across the electrodes. In a cylindrical cell, heat can be exchanged with the environment via the lateral surface as well as the top and bottom surfaces. This leads to temperature gradients in both parallel and perpendicular direction to the cylinder surface.^{28,29} Temperature gradients could cause two effects: first, via temperature-dependent electrode kinetics and transport, they lead to gradients in current density, which in turn may lead to a non-uniform SOC. Second, in conjunction with non-zero entropic coefficients, a difference in temperatures results in different equilibrium potentials of the electrodes. The entropic coefficient of graphite varies between -0.2 mV K^{-1} and 0.2 mV/K ^{35,36} and that of LFP between -0.1 mV K^{-1} and 0.1 mV/K ^{35,37}. The full cell entropic coefficient is positive over a wide range of medium SOC,³⁷ as the entropic coefficient of graphite is positive and is larger in absolute values than the negative LFP coefficient.

If the potential in each electrode is assumed to be uniform, the local SOC would need to diverge according to the cell or electrode equilibrium potential curve to adjust for the entropic voltage change. This could potentially affect the local cell SOC as well as the local

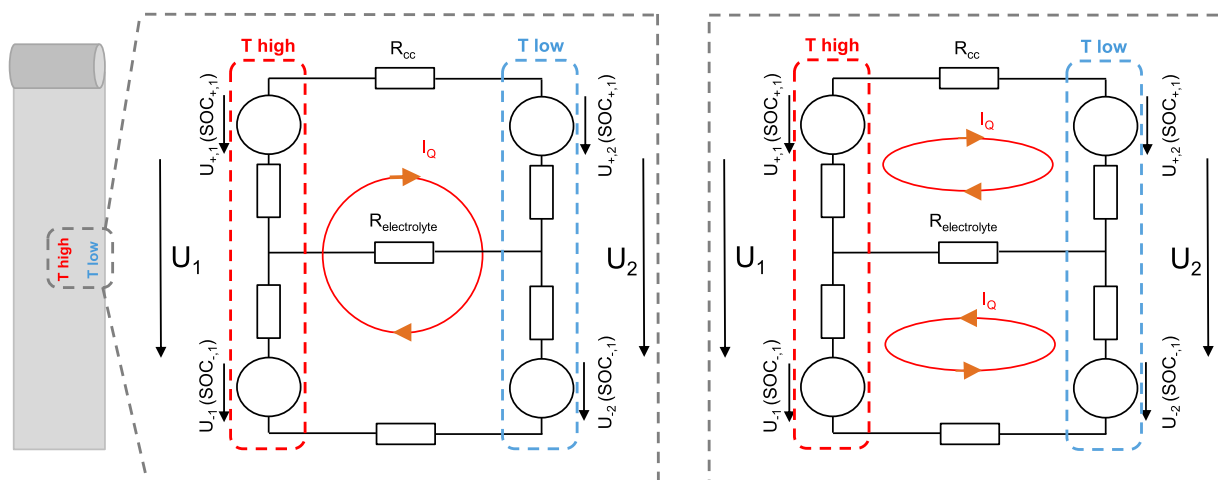


Figure 10. Two mechanisms of temperature-driven charge reallocation based on a simple cell model. Each cell consists of two unit cells connected in parallel via a current collector resistance and an electrolyte resistance. Each unit cell consists of two “electrodes” represented by a voltage source (circles) and a resistance (rectangles). In both schematics, the left unit cell has a higher temperature than the right unit cell. In the right schematic, in-plane currents alter the local electrode SOC. In the left schematic, through-plane currents alter the local cell SOC.

electrode SOC. In Fig. 10, two hypothetical mechanisms based on a simple cell model are sketched out. Each model cell consists of two elementary cells at different temperatures (high and low) which are connected in parallel via the current collectors and an ionic path through the electrolyte. Their voltages, U_1 and U_2 , are virtually identical due to the parallel connection via the current collectors. In both model cells, no external current flows into or out of the cell. In the left model cell, through-plane currents alter the local cell SOC. This is an instantaneous reaction to any temperature gradient within a cell, provided the full cell entropic coefficient is non-zero. In the right model cell, in-plane currents alter the local electrode SOC. As these currents must take the ionic path through the electrolyte, they should be much smaller than the through-plane currents. Nevertheless, they would slowly redistribute the lithium content within each electrode until a new equilibrium dictated by the electrode’s entropic coefficient, local equilibrium potential and temperature was reached. In a real cell, both mechanisms should occur simultaneously and influence one another. Could these mechanisms explain the non-uniform lithium distribution we have observed? In a spirally wound cell, due to the good heat conduction of the current collector foils, temperature gradients along the height of the cell are small.³⁸ However, the equilibrium potential curve of LFP is essentially flat, which means that SOC can differ considerably even with a temperature difference of a few Kelvin and an entropic coefficient of -0.1 mV K^{-1} . Admittedly, if we assume that the temperature at the electrode edge is slightly lower than in the center, the negative entropic coefficient would result in a lower local SOC at the edge compared to the center, opposite to what is actually observed.

Anode/cathode overlap.—Another possible factor in creating SOC non-uniformity could be geometrical. At the electrode edges, the anode surface projects beyond that of the cathode. This overlap is designed with the aim of avoiding lithium plating on the anode surface. The additional anode surface in the overlap absorbs the locally higher current densities that result from the exposed side faces of the electrodes.³⁴ Assuming current density and, in consequence, cycle depth are higher at the edges than in the rest of the electrode, two mechanisms that redistribute the lithium content in the electrodes can be conceived:

First, in the back and forth motion of ions between the electrodes, we may think of the location of arrival of an individual ion on the intercalating electrode as following a probability density function: The ion is most likely to take the shortest path, perpendicular to the

electrode surface, and to arrive just opposite from where it de-intercalated. It is less likely to move at a more acute angle to the electrode surface and take a longer path. In an ideal cell this would not lead to non-uniform SOC as on average, the lateral movements would balance themselves out. However, if there is a “disturbance,” this balance may be lost. The edge region, where we assume current densities are higher than elsewhere, could attract more lithium ions than average. Upon repeated cycling, lithium ions would become concentrated at the edges. In electrodes that have significant gradients in their equilibrium potential curves increasing local potentials would counteract these high local current densities, but this would not be the case with LFP.

Second, a “pumping mechanism”: If cycle depth is higher at the edges, there will be an in-plane movement of ions to equalize the local SOC within the electrodes. If this equalization process is much slower in one electrode than in the other (it could be slow in LFP due to its flat voltage characteristic), lithium ions would slowly accumulate at the edge of that electrode. The other electrode’s lithium distribution would be uniform. This also disagrees with the experimental evidence. There would need to be some directional process to explain charge accumulation in both electrodes by this pumping mechanism. A possible candidate for this could be asymmetric overpotential in charge/discharge due to hysteresis in the equilibrium potential curves of LFP.³⁹

Passivating layer.—A covering layer in the electrode center could lead to higher current densities in the uncovered areas, and have similar consequences to the electrode overlap mechanism described above. However, the grey stripe that can be seen in Fig. 8c, which may be a covering layer, only covers about one fifth of its height and fails to extend to the edge area in which the observed inhomogeneities emerge.

Pressure gradients.—The cylindrical cell case can be assumed to have a higher stiffness at the top and bottom than in the center. Upon intercalation-driven expansion of the electrodes during cycling, pressure on the electrodes would be higher in the edge regions compared to the center. This higher pressure could increase current density and electrode utilization and, again, have similar consequences to the electrode overlap mechanism.

In summary, while we may reasonably assume that non-uniform charge distribution causes the loss of accessible capacity, we cannot yet determine the reasons for the non-uniformity with certainty. As a starting point, cylindrical cells with other chemistries than LFP/C

must be investigated in shallow-cycle scenarios. Additionally, temperature and pressure gradients could be applied from the outside to the LFP/C cells used in this study. Furthermore, LFP/C cells in pouch format could provide valuable insights regarding the influence of cell design, especially if their surface temperature could be controlled locally. Finally, the possibility of charge accumulation at electrode edges under some of the proposed scenarios could also be examined using physicochemical models.

Conclusions

This work shows that strongly non-uniform charge distribution may be the cause of significant reversible capacity losses in LFP/C cells. Commercial cylindrical LFP/C cells were cycled continuously with low cycle depths, an experiment which reproduces the operating conditions in primary control reserve applications.⁴⁰ Cycling with these low cycle depths led to significantly higher capacity losses than with full cycles. A large portion of the capacity losses with low cycle depths could be recuperated. The most effective recuperation method was holding the cells at their lower cut-off voltage. After recuperation, the relative capacity of low cycle depth cells was higher than that of full cycle cells. DVA, color differences in the graphite anode and experiments with harvested electrode material have provided both direct and indirect experimental evidence of non-uniform charge distribution in the low cycle depth cells.


We have argued that the low potential gradients of LFP and graphite over a large SOC range may not provide enough driving force to re-homogenize the charge distribution in the electrodes, once it has become non-uniform. We have discussed hypotheses based on temperature, entropy and cell design that provide clues for identifying the true origin of the non-uniformity in the future.

Acknowledgments

This work was financially supported by the German Federal Ministry of Education and Research (BMBF) in the projects ExZellTUM II (03XP0081) and ExZellTUM III (03XP0255) and by the Technical University of Munich. The responsibility for this publication rests with the authors.

ORCID

Franz B. Spingler  <https://orcid.org/0000-0002-6523-3986>

Maik Naumann  <https://orcid.org/0000-0002-1995-3069>

Andreas Jossen  <https://orcid.org/0000-0003-0964-1405>

References

1. J. Wilhelm, S. Seidlmayer, P. Keil, J. Schuster, A. Kriele, R. Gilles, and A. Jossen, *J. Power Sources*, **365**, 327 (2017).
2. M. Lewerenz, J. Münnix, J. Schmalstieg, S. Käbitz, M. Knips, and D. U. Sauer, *J. Power Sources*, **345**, 254 (2017).
3. M. Lewerenz, G. Fuchs, L. Becker, and D. U. Sauer, *Journal of Energy Storage*, **18**, 149 (2018).
4. M. Lewerenz, P. Dechent, and D. U. Sauer, *Journal of Energy Storage*, **21**, 680 (2019).
5. M. Naumann, M. Schimpe, P. Keil, H. C. Hesse, and A. Jossen, *Journal of Energy Storage*, **17**, 153 (2018).
6. M. Naumann, F. B. Spingler, and A. Jossen, *J. Power. Sources.*, **451**, 227 (2020).
7. K. Rumpf, M. Naumann, and A. Jossen, *Journal of Energy Storage*, **14**, 224 (2017).
8. E. Sarasketa-Zabala, I. Gandiaga, E. Martinez-Laserna, L. M. Rodriguez-Martinez, and I. Villarreal, *J. Power Sources*, **275**, 573 (2015).
9. P. Keil and A. Jossen, *Journal of Energy Storage*, **6**, 125 (2016).
10. M. Petzl and M. A. Danzer, *J. Power Sources*, **254**, 80 (2014).
11. C. von Lüders, V. Zinth, S. V. Erhard, P. J. Osswald, M. Hofmann, R. Gilles, and A. Jossen, *J. Power Sources*, **342**, 17 (2017).
12. S. Schindler, M. Bauer, M. Petzl, and M. A. Danzer, *J. Power Sources*, **304**, 170 (2016).
13. I. D. Campbell, M. Marzook, M. Marinescu, and G. J. Offer, *J. Electrochem. Soc.*, **166**, A725 (2019).
14. M. C. Smart, B. V. Ratnakumar, M. C. Smart, and B. V. Ratnakumar, *J. Electrochem. Soc.*, **158**, A379 (2011).
15. M. C. Smart, B. V. Ratnakumar, L. Wbitcanack, K. Chin, M. Rodriguez, and S. Surampudi, *Seventeenth Annual Battery Conference on Applications and Advances* (2002).
16. J. Dahn, *Phys. Rev. B*, **44**, 9170 (1991).
17. T. Ohzuku, *J. Electrochem. Soc.*, **140**, 2490 (1993).
18. M. Dubarry and B. Y. Liaw, *J. Power Sources*, **194**, 541 (2009).
19. S. Schindler and M. A. Danzer, *J. Power Sources*, **343**, 226 (2017).
20. M. Lewerenz, A. Marongiu, A. Warnecke, and D. U. Sauer, *J. Power Sources*, **368**, 57 (2017).
21. D. Guérard and A. Herold, *Carbon*, **13**, 337 (1975).
22. V. A. Nalimova, D. Guérard, M. Lelaurain, and V. Fateev, *Carbon*, **33**, 177 (1995).
23. S. J. Harris, A. Timmons, D. R. Baker, and C. Monroe, *Chem. Phys. Lett.*, **485**, 265 (2010).
24. M. Petzl, M. Kasper, and M. A. Danzer, *J. Power Sources*, **275**, 799 (2015).
25. D. Burrow, K. Sergeeva, S. Calles, K. Schorb, A. Börger, C. Roth, and P. Heitjans, *J. Power Sources*, **307**, 806 (2016).
26. Q. Q. Liu, D. J. Xiong, R. Petibon, C. Y. Du, and J. R. Dahn, *J. Electrochem. Soc.*, **163**, A3010 (2016).
27. J. Wandt, P. Jakes, J. Granwehr, R.-A. Eichel, and H. A. Gasteiger, *Mater. Today*, **21**, 231 (2017).
28. Y. Zhao, Y. Patel, T. Zhang, and G. J. Offer, *J. Electrochem. Soc.*, **165**, A3169 (2018).
29. M. Klett, R. Eriksson, J. Groot, P. Svens, K. Ciosek Högström, R. W. Lindström, H. Berg, T. Gustafson, G. Lindbergh, and K. Edström, *J. Power Sources*, **257**, 126 (2014).
30. T. C. Bach, S. F. Schuster, E. Fleder, J. Müller, M. J. Brand, H. Lorrmann, A. Jossen, and G. Sextl, *Journal of Energy Storage*, **5**, 212 (2016).
31. P. J. Osswald, S. V. Erhard, A. Noel, P. Keil, F. M. Kindermann, H. Hoster, and A. Jossen, *J. Power Sources*, **314**, 93 (2016).
32. P. J. Osswald, S. V. Erhard, J. Wilhelm, H. E. Hoster, and A. Jossen, *J. Electrochem. Soc.*, **162**, A2099 (2015).
33. J. Cannarella and C. B. Arnold, *J. Electrochem. Soc.*, **162**, A1365 (2015).
34. M. Tang, P. Albertus, and J. Newman, *J. Electrochem. Soc.*, **156**, A390 (2009).
35. V. V. Viswanathan, D. Choi, D. Wang, W. Xu, S. Towne, R. E. Williford, J.-G. Zhang, J. Liu, and Z. Yang, *J. Power Sources*, **195**, 3720 (2010).
36. Y. Reynier, R. Yazami, and B. Fultz, *J. Power Sources*, **119–121**, 850 (2003).
37. S. J. Bazinski and X. Wang, *J. Electrochem. Soc.*, **161**, A168 (2014).
38. S. J. Drake, D. A. Wetz, J. K. Ostanek, S. P. Miller, J. M. Heinzel, and A. Jain, *J. Power Sources*, **252**, 298 (2014).
39. Y. Zhu and C. Wang, *J. Power Sources*, **196**, 1442 (2011).
40. A. Zeh, M. Müller, M. Naumann, H. Hesse, A. Jossen, and R. Witzmann, *Batteries*, **2**, 29 (2016).

6 Summary, Discussion and Outlook

The objective of this thesis was to deepen the understanding of cause-effect relationships between non-uniform physical properties and operating states in lithium-ion cells. Based on a review of the relevant literature, specific research questions were defined in the introduction and addressed in an initial *methods* chapter and three subsequent main chapters. Below, the contents of these chapters are summarized, followed by a discussion of the findings based on the research questions. Finally, the relevance of this contribution to research and application is discussed and suggestions on possible research approaches for the most pressing remaining challenges is provided.

Summary and Discussion

In chapter 2, the development of the methods used in the subsequent chapters which exceed the state-of-the-art were discussed in greater detail. First, the application of a multi-dimensional laser scan of pouch cells for the detection of lithium plating was presented. Based on the difference between the volume requirements of deposited, metallic lithium and lithium intercalated into graphite and considering thermal expansion, the occurrence of localized abnormal thickness change events could be verified and associated with the local onset of lithium plating. Second, the optimization of an electrochemical dilatometry cell setup that facilitates the measurement of the intercalation-based expansion and contraction of single electrodes was described. The setup was improved to the point that it enabled electrochemically stable experiments with coulombic efficiencies comparable to those of coin cells and, in consequence, provided trustworthy data. Third, methods to detect and quantify cell- and electrode-level SOC inhomogeneity were discussed. It was shown that coin cells, with their reliability and ease of assembly, are a well-suited, alternative means to assess the amount of cyclable lithium in specific electrode areas.

In chapter 3, the multi-dimensional laser scan was applied to the investigation of commercial pouch cells with capacities of 3.3 Ah and 5.0 Ah manufactured by Kokam, South Korea. In four locations, which were similar in both cells, abnormal thickness change behavior was detected. This could be traced back to an apparently pore-clogging contaminant that was found on every second layer in all of the investigated cells. The contamination was assumed to originate from the manufacturing process. Using the 3.3 Ah cell, the assumed causality between localized lithium plating and the occurrence of localized, excessive thickness change events was investigated thoroughly and confirmed. Proof of lithium plating was provided by

voltage relaxation analysis and post-mortem inspection. The experiments suggested that the sensitivity of the proposed thickness measurements for lithium plating detection was higher than for the voltage relaxation analysis. The applicability of the method was demonstrated by parameterizing a multi-stage CC-CV fast charging protocol based solely on limiting thickness change. In a cycle test with 1000 cycles, the charging protocol compared favorably to standard 1C CC-CV charging.

In chapter 4, mechanical-electrochemical interactions in constrained lithium-ion cells were investigated. Initially, the improved dilatometry setup was used to measure the intercalation-based thickness changes of a variety of graphite and NMC-based electrodes, including the harvested negative and positive electrodes of the 3.3 Ah Kokam cell. The reversible thickness changes observed for graphite of between 4.9 % and 6.5 % are in agreement with literature values. For NMCs, for which literature data had been scarce and imprecise, maximum reversible expansions of between 1.3 % and 1.7 % were observed. A comparison of the NMC electrode thickness changes to crystal structure changes measured by XRD revealed significant differences, suggesting that the micro-mechanical behavior cannot be directly transferred to that of the electrode level.

In the second part of the chapter, the dilatometry results served as input parameters for an electrochemical-mechanical model. A Newman-type pseudo-3D model was set up to represent a partially compressed cell, so that the through- and in-plane current densities, as well as the local lithium concentrations within the compressed and uncompressed areas and at their boundaries, could be analyzed. For the compressed areas, a simplified mechanical model was devised, which computes the layer thickness and the porosity of both electrodes and the separator as a function of the degree of lithiation and the applied stack pressure. In addition to the dilatometry parameter input, the model relied on compressive moduli of the cell components which were also determined experimentally. The modeling was followed by a validation experiment, where the 2.1 Ah Kokam cell was cycled while being locally compressed by a 1.4 cm² punch. Model and experimental results coherently showed that the risk of lithium plating in the compressed area increases with pressure, with visible deposits on the anode surface above 1 MPa.

In chapter 5, the causes and effects of laterally non-uniform lithium distributions in the electrodes of lithium-ion cells were analyzed. It was found that commercial, cylindrical LFP/graphite cells lose usable capacity at a high rate when being subjected to continuous shallow cycling around intermediate SOC. The capacity losses were reversed almost completely by storing the cells at 0 % SOC or 100 % SOC for several days. With the help of coin cells, as described in the methods chapter, and by DVA, it was shown that the redistribution of lithium was the cause of this behavior. During shallow cycling, the lithium seemed to accumulate at the top and bottom edges of the jelly roll. This was assumed to be possible because of the absence of significant potential differences in both graphite and LFP at intermediate SOC that would counteract such a reallocation. This led to the question of which

forces might drive such a process. Mechanisms based on temperature, mechanical pressure, and geometry effects were proposed and discussed.

1. Research Question: *Is it possible to detect manufacturing inhomogeneity during cell operation and adjust the operational strategy accordingly?*

The results from chapter 3 indicate that a defect or contaminant which produces a local thickness change irregularity can be detected by a locally-resolved thickness measurement. These thickness-change irregularities can result from an anomalous utilization of the electrode material around the inhomogeneity. Chapter 4 has shown that depending on the induced local transport property change, either a local underutilization resulting in less intercalation-driven expansion or local overutilization resulting in more intercalation-driven expansion or even lithium plating can occur. It was also discussed in section 3.1 that a differing thermal expansion behavior of a production contaminant could lead to abnormal, local thickness changes. In the cell investigated in section 3.2, a pore-blocking contaminant appeared on 8 out of 16 layers, producing thickness change irregularities due to lithium plating in the 10 μm -range. Given the repeatability of 0.8 μm of the employed 2330 series sensor by LMI3D, Canada, even isolated contaminations on a single cell layer should be detectable. Even more sensitive sensors with a repeatability of up to 0.2 μm are available from the same manufacturer as well [104]. Furthermore, section 3.2 suggests that once an inhomogeneity provoking lithium plating is detected by its thickness change footprint, adjusting the charging current so that excessive local thickness changes do not appear, can extend battery life considerably.

For application, however, optical cell thickness measurements are impractical. Cells are usually fixated at their surfaces and/or housed from all sides. Monitoring the resulting pressure across the cell surface could be a realistic alternative. Chapter 4 shows that the expansion of a freestanding cell translates into a pressure increase when the cell is mechanically constrained. Of course, monitoring the pressure would mean additional space requirements and cost, but especially for large format BEV2 cells with capacities of 100 Ah and more, the benefits may dominate. Besides the ability to detect aging phenomena in real-time, as in section 3.1, the stack pressure evolution could also be tracked over time. By coupling mechanical and electrochemical models as in chapter 4, transport property changes in the electrodes and the separator could be identified and the operational strategy adapted.

2. Research Question: *Does an uneven compression of cell stacks provoke localized lithium plating?*

The modeling results from section 4.1 demonstrate that the risk of localized lithium plating is tied to the current density distribution, which in turn, is affected by an uneven compression of the cell stack. For the extreme case where a separator is compressed to such an extent that it effectively blocks ion transport, it was found that the current density peaks at the edge of the compressed area cause lithium plating, confirming the findings of Cannarella et al. [27]. It can be assumed that the same principal mechanism was responsible for the localized lithium plating found around the pore-blocking contaminations in section 3.2. For the more

realistic case of a local stack compression that reduces the porosity in the separator and in the electrodes, but does not lead to a total ion transport blockage, the findings were different. Here, lithium plating occurred almost uniformly on the compressed area. Even though the current density there was reduced, the fact that the ion transport into the depth of the anode was slowed down, led to an overcharge of the anode at the separator interface. This illustrates that ultimately, whether plating is more likely to occur in the compressed area or at its edge depends on the effective transport vs. compressive force relationships of the electrodes and the separator. These relationships are determined by the macroscopic structural stability of the components as well as their microstructure.

In any case, with real, compressible cell components, an uneven compression will affect the current density distribution and invariably increase the risk of lithium plating. Whether plating actually occurs in a given scenario of local compression depends on the margin of safety determined by the cell design and the other operating conditions. Generalized statements would therefore not be appropriate. However, this thesis provides the methods necessary to assess the risk of localized lithium plating for any lithium-ion cell under uneven compression.

3. Research Question: *Can non-uniformities of operating states cause significant variations of the usable capacity?*

In the commercial 26650 cylindrical cells investigated in chapter 5, a usable capacity loss and subsequent recuperation of 19% of the initial capacity was observed. It was shown that the underlying cause was laterally diverging SOC_s in the electrodes. Lithium was accumulated near the electrode edges and was later redistributed. The capacity loss can be explained by the voltage monitored at the tabs, i.e. the combined local voltages across the electrode, reaching the lower and upper cut-off prematurely. This occurs when the OCV characteristic is rather flat in the intended operational range and steep at the margins, a common feature of lithium-ion batteries and especially pronounced in LFP/graphite cells. During charging, for example, the overcharging of just a fraction of the total electrode area would push up the average voltage disproportionately. This is different from the *anode overhang effect* described in the literature [56, 57], where lithium slowly redistributes into parts of the anode that do not have a cathode counterpart. In overhanging regions of the anode, intercalated lithium is virtually inaccessible in the time frame of normal cycling but, depending on the operating conditions, it can diffuse back and the usable capacity is regained.

The post-mortem analysis in chapter 5 also hinted at the occurrence of lithium plating near the edges, where lithium had accumulated. This seems to be a logical consequence of SOC non-uniformities. The relatively more-lithiated anode areas may push up the average cell voltage during charging and eventually cause the reaching of the voltage cut-off and the charging process to stop, but only after they have been overlithiated to a certain degree. This means that the intrinsically reversible mechanism of SOC non-uniformity may well lead to irreversible capacity losses. The origin of these SOC non-uniformities, however, could not be definitely determined. The proposed mechanisms based on temperature, mechanical pressure inhomogeneity, and geometry effects may all contribute to laterally diverging SOC_s. In particular,

the effect of locally different compressive forces on the current density distribution has been demonstrated in section 4.2. Unfortunately, the individual contributions of those mechanisms remain unclear as does the degree to which the interplay of different mechanisms creates the effect.

Outlook

The relevance of this work results on the one hand from the proposed methods and on the other hand from the obtained results and findings. Some issues require further work and many of the results also imply new challenges and questions.

The multi-dimensional laser scanning method and the relationships between manufacturing inhomogeneity, lithium plating and thickness changes could be applied in end-of-line testing as well as in online monitoring of cells wherever they are installed. As pouch and prismatic cells in module assemblies are usually embedded and constrained at their faces, a locally resolved thickness measurement is difficult to implement. Therefore, a suggested avenue for further research is the investigation of local mechanical pressure as an indicator of inhomogeneity and local aging processes. This also relates to the improved dilatometry setup. With its high electrochemical stability, it enables the differentiation between the thickness change behavior during the first cycles of a fresh electrode and thickness changes in subsequent cycles. For research on new silicon-containing anode materials that undergo complex structural changes, this differentiation becomes increasingly important. Furthermore, the finding that the electrode-level thickness change behavior is quite different from the microstructural changes observable by XRD warrants further investigation of the relationships between SOC, thickness change, external pressure, and electrode porosity. Meanwhile, the obtained lithiation vs. thickness change relationships of graphites and NMC-based electrodes should prove useful for modeling purposes and help guide the mechanical design of battery modules.

Further, the combined material testing and electrochemical-mechanical modeling provide a blueprint for the evaluation of the effects of uniform and non-uniform mechanical compression on lithium-ion cells. Due to the aforementioned discrepancies between crystal-level structure change and electrode-level thickness change, future work should aim to incorporate more realistic dependencies between electrode or separator compression and their transport property changes. Beyond the qualitative insights provided, this would add reliability to the quantitative modeling results. Thus, it should ultimately be possible to accurately predict the local pressure limit that would trigger the onset of lithium plating as a function of the remaining operating conditions.

The finding of significant usable capacity losses upon long-term shallow cycling of LFP/graphite cells highlights the importance of understanding the possibly severe effects of non-uniform operating states and is practically relevant for applications with the corresponding usage profiles. For example, frequency regulation using stationary battery systems, where the cell SOCs

mostly oscillate around intermediate SOCs or self-driving taxis in 24 h operation that would frequently partially charge between passenger rides. The mechanism by which the lithium distribution in the cell becomes so strongly non-uniform in the shallow cycling regime is yet to be fully understood. Future work should attempt to detangle the different proposed influencing factors related to temperature, mechanical pressure, and electrode geometry.

Overall, this thesis has shown that manufacturing inhomogeneity or other physical imperfections, geometric effects, and gradients of temperature and mechanical pressure must all be considered simultaneously when operating lithium-ion cells. Methods that should improve both the characterization and assessment of the effects of those non-uniform physical properties and operating states have been proposed. Understanding these effects will help optimize operation strategies and inform decisions on the necessity of investing in the improvement of manufacturing processes, end-of-line testing, or in-operation monitoring in order to maximize battery safety and lifetime at the lowest possible cost.

References

- [1] C. Pillot. *The Rechargeable Battery Market and Main Trends 2011-2020*. Paris, France, May 28th, 2019.
- [2] Bloomberg Finance L.P. *Electric Vehicle Outlook 2020*. 2020.
- [3] T. R. Hawkins, B. Singh, G. Majeau-Bettez, and A. H. Strømman. “Comparative Environmental Life Cycle Assessment of Conventional and Electric Vehicles”. In: *Journal of Industrial Ecology* 17.1 (2013), pp. 53–64.
- [4] W. Kempton and J. Tomić. “Vehicle-to-grid power implementation: From stabilizing the grid to supporting large-scale renewable energy”. In: *Journal of Power Sources* 144.1 (2005), pp. 280–294.
- [5] D. B. Agusdinata, W. Liu, H. Eakin, and H. Romero. “Socio-environmental impacts of lithium mineral extraction: towards a research agenda”. In: *Environmental Research Letters* 13.12 (2018), p. 123001.
- [6] Hinrich Helms, Claudia Kämper, Kirsten Biemann, Udo Lambrecht, Julius Jöhrens, Kerstin Meyer. *Klimabilanz von Elektroautos: Einflussfaktoren und Verbesserungspotenzial*. Ed. by Agora Energiewende. 2019. URL: https://www.agora-verkehrswende.de/fileadmin/Projekte/2018/Klimabilanz_von_Elektroautos/Agora-Verkehrswende_22_Klimabilanz-von-Elektroautos_WEB.pdf (visited on 09/14/2021).
- [7] Anika Regett, Wolfgang Mauch, Ulrich Wagner. *Carbon footprint of electric vehicles - a plea for more objectivity*. Ed. by Forschungsstelle für Energiewirtschaft (FfE) e.V. 2021. URL: https://www.ffe.de/attachments/article/856/Carbon_footprint_EV_FfE.pdf (visited on 09/14/2021).
- [8] H. Ambrose, A. Kendall, M. Lozano, S. Wachche, and L. Fulton. “Trends in life cycle greenhouse gas emissions of future light duty electric vehicles”. In: *Transportation Research Part D: Transport and Environment* 81 (2020), p. 102287.
- [9] Cordella, M., Alfieri, F. and Sanfelix Forner, J. *Guidance for the assessment of material efficiency: application to smartphones*. Ed. by Joint Research Council of the European Commission. Luxembourg, 2020. URL: <https://publications.jrc.ec.europa.eu/repository/handle/JRC116106> (visited on 09/14/2021).
- [10] L. Bravo Diaz, X. He, Z. Hu, F. Restuccia, M. Marinescu, J. V. Barreras, Y. Patel, G. Offer, and G. Rein. “Review—Meta-Review of Fire Safety of Lithium-Ion Batteries: Industry Challenges and Research Contributions”. In: *Journal of The Electrochemical Society* 167.9 (2020), p. 090559.

- [11] A. Mayyas, D. Steward, and M. Mann. “The case for recycling: Overview and challenges in the material supply chain for automotive li-ion batteries”. In: *Sustainable Materials and Technologies* 19 (2019), e00087.
- [12] C. P. Grey and D. S. Hall. “Prospects for lithium-ion batteries and beyond—a 2030 vision”. In: *Nature communications* 11.1 (2020), p. 6279.
- [13] H.-H. Ryu, H. H. Sun, S.-T. Myung, C. S. Yoon, and Y.-K. Sun. “Reducing cobalt from lithium-ion batteries for the electric vehicle era”. In: *Energy & Environmental Science* 14.2 (2021), pp. 844–852.
- [14] Y. Ding, Z. P. Cano, A. Yu, J. Lu, and Z. Chen. “Automotive Li-Ion Batteries: Current Status and Future Perspectives”. In: *Electrochemical Energy Reviews* 2.1 (2019), pp. 1–28.
- [15] K. Ozawa. “Lithium-ion rechargeable batteries with LiCoO₂ and carbon electrodes: the LiCoO₂/C system”. In: *Solid State Ionics* 69.3-4 (1994), pp. 212–221.
- [16] J. Xie and Y.-C. Lu. “A retrospective on lithium-ion batteries”. In: *Nature communications* 11.1 (2020), p. 2499.
- [17] N. Nitta, F. Wu, J. T. Lee, and G. Yushin. “Li-ion battery materials: Present and future”. In: *Materials Today* 18.5 (2015), pp. 252–264.
- [18] J.-M. Tarascon and M. Armand. “Issues and challenges facing rechargeable lithium batteries”. In: *Nature* 414.6861 (2001), pp. 359–367.
- [19] A. Jossen and W. Weydanz. *Moderne Akkumulatoren richtig einsetzen*. 2. Auflage. Göttingen: Cuvillier Verlag, 2019.
- [20] D. Linden and T. B. Reddy. *Handbook of batteries*. 3rd ed. McGraw-Hill handbooks. New York: McGraw-Hill.
- [21] R. Korthauer, ed. *Handbuch Lithium-Ionen-Batterien*. Berlin, Heidelberg and s.l.: Springer Berlin Heidelberg, 2013.
- [22] Jeff Dahn and Grant M. Ehrlich, ed. *Chapter 26: Lithium-Ion Batteries*. McGraw-Hill Education, 2011.
- [23] A. Kwade, W. Haselrieder, R. Leithoff, A. Modlinger, F. Dietrich, and K. Droeder. “Current status and challenges for automotive battery production technologies”. In: *Nature Energy* 3.4 (2018), pp. 290–300.
- [24] T. Hetteshaimer et al. *Entwicklungsperspektiven für Zellformate von Lithium-Ionen-Batterien in der Elektromobilität*. Ed. by Fraunhofer-Allianz Batterien. Pfinztal, 2017.
- [25] S. Müller, J. Eller, M. Ebner, C. Burns, J. Dahn, and V. Wood. “Quantifying Inhomogeneity of Lithium Ion Battery Electrodes and Its Influence on Electrochemical Performance”. In: *Journal of The Electrochemical Society* 165.2 (2018), A339–A344.
- [26] D. Beck, P. Dechent, M. Junker, D. U. Sauer, and M. Dubarry. “Inhomogeneities and Cell-to-Cell Variations in Lithium-Ion Batteries, a Review”. In: *Energies* 14.11 (2021), p. 3276.

-
- [27] J. Cannarella and C. B. Arnold. “The Effects of Defects on Localized Plating in Lithium-Ion Batteries”. In: *Journal of The Electrochemical Society* 162.7 (2015), A1365–A1373.
- [28] D. Mohanty, E. Hockaday, J. Li, D. K. Hensley, C. Daniel, and D. L. Wood. “Effect of electrode manufacturing defects on electrochemical performance of lithium-ion batteries: Cognizance of the battery failure sources”. In: *Journal of Power Sources* 312 (2016), pp. 70–79.
- [29] L. David, R. E. Ruther, D. Mohanty, H. M. Meyer, Y. Sheng, S. Kalnaus, C. Daniel, and D. L. Wood. “Identifying degradation mechanisms in lithium-ion batteries with coating defects at the cathode”. In: *Applied Energy* 231 (2018), pp. 446–455.
- [30] M. Schindler, J. Sturm, S. Ludwig, A. Durdel, and A. Jossen. “Comprehensive Analysis of the Aging Behavior of Nickel-Rich, Silicon-Graphite Lithium-Ion Cells Subject to Varying Temperature and Charging Profiles”. In: *Journal of The Electrochemical Society* 168.6 (2021), p. 060522.
- [31] A. A. Franco. “Multiscale modelling and numerical simulation of rechargeable lithium ion batteries: Concepts, methods and challenges”. In: *RSC Advances* 3.32 (2013), pp. 13027–13058.
- [32] W. Bauer and D. Nötzel. “Rheological properties and stability of NMP based cathode slurries for lithium ion batteries”. In: *Ceramics International* 40.3 (2014), pp. 4591–4598.
- [33] V. Wenzel, H. Nirschl, and D. Nötzel. “Challenges in Lithium-Ion-Battery Slurry Preparation and Potential of Modifying Electrode Structures by Different Mixing Processes”. In: *Energy Technology* 3.7 (2015), pp. 692–698.
- [34] H. Bockholt, M. Indrikova, A. Netz, F. Golks, and A. Kwade. “The interaction of consecutive process steps in the manufacturing of lithium-ion battery electrodes with regard to structural and electrochemical properties”. In: *Journal of Power Sources* 325 (2016), pp. 140–151.
- [35] S. Jaiser, M. Müller, M. Baunach, W. Bauer, P. Scharfer, and W. Schabel. “Investigation of film solidification and binder migration during drying of Li-Ion battery anodes”. In: *Journal of Power Sources* 318 (2016), pp. 210–219.
- [36] M. Müller, L. Pfaffmann, S. Jaiser, M. Baunach, V. Trouillet, F. Scheiba, P. Scharfer, W. Schabel, and W. Bauer. “Investigation of binder distribution in graphite anodes for lithium-ion batteries”. In: *Journal of Power Sources* 340 (2017), pp. 1–5.
- [37] S. Jaiser, J. Kumberg, J. Klaver, J. L. Urai, W. Schabel, J. Schmatz, and P. Scharfer. “Microstructure formation of lithium-ion battery electrodes during drying – An ex-situ study using cryogenic broad ion beam slope-cutting and scanning electron microscopy (Cryo-BIB-SEM)”. In: *Journal of Power Sources* 345 (2017), pp. 97–107.

- [38] F. Font, B. Protas, G. Richardson, and J. M. Foster. “Binder migration during drying of lithium-ion battery electrodes: Modelling and comparison to experiment”. In: *Journal of Power Sources* 393 (2018), pp. 177–185.
- [39] M. M. Forouzan, B. A. Mazzeo, and D. R. Wheeler. “Modeling the Effects of Electrode Microstructural Heterogeneities on Li-Ion Battery Performance and Lifetime”. In: *Journal of The Electrochemical Society* 165.10 (2018), A2127–A2144.
- [40] X. M. Liu, A. Fang, M. P. Haataja, and C. B. Arnold. “Size Dependence of Transport Non-Uniformities on Localized Plating in Lithium-Ion Batteries”. In: *Journal of The Electrochemical Society* 165.5 (2018), A1147–A1155.
- [41] R. Schröder, M. Aydemir, A. Glodde, and G. Seliger. “Design and Verification of an Innovative Handling System for Electrodes in Manufacturing Lithium-ion Battery Cells”. In: *Procedia CIRP* 50 (2016), pp. 641–646.
- [42] L. Hoffmann, J.-K. Grathwol, W. Haselrieder, R. Leithoff, T. Jansen, K. Dilger, K. Dröder, A. Kwade, and M. Kurrat. “Capacity Distribution of Large Lithium–Ion Battery Pouch Cells in Context with Pilot Production Processes”. In: *Energy Technology* 8.2 (2020), p. 1900196.
- [43] J. Kurfer, M. Westermeier, C. Tammer, and G. Reinhart. “Production of large-area lithium-ion cells – Preconditioning, cell stacking and quality assurance”. In: *CIRP Annals* 61.1 (2012), pp. 1–4.
- [44] A. Fröhlich, R. Leithoff, C. von Boeselager, K. Dröder, and F. Dietrich. “Investigation of particulate emissions during handling of electrodes in lithium-ion battery assembly”. In: *Procedia CIRP* 78 (2018), pp. 341–346.
- [45] Y. Zhao, F. B. Spingler, Y. Patel, G. J. Offer, and A. Jossen. “Localized Swelling Inhomogeneity Detection in Lithium Ion Cells Using Multi-Dimensional Laser Scanning”. In: *Journal of The Electrochemical Society* 166.2 (2019), A27–A34.
- [46] Le Yang, H.-S. Chen, W.-L. Song, and D. Fang. “Effect of Defects on Diffusion Behaviors of Lithium-Ion Battery Electrodes: In Situ Optical Observation and Simulation”. In: *ACS applied materials & interfaces* 10.50 (2018), pp. 43623–43630.
- [47] O. Badmos, A. Kopp, T. Bernthaler, and G. Schneider. “Image-based defect detection in lithium-ion battery electrode using convolutional neural networks”. In: *Journal of Intelligent Manufacturing* 31.4 (2020), pp. 885–897.
- [48] G. Zhang, C. E. Shaffer, C.-Y. Wang, and C. D. Rahn. “Effects of Non-Uniform Current Distribution on Energy Density of Li-Ion Cells”. In: *Journal of The Electrochemical Society* 160.11 (2013), A2299–A2305.
- [49] Kiyomi Kozuki. “Sealed Rechargeable Battery: United States Patent”. 11/646327. 2010.
- [50] M. Defer, Y. Borthomieu, E. Ligneel, S. Badet, and D. Chocinski. “VL51ES (Generation 6) Li-Ion Cell for Satellites”. In: *E3S Web of Conferences* 16 (2017), p. 08004.

-
- [51] P. J. Osswald, S. V. Erhard, J. Wilhelm, H. E. Hoster, and A. Jossen. “Simulation and Measurement of Local Potentials of Modified Commercial Cylindrical Cells”. In: *Journal of The Electrochemical Society* 162.10 (2015), A2099–A2105.
- [52] S. V. Erhard et al. “Simulation and Measurement of the Current Density Distribution in Lithium-Ion Batteries by a Multi-Tab Cell Approach”. In: *Journal of The Electrochemical Society* 164.1 (2017), A6324–A6333.
- [53] M. Tang, P. Albertus, and J. Newman. “Two-Dimensional Modeling of Lithium Deposition during Cell Charging”. In: *Journal of The Electrochemical Society* 156.5 (2009), A390–A399.
- [54] B. Son, M.-H. Ryou, J. Choi, S.-H. Kim, J. M. Ko, and Y. M. Lee. “Effect of cathode/anode area ratio on electrochemical performance of lithium-ion batteries”. In: *Journal of Power Sources* 243 (2013), pp. 641–647.
- [55] B. Gyenes, D. A. Stevens, V. L. Chevrier, and J. R. Dahn. “Understanding Anomalous Behavior in Coulombic Efficiency Measurements on Li-Ion Batteries”. In: *Journal of The Electrochemical Society* 162.3 (2015), A278–A283.
- [56] J. Wilhelm, S. Seidlmayer, P. Keil, J. Schuster, A. Kriele, R. Gilles, and A. Jossen. “Cycling capacity recovery effect: A coulombic efficiency and post-mortem study”. In: *Journal of Power Sources* 365 (2017), pp. 327–338.
- [57] M. Lewerenz, G. Fuchs, L. Becker, and D. U. Sauer. “Irreversible calendar aging and quantification of the reversible capacity loss caused by anode overhang”. In: *Journal of Energy Storage* 18 (2018), pp. 149–159.
- [58] M. Lewerenz and D. U. Sauer. “Evaluation of cyclic aging tests of prismatic automotive LiNiMnCoO₂-Graphite cells considering influence of homogeneity and anode overhang”. In: *Journal of Energy Storage* 18 (2018), pp. 421–434.
- [59] M. Loveridge et al. “Looking Deeper into the Galaxy (Note 7)”. In: *Batteries* 4.1 (2018), p. 3.
- [60] F. Ebert, M. Spielbauer, M. Bruckmoser, and M. Lienkamp. *Simulation of Spatial Strain Inhomogeneities in Lithium-Ion-Cells Due to Electrode Dilation Dependent on Internal and External Cell Structures*. 2020.
- [61] A. Pfrang, A. Kersys, A. Kriston, D. U. Sauer, C. Rahe, S. Käbitz, and E. Figgemeier. “Geometrical Inhomogeneities as Cause of Mechanical Failure in Commercial 18650 Lithium Ion Cells”. In: *Journal of The Electrochemical Society* 166.15 (2019), A3745–A3752.
- [62] M. Hahn, H. Buqa, P. W. Ruch, D. Goers, M. E. Spahr, J. Ufheil, P. Novák, and R. Kötz. “A Dilatometric Study of Lithium Intercalation into Powder-Type Graphite Electrodes”. In: *Electrochemical and Solid-State Letters* 11.9 (2008), A151–A154.

- [63] O. Dolotko, A. Senyshyn, M. Mühlbauer, K. Nikolowski, and H. Ehrenberg. “Understanding structural changes in NMC Li-ion cells by in situ neutron diffraction”. In: *Journal of Power Sources* 255 (2014), pp. 197–203.
- [64] K. Funayama, T. Nakamura, N. Kuwata, J. Kawamura, T. Kawada, and K. Ameszawa. “Electromotive force measurements of LiCoO₂ electrode on a lithium ion-conducting glass ceramics under mechanical stress”. In: *Solid State Ionics* 285 (2016), pp. 75–78.
- [65] T. Pereira, Z. Guo, S. Nieh, J. Arias, and H. T. Hahn. “Embedding thin-film lithium energy cells in structural composites”. In: *Composites Science and Technology* 68.7-8 (2008), pp. 1935–1941.
- [66] T. Pereira, R. Scaffaro, Z. Guo, S. Nieh, J. Arias, and H. T. Hahn. “Performance of Thin-Film Lithium Energy Cells under Uniaxial Pressure”. In: *Advanced Engineering Materials* 10.4 (2008), pp. 393–399.
- [67] S. Golmon, K. Maute, and M. L. Dunn. “Numerical modeling of electrochemical–mechanical interactions in lithium polymer batteries”. In: *Computers & Structures* 87.23-24 (2009), pp. 1567–1579.
- [68] J. Gnanaraj, Y. S. Cohen, M. Levi, and D. Aurbach. “The effect of pressure on the electroanalytical response of graphite anodes and LiCoO₂ cathodes for Li-ion batteries”. In: *Journal of Electroanalytical Chemistry* 516.1-2 (2001), pp. 89–102.
- [69] J. Cannarella and C. B. Arnold. “Ion transport restriction in mechanically strained separator membranes”. In: *Journal of Power Sources* 226 (2013), pp. 149–155.
- [70] J. Cannarella, X. Liu, C. Z. Leng, P. D. Sinko, G. Y. Gor, and C. B. Arnold. “Mechanical Properties of a Battery Separator under Compression and Tension”. In: *Journal of The Electrochemical Society* 161.11 (2014), F3117–F3122.
- [71] Y. Pan and Z. Zhong. “Modeling the Ion Transport Restriction in Mechanically Strained Separator Membranes”. In: *Journal of The Electrochemical Society* 161.4 (2014), A583–A586.
- [72] V. Müller, R.-G. Scurtu, M. Memm, M. A. Danzer, and M. Wohlfahrt-Mehrens. “Study of the influence of mechanical pressure on the performance and aging of Lithium-ion battery cells”. In: *Journal of Power Sources* 440 (2019), p. 227148.
- [73] T. C. Bach, S. F. Schuster, E. Fleder, J. Müller, M. J. Brand, H. Lorrmann, A. Jossen, and G. Sextl. “Nonlinear aging of cylindrical lithium-ion cells linked to heterogeneous compression”. In: *Journal of Energy Storage* 5 (2016), pp. 212–223.
- [74] M. Lewerenz, A. Warnecke, and D. U. Sauer. “Post-mortem analysis on LiFePO₄ | Graphite cells describing the evolution & composition of covering layer on anode and their impact on cell performance”. In: *Journal of Power Sources* 369 (2017), pp. 122–132.

-
- [75] H. Maleki, S. A. Hallaj, J. R. Selman, R. B. Dinwiddie, and H. Wang. “Thermal Properties of Lithium–Ion Battery and Components”. In: *Journal of The Electrochemical Society* 146.3 (1999), pp. 947–954.
- [76] M. Steinhardt, E. I. Gillich, A. Rheinfeld, L. Kraft, M. Spielbauer, O. Bohlen, and A. Jossen. “Low-effort determination of heat capacity and thermal conductivity for cylindrical 18650 and 21700 lithium-ion cells”. In: *Journal of Energy Storage* 42 (2021), p. 103065.
- [77] Y. Zhao, Y. Patel, T. Zhang, and G. J. Offer. “Modeling the Effects of Thermal Gradients Induced by Tab and Surface Cooling on Lithium Ion Cell Performance”. In: *Journal of The Electrochemical Society* 165.13 (2018), A3169–A3178.
- [78] J. B. Robinson, J. A. Darr, D. S. Eastwood, G. Hinds, P. D. Lee, P. R. Shearing, O. O. Taiwo, and D. J. Brett. “Non-uniform temperature distribution in Li-ion batteries during discharge – A combined thermal imaging, X-ray micro-tomography and electrochemical impedance approach”. In: *Journal of Power Sources* 252 (2014), pp. 51–57.
- [79] J. Hou, M. Yang, D. Wang, and J. Zhang. “Fundamentals and Challenges of Lithium Ion Batteries at Temperatures between -40 and 60 °C”. In: *Advanced Energy Materials* 10.18 (2020), p. 1904152.
- [80] M. Steinhardt, E. I. Gillich, M. Stiegler, and A. Jossen. “Thermal conductivity inside prismatic lithium-ion cells with dependencies on temperature and external compression pressure”. In: *Journal of Energy Storage* 32 (2020), p. 101680.
- [81] P. J. Osswald, S. V. Erhard, A. Rheinfeld, B. Rieger, H. E. Hoster, and A. Jossen. “Temperature dependency of state of charge inhomogeneities and their equalization in cylindrical lithium-ion cells”. In: *Journal of Power Sources* 329 (2016), pp. 546–552.
- [82] B. Klein. *FEM: Grundlagen und Anwendungen der Finite-Element-Methode im Maschinen- und Fahrzeugbau : mit 12 Fallstudien und 20 Übungsaufgaben*. 9., verb. und erw. Aufl. Studium. Wiesbaden: Springer Vieweg, 2012.
- [83] W. Song, M. Chen, F. Bai, S. Lin, Y. Chen, and Z. Feng. “Non-uniform effect on the thermal/aging performance of Lithium-ion pouch battery”. In: *Applied Thermal Engineering* 128 (2018), pp. 1165–1174.
- [84] D. Werner, S. Paarmann, A. Wiebelt, and T. Wetzel. “Inhomogeneous Temperature Distribution Affecting the Cyclic Aging of Li-Ion Cells. Part I: Experimental Investigation”. In: *Batteries* 6.1 (2020), p. 13.
- [85] D. Werner, S. Paarmann, A. Wiebelt, and T. Wetzel. “Inhomogeneous Temperature Distribution Affecting the Cyclic Aging of Li-Ion Cells. Part II: Analysis and Correlation”. In: *Batteries* 6.1 (2020), p. 12.

- [86] M. Naumann, F. B. Spingler, and A. Jossen. “Analysis and modeling of cycle aging of a commercial LiFePO₄/graphite cell”. In: *Journal of Power Sources* 451 (2020), p. 227666.
- [87] T. Ohzuku. “Formation of Lithium-Graphite Intercalation Compounds in Nonaqueous Electrolytes and Their Application as a Negative Electrode for a Lithium Ion (Shuttlecock) Cell”. In: *Journal of The Electrochemical Society* 140.9 (1993), pp. 2490–2498.
- [88] J. Li, C. F. Yuan, Z. H. Guo, Z. A. Zhang, Y. Q. Lai, and J. Liu. “Limiting factors for low-temperature performance of electrolytes in LiFePO₄/Li and graphite/Li half cells”. In: *Electrochimica Acta* 59 (2012), pp. 69–74.
- [89] M. F. Hasan, C.-F. Chen, C. E. Shaffer, and P. P. Mukherjee. “Analysis of the Implications of Rapid Charging on Lithium-Ion Battery Performance”. In: *Journal of the Electrochemical Society* 162.7 (2015), A1382–A1395.
- [90] V. Zinth, C. von Lüders, M. Hofmann, J. Hattendorff, I. Buchberger, S. Erhard, J. Rebelo-Kornmeier, A. Jossen, and R. Gilles. “Lithium plating in lithium-ion batteries at sub-ambient temperatures investigated by in situ neutron diffraction”. In: *Journal of Power Sources* 271 (2014), pp. 152–159.
- [91] J. Wandt, P. Jakes, J. Granwehr, R.-A. Eichel, and H. A. Gasteiger. “Quantitative and time-resolved detection of lithium plating on graphite anodes in lithium ion batteries”. In: *Materials Today* (2017).
- [92] S. P. Rangarajan, Y. Barsukov, and P. P. Mukherjee. “In operando signature and quantification of lithium plating”. In: *Journal of Materials Chemistry A* 7.36 (2019), pp. 20683–20695.
- [93] M. C. Smart, B. V. Ratnakumar, L. Whitcanack, K. Chin, M. Rodriguez, and S. Surampudi. “Performance Characteristics of Lithium Ion Cells at Low Temperatures”. In: *Seventeenth Annual Battery Conference on Applications and Advances* (2002).
- [94] C. von Lüders, V. Zinth, S. V. Erhard, P. J. Osswald, M. Hofmann, R. Gilles, and A. Jossen. “Lithium plating in lithium-ion batteries investigated by voltage relaxation and in situ neutron diffraction”. In: *Journal of Power Sources* 342 (2017), pp. 17–23.
- [95] F. B. Spingler, S. Friedrich, S. Kücher, S. Schmid, D. López-Cruz, and A. Jossen. “The Effects of Non-Uniform Mechanical Compression of Lithium-Ion Cells on Local Current Densities and Lithium Plating”. In: *Journal of The Electrochemical Society* 168.11 (2021), p. 110515.
- [96] F. B. Spingler, W. Wittmann, J. Sturm, B. Rieger, and A. Jossen. “Optimum fast charging of lithium-ion pouch cells based on local volume expansion criteria”. In: *Journal of Power Sources* 393 (2018), pp. 152–160.

-
- [97] F. Orsini, A. Du Pasquier, B. Beaudoin, J. Tarascon, M. Trentin, N. Langenhuizen, E. de Beer, and P. Notten. “In situ Scanning Electron Microscopy (SEM) observation of interfaces within plastic lithium batteries”. In: *Journal of Power Sources* 76.1 (1998), pp. 19–29.
- [98] L. Gireaud, S. Grugeon, S. Laruelle, B. Yrieix, and J.-M. Tarascon. “Lithium metal stripping/plating mechanisms studies: A metallurgical approach”. In: *Electrochemistry Communications* 8.10 (2006), pp. 1639–1649.
- [99] V. A. Agubra, J. W. Fergus, R. Fu, and S.-Y. Choe. “Analysis of the Deposit Layer from Electrolyte Side Reaction on the Anode of the Pouch Type Lithium Ion Polymer Batteries: The Effect of State of Charge and Charge Rate”. In: *Electrochimica Acta* 149 (2014), pp. 1–10.
- [100] Z. Li, J. Huang, B. Yann Liaw, V. Metzler, and J. Zhang. “A review of lithium deposition in lithium-ion and lithium metal secondary batteries”. In: *Journal of Power Sources* 254 (2014), pp. 168–182.
- [101] D. Burow, K. Sergeeva, S. Calles, K. Schorb, A. Börger, C. Roth, and P. Heitjans. “Inhomogeneous degradation of graphite anodes in automotive lithium ion batteries under low-temperature pulse cycling conditions”. In: *Journal of Power Sources* 307 (2016), pp. 806–814.
- [102] B. Bitzer and A. Gruhle. “A new method for detecting lithium plating by measuring the cell thickness”. In: *Journal of Power Sources* 262 (2014), pp. 297–302.
- [103] B. Rieger, S. F. Schuster, S. V. Erhard, P. J. Osswald, A. Rheinfeld, C. Willmann, and A. Jossen. “Multi-directional laser scanning as innovative method to detect local cell damage during fast charging of lithium-ion cells”. In: *Journal of Energy Storage* 8 (2016), pp. 1–5.
- [104] LMI Technologies Inc. *Gocator 2400 Series: 3D Smart Line Profile Sensors*. 2020. URL: https://lmi3d.com/wp-content/uploads/2020/07/DATASHEET_Gocator_2400_Series_US_WEB.pdf (visited on 10/28/2021).
- [105] M. Nagayama, K. Ariyoshi, Y. Yamamoto, and T. Ohzuku. “Characterization of Lithium Insertion Electrodes by Precision Dilatometer: Area-Specific Deformation of Single Electrode”. In: *Journal of The Electrochemical Society* 161.9 (2014), A1388–A1393.
- [106] M. Winter, G. H. Wrodnigg, J. O. Besenhard, W. Biberacher, and P. Novák. “Dilatometric Investigations of Graphite Electrodes in Nonaqueous Lithium Battery Electrolytes”. In: *Journal of The Electrochemical Society* 147.7 (2000), pp. 2427–2431.
- [107] W. Biberacher, A. Lurf, J. O. Besenhard, H. Möhwald, and T. Butz. “A high resolution dilatometer for in situ studies of the electrointercalation of layered materials”. In: *Materials Research Bulletin* 17.11 (1982), pp. 1385–1392.

- [108] D. Sauerteig, S. Ivanov, H. Reinshagen, and A. Bund. “Reversible and irreversible dilation of lithium-ion battery electrodes investigated by in-situ dilatometry”. In: *Journal of Power Sources* 342 (2017), pp. 939–946.
- [109] S. Ivanov, D. Sauerteig, A. Dimitrova, S. Krischok, and A. Bund. “Irreversible dilation of graphite composite anodes influenced by vinylene carbonate”. In: *Journal of Power Sources* 457 (2020), p. 228020.
- [110] M. Hahn, O. Barbieri, F. P. Campana, R. Kötz, and R. Gallyay. “Carbon based double layer capacitors with aprotic electrolyte solutions: the possible role of intercalation/insertion processes”. In: *Applied Physics A* 82.4 (2006), pp. 633–638.
- [111] B. Rieger, S. Schlueter, S. V. Erhard, J. Schmalz, G. Reinhart, and A. Jossen. “Multi-scale investigation of thickness changes in a commercial pouch type lithium-ion battery”. In: *Journal of Energy Storage* 6 (2016), pp. 213–221.
- [112] A. Y. R. Prado, M.-T. F. Rodrigues, S. E. Trask, L. Shaw, and D. P. Abraham. “Electrochemical Dilatometry of Si-Bearing Electrodes: Dimensional Changes and Experiment Design”. In: *Journal of The Electrochemical Society* 167.16 (2020), p. 160551.
- [113] H. Michael, F. Iacoviello, T. M. M. Heenan, A. Llewellyn, J. S. Weaving, R. Jervis, D. J. L. Brett, and P. R. Shearing. “A Dilatometric Study of Graphite Electrodes during Cycling with X-ray Computed Tomography”. In: *Journal of The Electrochemical Society* 168.1 (2021), p. 010507.
- [114] G. M. Nishioka. “Adsorption/desorption of water on glass fiber surfaces”. In: *Journal of Non-Crystalline Solids* 120.1-3 (1990), pp. 34–39.
- [115] M. Stich, N. Pandey, and A. Bund. “Drying and moisture resorption behaviour of various electrode materials and separators for lithium-ion batteries”. In: *Journal of Power Sources* 364 (2017), pp. 84–91.
- [116] E. R. Logan, H. Hebecker, A. Eldesoky, A. Luscombe, M. B. Johnson, and J. R. Dahn. “Performance and Degradation of LiFePO₄/Graphite Cells: The Impact of Water Contamination and an Evaluation of Common Electrolyte Additives”. In: *Journal of The Electrochemical Society* 167.13 (2020), p. 130543.
- [117] J. Landesfeind, J. Hattendorff, A. Ehrl, W. A. Wall, and H. A. Gasteiger. “Tortuosity Determination of Battery Electrodes and Separators by Impedance Spectroscopy”. In: *Journal of The Electrochemical Society* 163.7 (2016), A1373–A1387.
- [118] D. A. G. Bruggeman. “Berechnung verschiedener physikalischer Konstanten von heterogenen Substanzen. I. Dielektrizitätskonstanten und Leitfähigkeiten der Mischkörper aus isotropen Substanzen”. In: *Annalen der Physik* 416.7 (1935), pp. 636–664.
- [119] L. O. Valøen and J. N. Reimers. “Transport Properties of LiPF₆-Based Li-Ion Battery Electrolytes”. In: *Journal of The Electrochemical Society* 152.5 (2005), A882–A891.

-
- [120] K. Oldiges, D. Diddens, M. Ebrahimi, J. B. Hooper, I. Cekic-Laskovic, A. Heuer, D. Bedrov, M. Winter, and G. Brunklau. “Understanding transport mechanisms in ionic liquid/carbonate solvent electrolyte blends”. In: *Physical chemistry chemical physics : PCCP* 20.24 (2018), pp. 16579–16591.
- [121] I. Bloom, A. N. Jansen, D. P. Abraham, J. Knuth, S. A. Jones, V. S. Battaglia, and G. L. Henriksen. “Differential voltage analyses of high-power, lithium-ion cells: Technique and application”. In: *Journal of Power Sources* 139.1-2 (2005), pp. 295–303.
- [122] I. Bloom, J. Christophersen, and K. Gering. “Differential voltage analyses of high-power lithium-ion cells: Applications”. In: *Journal of Power Sources* 139.1-2 (2005), pp. 304–313.
- [123] P. Keil, S. F. Schuster, J. Wilhelm, J. Travi, A. Hauser, R. C. Karl, and A. Jossen. “Calendar Aging of Lithium-Ion Batteries”. In: *Journal of The Electrochemical Society* 163.9 (2016), A1872–A1880.
- [124] M. Lewerenz, A. Marongiu, A. Warnecke, and D. U. Sauer. “Differential voltage analysis as a tool for analyzing inhomogeneous aging: A case study for LiFePO₄|Graphite cylindrical cells”. In: *Journal of Power Sources* 368 (2017), pp. 57–67.
- [125] M. Lewerenz, A. Warnecke, and D. U. Sauer. “Introduction of capacity difference analysis (CDA) for analyzing lateral lithium-ion flow to determine the state of covering layer evolution”. In: *Journal of Power Sources* 354 (2017), pp. 157–166.
- [126] S. Nowak and M. Winter. “Elemental analysis of lithium ion batteries”. In: *Journal of Analytical Atomic Spectrometry* 32.10 (2017), pp. 1833–1847.
- [127] B. Vortmann-Westhoven, M. Winter, and S. Nowak. “Where is the lithium? Quantitative determination of the lithium distribution in lithium ion battery cells: Investigations on the influence of the temperature, the C-rate and the cell type”. In: *Journal of Power Sources* 346 (2017), pp. 63–70.
- [128] C. Lürenbaum, B. Vortmann-Westhoven, M. Evertz, M. Winter, and S. Nowak. “Quantitative spatially resolved post-mortem analysis of lithium distribution and transition metal depositions on cycled electrodes via a laser ablation-inductively coupled plasma-optical emission spectrometry method”. In: *RSC Advances* 10.12 (2020), pp. 7083–7091.
- [129] H. Takahara, M. Shikano, and H. Kobayashi. “Quantification of lithium in LIB electrodes with glow discharge optical emission spectroscopy (GD-OES)”. In: *Journal of Power Sources* 244 (2013), pp. 252–258.
- [130] H. Takahara, H. Miyauchi, M. Tabuchi, and T. Nakamura. “Elemental Distribution Analysis of LiFePO₄ /Graphite Cells Studied with Glow Discharge Optical Emission Spectroscopy (GD-OES)”. In: *Journal of The Electrochemical Society* 160.2 (2013), A272–A278.

- [131] D. Guerard and A. Herold. “Intercalation of lithium into graphite and other carbons”. In: *Carbon* 13.4 (1975), pp. 337–345.
- [132] V. A. Nalimova, D. Guérard, M. Lelaurain, and V. Fateev. “X-ray investigation of highly saturated Li-graphite intercalation compound”. In: *Carbon* 33.2 (1995), pp. 177–181.
- [133] S. J. Harris, A. Timmons, D. R. Baker, and C. Monroe. “Direct in situ measurements of Li transport in Li-ion battery negative electrodes”. In: *Chemical Physics Letters* 485.4-6 (2010), pp. 265–274.
- [134] T. F. Fuller, M. Doyle, and J. Newman. “Relaxation Phenomena in Lithium-Ion-Insertion Cells”. In: *Journal of The Electrochemical Society* 141.4 (1994), pp. 982–990.
- [135] E. Zhao, Z.-G. Zhang, X. Li, L. He, X. Yu, H. Li, and F. Wang. “Neutron-based characterization techniques for lithium-ion battery research”. In: *Chinese Physics B* 29.1 (2020), p. 018201.
- [136] P. J. Withers. “Depth capabilities of neutron and synchrotron diffraction strain measurement instruments. I. The maximum feasible path length”. In: *Journal of Applied Crystallography* 37.4 (2004), pp. 596–606.
- [137] J. B. Siegel, X. Lin, A. G. Stefanopoulou, D. S. Hussey, D. L. Jacobson, and D. Gorsich. “Neutron Imaging of Lithium Concentration in LFP Pouch Cell Battery”. In: *Journal of The Electrochemical Society* 158.5 (2011), A523.
- [138] J. Wilhelm, S. Seidlmayer, S. Erhard, M. Hofmann, R. Gilles, and A. Jossen. “In Situ Neutron Diffraction Study of Lithiation Gradients in Graphite Anodes during Discharge and Relaxation”. In: *Journal of The Electrochemical Society* 165.9 (2018), A1846–A1856.
- [139] M. J. Mühlbauer, D. Petz, V. Baran, O. Dolotko, M. Hofmann, R. KostECKI, and A. Senyshyn. “Inhomogeneous distribution of lithium and electrolyte in aged Li-ion cylindrical cells”. In: *Journal of Power Sources* 475 (2020), p. 228690.
- [140] D. Petz, M. J. Mühlbauer, A. Schökel, K. Achterhold, F. Pfeiffer, T. Pirling, M. Hofmann, and A. Senyshyn. “Heterogeneity of Graphite Lithiation in State-of-the-Art Cylinder-Type Li-Ion Cells”. In: *Batteries & Supercaps* 4.2 (2021), pp. 327–335.
- [141] A. Senyshyn, M. J. Mühlbauer, O. Dolotko, M. Hofmann, and H. Ehrenberg. “Homogeneity of lithium distribution in cylinder-type Li-ion batteries”. In: *Scientific reports* 5 (2015), p. 18380.
- [142] J. F. Ziegler, G. W. Cole, and J. E. E. Baglin. “Technique for determining concentration profiles of boron impurities in substrates”. In: *Journal of Applied Physics* 43.9 (1972), pp. 3809–3815.

-
- [143] T. W. Verhallen, S. Lv, and M. Wagemaker. “Operando Neutron Depth Profiling to Determine the Spatial Distribution of Li in Li-ion Batteries”. In: *Frontiers in Energy Research* 6 (2018).
- [144] F. Linsenmann, M. Trunk, P. Rapp, L. Werner, R. Gernhäuser, R. Gilles, B. Märkisch, Z. Révay, and H. A. Gasteiger. “A Liquid Electrolyte-Based Lithium-Ion Battery Cell Design for Operando Neutron Depth Profiling”. In: *Journal of The Electrochemical Society* 167.10 (2020), p. 100554.
- [145] J. Wilhelm. “Diffraction analysis of anode inhomogeneity in lithium-ion batteries”. PhD thesis. Technische Universität München. URL: <https://mediatum.ub.tum.de/?id=1574633>.
- [146] J. Sieg, M. Storch, J. Fath, A. Nuhic, J. Bandlow, B. Spier, and D. U. Sauer. “Local degradation and differential voltage analysis of aged lithium-ion pouch cells”. In: *Journal of Energy Storage* 30 (2020), p. 101582.
- [147] H. Wang and J. F. Whitacre. “Inhomogeneous aging of cathode materials in commercial 18650 lithium ion battery cells”. In: *Journal of Energy Storage* 35 (2021), p. 102244.
- [148] M. Storch, J. P. Fath, J. Sieg, D. Vrankovic, C. Krupp, B. Spier, and R. Riedel. “Temperature and Lithium Concentration Gradient Caused Inhomogeneous Plating in Large-format Lithium-ion Cells”. In: *Journal of Energy Storage* 41 (2021), p. 102887.

List of Publications

First Author Journal Publications Incorporated in the Main Text

- I **Franz B. Spingler**, Wilhelm Wittmann, Johannes Sturm, Bernhard Rieger, Andreas Jossen: *Optimum fast charging of lithium-ion pouch cells based on local volume expansion criteria*, in: *Journal of Power Sources* 393, pp. 152–160, 2018
- II Yan Zhao, **Franz B. Spingler**, Yatish Patel, Gregory J. Offer, Andreas Jossen.: *Localized Swelling Inhomogeneity Detection in Lithium Ion Cells Using Multi-Dimensional Laser Scanning*, in: *Journal of The Electrochemical Society* 166 (2), pp. A27–A34, 2019
- III **Franz B. Spingler**, Maik Naumann, Andreas Jossen: *Capacity Recovery Effect in Commercial LiFePO₄ / Graphite Cells*, in: *Journal of The Electrochemical Society* 167, 040526, 2020
- IV **Franz B. Spingler**, Simon Kücher, Robert Phillips, Erfan Moyassari Andreas Jossen: *Electrochemically Stable In-Situ Dilatometry of NMC, NCA and Graphite Electrodes for Lithium-Ion Cells compared to XRD measurements*, in: *Journal of The Electrochemical Society* 168 040515, 2021
- V **Franz B. Spingler**, Sven Friedrich, Simon Kücher, Simon Schmid, Daniel López-Cruz, Andreas Jossen: *The Effects of Non-Uniform Mechanical Compression of Lithium-Ion Cells on Local Current Densities and Lithium Plating*, in: *Journal of The Electrochemical Society* 168 110515, 2021

Other Relevant Co-Author Journal Publications

- I Till Günther, Nicolas Billot, Jörg Schuster, Joscha Schnell, Franz B. Spingler, Hubert A. Gasteiger: *The Manufacturing of Electrodes: Key Process for the Future Success of Lithium-Ion Batteries*, in: *Advanced Materials Research* 1140, pp. 304–311, 2016
- II Simon V. Erhard, Patrick J. Osswald, Peter Keil, Eike Höffer, Manuel Haug, Andreas Noel, Jörn Wilhelm, Bernhard Rieger, Korbinian Schmidt, Stephan Kosch, Frank M. Kindermann, Franz B. Spingler, Hauke Kloust, Torge Thoennessen, Alexander Rhein-feld, Andreas Jossen: *Simulation and Measurement of the Current Density Distribution in Lithium-Ion Batteries by a Multi-Tab Cell Approach*, in: *Journal of The Electrochemical Society* 164 A6324, 2017

- III Johannes Sturm, Franz B. Spingler, Bernhard Rieger, Alexander Rheinfeld, Andreas Jossen: *Non-Destructive Detection of Local Aging in Lithium-Ion Pouch Cells by Multi-Directional Laser Scanning*, in: *Journal of The Electrochemical Society* 164 A1342, 2017
- IV Markus H. Hofmann, Kevin Czyrka, Martin J. Brand, Marco Steinhardt, Andreas Noel, Franz B. Spingler, Andreas Jossen: *Dynamics of current distribution within battery cells connected in parallel*, in: *Journal of Energy Storage* 20, pp. 120 – 133, 2018
- V Johannes Sturm, Alexander Rheinfeld, Ilya Zilberman, Franz B. Spingler, Stephan Kosch, Fabian Frie, Andreas Jossen: *Modeling and simulation of inhomogeneities in a 18650 nickel-rich, silicon-graphite lithium-ion cell during fast charging*, in: *Journal of Power Sources* 412, pp. 204 – 223, 2019
- VI Maik Naumann, Franz B. Spingler, Andreas Jossen: *Analysis and modeling of cycle aging of a commercial LiFePO₄/graphite cell*, in: *Journal of Power Sources* 451 227666, 2020
- VII Erfan Moyassari, Thomas Roth, Simon Kücher, Chia-Chin Chang, Shang-Chieh Hou³, Franz B. Spingler, Andreas Jossen: *The Role of Silicon in Silicon-Graphite Composite Electrodes Regarding Specific Capacity, Cycle Stability, and Expansion*, Submitted to *Journal of The Electrochemical Society*, 11/2021

Acknowledgment

I am grateful for the privileged working conditions I have enjoyed over the past six years at the Chair of Electrical Energy Storage: extensive autonomy in research and in the completion of other tasks, far-reaching technical and financial possibilities and a great, collegial atmosphere. In addition to advice, support, and trust, I would like to thank Prof. Dr. Andreas Jossen for creating this working environment, and TUM and the Free State of Bavaria for providing the necessary means.

I am also indebted to: Carolin Nierwetberg, who helped me in all administrative matters, Korbinian Schmidt and Jens Dietrich for building every test rig imaginable, and Dr. Gudrun Rahn-Koltermann, who always found a suitable source for funding. To my colleagues past and present, for being true companions and my ex-supervisor become colleague, Dr. Simon Erhard, for introducing my sense-seeking student self to battery research. To my students for their numerous contributions to my research, especially to Simon Kücher, who had my back in all laboratory matters while I wrote this thesis.

Finally, I would like to thank Prof. Dr. Michael Danzer for acting as second examiner, and Robert Phillips, Sven Friedrich, Dr. Markus Schindler and my father for proofreading my thesis manuscript.

